Process Monitoring and Closed Loop Control in Electron Beam Melting Process using Near Infrared Imaging

Yuxing Cui

Engineering Doctorate in Material Science and Engineering

October 2018

I. SUMMARY

The camera installed by ARCAM into the Q series machine is able to take images after each layer is completed; as such, it is able to capture images of defects within each layer, the majority of which are tunnelling or chimney defects, referred to as Lack of Fusion (LOF) in this thesis.

A programme has been developed over the course of this Engineering Doctorate project, named LayerDD. Using MatLab and based on the images taken during the EBM process, it is able to automatically detect, filter and extract defects found in each layer and output these defects in a 3D STL file format. The output defect prediction is capable of overlaying with the original build configuration. Verification of LayerDD result has performed against CT and cut-up specimen, which has shown a good consistency in LOF prediction. Some of the small defects from the LayerDD prediction have resulted in dimensional error or have not been able to be found. These limitations are mainly due to the LayerDD system being unable to know what is happening beneath the current layer.

on the results from the LayerDD system, a close loop control algorithm can be used to rectify the defects during the process. Experiments have been performed manually with the current Q20 Plus system and it has been found out from this research that the ability to fix defects is mainly associated with the depth of melt pool.

Further testing is required to prove the LayerDD system is stable and produce accurate results in order for it to be applied to the aerospace industry. Further development on the close loop control is required for it to be fully integrated with the EBM system

II. Contents

III. NOMENCLATURE

Abbreviation	Meaning
Bo	Bond Number
C-bar	Cut up Specimen
CLF	Close loop Control
CMM	Coordinate Measurement Machine
DFD	Defect Fixing Depth
DR	Defect remain
EBM	Electron Beam Melting
ED	Energy Density
EDM	Electron Discharge Machine
EDR	Energy Density Ratio
FFC	Fray Farthing Chen
FO	Focus Offset
FWHM	Full Width at Half Maximum
HIP	Hot Isostatic Pressing
IR	Infrared
LO	Line Offset
LOF	Lack of Fusion
LRP	LOF removal probability
NIR	Near Infrared
P-bar	Prolongation Specimen
RP	Rapid Prototyping
S-bar	Separated Specimen
SF	Speed Function
SLM	Selective Laser Melting
TRL	Technology Review Level

IV. ACKNOWLEDGEMENTS

It would not been possible to complete this project without the help and support of many people from the University of Sheffield Department of Engineering Material and GKN Aerospace AMC department. This work is testament to the generosity of the people I have worked with in terms of both their time and expertise.

My initial thanks go to my supervisor Professor Iain Todd and my industrial supervisor Dr Simon Mckown who made my transition back to the department seamless and supplied me with more ideas in four years than I will ever have. I shall always be grateful for his advice, support and meetings.

I would like to thank Dr Bob Bradley who is my Additive Manufacturing mentor and trusting me with the opportunity of this Engineering Doctorate research; I also appreciate help received from my line manager in GKN Aerospace Tim Hope who give me plenty of support and freedom to pursue my research.

I would like to acknowledge the titanium alloy knowledge from Dr Alphons Antonysamy; process knowledge from Dr Simon Mckown; testing knowledge from Vukile Dumani; Aerospace knowledge from Hamish Rudram; and all information acquired from GKN AMC team members.

I would like to appreciate the help from my colleagues to help me proofread my thesis: Jon McAlinden, Hamish Rudram, Catherine Bulter, Dr. Martin White.

Finally, I would like to thank my wife Huamei Wu for supporting me with my research, and my three year old daughter Yanran Cui who keeps my life entertained.

Chapter 1 : Introduction

1.1 Additive Manufacturing

Additive Manufacturing (AM) or 3D-Printing is generally defined as a process that manufactures a component layer by layer from a CAD file. The key characteristic of AM technology is that it is capable of making a new physical object directly from CAD with the least amount of time compared to any other traditional manufacturing methods. The technology has attracted significant attention over the last few decades, with many people stating the AM could be starting the next 'industrial revolution' [1,2,3]. In 2018, AM technology has already been used in many industries including food, automotive, aerospace, sport, fashion with a plethora of the materials from almost a wide array of families and for many diverse applications [4,5,6,7].

The use of metallic components in the aerospace industry is significant because the cost of aircraft parts is primarily determined by the 'buy to fly' ratio. AM technologies are capable of offering direct manufacturing and a minimal requirement for machining and post processing. In addition, the complex optimized structures that can be made using AM could create a huge potential saving on both aerospace production cost and fuel consumption. However, as the aerospace industry has one of the highest quality standards and AM's metallic capability is still in its infancy, there are still many challenges to overcome before the current AM processes become a mature aerospace manufacturing technology.

In this work, research is primarily focused on the Electron Beam Melting AM technology developed by ARCAM, with the material used being Ti6Al4V. Electron Beam Melting (EBM) is a type of powder bed AM technique which uses an electron beam as the energy source to melt the powder at an already elevated temperature inside a high vacuum chamber. The EBM

system is built based on a one-dimensional thermal model with many functions to predict the best energy input for each individual location in a layer. As the system control is constructed based on prediction, uncertainty is always associated with the process, and the consequence of these uncertainties is eventually a degrading of the final product quality.

Due to the likelihood of presenting large defects during the EBM process, the main focus of this work to understand, identify, monitor and fix the defects to improve both process and product quality.

The project is fully funded by GKN AMC in collaboration with University of Sheffield.

1.2 Project Aim

The aim of this work is to use the ARCAM installed camera to monitor the accuracy of defect growth during the printing process, and subsequently predict the spread of defects within a finished component. The research further investigates the possibility of fixing the defect during the process with a developed closed loop control (CLC) algorithm.

1.3 Thesis Outline

Chapter 1 is an introduction to the research and processes involved

Chapter 2 is a literature review section focusing on the EBM process and the corresponding defects. Additionally, some existing research regarding process monitoring and EBM related post processing in aerospace are also introduced.

Chapter 3 details the general experimental instruments used in this thesis and the corresponding experimental steps. Some self-developed tools are described in this section, which are used to analyse and interpret experimental data.

Chapter 4 illustrates Lack of Fusion (LOF), the possible causes of LOF and how LOF appears in the layer-wise images.

Chapter 5 illustrates a technique for finding Lack of Fusion (LOF) type defects in EBM processes which is named LayerDD (**Layer**wise **D**efect **D**etection). The chapter begins with the procedure and algorithm used to identify the LOF and compares the identified LOF with other existing LOF identification techniques, illustrating the technical ability and corresponding limitations of the LayerDD system.

Chapter 6 illustrates the potential of fixing the LOF layer-wisely during the EBM process by changing the process parameters. The experiment is investigated through three main parameters modifications: Line offset, Speed Function and Focus offset. The effectiveness of different parameters on the LOF fixing is assessed by the software stated in Chapter 4.

Chapter 7 documents the key conclusions from this work.

Chapter 8 suggests avenues for further work which are discussed as a result of the investigations in previous chapters.

Chapter 2 : Literature Review

2.1. Titanium

Titanium was first found by chemist William Gregor in 1791. Two years later, in 1793, a German chemist, Martin Heinrich Klaproth, discovered the same element in ilmenite ore (mineral contain mainly $FeTiO_3$) and gave it the name Titanium.[8] Both Gregor and Klaproth proved the element difficult to be isolated, due to titanium having a high reactivity at high temperature with oxygen and nitrogen. Thus the manufacturing of titanium requires a high concentration of inert gas or vacuum conditions.[9]

Not until 1910 did metallurgist Matthew Albert Hunter successfully isolate the titanium element using the Hunter process, with the use of sodium. Later, in 1940, the Hunter process was replaced with the more economical Kroll process, where magnesium is used to reduce $TiCl_4$.[9]

In 2000, the Fray-Farthing-Chen (FFC) Cambridge process used a direct electrochemical reduction of TiO2 in a molten bath of CaCl2,[10] which involves fewer steps and less time. This method is currently being developed into a commercial process with the aim of producing cheap titanium powder. The current commercial purity of titanium is approximately 99.2-99.5%.[11]

In general, titanium is a very reactive and low thermal conductivity element, the properties of the element are listed in Table 2.1.

Table 2.1. Properties of elemental titanium

Property	***Value***
Atomic Number	22
Electron configuration	[Ar] 3d2 4s2
Atomic Weight	47.9
Colour	Dark grey
Density	4.51 g/cm^3
Melting Point	1668+/-10 °C
Boiling Point	3260 °C
Solidus/liquidus	1725 °C
Specific heat at 25 °C	522.3 J/(kgK)
Thermal Conductivity	11.4 W/(mK)
Heat of fusion	440 kJ/kg
Heat of vaporization	9830 kJ/kg

2.1.1. Titanium Alloy

Pure titanium, as well as the majority of titanium alloys, has an ideal hexagonal body-centred cubic (hcp) structure at low temperature, which is termed as α titanium; when the temperature of titanium is higher (882 ± 2 °C), the body-centred cubic (bcc) structure is more stable, which is termed as β titanium. As shown in Figure 2.1, both α and β titanium are shown in a schematic diagram with the densest plane of atoms highlighted.[12]

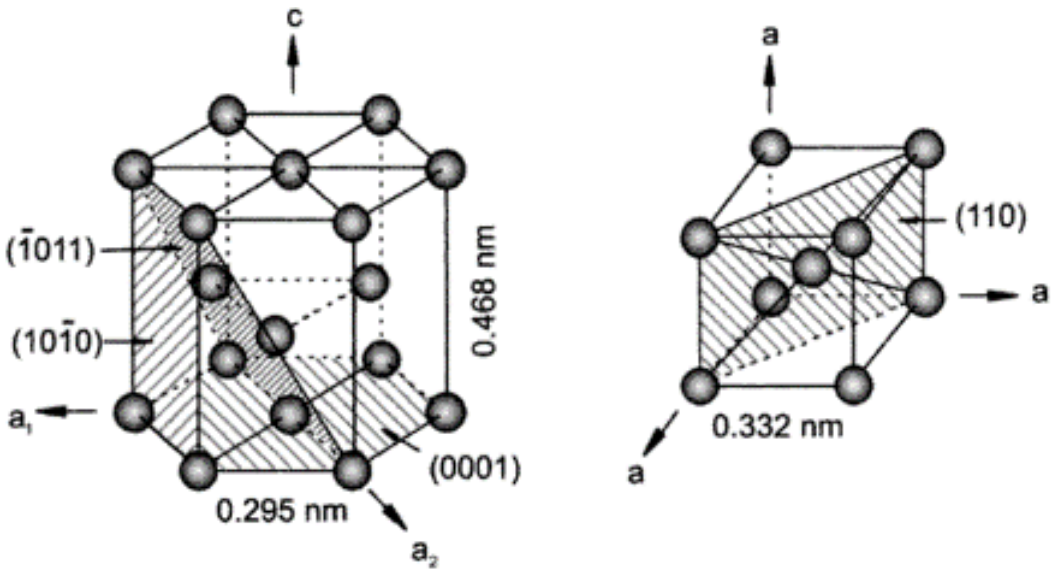

Figure 2.1 Crystal structure of hcp α and bcc β phase (schematic)[12]

Pure titanium has a Yield Strength from 170 MPa to 485 [13], The highest equivalent to some low carbon steel, but less dense; some alloys of titanium can achieve tensile strength of more than 1400 MPa,[14,15] such as TIMETAL LCB (β titanium alloy).

Ti-6Al-4V (Ti6Al4V) is a popular α/β alloy with key chemical composition, as described by its name, of 6% aluminium and 4% vanadium. The aluminium is to increase the strength of the alloy by solid solution hardening and α-phase stabilisation. The vanadium addition stabilises β phase, which significantly improves the room temperature ductility.[16]

According to ASTM grading systems [13], there are three different grades of Ti6Al4V, as shown in Table 2.2. Grade 5 Ti6Al4V is a typical α/β titanium alloy; the ELI Ti6Al4V improves the corrosion cracking properties in seawater with reduced interstitial elements (O, N, C); by further adding of ruthenium to the ELI, the corrosion resistance is further improved. For most of the last half of the twentieth century, Ti6Al4V accounted for about 45% of the total weight of all titanium shipped[13].

Table 2.2 Different ASTM grades of Ti6Al4V [13]

Name	Grade	Weight Percentage [%]								
		O	N	C	H	Fe	Al	V	Ru	Residual
Ti-6Al-4V Alpha beta alloy	5	0.2	0.05	0.08	0.015	0.4	5.5-6.75	3.5-4.5		0.4
Ti-6Al-4V Extra low interstitials (ELI)	23	0.13	0.03	0.08	0.013	0.25	5.5-6.5	3.5-4.5		0.4
Ti-6Al-4V Ru Extra low interstitials (ELI)	29	0.13	0.03	0.08	0.013	0.25	5.5-6.5	3.5-4.5	0.08-0.14	0.4

Apart from good corrosion resistance, Ti6Al4V has very high yield strength, fatigue strength and high modulus of elasticity, but relatively low ductility; the maximum service temperature

is 300 to 400C. Ti6Al4V has been used in aircraft fans, low pressure compressors and front stages in high pressure compressor regions of gas turbine engines.[9,17] In the airframe section, Ti6Al4V is also used for general structural materials, bolts and seat rails, etc.[17]

2.1.2. Titanium Alloy Application in the Aerospace Industry

Titanium alloys use has been very popular in the aerospace industry is the last few decades due the several advantages over the traditional steel, aluminium alloys and nickel based super alloys:[18,19,20]

- The density of titanium is only about 60% of that of steel or nickel-base super alloys, but the tensile strength of titanium alloy can be comparable to lower-strength martensitic stainless steel.[18]
- Space saving due to strength to volume ratio, which has substituted for Al alloys and steels in Boeing 737,747,757 in the landing gear design[21]
- High operating temperature, where it can be achieved up to 595°C, can be used in plug and nozzle area in aircraft [9,21]
- Titanium forms a layer of titanium oxide upon exposure to the air, which is corrosion resistant apart from very strong acid [20]
- Titanium alloy is more compatible to composite than aluminium, since the thermal expansion is nearly 1/3 of aluminium alloy, which creates less stress when there is temperature variation [21]

The combination of the above advantages of titanium is significant to the aerospace industry, and the usage of titanium has increased from year to year as the aircraft history shows in Figure 2.2, but the high cost associated with titanium alloy components has become the major limiting factor for many applications.

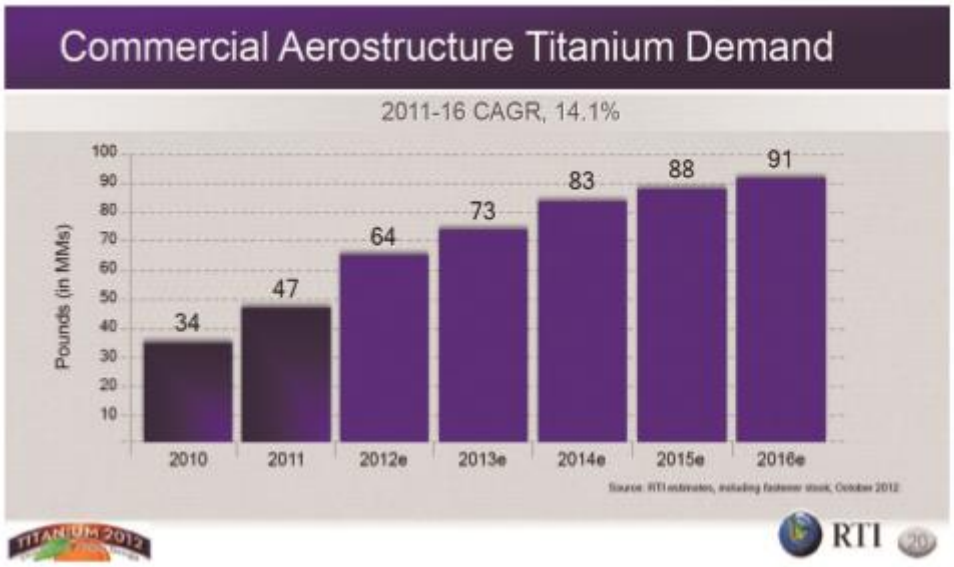

Figure 2.2 Growth of use titanium in aerospace [22]

Titanium is an expensive material to begin with. The high melting temperature of titanium (1668 °C compared to aluminium of 660 °C) leads to high energy for ore separation, ingot melting. The high material reactivity requires an inert or vacuum atmosphere with an extra step for material extraction.[21] A sample cost comparison in shown in Table 2.3,[23] where a sponge (metal) of titanium is already more expensive than a sheet of aluminium by weight. Titanium alloy has also very poor machinability[24,25] due to its chemical reactivity and low thermal conductivity (11.4 W/ (Km) compared to aluminium of 227 W/ (Km)), which tends to weld to the cutting tool during machining and reduces the tool lifetime.[25] This contributes to a much higher machining/milling cost compared to aluminium or steel. As a result, all these challenges have driven the need of net shape or near net shape technology, such as AM.

Table 2.3 Cost of Titanium, Steel, and Aluminium to manufacture [23]

Material Cost ($/pound)			
Item	Steel	Aluminium Alloy	Titanium Alloy
Ore	0.02	0.01	0.22 (rutile)
Metal	0.1	1.1	5.44
Ingot	0.15	1.15	9.07
Sheet	0.30-0.60	1.00-5.00	15.00-50.00

2.2. Additive Manufacturing Background

Additive manufacturing (AM), additive layer manufacturing (ALM), 3D printing and rapid prototyping (RP) all refer to a process defined as a methodology for manufacturing parts by the method of adding material in a ayerwise manner. Figure 2.3 illustrates a general process of AM which covers the steps from the design of CAD to the final part manufacture.

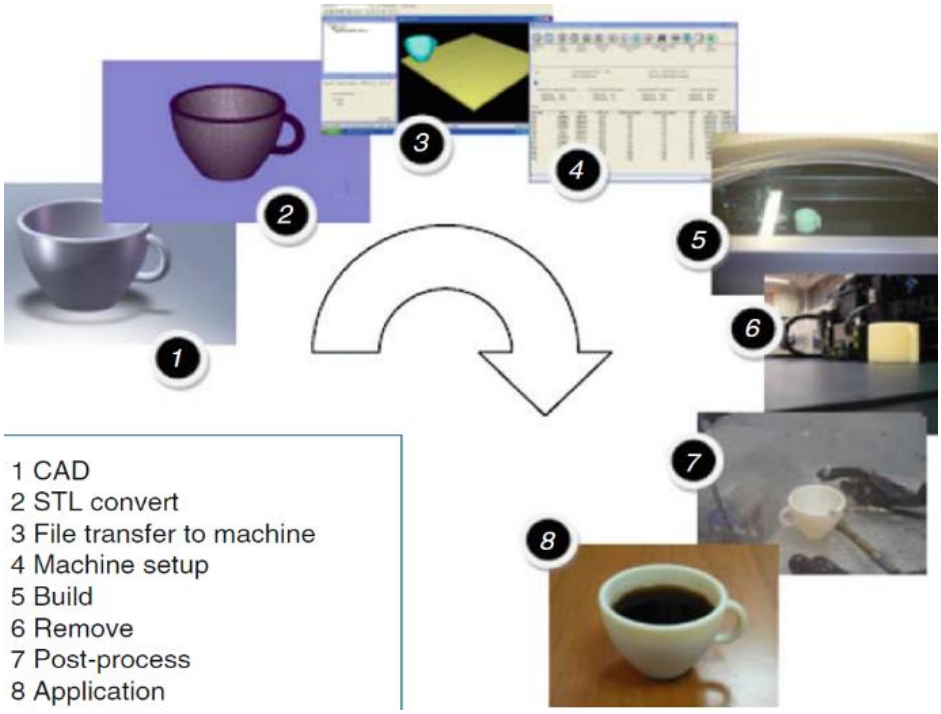

Figure 2.3 Generic process of CAD to parts [26]

The technology has been rapidly developed in the last few decades, which has adapted numerous energy sources, multiple material feeding systems and is capable of manufacturing parts with many different material types. The technology has branched itself to many different sub-categories, [27,28,29] some popular AM technologies are shown in Table 2.4.

All the different AM technologies have the following common advantages of:

- ✓ Material Saving
- ✓ Mould free
- ✓ Fast speed prototyping
- ✓ High design freedom
- ✓ Geometry complexity

Table 2.4 Common AM technologies[27,28,29]

Technology Name	Abbr.	Material Feeding System	Energy Source	Primary material
Fuse Deposition Modelling	FDM	extrusion nozzle	electric heater	polymer, food, composite, etc.
Multijet Modelling	MJM	extrusion nozzle	UV radiation	polymer
StereoLithography	SLA	liquid bed	UV radiation	resin/polymer
Liquid Thermal Polymerization	LTP	liquid bed	thermal radiation	polymer
Beam Interference Solidification	BIS	liquid bed	laser interference	polymer
Selective Laser Melting	SLM	powder bed	laser	metallic
Electron Beam Melting (ARCAM)	EBM	powder bed	electron beam	metallic
Selective Laser Sintering	SLM	powder bed	laser	polymer, metal
Binder Jet		powder bed	glue/binders	metallic
Direct metal Deposition	DMD	powder blown	laser	metallic
Electron Beam Additive Melting (Sciaky)	EBAM	wire feed	electron beam	metallic
Laser Wire Deposition	LWD	wire feed	laser	metallic

2.3. Electron Beam Melting

Electron Beam Melting (EBM) process is a hot powder bed fusion process. The powders are pre-alloyed and spread from the material storage hopper to the bed with a rake. The process uses electron as the energy beam to the powder according to the cross-section of geometry, and then fuses the powder together layer by layer to build a part. The schematic diagram of the EBM process is shown in Figure 2.4b, and currently (2018), the only commercial manufacturer for EBM machine is ARCAM AB (Sweden) founded in 1997.

Figure 2.4 shows the design of an EBM system by ARCAM AB, where the electrons are generated from heated cathode (tungsten or LaB6 crystal) and accelerated to the anode direction. The electron beam is shaped, focused and deflected by astigmatism coil, focus coil and deflection coil, correspondingly. Since the deflection of beam is done through the magnetic force, the beam deflection will be almost instantaneous. A thermocouple is placed near to the coils to monitor the temperature, which prevent overheating of coil section due to the smoke generated during the melting process.

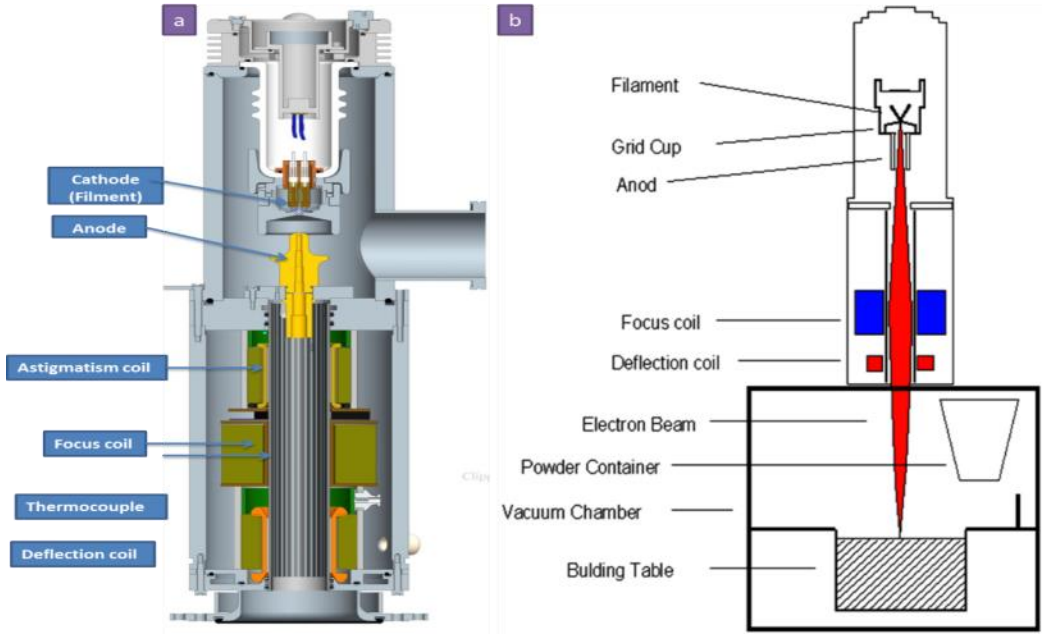

Figure 2.4 [a] EBM gun [b] Schematic diagram of EBM process [30]

Since electrons can be easily attracted to any gas particle and titanium is very oxygen-affinitive at elevated temperature, the build chamber must be vacuumed to mbar before the process starts. A small amount of helium (mbar) is then introduced, this small amount of inert gas helps to suppress evaporation and static charge build up in the powder. dvantage of using helium rather than argon is due to helium a smaller atomic number which is less likely to interact with the electron beam.

2.3.1. EBM Melt Pool of TI6Al4V

Spattering

In general, the melt pool characteristics between electron beam melting (EBM) and selective laser melting (SLM) are very similar apart from the electron-material interaction and the surrounding temperature. Spatter formation in the powder bed process could have a great influence on the top surface quality, internal defects and mechanical properties. Most of the time, the spattering level is directly proportional to the energy density level of the process.[31,32] Di et al.[32] have investigated on the formation of spattering in the SLM process, and categorised spatter formation into three types, as shown in Figure 2.5.

During the process, the temperature at the beam incident region increases rapidly, which causes violent vaporisation of liquid metal. The gas from the melt pool expands rapidly which causes recoil pressure.[33] The recoil pressure from the expanded gas will eject metal liquid, which forms Type-I spatter. Due to the Marangoni effect, the metal liquid flows from the high temperature region (bottom of the melt pool) to the low temperature region (sidewall and edge). The recoil pressure occasionally jet out the low viscidity metal liquid and then forms spherical droplets, which is the Type-II spatters. Moreover, some liquid metal at the front of the beam location with the cold particle could also 'blown' away by the gas flow and splashes onto front-end powder particles, forming the Type-III spatter.[34]

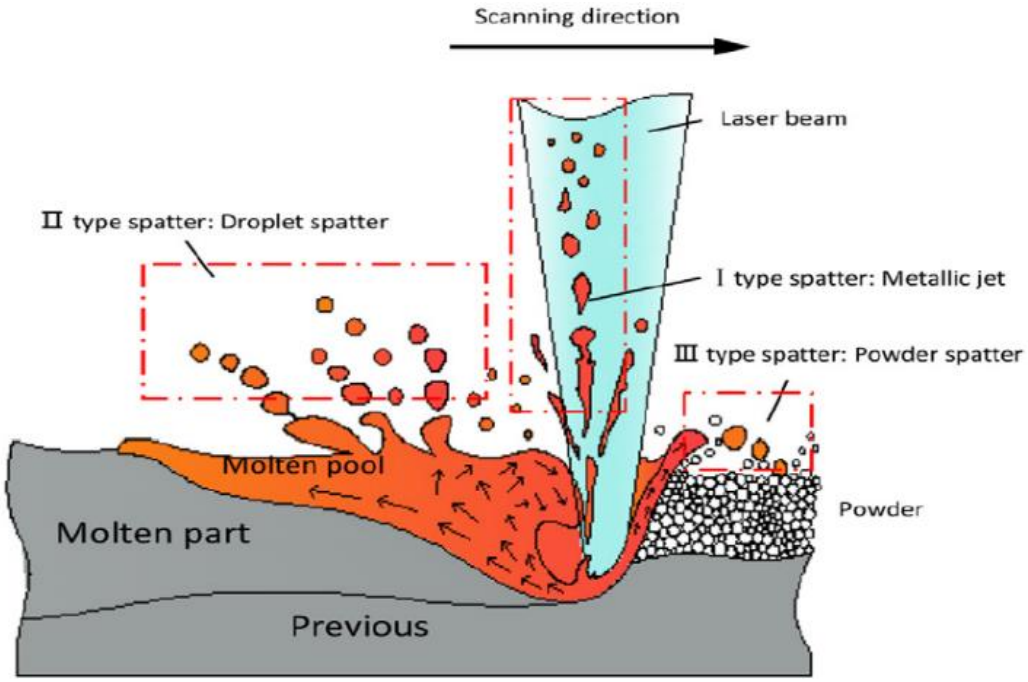

Figure 2.5 Spatter formed in SLM process[34]

In most SLM machines, the majority of spatter is removed from the powder bed surface by a high velocity shielding gas.[35] As in vacuum processes such as EBM, the spatter can formed more easily due to a low chamber pressure. Without any shielding gas, spatters become more harmful to the parts' quality.[36,37]

For the melt pool of the AM process, the pressure within the keyhole needs to maintain the vapour cavity (keyhole) open, while the pressure of atmosphere and force of surface tension will try to close the cavity. Thus, the pressure generated within the melt pool must be greater or equal to the pressure closing force.[38,39] Therefore, the equation of pressure (P) is:

Equation 2.1

$$P = P_{atm} + \sigma/r$$

Where P_{atm} is the atmosphere pressure; σ is the surface tension and r is the dimension of melt pool diameter. Since the EBM process is carried out under controlled vacuum conditions, the atmospheric pressure will be considered negligible in comparison with the pressure from surface tension.

Surface Tension on the Shape of the Melt Pool

The surface tension not only closes up the keyhole opening, but is also responsible for the shape of the melt pool. The bond number is a measure for the ratio of volume forces (gravity force over surface tension):

Equation 2.2

$$Bo = \frac{\rho \times g \times L^2}{\sigma}$$

Where ρ, g, L and σ are denote the density, gravity, characteristic length scale and surface tension, respectively.[40]

Due to the size of the melt pool being significantly small in the EBM process, the bond number is thus only approximately 10^{-3} to 10^{-5}, which indicates that the fundamental behaviour of the melt pool is governed by surface tension and capillary force.[41]

Marangoni flow is driven by the surface tension gradient, thus the flow in the EBM melt pool will be either positive or negative depending on the gradient of surface tension vs. temperature. Figure 2.6 shows the melt pool flow due to surface tension. As investigated by Egry et al.[42], the surface tension properties of molten Ti6Al4V have negative gradient with respect to the temperature, as shown in Figure 2.7, thus the Marangoni flow direction in the Ti6Al4V melt pool will be negative (Figure 2.6 a & b).

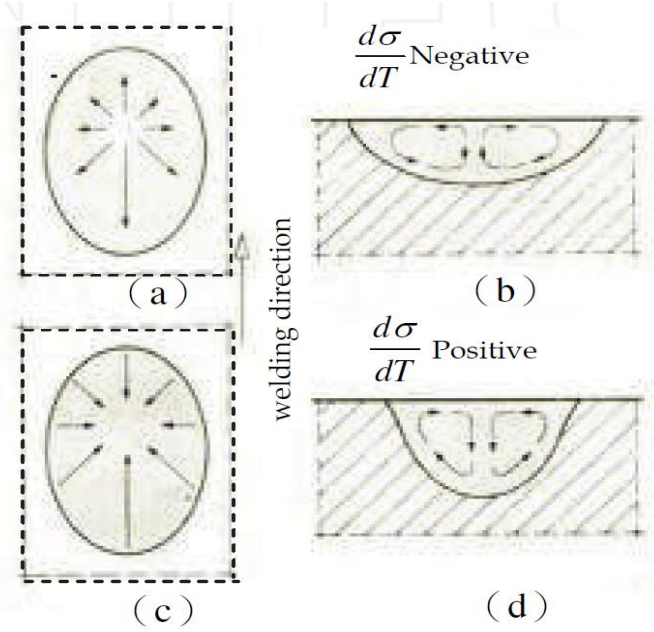

Figure 2.6 Effect of surface tension on melt pool flow [43]

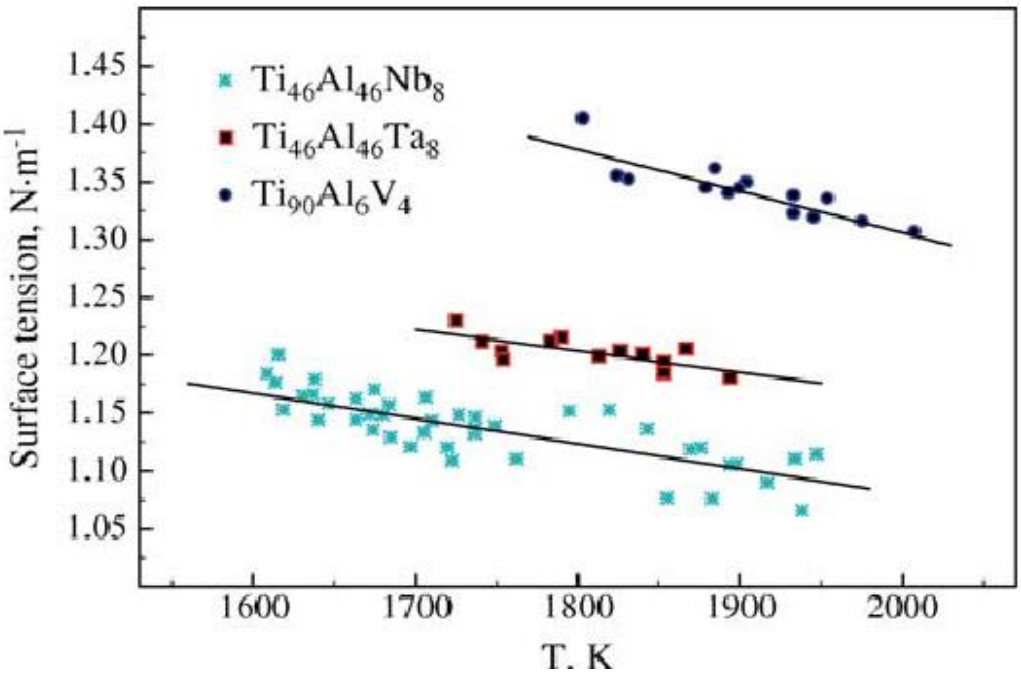

Figure 2.7 Surface tension of Ti6Al4V vs. Temperature [42]

The effect of surface tension on the melt pool is also the reason for balling and discontinuous melt track.[44] Balling often occurs when the melt pool is very small or the length to width ratio is very large.[44] In the EBM or SLM process, the melt pool is approximately the shape of a half cylinder; therefore, the reduction of surface energy will lead the melt material to curve up (balling).[45] A similar effect will be produced when the melt pool is very small, which could

break the melt track (discontinuous melt track). Thus, many researches mention that, due to the melt pool size in SLM or EBM being very small, in order to establish a good melt track, the melt pool needs to have a low length to width ratio.[44,45,46]

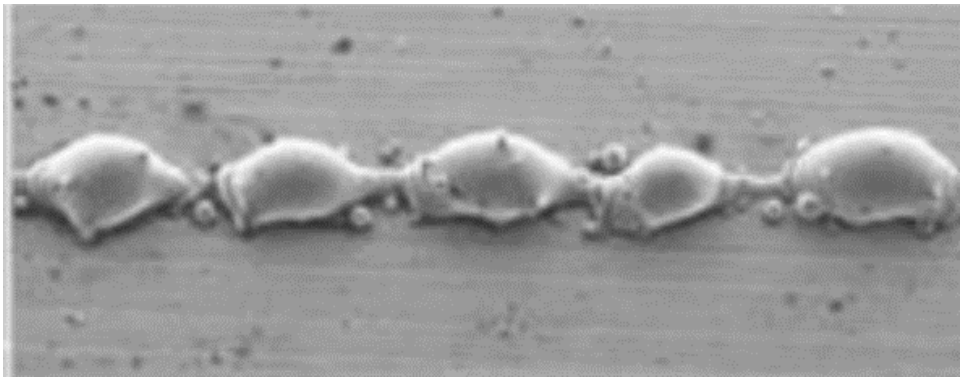

Figure 2.8 Discontinuous melt or ball effect due to surface tension [44]

Effect of Process Parameter

Energy density is used as a popular term in the AM process. In general, it is expressed as energy per unit volume. As long as the printed parts , reduction in beam power will decrease the size of melt pool and increase the cooling rate. As a result, the microstructure will become finer and the tensile properties (TS and YS) will be slightly improved. Further decrease in energy density will unfortunately increase the porosity percentage.

Gong et al.[47] have performed mechanical testing on the different parameter settings for the EBM process on an S400 machine. The test matrix and result is shown in Figure 2.9.

Parameter	EBM-OP 1	EBM-MP 2	EBM-MP 3
Max Current (mA)	21	30	20
Speed Function	98	60	180
Line offset (mm)	0.1	0.2	0.2
Focus offset (mA)	3	15	5
Estimated Porosity (vol%)	0	1	5
0.2% Proof Stress (MPa)	962	947	-
UTS (MPa)	1012	1011	423
Elongation (%)	8.8	9	0.4
Young's Modulus (GPa)	121	120	92

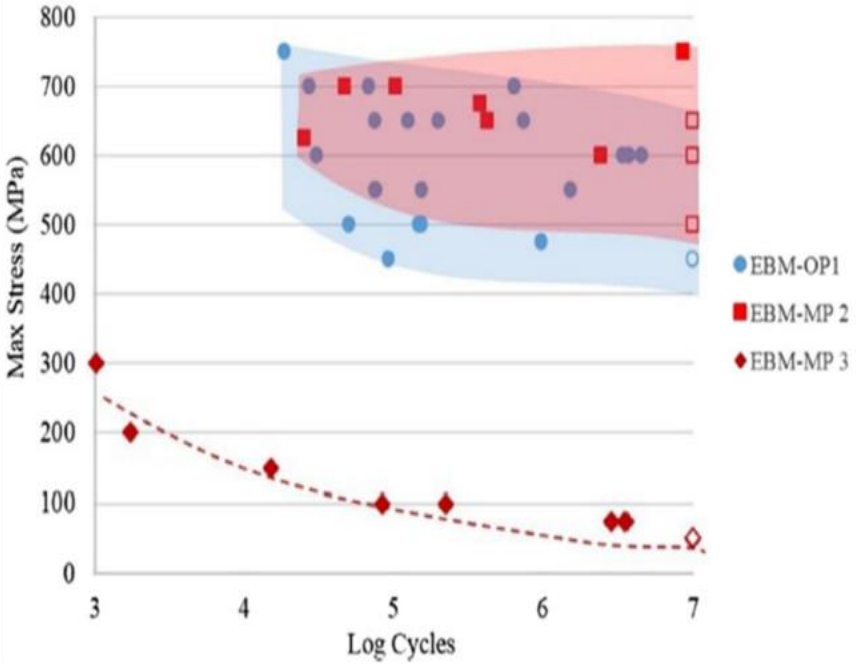

Figure 2.9 EBM process parameter and mechanical result[47]

Al-Bermani [9] has performed some investigation on the effect of EBM focus offset on the shape of melt pool on Ti6Al4V base plate with beam speed 49 mm/s and beam current 6 mA as shown in Figure 2.10.

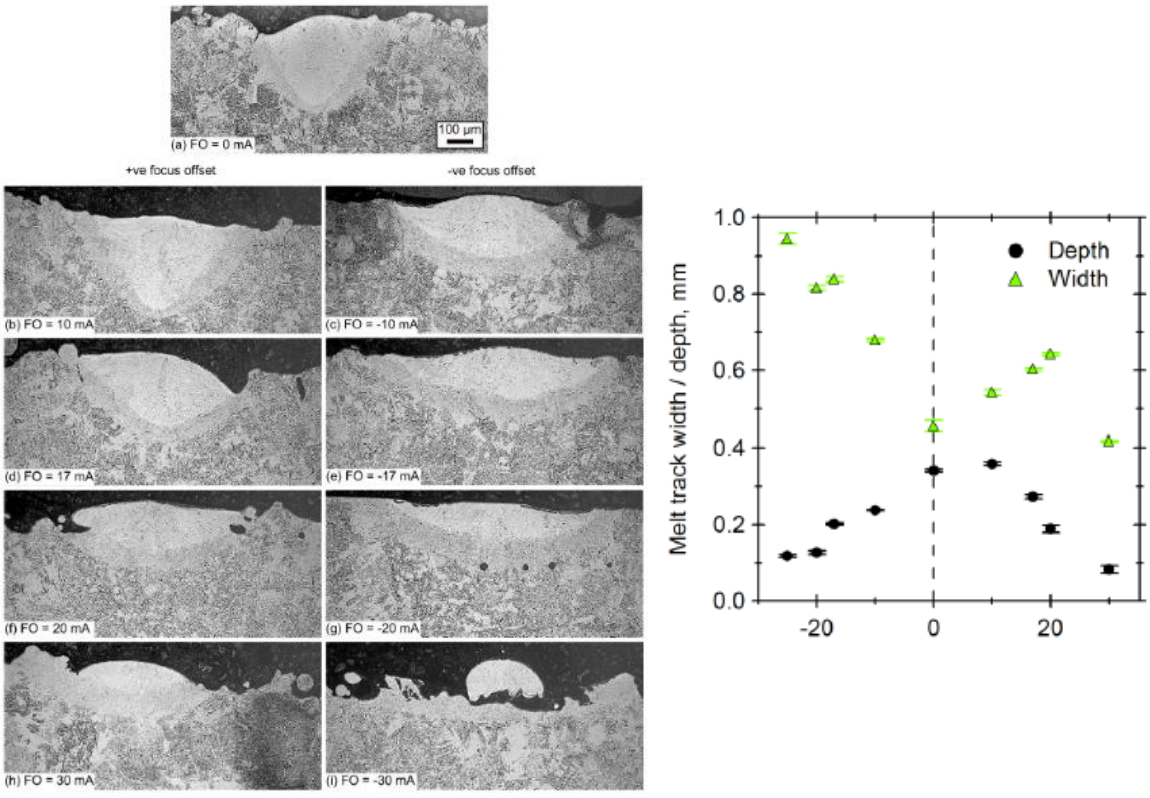

Figure 2.10 Melt track width and depth using 6 mA beam current and 49 mm/s beam speed [9]

2.3.2. Defect in EBM process

Defects or porosities are always key influencing factors on the dynamic properties of any product. As for the current technology of EBM, there are main types of defects: gas pores, keyhole porosity, swelling and lack of fusion (LOF).

Gas Pores

Gas pores are generally smaller in size (<100μm) and circular in shape.[57] In the EBM process, although the process is taken under vacuum, the contamination of the powder could be the source of the gas pore. Tammas-Williams et al. [61] measured the gas entrapped inside the powder using XCT for both gas-atomised and plasma-atomised powder, the result is shown in Figure 2.12. They revealed a significant level of pores within larger powder particles.

As explained by Tammas-Williams, during the EBM process, gas within the powder will be released. The pressure of the gas within the powder is manufactured in standard condition; the low pressure EBM chamber will have an effect of expanding the original gas pore size. Due to the rapid cooling rate, gas will not have enough time to escape, which results in gas porosity in the final product.[61]]

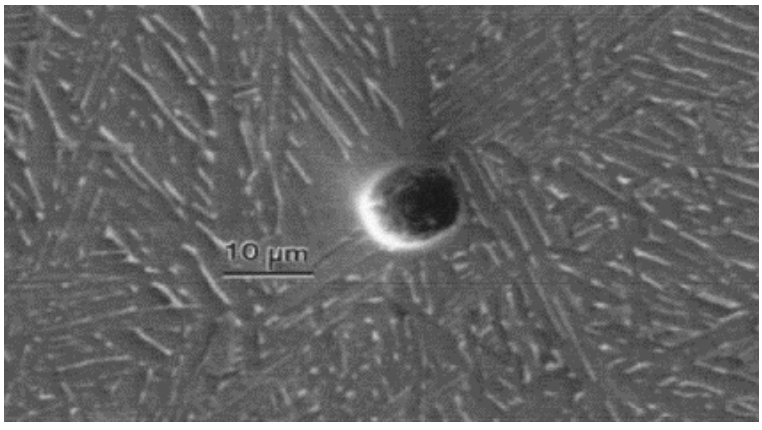

Figure 2.11 Spherical gas pores in the EBM process [57]

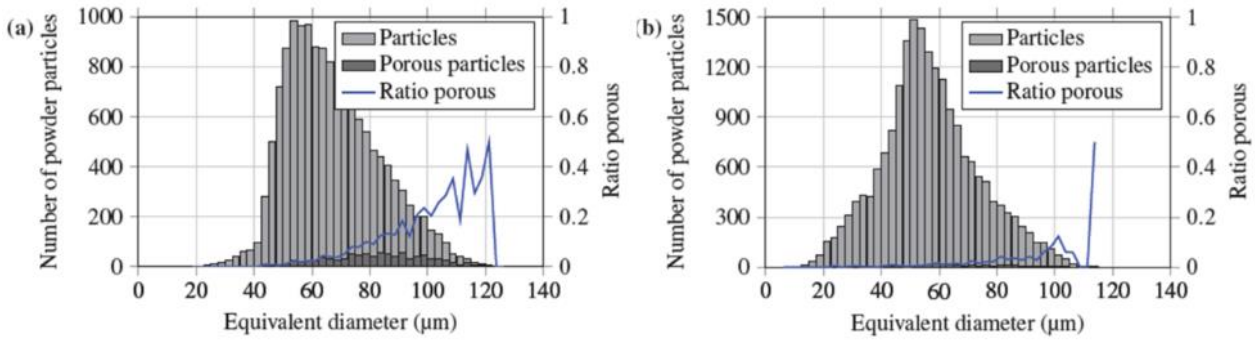

Figure 2.12 Powder size distribution with powder contains porosity. [a] plasma atomised powder [b] gas atomised powder [61]

Keyhole Porosity

When the power density of the energy beam is very high, strong evaporation occurs on the melt surface. The recoil pressure associated with energetic evaporation is sufficient to produce a deep, narrow depression in the molten material. This results in the formation of keyhole type porosity, which is generally filled with vapour and ambient gas. [48]

The formation of a keyhole is very common in deep melt pool welding for both laser and electron beam welding processes. As for the EBM process, due to the power of beam and depth of melt pool being much smaller than in welding, the keyhole defects are less likely to be formed and size of keyhole defects are much smaller.

Swelling

Swelling is a type of defect where the top surface of the part is elevated above the current print height. Some examples of swelling defects are shown in Figure 2.13. It has been noticed that the swelled regions usually happen on the edge of the part. Many researchers have reported a similar result with EBM parts across different materials and it is believed that the main cause of the swelling is due to the local overheat.[9,49,50,51,52] The detailed reason of how swelling happens during the process has not yet been studied or confirmed, but Sames et al.[53] believe the fundamental of swelling in EBM is similar to the 'humping' behaviour in high speed

welding.[54,55] As described by Nguyen et al.[54], humping is a periodic undulation of the weld bead with humps and valley due to the surface tension inducing melt pool dynamics.

The consequence of swelling during the EBM process is relatively severe. The elevated region is very likely to contact and break the rake system, thereby affecting the powder distribution on the powder bed, which eventually stops and fails the build.

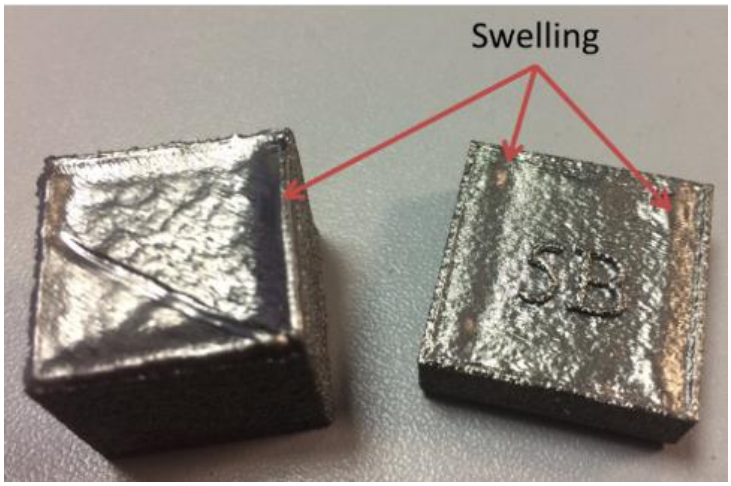

Figure 2.13 Swelling on the EBM parts

Lack of Fusion (LOF)

The term Lack of Fusion (LOF) as applied to defects in AM generally refers to the section of a part which did not melt completely, leaving un-melted powder or a 'gap' inside the part, as shown in Figure 2.14.

One reason for lack of fusion proposed by Thijs et al.[60] is the low energy density beam causing insufficient overlap of melt track which embedded loose powder in between, shown in Figure 2.15. The other case is due to the interruption during the melt scan causing the energy beam to be diffracted or not generated, which makes it unable to reach the powder bed.

Sometimes when a pore or defect forms initially, it can be relatively small, but, during the process, the pore might be changed in shape or grow in size due to the residual stress within the solid or surface tension of molten metal.[56]

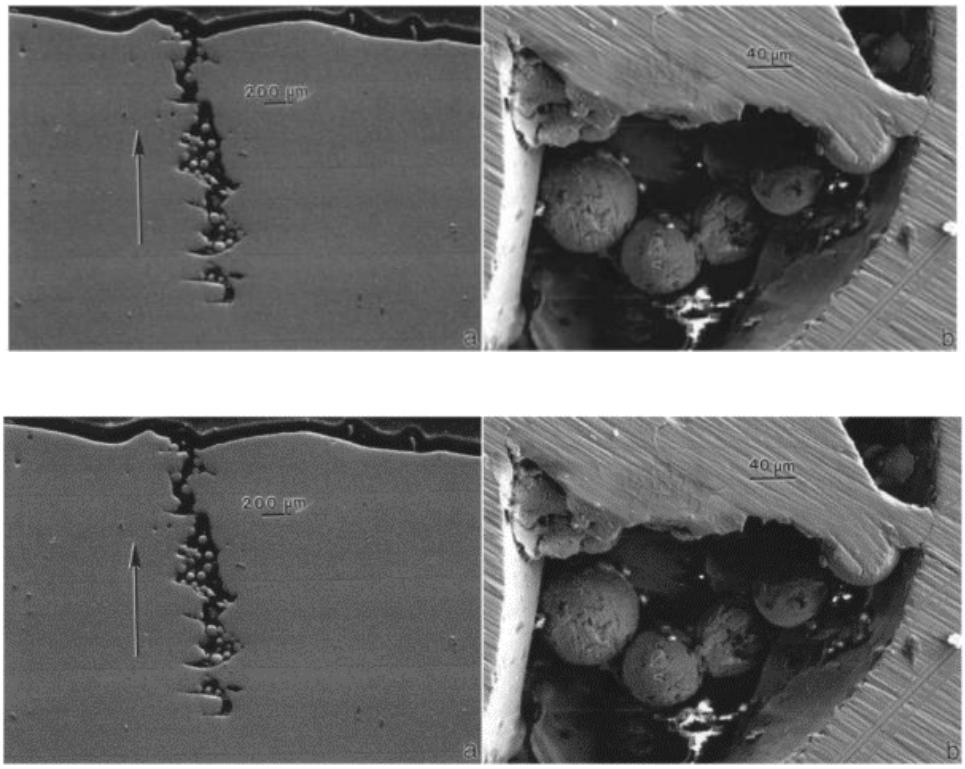

Figure 2.14 Lack of Fusion examples [57]

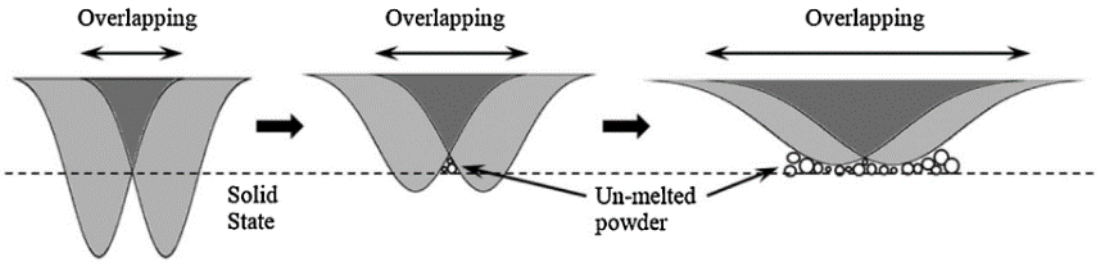

Figure 2.15 Schematic of melt pool [60]

Tunnelling

Another type of lack of fusion is more orientated in the vertical direction with un-melted in-between the defects. These defects are generally very large in size (500 µm to 10 mm+) and it is very unique to powder based AM technique. Some documents in the public domain also refer it as the 'tunnelling' or 'chimneys' defects due to the propagating characteristic. An example of typical LOF is shown in Figure 2.16.

There is numerous research showing that LOF is 'growing like tree branches', [and defect length can be as long as a part's build height. As the nature of this type of defect is irregular and large in size, it is very detrimental to the final part's mechanical properties.

Figure 2.16 3D LOF on the left, 2D LOF after machine on the right

Bauerei et al.[56] made a computational model to explain the defect propagation in SLM process, as shown in Figure 2.17. They suggested that the energy of the beam is deposited uniformly over the cavity, which could to melt the powder and close the cavity. However, due to the fast coalescence of the powder particles and the long exposure time to the laser, most of the energy deposited in the middle of the cavity is pulled away.

As a consequence, the surface of the cavity is unlikely to be heated by the beam and only left conduction to increase the temperature of the cavity. If the thermal energy within the powder particles is not high enough to melt down the entire cavity, a defect remains. Correspondingly, the voids are only partially refilled during applying the next powder layer, even if the cavities are filled with powder again, surface tension is capable of pulling the molten material out of the cavity. If the size of the defect is large enough, the defect cannot be filled anymore. To

overcome the defect, the entire surface of the cavity has to be molten. Therefore, once a cavity has grown to a certain size, defects will be permanently within the solid.

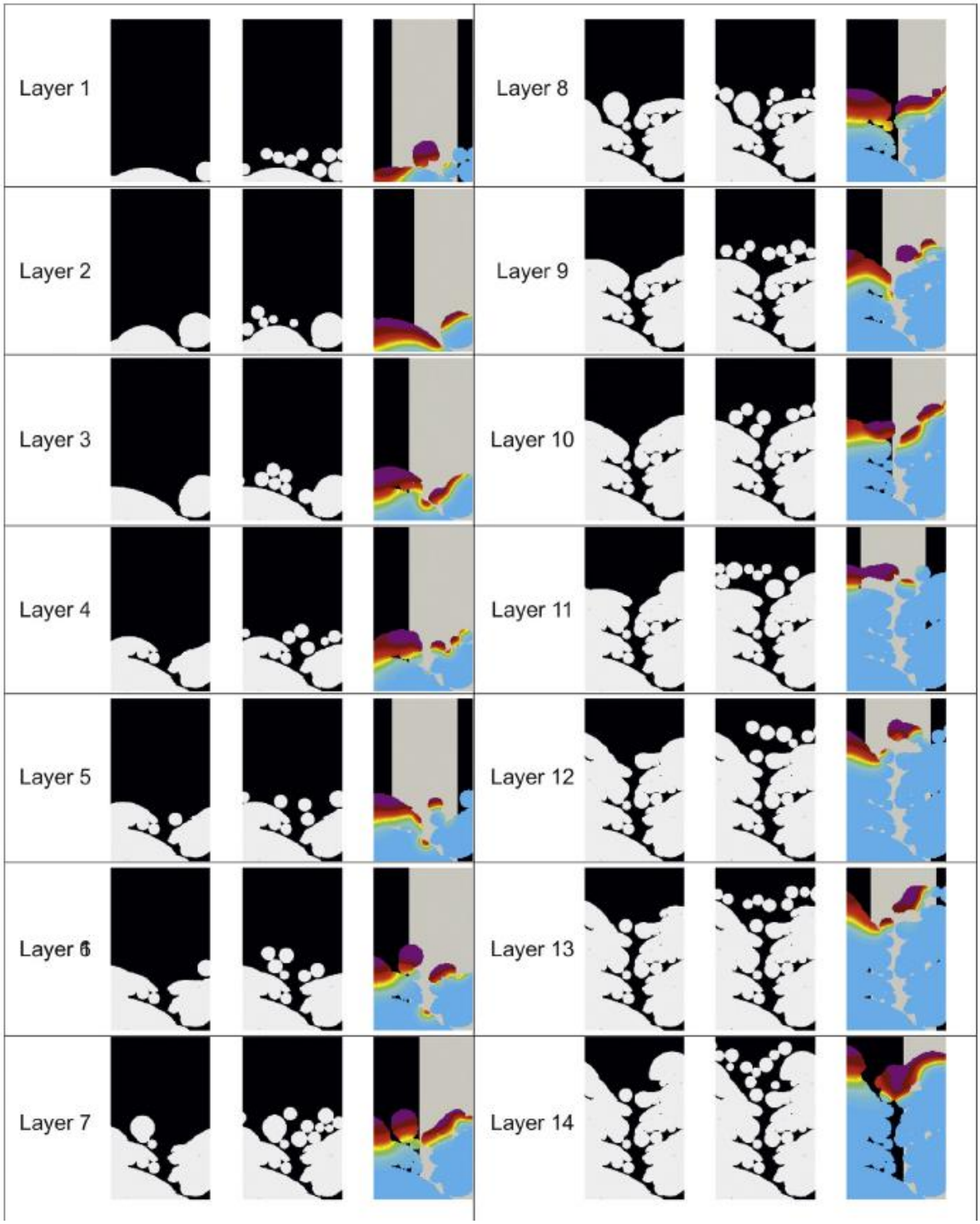

Figure 2.17 Evolution of LOF, simulation done by Bauerei et al.[56]

Defect Formation due to Insufficient Energy

Researchers have found there is a relation between energy density and the amount of porosity formed during the process. Thijs et al. researched the effects of the above parameters on the formations of microstructure, while Karina et al.[58] have researched the effect of hatching distance on porosity and concluded that, *"increase melt scan rate increases the porosity by creating un-sintered powder volumes within the layers."*[58] Nesma et al. [59] have also proven a similar theory of un-melted AlSi10Mg powder entrapment during high scan speed melt path.

In addition, research from Gong et al.[60] shows the influences of laser power and scan speed on the number of pores formed during the SLM process. Figure 2.18 shows the SLM result from Gong et al. at different power levels of 160W, 120W, 80W and 40W. In addition, they have divided the process window for SLM into four zones, as shown in Figure 2.19:

Zone I: full dense zone, where the parameter gives lowest amount of porosity

Zone II: Over melt zone, due to excess energy input

Zone III: Incomplete melt zone, due to insufficient energy

Zone OH: Over heat, too much excess energy result in heavy deformation

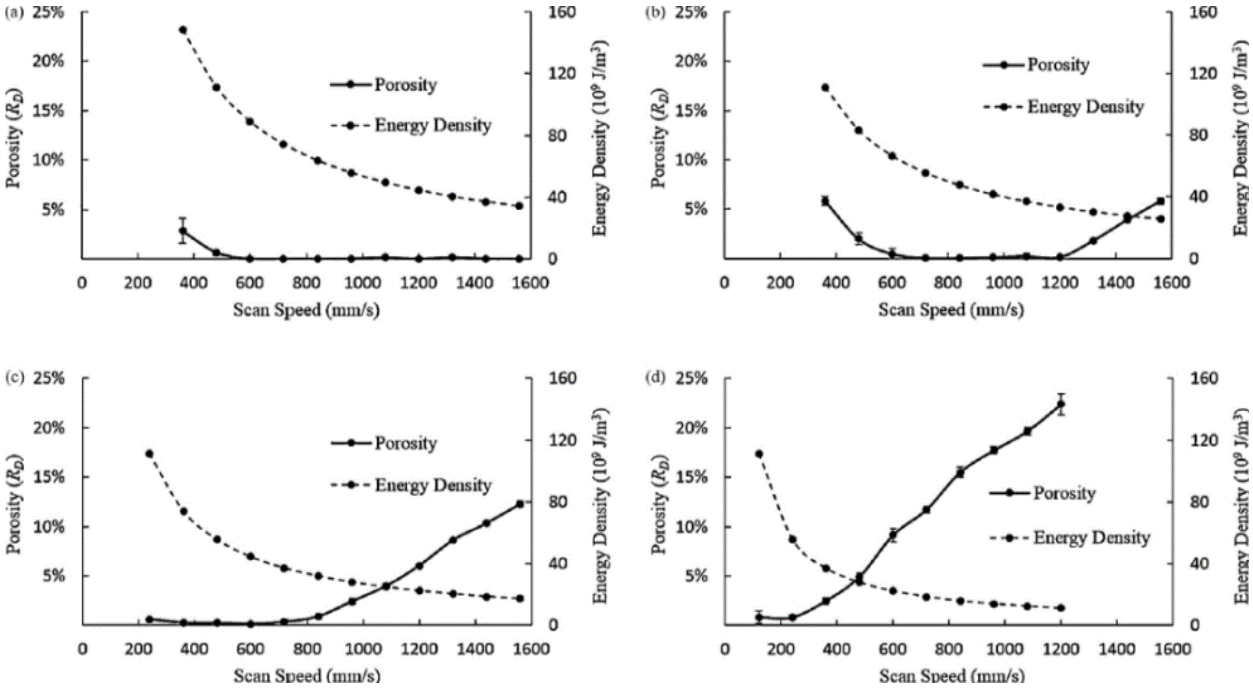

Figure 2.18 Porosity of SLM produced Ti6Al4V samples with beam power: (a) 160W. (b) 120W (c) 80W. (d) 40W [60]

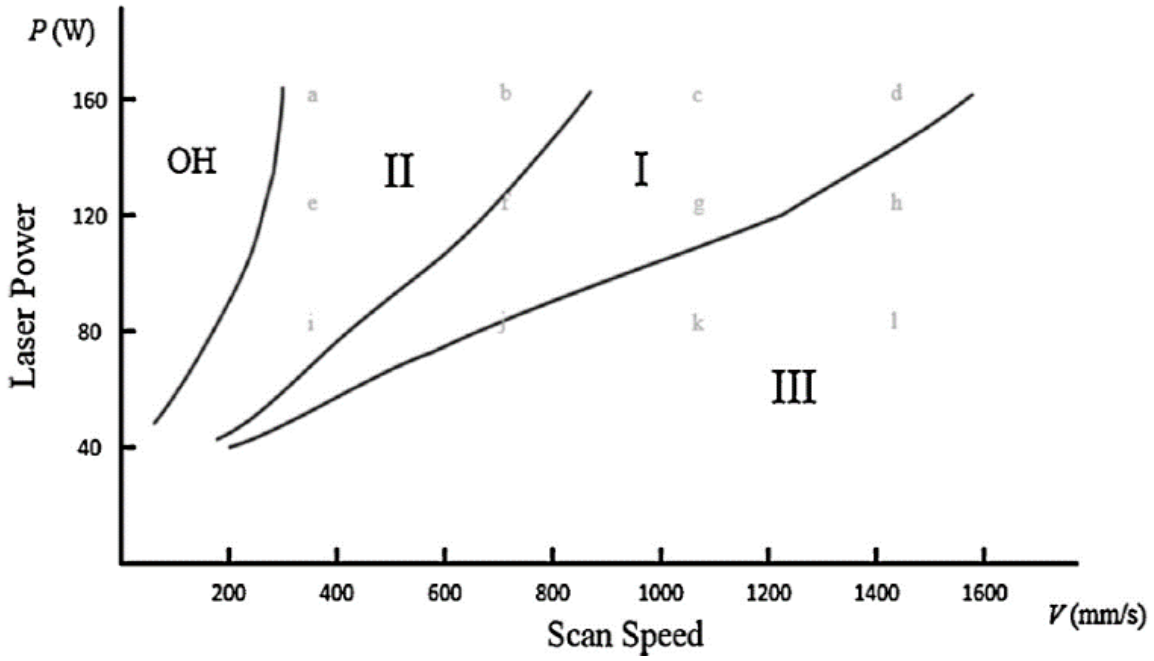

Figure 2.19 Process windows for SLM with Ti-6Al-4V powder [60]

In this same work similar tests were also performed using the EBM process, with the variation of hatching distance, and focus offset corresponding to the amount of porosity formed, as shown in Figure 2.20

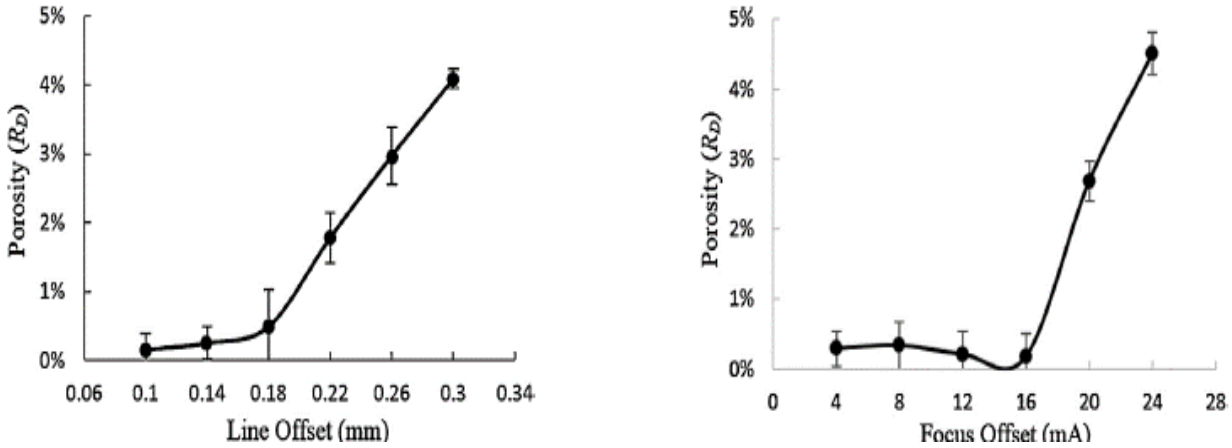

Figure 2.20 Porosity of EBM Ti6Al4V samples vs. Line offset and Focus offset [60]

Due to the complicity in EBM and the parameters being controlled by different functions in the EBM process built-in the machine, as mentioned in the previous section, direct control for the EBM process is not as easy as the SLM process. A more detailed parameters study from Tammas-Williams et al.[61] was performed on the EBM process. The study took into account the melt strategies, turning function, hatch distance, focus offset and quality of the input

powder, and the XCT scan result is shown in Figure 2.21. They made some predictions about the porosities for the EBM manufactured part:

1) With the default machine parameter, most of the pores were found to be in spherical shape. The origin of the pores is from gas in the supplied powder that expands in the melt pool, due to the reduced pressure in the chamber.
2) The majority of the pores are from the hatching region due to the lower energy density. Highly irregular pores were found in the contour area which could be the consequence of sufficient overlap from the multi-spot setting in contour parameters.
3) The turning function is used to compensate for the residual heat, but there could be some overcompensation from the parameter setting, as there is more pore formation in the turning point regions.

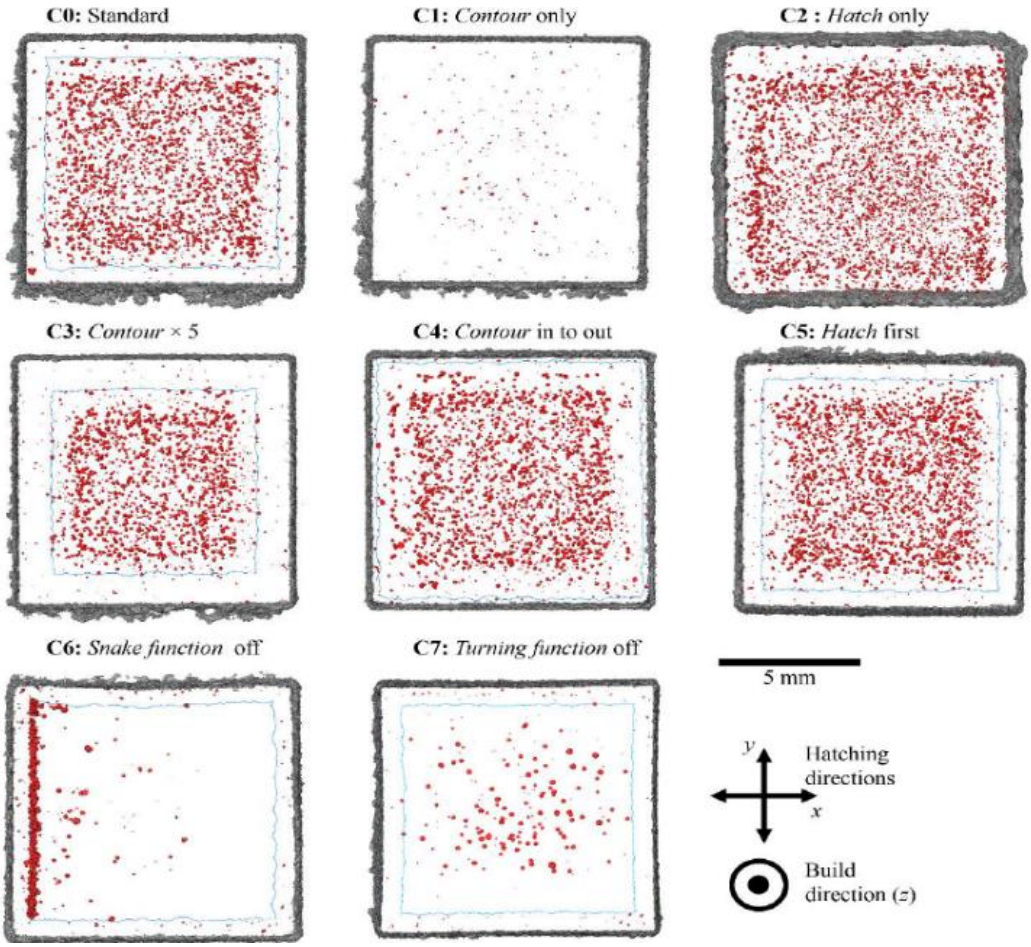

Figure 2.21 XCT full sample scans showing pores (red) projected in X-Y plane [61]

From the above information, a common finding from every researcher is that, the degree of porosities or defects in the component or any location within a part is mainly linked with amount of energy put into that location.

Flaking

During the EBM process, the melt pool often has temperature boiling temperature of the Ti6Al4V, thus some vapour will be evaporating from the melting pool and start condensing on the wall of the protective shield. The condensed material consists of a much higher concentration of aluminium, due to boiling point of aluminium being much lower than titanium. When the accumulation of the material condensation reaches a certain level, it is very likely to peel away from the protective heat shield and fall off. Some of examples of flaking are shown in Figure 2.22.

Figure 2.22 Flaking in EBM process, photo taken after the build [62]

There are various different consequences when the flake drops into the bed. If the flake drops right on the part, it is very likely to fuse the flake into the part. Unfortunately, the melting on the flake could initialise some defects due to the reasons of a non-powder like structure, very different chemistry and being much colder compared to the powder bed. If the flakes have not melted with the part, then the rake system will drag the flake around the powder bed, which could disrupt powder regulation, and eventually lead to a process failure.

2.3.3. EBM vs SLM

Selective laser melting is another powder bed AM process, which works in a similar way to the EBM process. Different from the EBM machines only manufactured by ARCAM, there are a few companies developing SLM machines, such as EOS, Renishaw, Concept Laser, etc.

As described in its name, the process uses laser as the energy source, since the laser has no requirement for the high vacuum, the atmosphere of SLM takes place under inert gas condition, such as Argon. Unlike the electron beam, the laser does not carry any magnetic charges, thus the powder does not float into the air as it does in the EBM process.

In most popular SLM machines, the productivity is relatively lower than the EBM machine. The common laser power used is up to 500W, which is much lower than the power in the EBM process of more than 2500W. In addition, the efficiency of the laser-lens system and the laser-material interaction are also much lower than electron beam interactions.

All the above reasons make the SLM process preferable and capable of printing parts with a thinner powder layer thickness and smaller powder size distribution than the EBM process. The nominal particle size distribution of powder used in SLM is 10 μm to 45 μm and in EBM is 45–106 μm.[63] As an advantage of using smaller powders, SLM gives a much better surface roughness than the EBM process, but still not smooth enough to provide good fatigue properties

in an aerospace environment.[64] Figure 2.23 shows the vertical surface roughness comparison for SLM and EBM processes.[65]

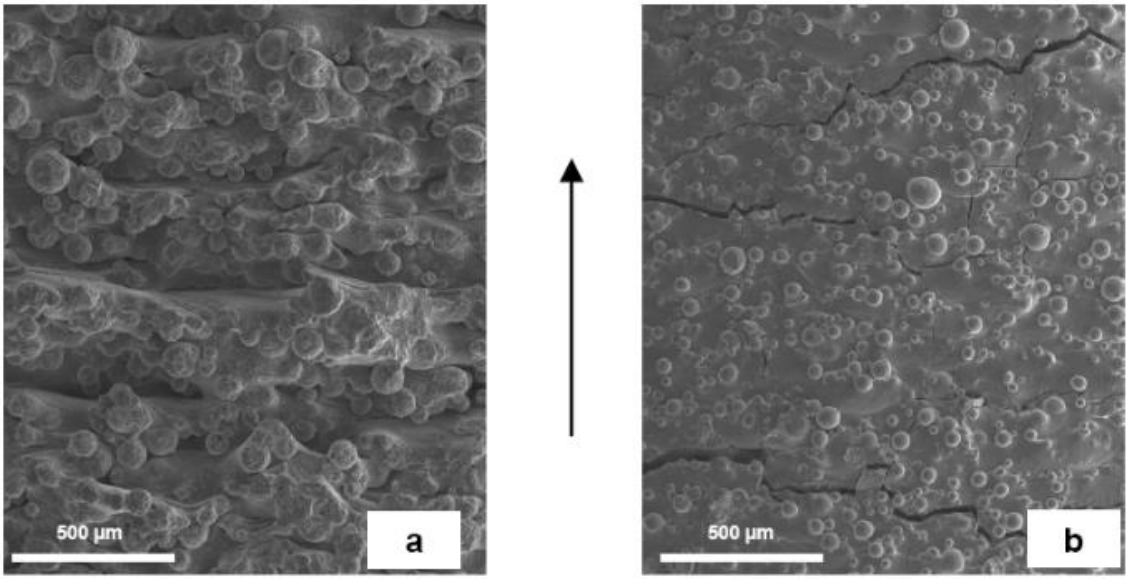

Figure 2.23 Vertical surface profiles for [a] EBM part [b] SLM part [65]

Due to the least requirement of preheat to sinter the powder, in general, SLM is a cold bed process and, thus, the cooling rate is much higher than the EBM process, which gives a slightly better tensile strength.

A drawback from a higher cooling rate is corresponding higher residual stress. The high stress during the process is very likely to heavily deform the part and cause process failure, thus one of the main technology developments of last decade has focused on the simulation of the residual or deformation for the SLM process.

Figure 2.24 shows an unrecoverable crack formed during the SLM process caused by residual stress. In addition, due to the inevitable high residual stress of SLM, the parts are commonly welded to the base plate and to the support structure. Stress relief is usually performed before the parts are removed from the base plate.

Ali et al. [66] carried out some research to increase the bed temperature of Renishaw SLM125 with a conduction heater to maintain bed temperature up to 770 °C. They demonstrated a

successful reduction in the residual stress (Figure 2.25); in addition, the result also indicates that the formation of martensitic microstructure has stopped with bed temperature of 570 °C and above.

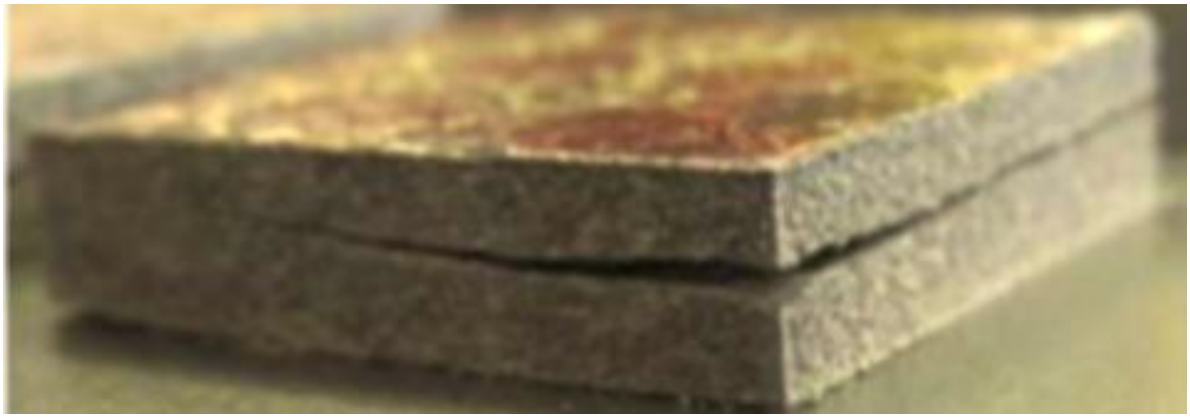

Figure 2.24 Crack in SLM cause by residual stress

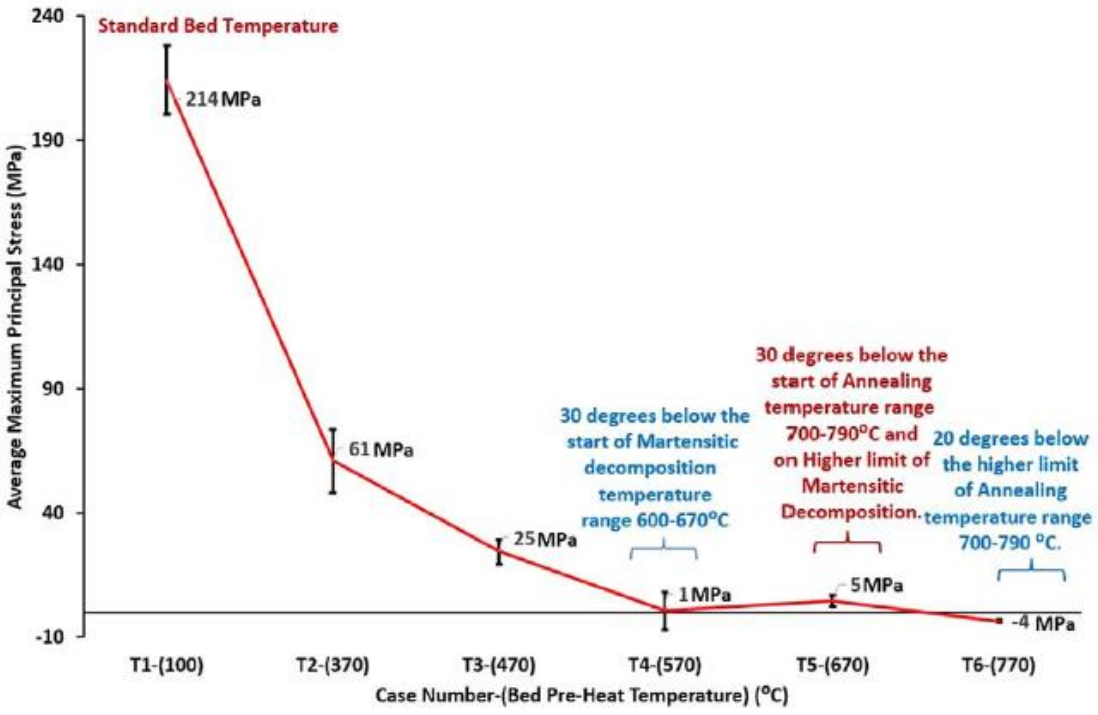

Figure 2.25 residual stress vs bed temperature in Renishaw AM125 [66]

2.4. HIP

Hot Isostatic Pressing (HIP) has been developed since 1955 and involves the simultaneous application of heat and pressure, [67] as shown schematically in Figure 2.26. The major objective of HIP treatment is to remove the internal porosity by applying a hydrostatic pressure. HIP

treatment has been used on a range of materials, including ceramics, steels, aluminium and titanium. The pressure is generally applied with inert argon gas. The high temperature 'softens' the material, and the material is plastically changed and diffused on a microscopic scale. By collapsing the pore, the interface of the pores will contact each other and be bonded by diffusion.

As mentioned in the previous sections, the defects presented inside the parts have a big impact on the dynamic properties of the product. Thus, for today's EBM in aerospace applications, HIP is required for any AM parts designed for dynamics loading. According to the ASTM Ti6Al4V HIP standard for powder bed fusion process, the HIP conditions are set with pressure at least 100 MPa with temperature from 895 °C to 955 °C for two hours to four hours and cooled to below 425 °C under inert gas condition.[68]

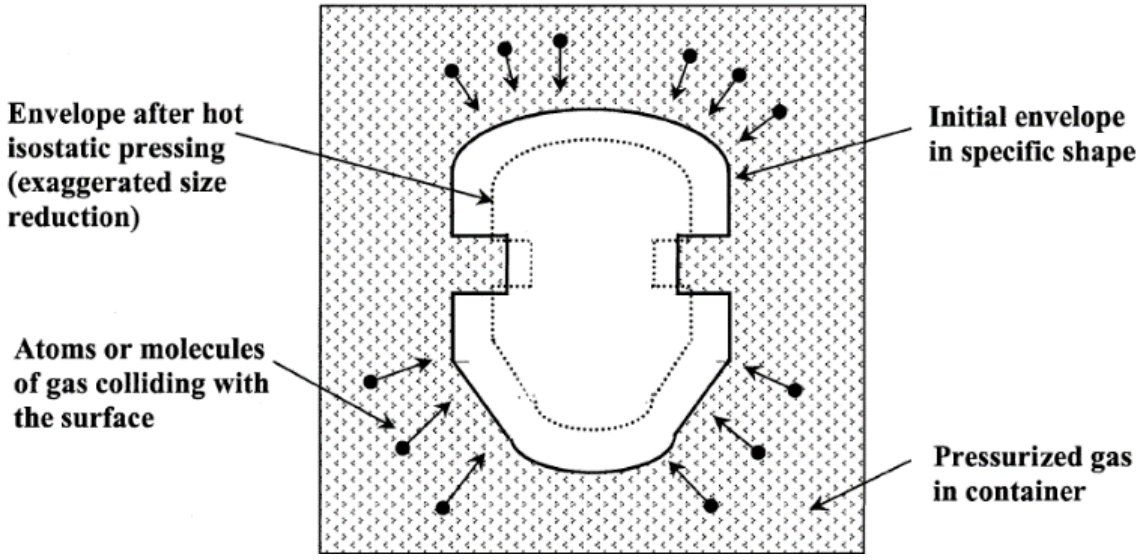

Figure 2.26 Schematic diagram of Hot Isostatic Pressing Operation [68]

As the EBM process takes place under high vacuum, the pore's internal pressure should be as low as the chamber pressure. Thus, during the HIP process, the pore will be greatly shrunk in size to an undetectable level. [61]

Tammas-Williams et al. further investigated the heat treatment of EBM sample after the HIP process and found that, the gas pore reappeared after the heat treatment. They indicated that

the reappeared gas pores are most likely to be argon, since the argon gases have very low diffusivity.

The key limitation of HIP is that it cannot remove porosities that are open to the surface. As mentioned in the previous section, the lack of fusion defect is very likely to 'travel' along the build direction and open to the surface. The high roughness of the EBM surface can make these defects very hard to detect using simple visual inspection methods, but the nature of these defects means that their presence is very detrimental to a part's quality. An example of a LOF defect which did not close up during the HIP process is shown in Figure 2.28.

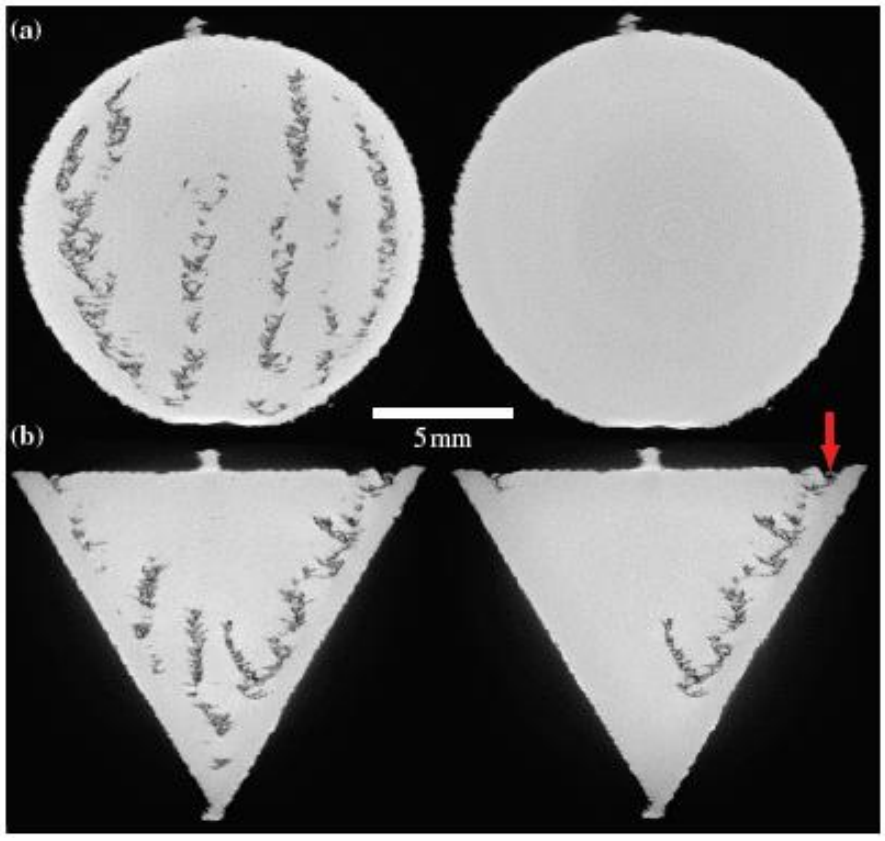

Figure 2.27 XCT data collected from EBM samples as built (left) and after HIPping (right) [61]

2.5. Today's EBM Process Flow in the Aerospace Industry

Technology Readiness Levels (TRLs) are a systematic metric/measurement system that supports assessments of the maturity of a particular technology and the consistent comparison of maturity between different types of technology. The TRL approach has been used on-and-

off in NASA space technology planning for many years and was recently incorporated in the NASA Management Instruction (NMI 7100) addressing integrated technology planning at NASA. A summary of different TRL level is shown as follows. [69]

TRL 1. Basic principles observed and reported

TRL 2. Technology concept and/or application formulated

TRL 3. Analytical and experimental critical function and/or characteristic proof-of concept

TRL 4. Component and/or breadboard validation in laboratory environment

TRL 5. Component and/or breadboard validation in relevant environment

TRL 6. System/subsystem model or prototype demonstration in a relevant environment

TRL 7. System prototype demonstration in a space environment

TRL 8. Actual system completed and 'flight qualified' through test and demonstration

TRL 9. Actual system 'flight proven' through successful mission operations

As for today, from the overview, the EBM process qualification is approximately at TRL3 or 4. In the current state of the art, to approve the overall EBM manufacturing process is still very difficult to achieve.

Part qualification is an alternative easier method for any product. Rather than qualify the whole process, the component is qualified according its own criteria. A summary of different post-processes and inspections for part qualification are summarized as follow. Different combinations can be made based on the part's requirement, function and cost.

2.5.1. Pre-inspection

After the part has been made, some basic and low cost inspection can be made to judge whether the part can be going forward or not.

Log file report/ Log file inspection

The log file contains built information about the part. The inspection is mainly looking for abnormal features, such as pressure level, smoke event, arc trip etc.

Part Visual Inspection

Often the parts are not finished perfectly as expected, some visible features might be evident on the part's surface, such as swelling, deformation, etc. In general, thin wall components are more easily distorted than thick components in the EBM process. To improve the accuracy, the visual inspections are often assisted with laser scanning and a coordinate measurement machine (CMM).

Traveller Specimen

Traveller specimens are simple small tensile coupons which are made in each build, their aim being to prove each build is within the build standard. The specimen is often tested with a deposited surface, where a fast result can be obtained. As the specimens do not have exactly the same geometry as the actual part, they should not be used to serve the evidence of mechanical properties of the actual component.

2.5.2. Post Process

HIP

The current EBM or any other metallic AM process has not been fully proved yet, whereby the process is yet a defect free process. Thus, after all the basic inspections, parts are usually required to have HIP treatment to close up all the internal defects.

Surface Finishing

Due to the fine microstructures, the EBM parts are very good in static properties, but the high roughness surface of the EBM surface is generally not acceptable for dynamic loading condition. Thus some degree of surface finish is required.

Machining has been well established for many decades and it gives the best surface finish, but not all the EBM parts can be machined easily and cost-effectively. Chemical milling or etching can smooth parts with decent surface finish with relatively reasonable cost and it is one of the current most prospective candidates for AM component surface finishing technique. Although the process does not give as good a surface as machining, it does give huge improvement on dynamic properties and is much more capable of processing high complexity geometries.

NDT

Testing can be divided into two categories: non-destructive testing (NDT) and destructive test. NDT are usually used to study the defect level, and destructive testing is used to study the material properties.

Non-destructive testing (NDT) is often required to perform on the actual part to prove the defect level is within the requirements. Dye penetrant inspections (DPI) or liquid penetrant inspections (LPI) are used to inspect any surface defects or cracks on the machined surface. DPI inspection is cheap and effective on smooth surface, but does not work well when the surface finish is very rough.

As for internal defects or non-machined component, the only aerospace-approved NDT methods are X-ray and ultrasound. Both of the techniques prefer simple and flat geometry, as the complexity of the geometry rises, the inspection become challenging and sometimes become impossible to achieve.

CT-scan is an upgrade version of X-ray, but in 3D. The technique is currently under significant development in many research institute and companies, which is believed to be an approved aerospace NDT technique in few year times. Unfortunately, compared to X-rays, the costs of a CT-scan are much more expensive.

Specimen Test: S-bar, P-bar, C-bar

S-bars (separated specimen) are individual specimen builds together with the actual part within the same chamber, orientated or placed in a most representative way to predict the mechanical properties of the actual part.

P-bars (prolongation specimen) are used commonly in forging industry, which is an extra portion of metal added in a mutually agreeable location of a forging to permit removal and subsequent testing without destroying the forging. As in EBM, the P-bars are the specimen actually attached to the original geometry, but in the shape specimen.

C-bars (Cut up Specimen) are the specimens extracted from the original geometry, generally requiring additional extraction drawing and machining.

Among the specimen tests, S-bar test is the cheapest, but it is least representable of the actual material properties. P-bar is better representable than S-bar in the forging industry, but not as much as in AM, since it could actually create a very different thermal history to the actual part. C-bar is the most representable testing, but it is associated with additional cost of cut-up design and extra machining or cutting.

Rig Test

Rig test is generally the final testing after all the previous post-processes or qualifications have been satisfied. Based on the component's application and complexities, the test can be very costly.

The test involves the actual component rather the specimens. The loading condition is simulated and designs need to be as similar as possible to the loading condition. Sometimes, the component will be also required to be tested in the actual assembly.

2.5.3. Production Inspection

After the component has passed the qualification, all the themes and configurations should be locked down during the production. During the production of the components, some NDT could be performed on a regular basis, depending on the level of the component's requirements and confidence of the production process flow. Occasionally, destructive testing will be carried out, such as cut-up testing for every 30 batches or every six months.

2.6. Process Monitoring

Although AM offers unique capabilities with tremendous application potential that cannot be matched by any other traditional manufacturing technologies, unfortunately, the quality and repeatability of the process is still a great drawback. This is particularly true in the aerospace industry due to the high production standard. [70] One approach to overcome this challenge is process monitoring and real-time process control to enhance part quality and repeatability, which has recently been receiving increased attention.

Optical monitoring method is the most popular monitoring technique for powder bed fusion AM technique, due to its simple understanding image output and that it gives researchers a straightforward interpretation of the process itself. In general, the optical monitoring method can be divided into two types: melt pool monitoring and layer wise overall image capture.

2.6.1. Layer-wise Monitoring

Layer-wise monitoring technique can be simply understood as taken picture of the process layer by layer. There are numerous studies performed with different types of cameras. Price et al.[71] put a thermal camera outside an EBM A2 machine and captured and layered the image

during the process through the machine's observation window, and showed that the temperature measurement is repeatable and able to collect high resolution image up to 12 µm, but only on a limited area.

Rodriguez et al. wrote the methodology to set and calibrate an IR thermal camera for EBM process, as shown in Figure 2.28. They state that, "*the system synchronized with the system's input signal voltage of three synchronized events (pre-heating, melting, and raking) to automatically capture image.*"[72]

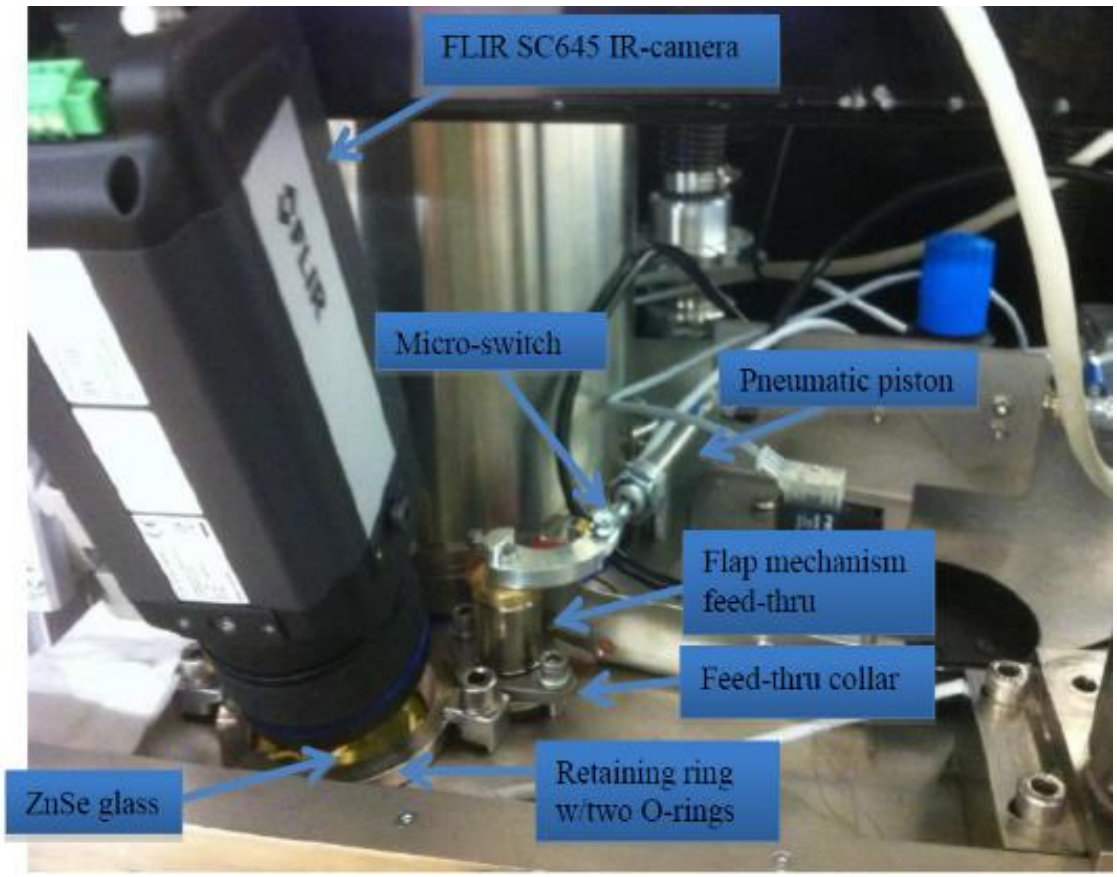

Figure 2.28 IR-Camera setup integrated to ARCAM A2 machine [72]

Mireles et al. created a closed-loop system for ARCAM A2 machine using the IR-camera through LabVIEW interface. [73,74] The system mainly consist of two algorithms. The Porosity Algorithm detects defects in each layer using the greyscale value of the image, and, if the porosity is above certain value, the algorithm will stop the build process. The grain control algorithm controls the grain size using *"layer thickness, layer to begin parameter changes to*

achieve coarse grain, layer to begin parameter changes to achieve refinement of grain, and amount to change parameter for both coarsening and refinement of grains."[73] Figure 2.29 is the interface for control of the A2 EBM machine. Since direct communication with ARCAM EBM control is restricted, the software controls the machine using mouse trigger events, which is one of the main disadvantages for this system, as it delays the parameter change to adjust the process.

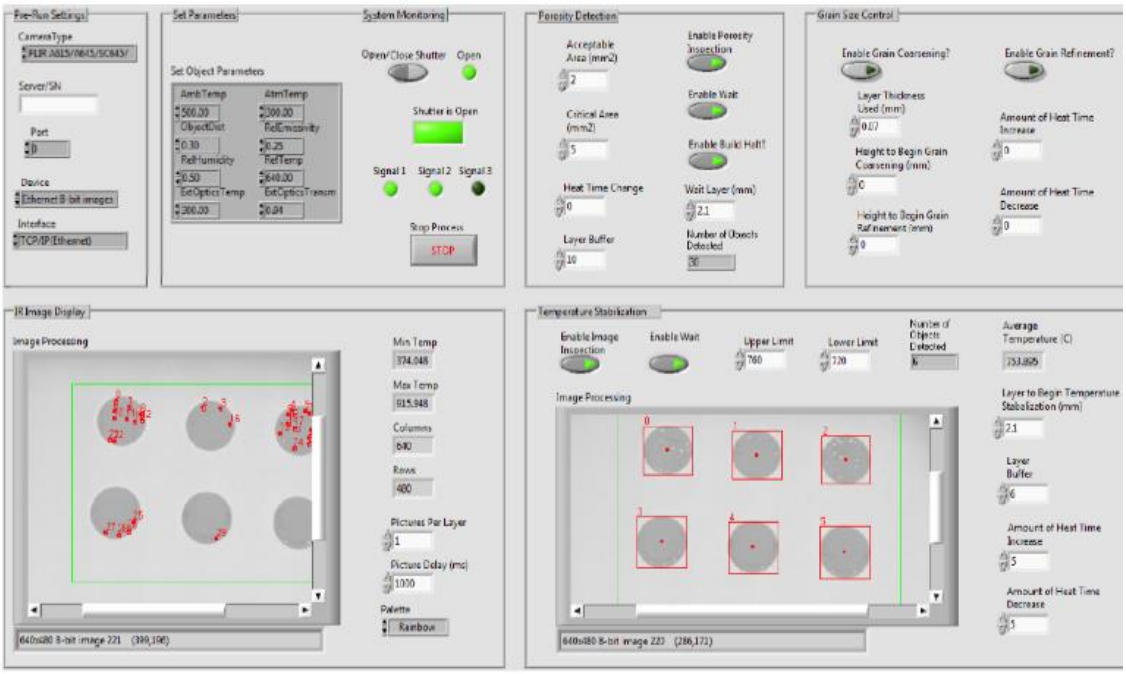

Figure 2.29 Closed loop control interface using IR-Camera in ARCAM A2 [73]

Zenzinger et al.[75] performed layer-wise monitoring using optical tomography on the SLM process and with stacked up layered image, but the system does not include a closed-loop feed back to the system. The pixel resolution of the system is approximately 0.1mm and an example of the output result is shown in Figure 2.30.

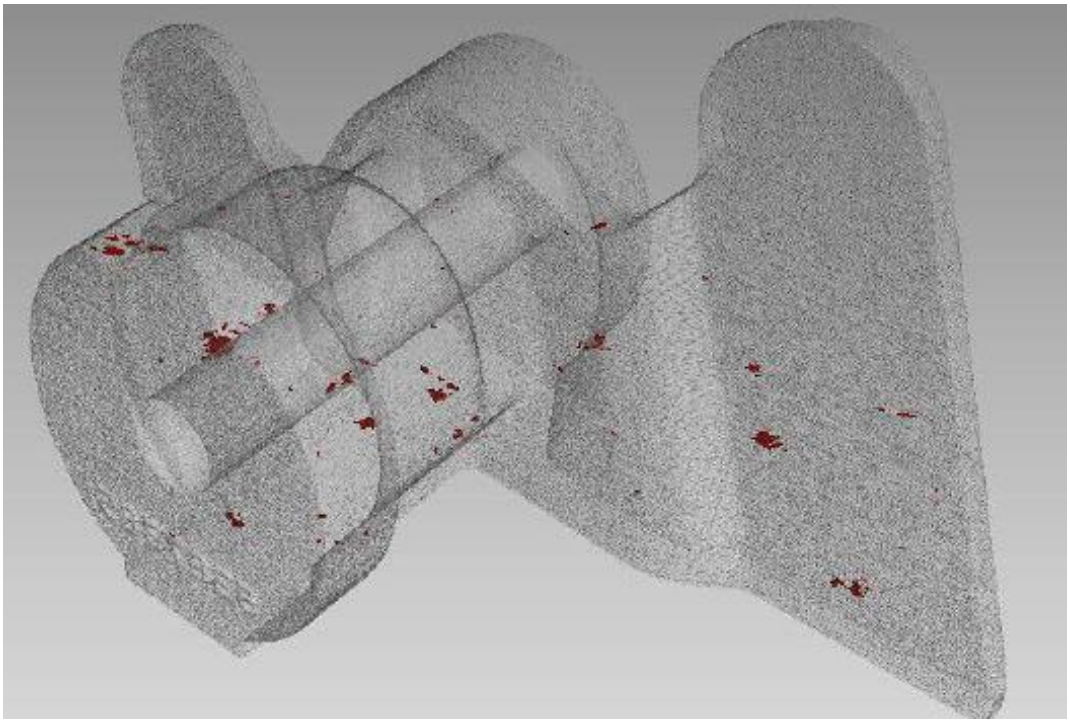

Figure 2.30 Image stacking by Zenzinger G. using professional CT software [75]

2.6.2. Melt Pool Monitoring

One of the main limitations about high resolution layer-wise monitoring is the close loop control can be only done layer-wise rather than in real time. To process high speed monitoring with high resolution image requires a tremendous amount of computation power, which is very hard to be achieved economically.[76] In order to solve the problem, coaxial monitoring technique has been developed by Craeghs et al.[77] , as shown in Figure 2.31, who published this patent in 2009.[78]

Coaxial monitoring takes an image at zone of interact only (melt pool). Since the area of the melt pool is very small in the SLM process, even with high resolution image, the size of image is small enough to process with fast response control. The system is capable of taking images of more than 10,000fps.

As shown in Figure 2.31, Craeghs et al. [79] described the system as *"the setup the laser source (4) is deflected by means of a semi-reflective mirror (3) towards a Galvano scanner with focussing lens (2). The focussing lens of the scanner is a so called f-θ lens and has a focal*

length of 254 mm. The radiation from the melt pool is transmitted through the f-θ lens, scan head and semi-reflective mirror towards a beam splitter (6), which separates the radiation towards a planar photodiode (8) and a high-speed CMOS camera (10).''[77]

The camera in the coaxial system will capture the local information of the melt pool, determine the geometry or the shape of the melt pool, and the photodiode will give a general overview of the image captured area. The closed-loop control achieved by combining the feedback from camera and photodiode shows a significant improvement in the surface quality, as shown in Figure 2.32.

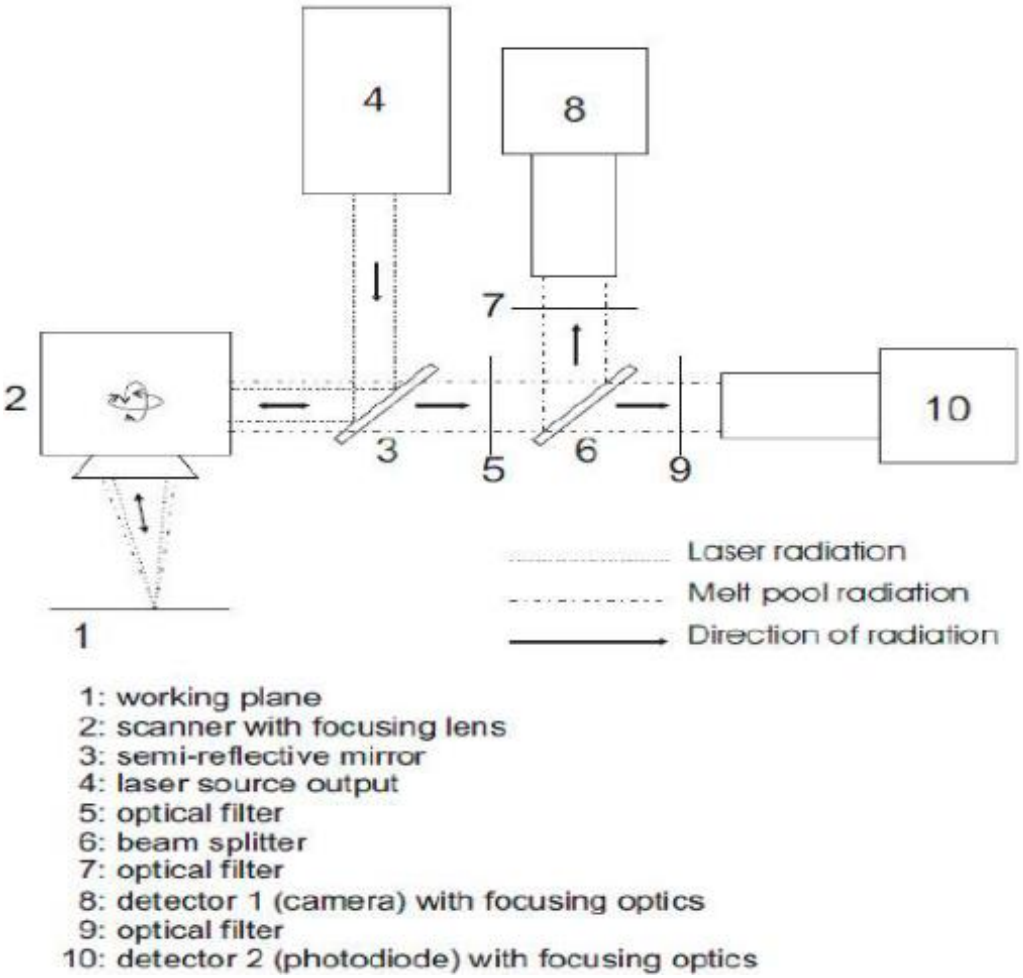

Figure 2.31 Schematic overview of the experimental setup of Coaxial Monitoring System designed by J.P. Kruth [77]

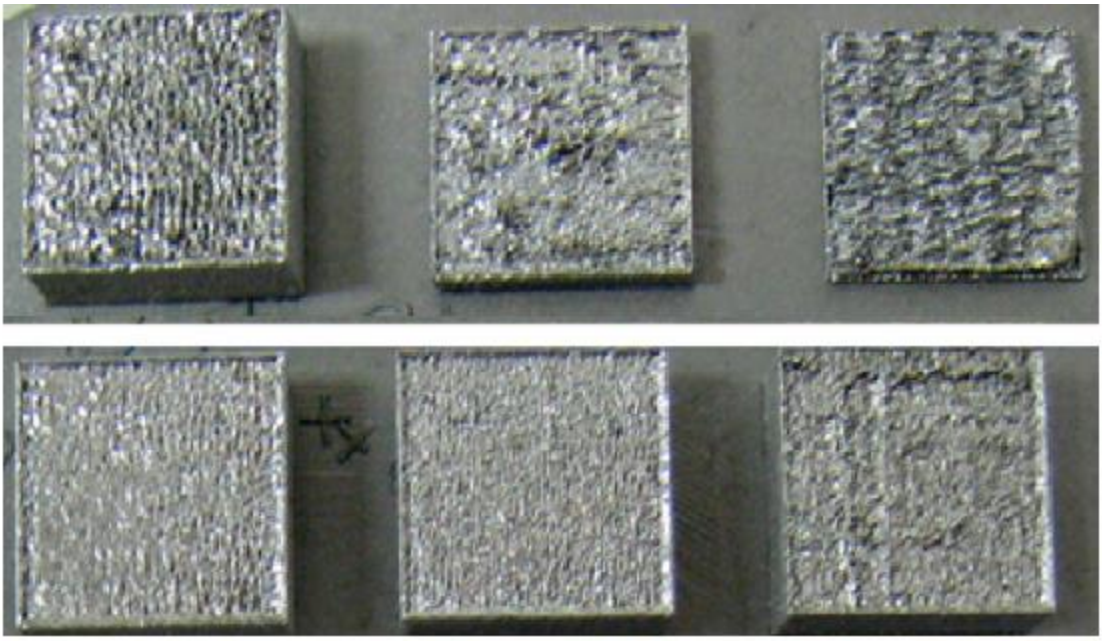

Figure 2.32 Processing of cubes without (top) and with (bottom) feedback control [77]

Clijsters et al.[80] have further developed a coaxial system which enables defect detection and closed-loop control to improve the quality by using a 'mapping algorithm', which is defined by Clijsters as "*transfers the measurements from a time-domain into a position-domain representation*."[80] The mapped defect has the lowest resolution of 100 µm by 100 µm. Figure 2.33 shows the defect comparison results between a CT scanned model and mapping model.

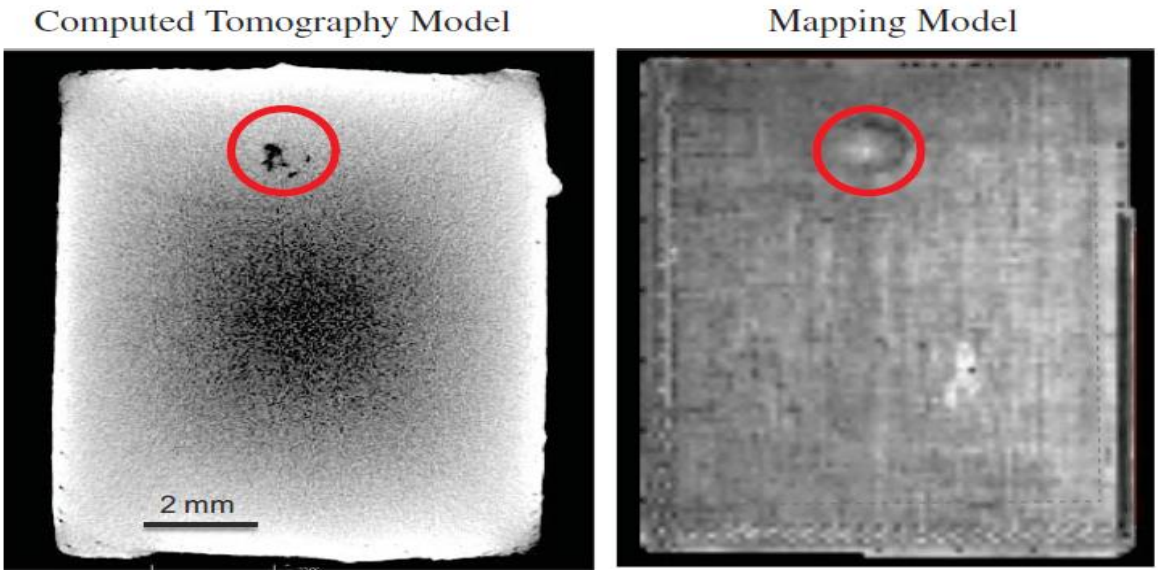

Figure 2.33 Comparison of mapping model and X-ray CT model [80]

Another coaxial research by Lott et al.[81] added an additional illumination laser and extra magnification lens to observe the process at high scanning velocities with a high resolution, which enabled to observe the melt pool dynamics of the SLM process. Figure 2.34 shows the coaxial design by Lott.

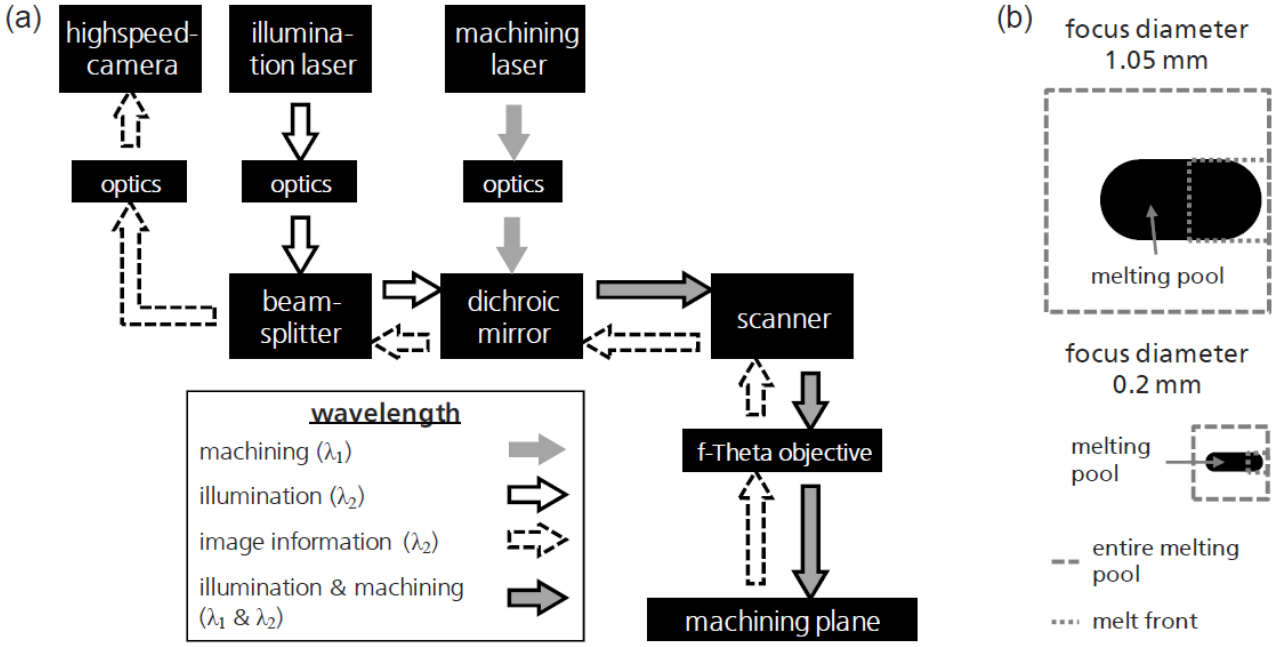

Figure 2.34 (a) Lott P's process monitoring system, (b) illustration of the different imaging sizes [81]

2.6.3. LayerQam

Apart from the university set-ups, some AM machine manufacturers have already combined thermal imaging technique with their AM machines. ARCAM has developed a system named LayerQam to be integrated with their EBM machines, which is a type of layer wise monitoring technique.

Within the design of ARCAM Q series machines, there is an installed camera (Prosilica GT6600), which is able to capture light wavelength from visible range to near infra-red range. Due to the electron gun being in the centre axis of the chamber, the location of the camera is slightly off-centre installed. The schematic drawing of the Q series chamber is shown inFigure 2.35.

Due to the extensive X-rays generated during the melting process, the camera is protected from the X-rays by lead glass and a metal shutter in front of the camera lens. During the process, after each layer is completed, the camera captures the image and outputs the photo into grayscale images.

On the camera, there is a wavelength filter applied to the camera which filters out the visible wavelength and leaving only the NIR wavelength range. The camera is believed to be capable of capturing lack of fusion type defect formed on each layer.

In the current state of the art, ARCAM offers software which predicts the density for each part from the built base on the analysis of the camera's image. The detail of how the analysis software works is not given and the analysis result does not yet have any verification. An example of a LayerQam result is shown in Figure 2.37

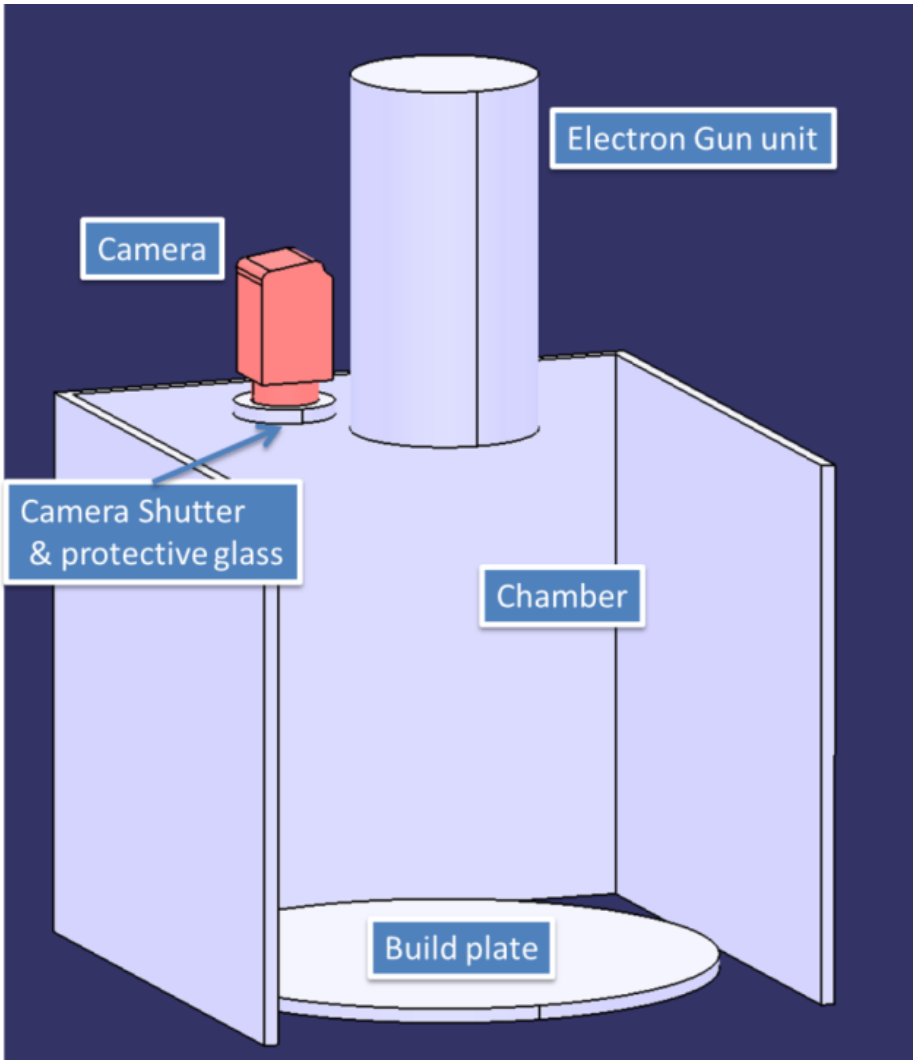

Figure 2.35 Location of installed camera in the EBM Q20 machine

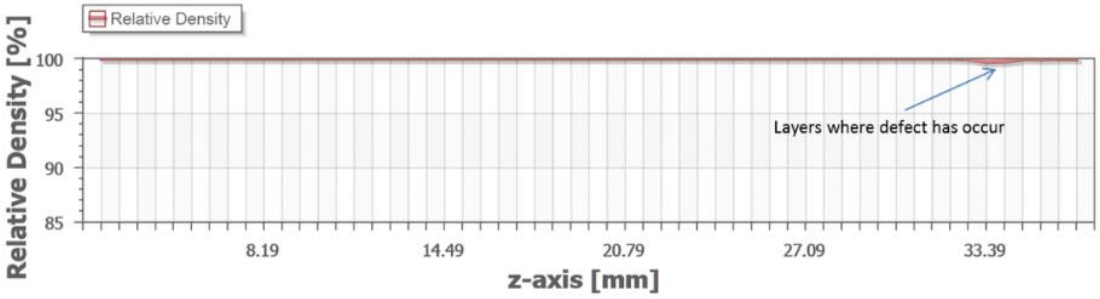

Figure 2.36 LayerQam report of a part, non-100% density indicates the potential of defects occurring

2.6.4. Other techniques

Apart from the three monitoring methods mentioned earlier, there are also some very earlier phase process-monitoring techniques developed for powder bed AM process.

Regional High Speed Monitoring

As the theory of coaxial monitoring is using the path of light to view the melt pool, thus a coaxial technique will not be very suitable for the EBM process since EBM uses electron beam rather than laser beam. In order to observe the melt pool dynamic, Schakowsky et al.[82] installed a high speed camera with illuminated laser observer and a mirror system into the EBM system. The system has the ability of capture maximum resolution of 17 µm and up to 6000 fps sampling rate. The setup of system is shown in Figure 2.37.

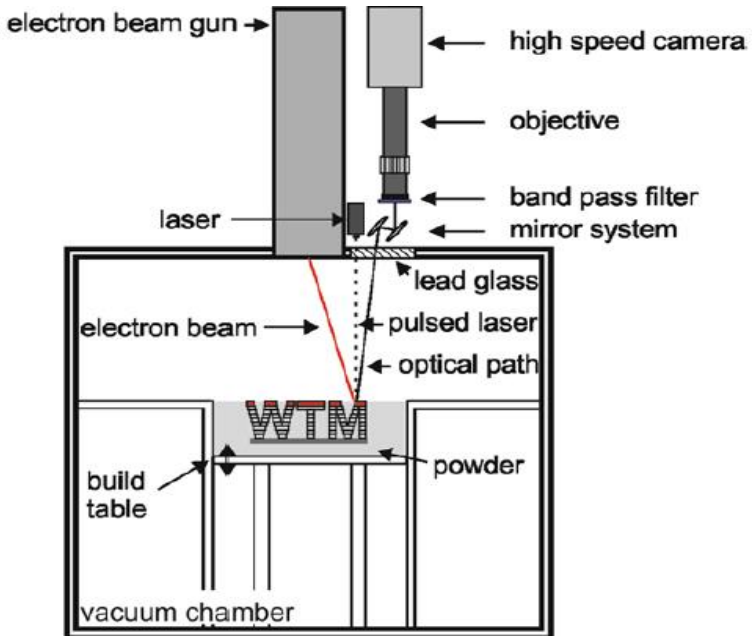

Figure 2.37 Schematic view of high speed monitoring in EBM process [82]

Low Coherence Interferometry

Low coherence interferometry, known as LCI, is a technique which measures optical field and analyses the interference of partially coherent beams. Compared to the image data from a camera monitoring system, the result from LCI gives distance information rather than brightness information. Neef et al., working with Precitec Optronik GmbH, installed an LCI device into the SLM system with the ability to inspect the powder bed, part elevations and defects searching.[83] The setup of integration of LCI with SLM has been patented by Precitec Optronik GmbH, and the arrangement is shown in Figure 2.38.

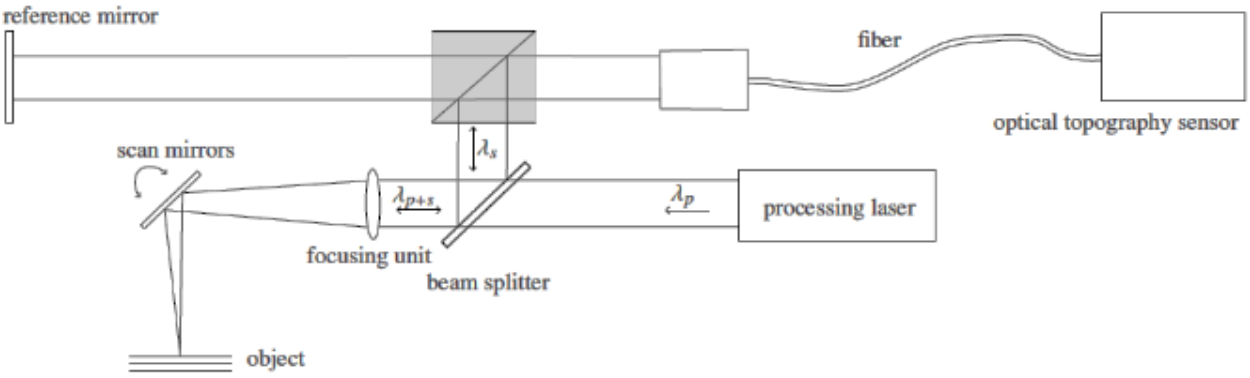

Figure 2.38 Integration of the interferometry sensor into the SLM process [83]

Accelerometer

An accelerometer is a device that measures any slight vibrations in the system, which has been applied by engineers in many fields. Kleszczynski et al.[84] put an acceleration senor on the recoating system of EOSINT M270 LBM system, as shown in Figure 2.39. This acceleration sensor can sense any vibration caused from the collision between the rake and any elevated part or balling effect. Kleszczynski's result showed a good correlation with the high resolution layer wise image. This system setup was patented by Eos Gmbh Electro Optical Systems in 2015.[85]

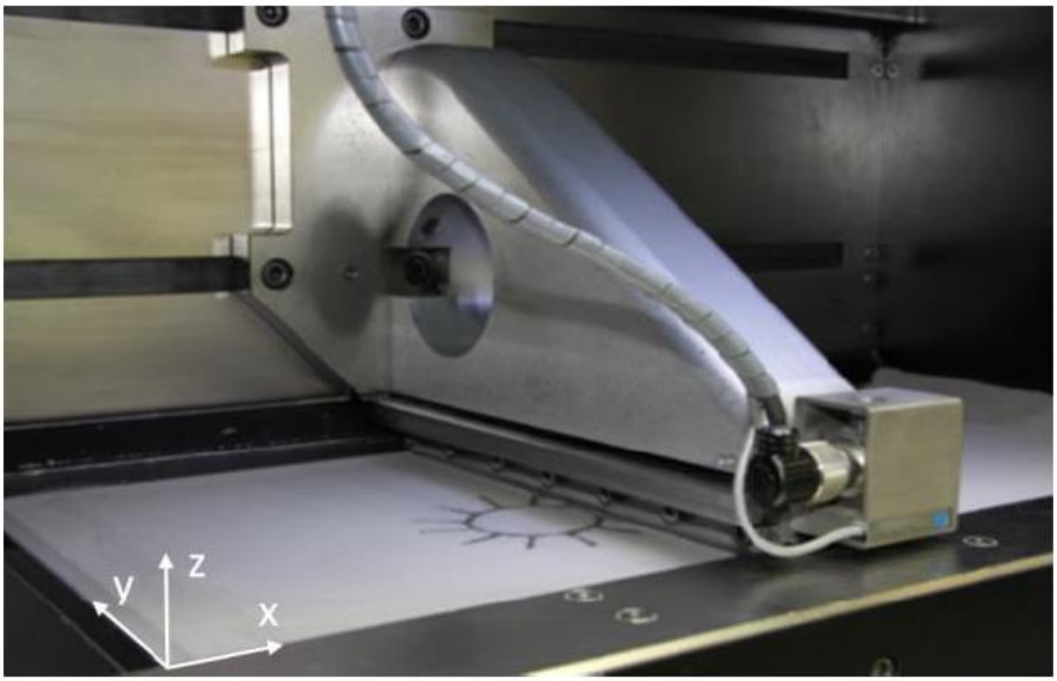

Figure 2.39 SLM machine with acceleration sensor on the rake [84]

Chapter 3 : Methodology & Instrumentation

3.1. ARCAM EBM Hardware

Figure 3.1 shows the typical hardware arrangement of the EBM Q Series machine chamber, and the following paragraphs explain the general hardware setting of the EBM machine.

- Camera glass: a protective window with shutter that protects the camera from damage by the X-rays generated during the build. The camera installed by ARCAM is the Prosilica GT6600 (Appendix A). The settings of the camera are synchronised with the EBM Control software and some of those can be adjusted through the EBM control user interface
- Heat Shield: a set of metal plates which serve for two reasons. The first one is to prevent metallic fumes generated during the process reaching any other components of the machine. The second is to deflect and keep the heat radiation into the build, thus less heat is lost during the process
- Powder table: the build area where each layer of the part is built on. The table is made of stainless steel (ASTM S30815),[87] which moves down after each layer finishes
- Rake: the metal bar with metal teeth designed in a way to swipe the powder onto the powder table
- Powder hopper: designed in a way to enable the gravity feeding of the powder, and store the unused powder during the process
- Build tank: stores the finished layers which have been built with the powder cake
- Rake regulator: controls the amount of powder to be deposited on the powder bed
- Linear feedthrough: enables the lowering of the powder table during the layer by layer process.

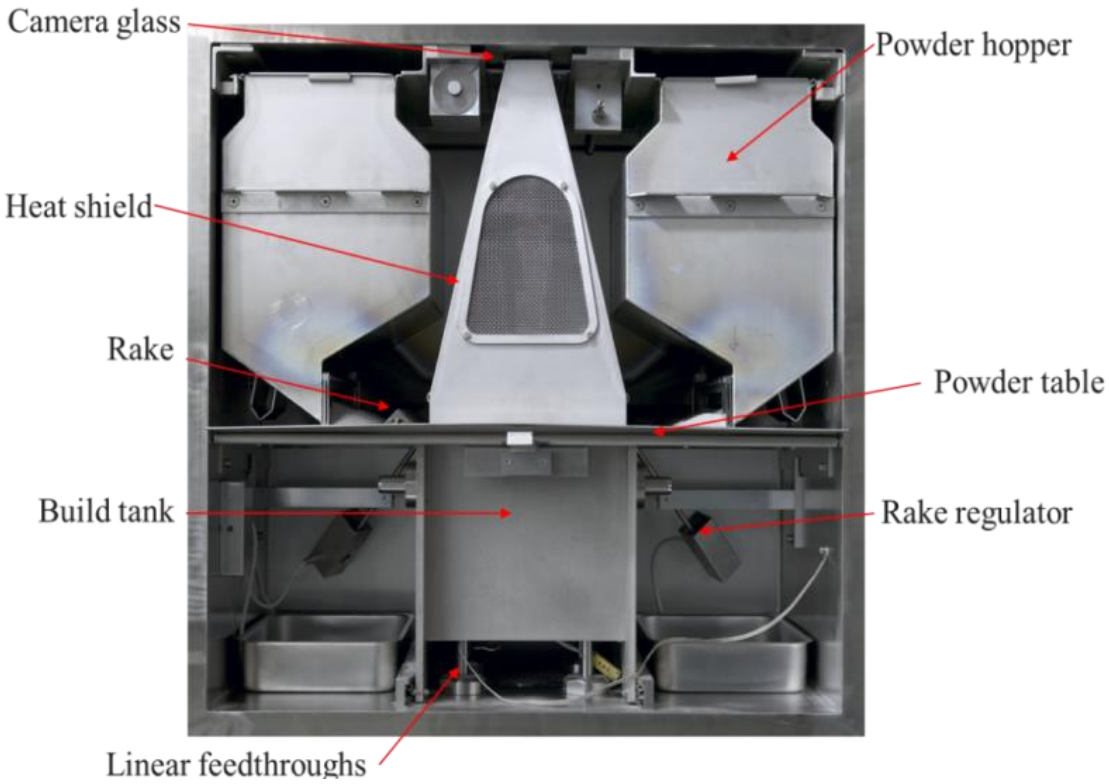

Figure 3.1 Build chamber of EBM machine

3.2. ARCAM EBM Process Functions

Due to the nature of the EBM process, powder particles absorb electrons from the electron beam and build up negative charges. As a consequence, every particle is repelling from each other. This repulsion force can make the powder particles to float into the chamber and block the incoming electron beam. Thus, before the actual melt start, the powder on the powder bed is preheated with maximum power but low intensity (defocused) beams. The power of the beam will not create a significant melt, but partially sinter the powder together to increase the bonding strength between the powder particles.

Although the chamber is under vacuum, there is still significant heat losses, such as the thermal conduction from the bolt connected to the base plate. In order to maintain a constant bed temperature, the EBM control system was built based on a 1D thermal model to estimate the heat loss. A graphical explanation of the algorithm acquired from ARCAM training document is shown in Figure 3.2 to illustrate the heat balancing system.

From the figure, the ‘Contour’ is the printing of the boundary of the part’s cross-section; ‘Hatching’ is the filling of the interior section of the part’s cross-section; ‘Raking’ is the process of spreading the powder onto the powder bed. In general, the processes of ‘Contour’, ‘Hatching’ and ‘Raking’ are considered as heat losing stages due to the rate energy input is lower than the heat loss. The only way to increase the temperature is by heating the chamber using a high power but defocused beam, which shows as red in Figure 3.2.

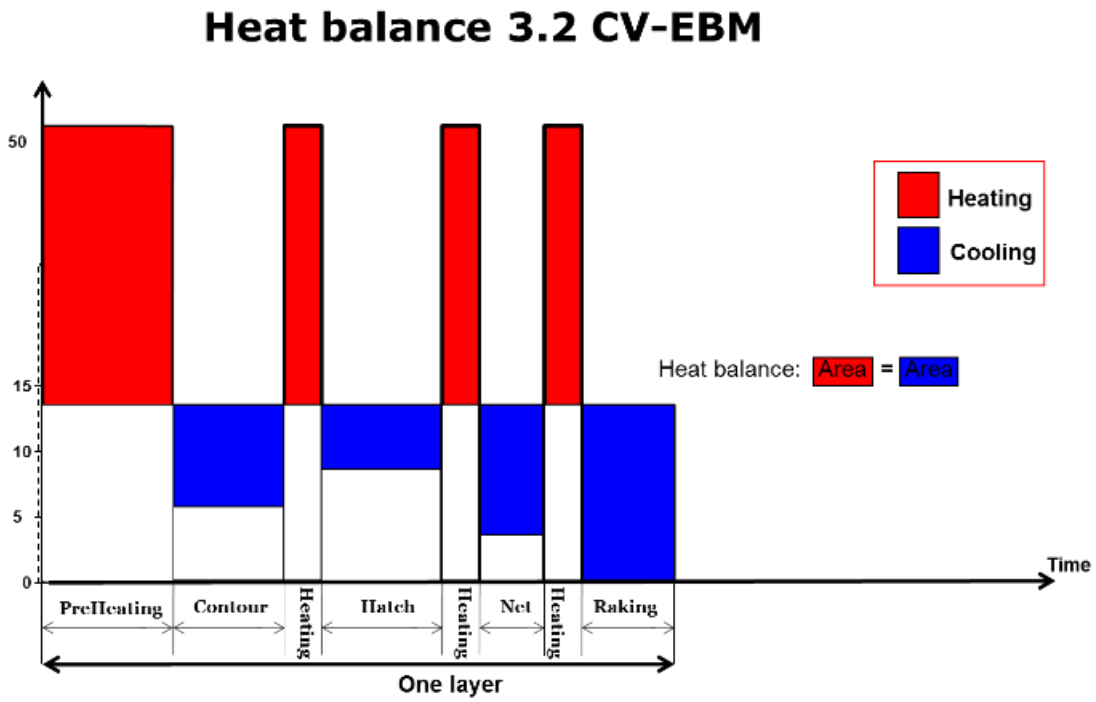

Figure 3.2 Heat balance strategy during EBM process[86]

Apart from the thermal model, the EBM process has over 300 different parameters which can influence the process. Some parameters, such as the raking settings, vacuum level, layer thickness etc. are directly linked to the hardware and can be straightforwardly controlled, but the majority of the parameters are linked more complicatedly with each other. The melting parameters (Preheat, Contour and Hatching) are the most directly linked to the quality of the part, and are grouped into many different functions. From the control software and the ARCAM trainings, some core functions are listed as follow.

3.2.1. Focus Offset

The diameter of the electron beam is an essential parameter for the EBM process, as it represents the energy distribution of the beam. As for the EBM process, the beam diameter is represented by the electrical current supply to the magnetic coil which is termed as focus offset.

ARCAM 'A' Series machines use tungsten as the material for the filament, but Q series machines use single crystal of lanthanum hexaboride (LaB6) thus the beam diameter is also varying differently with different focus offset. Figure 3.3 shows the relationship between actual beam diameter and focus offset values for both A-series and Q-series, as supplied by Arcam.

In the figure, the beam diameter is measured with full width at half maximum (FWHM). FWHM is an expression of beam diameter measured at the location where its intensity is half of the maximum intensity.

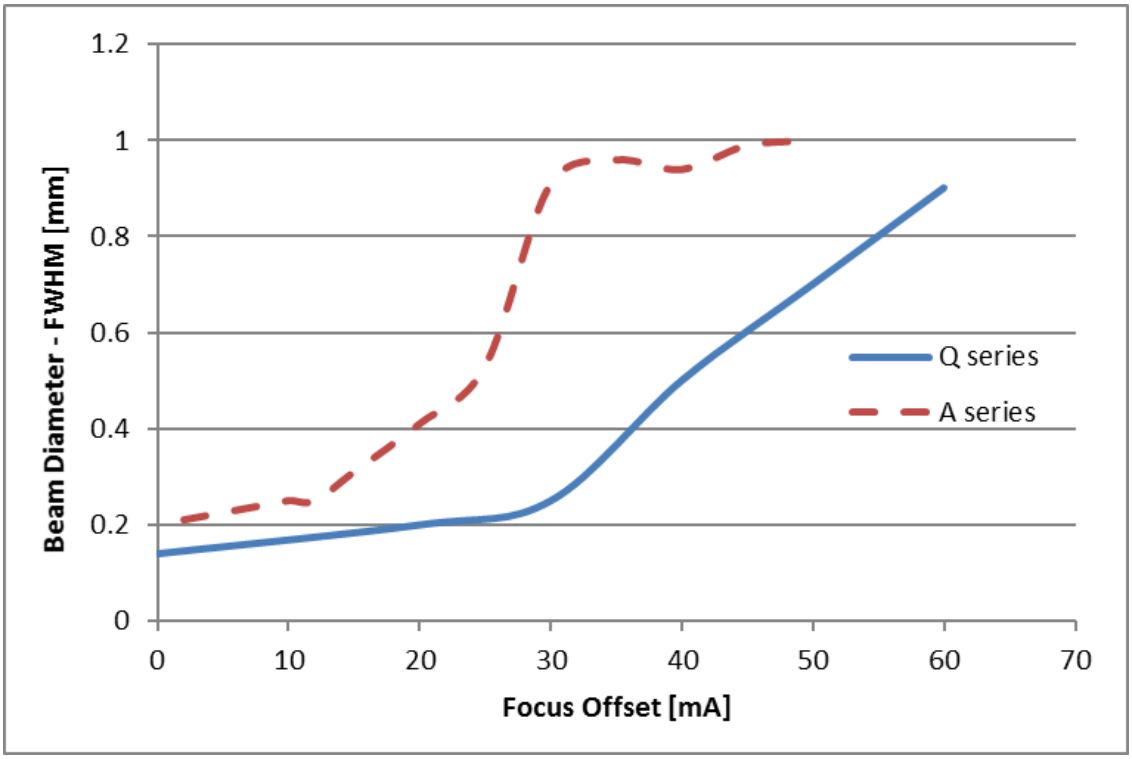

Figure 3.3 Graph of focus offset and beam diameter (supplied by ARCAM)

3.2.2. Contour Multisport

The contour is the melting of the boundary of a part's cross-section, which is melted with a 'dot' like action rather than a straight line. In the control software, the contour melting is mainly defined by the following settings which are schematically shown in Figure 3.4:

- 'Current' is the beam current of the electron beam.
- 'Spot number' is actually the number of the segment which melting simultaneously
- 'Multispot Overlap' is the overlap between two consecutive Spot
- 'Spot Time' is the duration the beam stays for each individual 'dot'.
- 'Speed' is the sum of speed of the electron beam travel for all spots which are melting at same instance, thus the speed in each 'spot' will be (speed/Spot number).

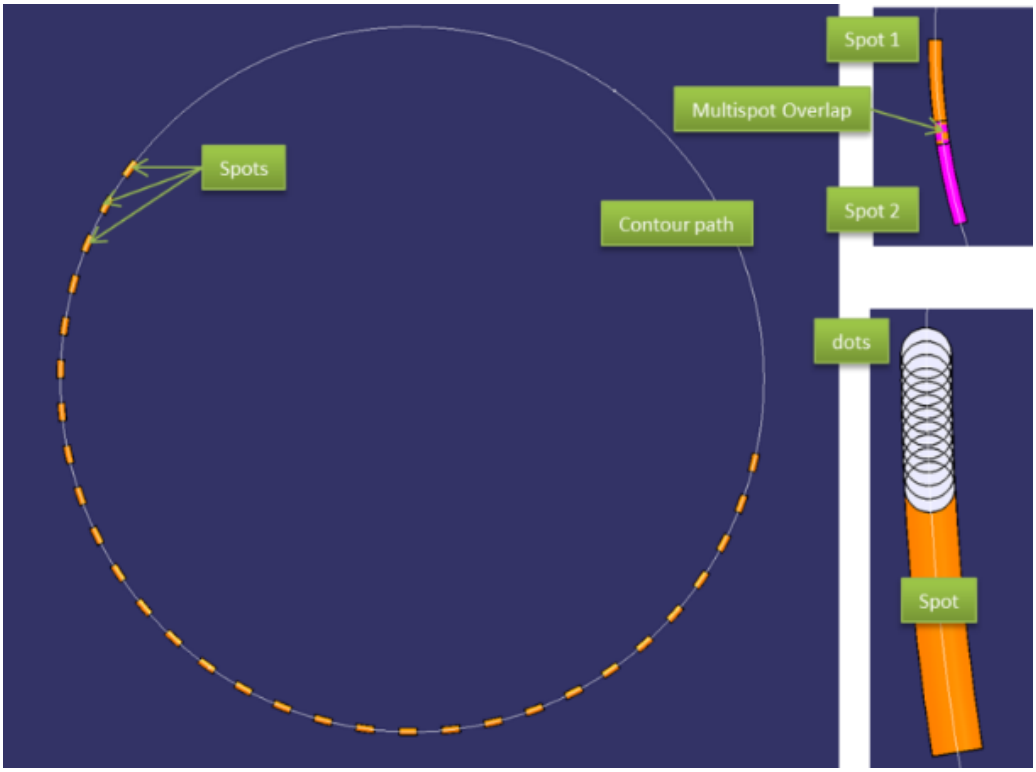

Figure 3.4 Contour in the EBM process

3.2.3. Scanlength Optimization

Scanlength is the length for each individual hatching line. Prior to Q series EBM machines, the hatching direction for each layer is the iteration between only vertical and horizontal scans. In

general, there is a maximum scanlength of 70 mm for any built, and if scanlength has exceeded this length, defects are more likely to be developed. Thus, parts are usually divided into different melt groups in order to avoid this problem.

As for the Q series machines, hatching lines are defaulted to rotate 67 degrees between each , and the scan-length optimisation algorithm shifts and divides the geometry to acquire optimum hatching length in each scan track, as shown in Figure 3.5. The aim of this algorithm is to improve the speed and stability of the process. Unfortunately, the detail or the equations of optimisation functions have not been given by ARCAM.

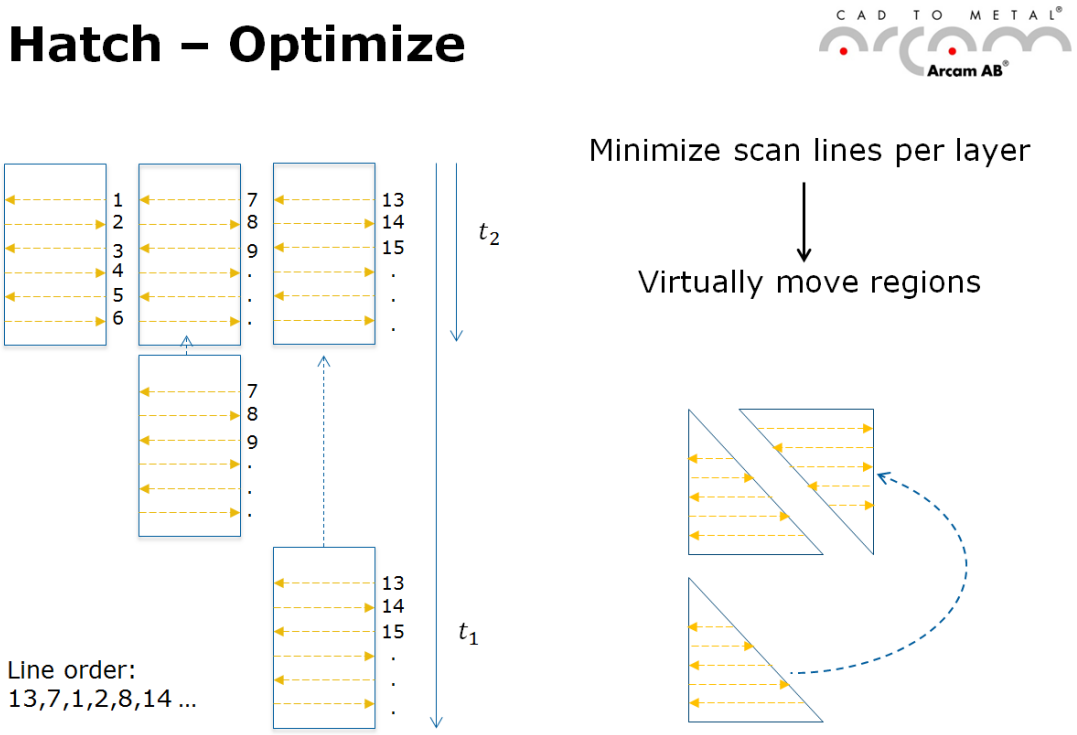

Figure 3.5 ARCAM Optimisation Function for the scanlength in each layer [87]

3.2.4. Speed Function

Speed function is the relation of speed and beam current during the 'melt' stage of the EBM process. In the most recent update for the Q20 Plus system, the hatching beam current is kept constant at 28mA through the entire 'melt' stage. With a constant current, the beam speed is

only dependent on the speed function number. The relation between speed function and beam speed at beam current of 28mA is shown in Figure 3.6.

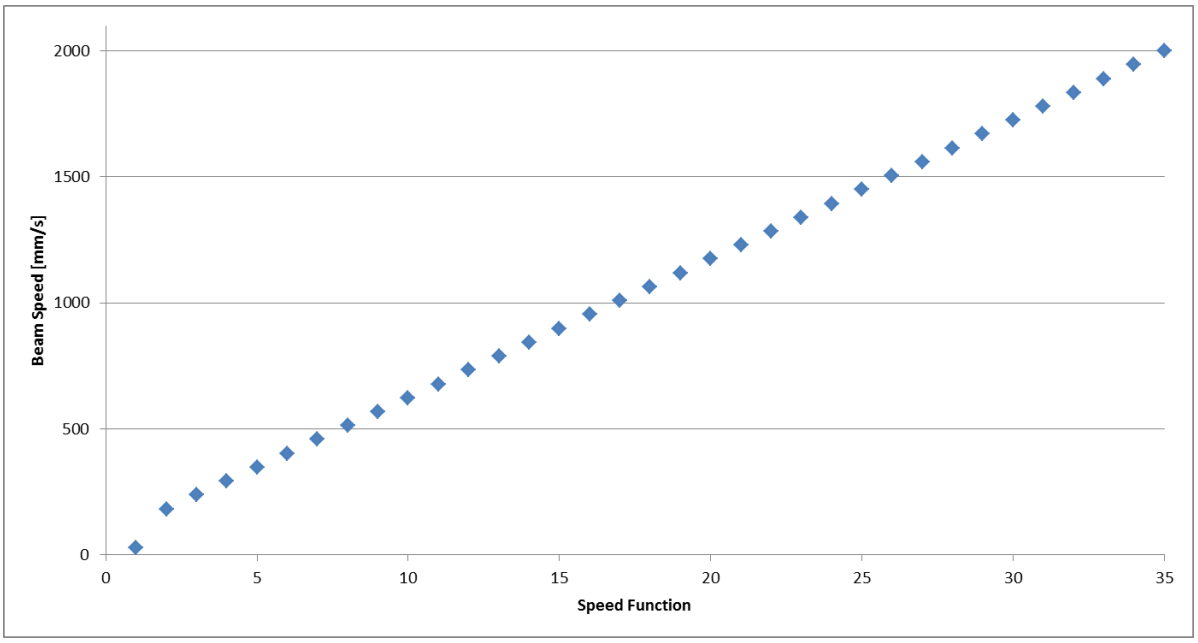

Figure 3.6 Beam speed vs. speed function at beam current of 28 mA

3.2.5. Turning Function

The default hatching strategy in EBM process is performed as zig-zag motion, thus the start location of the current hatch line is always influenced by the heat trail from the previous hatch line as shown in Figure 3.7. Thus, turning function is designed by ARCAM to increase the speed of the beam as it leaves the turning point to prevent overheating around the 'turning point'.

Equation 3.1

$$S_2 = S_1 \times (1 + I)$$

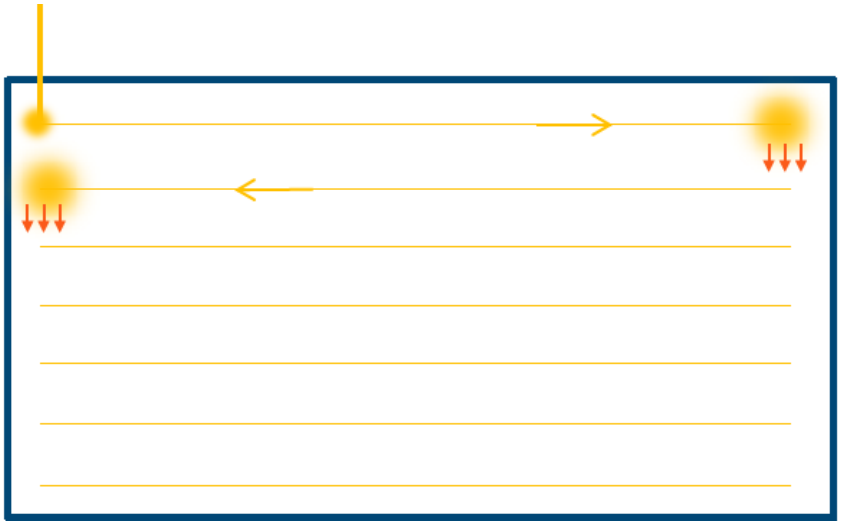

Figure 3.7 Drawing shows residual heat from previous hatching line's end trail [86]

3.2.6. Thickness function

Powder has much lower conductivity than solid material, thus if a location is surrounded by powder, then the rate of heat dissipation is much slower compared to a solid region. As in the EBM process, the main direction of heat dissipating is vertical downwards. If the part has overhang structures, then it is very likely to be overheated in these regions, as shown in Figure 3.8 .

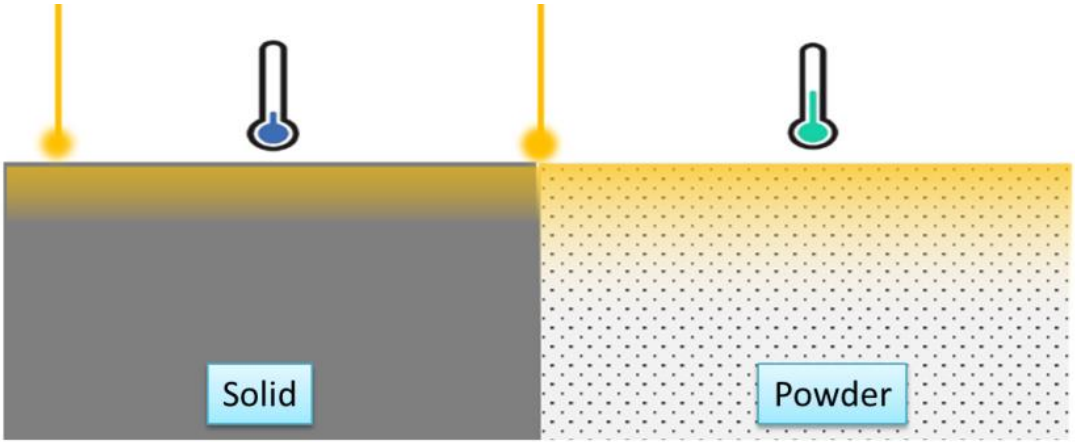

Figure 3.8 slow heat dissipation in overhang areas [86]

3.2.7. Thickness function is the equations used in the EBM process to increase the speed of the beam to avoid overheat on the overhang surfaces. The function is stated in Error! Reference source not found. and shown as follow, Line Offset Compensation

Line offset defines the distance between two individual parallel hatching lines, as shown in Figure 3.7. This function affects the distance between two hatch lines based on the scanlength, and the relation is schematically shown in Figure 3.9. The equation or algorithm for this function is not given.

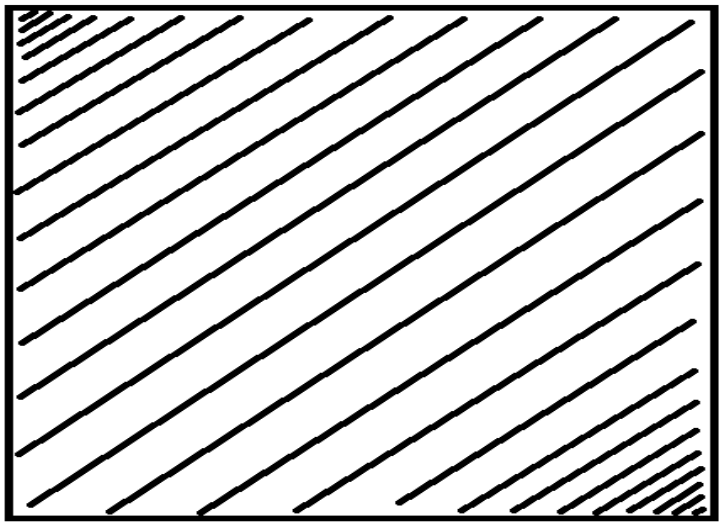

Figure 3.9 Effect of line offset compensation [87]

3.2.8. Thickness Focus

In the Q series EBM machine, a new function of Thickness Focus is added to compensate for the overhang surfaces also. The equation of this function has not been given, but it is known that, the thickness focus function modifies the focus offset value (beam diameter) when comes to overhang structure, just as the thickness function modifies the beam speed.

3.3. Cutting Samples

In this research many samples are cut with a Wire EDM machine. The machine is SODICK SLC600G as shown in Figure 3.10, with brass wire of 0.25mm diameter. The electrical current and cutting speed for Ti6Al4V material is chosen from Table 3.1, as suggested by the machine manufacturers.

Figure 3.10 Wire-cut EDM Sodick SLC600G

Table 3.1 EDM cut speed vs. thickness of component for Ti6Al4V [88]

Thickness [mm]	Cutting Speed [mm/min]
5	7.8
10	6.75
15	5.75
20	4.7
30	3.7
40	2.8
50	2

3.4. Microscope

In this research, the microscope used for observation is Alicona InfinityFocus as shown in Figure 3.11. The microscope is also used for surface roughness measurement according to ISO 4288-1996 standard.

Figure 3.11 Alicona InfinityFocus

3.5. Tensile Test and Fatigue Test

3.6. EBM Log File Reader

Some analysis during the research is analysed using MatLab self-created software to support the explanations and discussion. All the software have tested and run stable under MatLab 2016b environment.

There are three main developed algorithms in this research: EBM Log File Reader and Thermal Model will be explained in this section; the LayerDD software will be explained in detail in the later chapters with the corresponding algorithms.

The log file of the ARCAM EBM machine contains much information, such as beam current, smoke event, rake current, etc. ARCAM has supplied software (Log Studio) to interpret the log file. A disadvantage of the Log Studio is that all the data presented are expressed with regards to time. An example of a section of log file is shown in Figure 3.12, where the vertical axis is the beam current and the horizontal axis is the time.

In order to obtain more suitable output, in this research, the log files are further interpreted using the Log File Reader to extract information such as energy density, scanlength distribution, etc. In this software, all the data are mainly interpreted against the build heights.

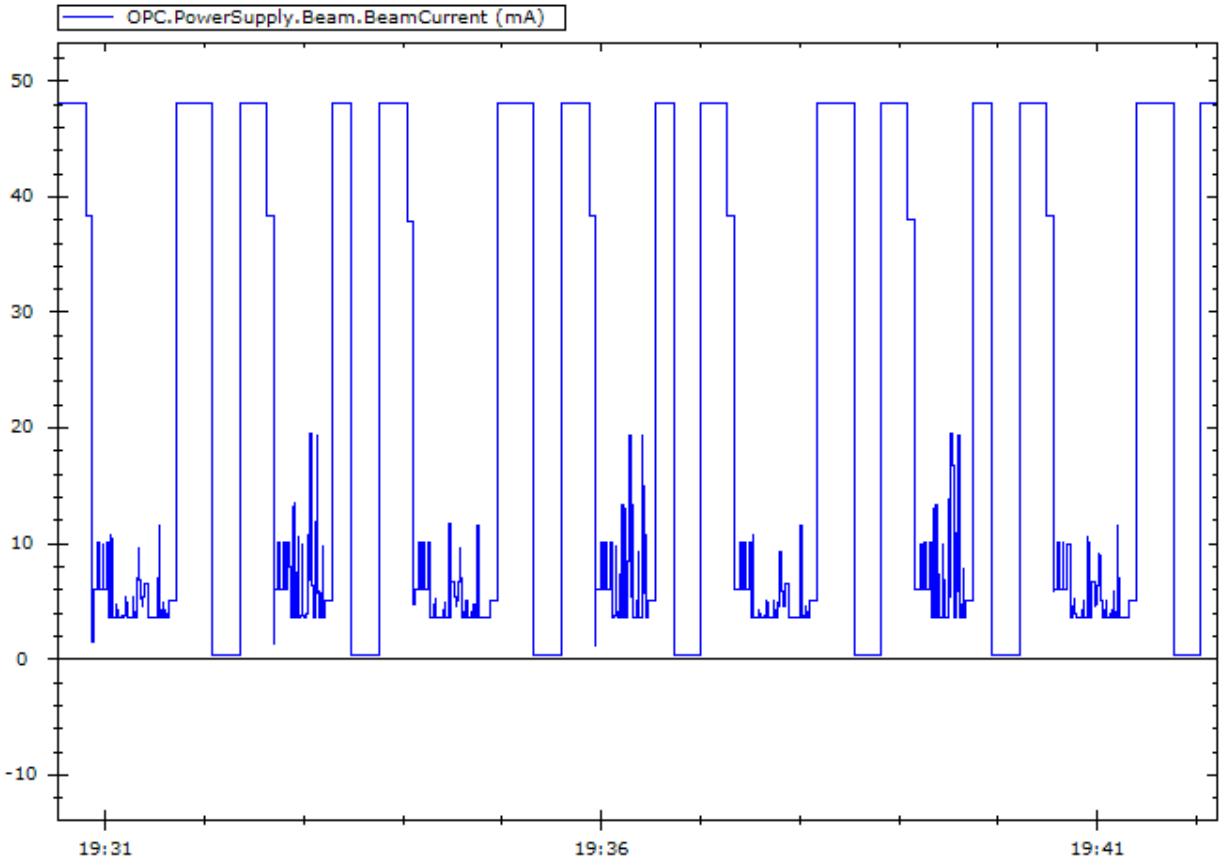

Figure 3.12 Example of log file interpreted by Log Studio, e.g. beam current presented in EBM log files

Energy Density Output

Energy density is a very popular term used in additive manufacture. It is defined as the energy per unit volume or area, and is used as an indication of the overall process parameters. In the SLM process, the energy density can be easily calculated since the melting is simply defined

by the beam speed, beam power, hatching offset and layer thickness. Unfortunately, in the EBM process, the existence of numerous unknown functions makes the energy density hard to predict. The following tool is developed in MatLab and can be used to find the energy density value from the log file rather than just predicted from the input equations.

EBM Control produces a single text file which includes all the information during the build, such as smoke, arc trip, rake sensor, beam information, etc. Thus, the first step will be filtering the required information out, as in the example shown in Table 3.2

From the table, 'Time' indicates the time of data recorded; 'Description 1 to 3' indicates what information is recorded, for example row 1 is the height of build and row 4 is where Preheat stage started; 'Value' indicates the value for any type of record, such as beam current or layer height.

Table 3.2 Example of beam current exacted from the EBM log file (Units are manually added in the example)

	Time	Description 1	Description 2	Description 3	Value	
1	'2017-07-14 14:22:41.449'	'Builds.State.CurrentBuild.CurrentHeight'	'[OnChange(Builds.State.CurrentBuild. CurrentZLevel)] Arcam. EBMControl. Process.ProcessManager. OnBuildStatusChanged() (Logic)'	''	'3.24'	
2	'2017-07-14 14:22:41.699'	'OPC.PowerSupply.Beam.BeamCurrent'	'R1181\ebm (OPC)'	''	'0.3761575'	
3	'2017-07-14 14:22:49.311'	'OPC.PowerSupply.Beam.BeamCurrent'	'R1181\ebm (OPC)'	''	'0.3472222'	
4	'2017-07-14 14:22:57.642'	'Builds.State.CurrentBuild.OutputDescription'	'(BeamControl)'	'Preheat'	'[1]'	
5	'2017-07-14 14:22:57.689'	'OPC.PowerSupply.Beam.BeamCurrent'	'R1181\ebm (OPC)'	''	'47.88773'	
6	'2017-07-14 14:23:09.747'	'OPC.PowerSupply.Beam.BeamCurrent'	'R1181\ebm (OPC)'	''	'38.85995'	
7	'2017-07-14 14:23:09.872'	'OPC.PowerSupply.Beam.BeamCurrent'	'R1181\ebm (OPC)'	''	'39.95949'	
8	'2017-07-14 14:23:12.805'	'OPC.PowerSupply.Beam.BeamCurrent'	'R1181\ebm (OPC)'	''	'47.91666'	
9	'2017-07-14 14:23:18.203'	'OPC.PowerSupply.Beam.BeamCurrent'	'R1181\ebm (OPC)'	''	'19.01041'	
10	'2017-07-14 14:23:20.075'	'OPC.PowerSupply.Beam.BeamCurrent'	'R1181\ebm (OPC)'	''	'27.92245'	
11	'2017-07-14 14:23:20.231'	'Builds.State.CurrentBuild.OutputDescription'	'(BeamControl)'	'Melt'	'[2]'	
12	'2017-07-14 14:23:28.000'	'OPC.PowerSupply.Beam.BeamCurrent'	'R1181\ebm (OPC)'	''	'8.940975'	
13	'2017-07-14 14:23:44.551'	'OPC.PowerSupply.Beam.BeamCurrent'	'R1181\ebm (OPC)'	''	'9.92477'	
14	'2017-07-14 14:23:44.692'	'Builds.State.CurrentBuild.OutputDescription'	(BeamControl)'	'Wafer Support'	'[3]'	
15	'2017-07-14 14:23:51.930'	'OPC.PowerSupply.Beam.BeamCurrent'	'R1181\ebm (OPC)'	''	'45.3125'	
16	'2017-07-14 14:23:52.164'	'Builds.State.CurrentBuild.OutputDescription'	'(BeamControl)'	''	''	

17	'2017-07-14 14:23:52.180'	'OPC.PowerSupply.Beam.BeamCurrent'	'R1181\ebm (OPC)'	''	'47.91666'	
18	'2017-07-14 14:24:04.940'	'OPC.PowerSupply.Beam.BeamCurrent'	'R1181\ebm (OPC)'	''	'0.4050925'	
19	'2017-07-14 14:24:05.128'	'Builds.State.CurrentBuild.CurrentHeight'	'[OnChange(Builds.State.CurrentBuild.CurrentZLevel)] Arcam.EBMControl.Process.ProcessManager.OnBuildStatusChanged() (Logic)'	''	'3.33'	

As the second column indicates the time of the beam current recorded, thus the difference between each consecutive time indicates how long the corresponding current has been used. By multiplying the current with accelerating voltage and the corresponding duration, the amount of energy input into any layer at any stage can be found.

In EBM process, contour and hatch have independent settings. Contour in the EBM process are printed with multi spots and constant energy without any addition of sophisticated functions. Thus the energy which goes into the contour can be computed from the EBM setting and the cross-section perimeter using Equation 3.2. The surface area can be also found from the original geometry's cross-section, thus energy density as energy per unit volume can be calculated.

The overall equations to calculate the energy density of hatching in any layer is listed from Equation 3.3 to Equation 3.5, and the definitions for the symbols are shown in Table 3.3. An example of energy density vs. build height is shown in Figure 3.13.

Figure 3.13Equation 3.2

$$E_C = \frac{N * OL + L}{S_c} \times I_c \times AccV$$

Equation 3.3

$$A_c = L \times LO_c$$

Equation 3.4

$$E = \sum I \times \partial t \times AccV$$

Equation 3.5

$$ED = \frac{E - E_C}{(A - A_c) \times Lt}$$

Table 3.3 Meanings for the symbol from Equation 3.2 to Equation 3.5

Symbol	Meaning
A	overall cross-sectional area
A_c	area of contour
$AccV$	accelerating voltage (60,000V)
E	total energy input to the overall layer
E_C	energy input to contour region
ED	energy density of the layer without contour
I	beam current from the log file
I_c	beam current input for the contour region
L	total length of contour
LO_c	line offset for the contour region
Lt	layer thickness
N	number of sub-segment create around the contour
OL	the overlap distance between each segment
S_c	beam speed for the contour region
∂t	time difference between consecutive record

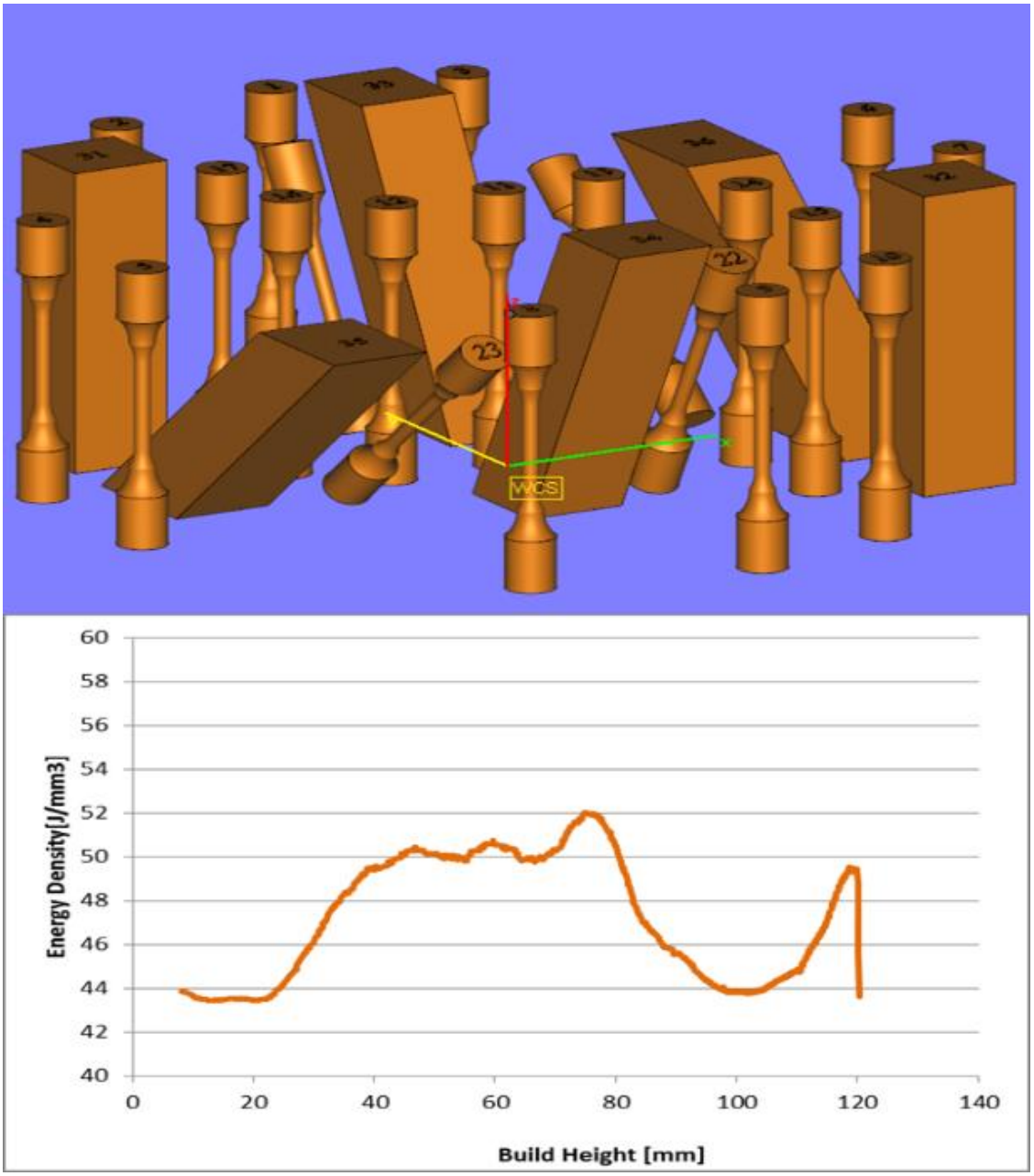

Figure 3.13 example of energy density interpreted using log file reader

Scanlength Distribution

In the EBM log file, the length of each scan track has not been recorded, but there is a section recording the distribution of scanlength in each layer. In the example shown in Figure 3.14, 'ScanlengthHistogram[0] – [6]' represents the number of scanlines computed between 0-10mm, 10- 20mm and so on. Similar to beam current logged data, the scanlength distribution is also logged with respect to time, by using MatLab, the data is then reanalysed and presented with respect to the build height, as shown in Figure 3.15.

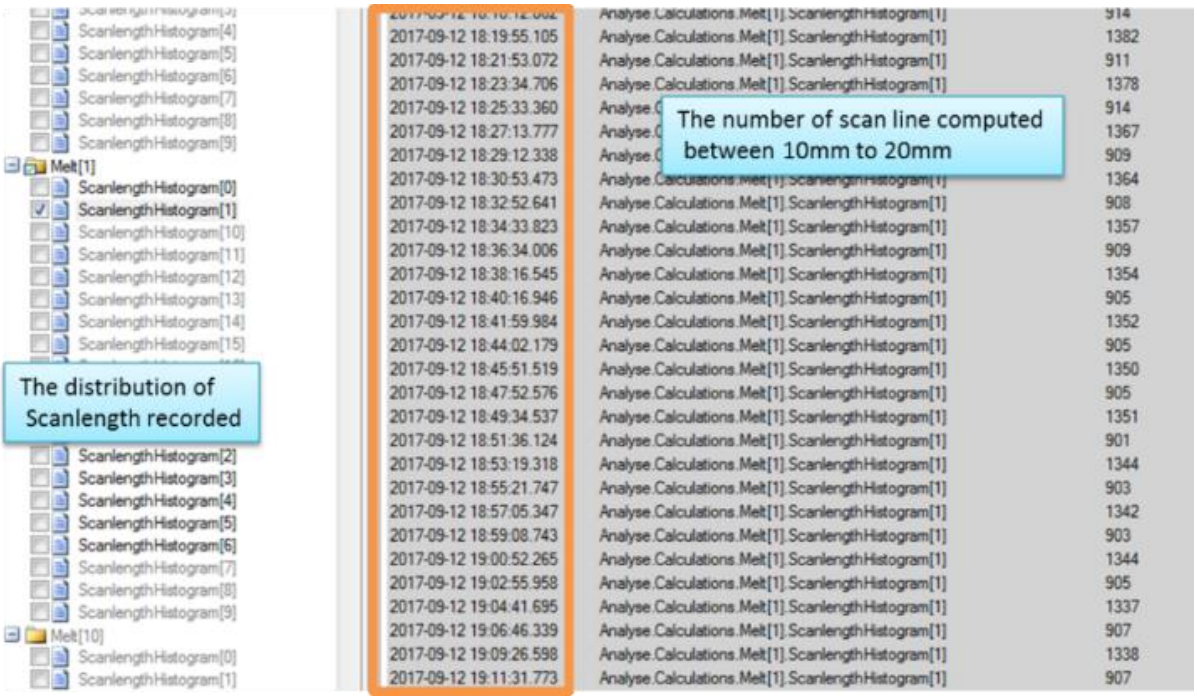

Figure 3.14 Scanlength distributions from EBM Log Studio (example only)

Build Height [mm]	0-10mm	10-20mm	20-30mm	30-40mm	40-50mm	50-60mm	60-70mm	Sum
11.8	608	470	191	256	110	68	107	1810
11.85	3308	1543	196	83	0	0	0	5130
11.9	590	472	194	250	103	68	118	1795
11.95	3293	1539	208	86	0	0	0	5126
12	579	478	197	247	93	67	130	1791
12.05	3274	1547	211	89	0	0	0	5121
12.1	561	477	200	249	84	64	141	1776
12.15	3261	1550	210	94	0	0	0	5115
12.2	559	483	197	248	67	62	162	1778
12.25	3243	1552	205	107	0	0	0	5107
12.3	550	490	194	251	64	36	191	1776
12.35	3222	1558	208	107	0	0	0	5095
12.4	543	493	197	252	57	36	198	1776
12.45	3204	1564	211	107	0	0	0	5086
12.5	548	491	198	252	45	33	213	1780

Figure 3.15 Example of scanlength distribution presented with respect to the build height

3.7. Simple Thermal Modelling using MatLab Matrix

A simple version of thermal model has been created in MatLab, which is aimed to explain the thermal history of EBM production, such as the shape of melt pool, etc. The thermal model is built based on the 3D matrix in MatLab, where each number in the matrix represents an individual voxel of the geometry, as per the example shown in Figure 3.16.

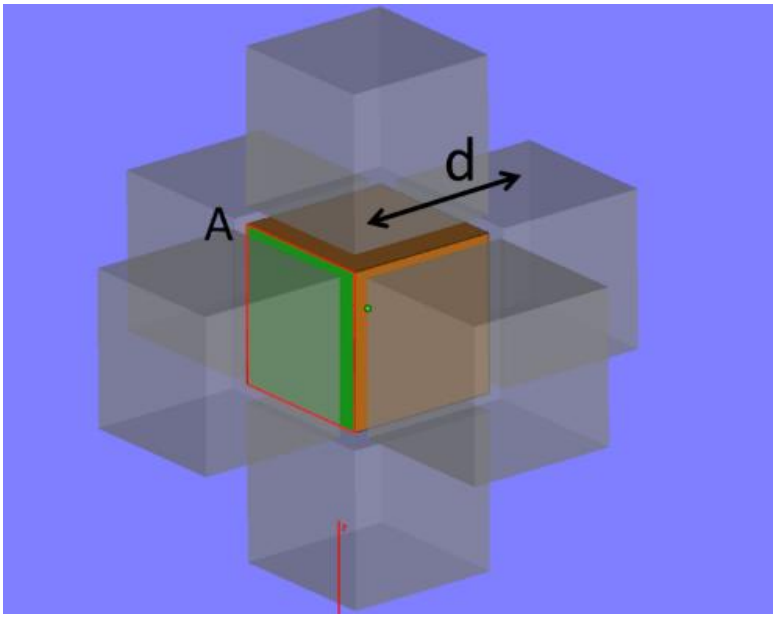

Figure 3.16 Diagram showing conduction model using MatLab matrix

The heat transfer by conduction is adapted with the fundamental Fourier's equation of heat conduction model, as shown in Equation 3.6 and Equation 3.7. In each time step, heat is exchanged between adjacent voxels. The boundary condition of the model is set to the base plate with a fixed temperature.

Equation 3.6

$$Q = kA \times \Delta T/d$$

Equation 3.7

$$\delta T = \frac{\mathrm{Q} \times \delta \mathrm{t}}{V \times \rho \times C_p}$$

In the above equations, Q is the heat flow rate by conduction; k is the thermal conductivity of the material; A is the cross-section area; ΔT is the temperature between adjacent voxels; d is the size of the voxel or the distance between the centre of adjacent voxel; $\delta T\ is$ the change of the temperature for the current voxel; δt is the time steps; $V, \rho\ and\ C_p$ is the volume, density and heat capacity of the current voxel. In every time step of iteration, the thermal properties values are changed with respect to the temperature, and the value is interpolated from the data in Table 3.4. In addition, the thermal conductivity of the powder is assumed to be 10% of the solid.[89]

Table 3.4 Thermal properties varied with temperature for Ti6Al4V [90]

	Temperature [°C]	Density [kg/m³]	Heat Capacity [J/(K×kg)]	Heat Conductivity [W/(mK)]
Symbol	**T**	**ρ**	**C_p**	**k**
	25	4420	546	7
	100	4406	562	7.45
	200	4395	584	8.75
	300	4381	606	10.2
	400	4366	629	11.35
	500	4350	651	12.6
	600	4336	673	14.2
	700	4324	694	15.5
	800	4309	714	17.8
	900	4294	734	20.2
	995	4282	753	22.7
	995	4282	641	19.3
	1100	4267	660	21
	1200	4252	678	22.9
	1300	4240	696	23.7
	1400	4225	714	24.6
	1500	4205	732	25.8
	1600	4198	750	27
	1650	4189	759	28.4
	1650	3920	831	33.4
	1700	3886	831	34.6
	1800	3818	831	-
	1900	3750	831	-
Uncertainty	±3%	±3%	±3%	±10%

The time step for the iterations of simulation is limited by the size of the voxel applied. In order to prevent the simulation from overshooting, Equation 3.8 which is derived from Equation 3.6 and Equation 3.7, is used to set the maximum time step (TS_l) for the simulation, where: Vx, Vy, Vz are the voxel dimensions in X, Y, Z direction. The number on the numerator of the equation is the minimum ratio of $C_p \times \rho / k$ calculated from Table 3.4.

Equation 3.8

$$TS_l = \frac{111952.5}{2 \times \left(\left(\frac{1}{V_x}\right)^2 + \left(\frac{1}{V_y}\right)^2 + \left(\frac{1}{V_z}\right)^2 \right) \times 10^6}$$

The heat lost by convection is assumed to be negligible in this simulation, as the pressure inside the chamber is only . As for the heat lost by radiation, this is assumed only to be happening to the top of the surface (voxel) by using Stefan-Boltzmann Law. The surrounding temperatures are assumed to be 342 °C.[91]

3.9.1 Electron Beam Energy Input

Electron beam are able to penetrate a certain depth of material and the maximum penetration depth of the electron beam is calculated by using Equation 3.9[92].

Equation 3.9

$$R = \frac{2.76 \times 10^{-2} \times m_A \times (E_0)^{\frac{5}{3}}}{Z^{\frac{8}{9}}} \times \frac{(1 + 0.978 \times 10^{-3} \times E_0)^{\frac{5}{3}}}{(1 + 1.957 \times 10^{-3} \times E_0)^{\frac{4}{3}}} \times \frac{1}{\rho}$$

Where R is in m, E_0 is the electron energy in keV, m_A the molar mass in Kg, ρ the density in kg/m^3, Z is the average atomic number of the material. The calculated result of the penetration depth for the electron beam in EBM process with 60 KeV accelerating voltage is approximately 21.3 µm.

To estimate the distribution of the electron beam along vertical direction, the following Equation 3.10 to Equation 3.14 are used: [92,93]

Equation 3.10

$$\frac{E_A}{E_0} = \left(1 - \eta_B * \frac{E_B}{E_0}\right) \times \left(1 - \eta_T * \frac{E_T}{E_0}\right)$$

Equation 3.11

$$\eta_B = \left(\frac{a_1}{\tau^{a_2}} \times \frac{1}{1+\left(a_3/\tau\right)^{a_4}} \times \frac{1}{1+\left(\tau/a_5\right)^{a_6-a_2}}\right)^{\cos(\Theta)}$$

Equation 3.12

$$\frac{E_B}{E_0} = 1 - \left(1 - \frac{d_1 \times Z^{d_2} \times \tau^{d_3}}{1+\left(\tau/d_4\right)^{d_3}+\left(\tau/d_5\right)^{d_3+d_6}+\left(\tau/7\right)^{d_3+d_8}}\right) * \cos(\Theta)$$

Equation 3.13

$$\eta_T = e\text{^}\left(-m_1 \times \left(Z/R\right)^{m_2} \Big/ \left(1 - Z/R\right)^{m_3}\right)$$

Equation 3.14

$$\frac{E_T}{E_0} = \left(1 - Z/R\right)^{n_1/(1+n_1)}$$

Where E_A, E_B and E_T refer to the mean energies of absorbed, backscattered and transmitted electrons in depth z; η_B and η_T are the electron striking a target being backscattered and transmitted; Θ is the angle between vertical and line of incident beam; τ is the ratio of E_0 to the rest energy of electron. The parameter of a_1 to a_6, d_1 to d_8, m_1 to m_3, n_1 to n_2 are listing in the Table 3.4.The vertical distribution is shown in Figure 3.17 with incident beam perfectly vertical. The overall absorbed energy fraction is calculated to be 0.83.

Table 3.5 parameters for the electron beam distribution equation[92,93]

a1	9.41×10^-3+1.132×exp(-((57.1/Z)^0.579))
a2	3.47/(1+(Z/0.163)^0.833)
a3	7.3×10^-4/(1+(58.5/Z)^5.14)
a4	0.574
a5	1.43×Z^0.447
a6	1.108+0.417/(1+(13/Z)^176)
d1	82.6
d2	0.2063
d3	1.075
d4	0.00656
d5	2.54
d6	2.08
d7	0.082
d8	0.509
m1	4.17×Z^0.04
m2	6.12/(Z^0.4)
m3	Z^0.92/72
n1	log10(0.77/8×Z^(1/6)×(E_0/13.6057))
n2	1+2×exp(-n1+2×10^-n2)

As for the lateral beam distribution, it is assumed to be 2D Gaussian distribution in this simulation, and the relation between FWHM of the electron beam and the focus offset value have been given by ARCAM's engineer as shown in Figure 3.3.

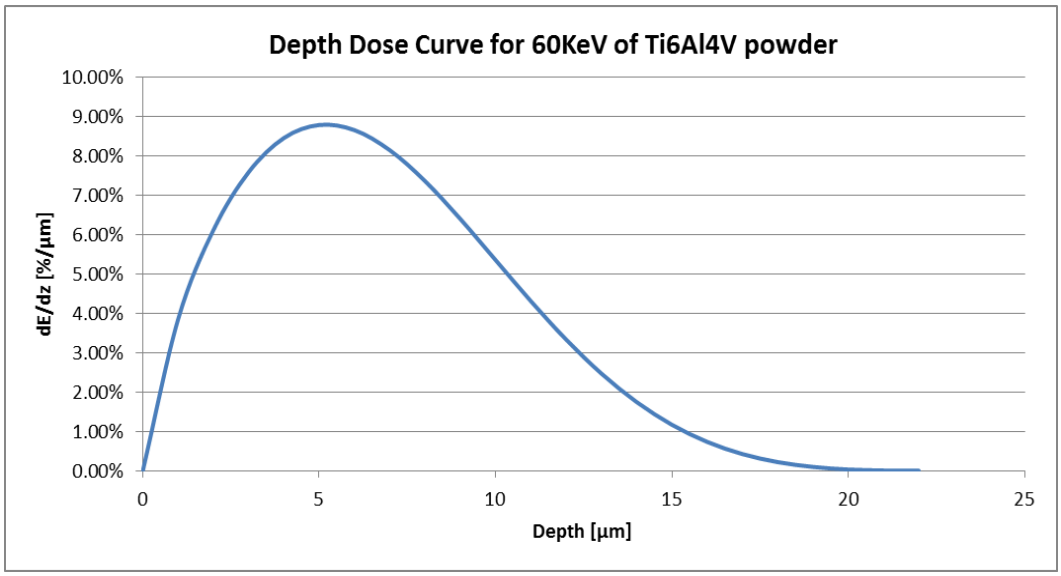

Figure 3.17 Depth dose curve for 60KeV electron beam on Ti6Al4V powder

3.9.2 Simulation Verification

In this research, the above thermal model is verified by comparing the current simulation result with the real EBM melt pool results of melt pool from Al-Bermani [94] and Price.[95] The comparison is shown in Table 3.6 and Table 3.7. The percentage error between all the data in the table is varied from -8.7% to 8.5%

Table 3.6 Simulation Result of melt pool depth comparing with Al-Bermani's experiment result

Surrounding Temperature [°C]	Beam Current [mA]	Beam Speed [mm/s]	Focus Offset [mA]	Al-Bermani S.S. Result		Current Result	
				Melt Pool Depth [µm]	Beta Trans. Depth [µm]	Melt Pool Depth [µm]	Beta Trans. Depth [µm]
650	6	187.8	17	306	528	307	535
650	8	375	17	253	434	240	430
650	10	496.8	17	247	423	236	417
650	12	608.4	17	244	418	238	412
650	15	802	17	238	407	232	397

Table 3.7 Simulation Result of melt pool depth comparing with Steven Price's experimental result [95]

Surrounding Temperature [°C]	Beam Current [mA]	Speed Function	Beam Speed [mm/s]	Beam Diameter [mm]	Steven Result		Current Result	
					length [mm]	width [mm]	length [mm]	width [mm]
730	7.7	20	481	0.65	2.3	0.95	2.1	1.02
730	7.7	36	853	0.65	1.7	0.95	1.6	0.9
730	7.7	50	1193	0.65	1.5	0.8	1.545	0.81
730	7.7	65	1595	0.65	1.3	0.8	1.35	0.73

Chapter 4 : Find LOF from Layer Image in EBM process

4.1. Introduction

From the literature review section, it can be seen that EBM parts mainly consist of the following types of defect: gas pores, keyhole porosities, swelling and lack of fusion.

Gas pore and keyhole porosities are generally smaller in size and usually contained within the part. If Hot Isostatic Pressing (HIP) treatment is used on EBM parts, it is very likely these type of defects will be removed.

During the EBM process, 'Swelling' is a very common observation when the energy input to the area is significantly overdosed. Although the key reason of why 'Swelling' happens has not yet to be confirmed, it is known that when the 'Swelling' is large enough, it is very likely to create un-evenly distributed powder layers or it may break the rake system, which eventually leads to a failed build.

The current approach of the EBM process given by the manufacturer's default theme is to lower the overall energy input of the process to fully avoid the potential of 'swelling' and ensure the build will complete. Although this approach lowers the chance of swelling, the probability of lack of fusion defects (LOF) is increased correspondingly. To resolve the problem of internal LOF, ARCAM has initially proposed that HIP treatment can be used to rectify the internal defects in a similar way as gas or keyhole pores.

LOF defects are able to propagate upwards through many layers and therefore they can be very large in size and irregular in shape. If the LOF is fully contained within the part, HIP treatment can be used to rectify the defects just as gas or keyhole porosities. However once this LOF has created an opening on the surface, the defect can no longer be fixed by HIP. Due to the fact

that as-built EBM components have very rough surfaces there is still no qualified method to inspect the existence of surface defects.

An example is provided by the GKN AMC and is shown in Figure 4.1. In this region of the component, the as-built surface looked very normal, but a LOF defect has developed and travelled to the part's surface and created openings, which results in the HIP processes failing to rectify the defects. The part shown has gone through chemical milling, where the corrosive liquid has pass through the surface openings and attacked the nearby material, eventually revealing the defect on the surface as shown in Figure 4.1b.

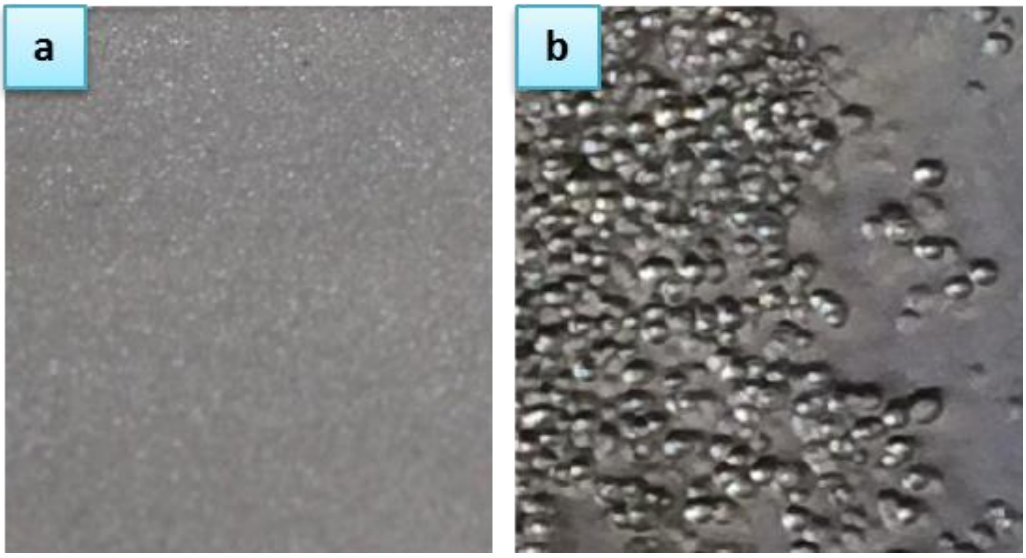

Figure 4.1 [a] part surface immediately after the EBM process which shows no indication of defects [b] defects revealed after the part has gone through HIP treatment and chemical milling

A camera has already been pre-installed within the machine, which is designed to take an image after each layer is completed. As the camera is taking the layer image only and not recording the melting process, defects such as gas porosity are unlikely to be detected. However it is expected that the camera is capable of accurately recoding the presence of defects such as lack of fusion (LOF) which are relatively large in size and exposed within each layer.

From previous reports and user experience of EBM it is considered that insufficient energy input would lead to the formation of a rough surface. The rough top surface in turn could be

responsible for initializing the formation lack of fusion. The following tests aim to illustrate the development of the LOF with seeded defects in the previous layer, and how LOF gradually changes during an EBM build.

Thus, the two main aims in this chapter are:

1. Understand the development of LOF.
2. Study the characteristics of the image took by the installed camera

4.2. Experiment Set-up

In this experiment, the LOF defects were seeded artificially within the part. The test samples consist of two sections: the base section and the top section, as shown in Figure 4.2. The base section is a simple block designed with five 0.8 mm square top to bottom through holes, and it was printed with the default Q20 theme with a 90 µm layer thickness (theme version 4.2.57). The top section was printed with the same theme but with the Thickness Function and Thickness Focus Function de-activated.

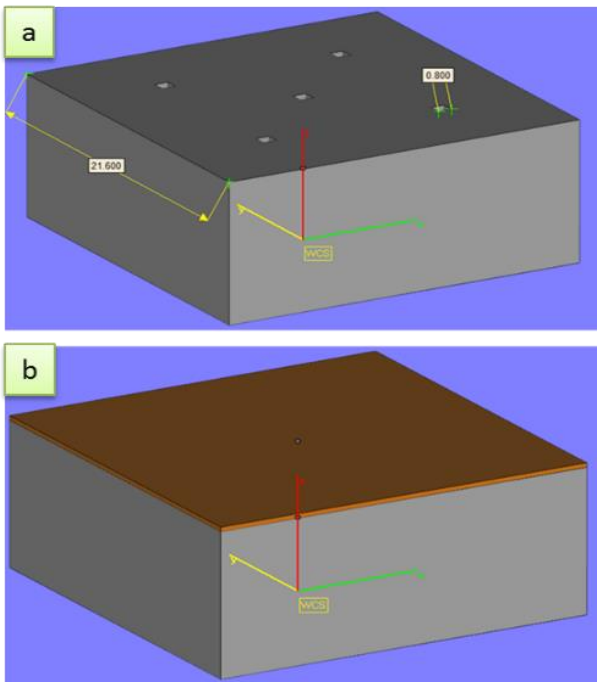

Figure 4.2 LOF test samples [a] where the base where have top to bottom induced holes [b] assembly with top and base, where the top is designed to be a full layer without any holes

In total, six samples were produced as shown from the configuration in Figure 4.3. The description of the samples are listed in Table 4.1, where Sample 0 was produced with no top, and Samples 1 to 5 were produced with the same cross-section as the base section, but with the top sections thickness being 0.09 mm, 0.18 mm, 0.27 mm, 0.36 mm, and 0.45 mm respectively.

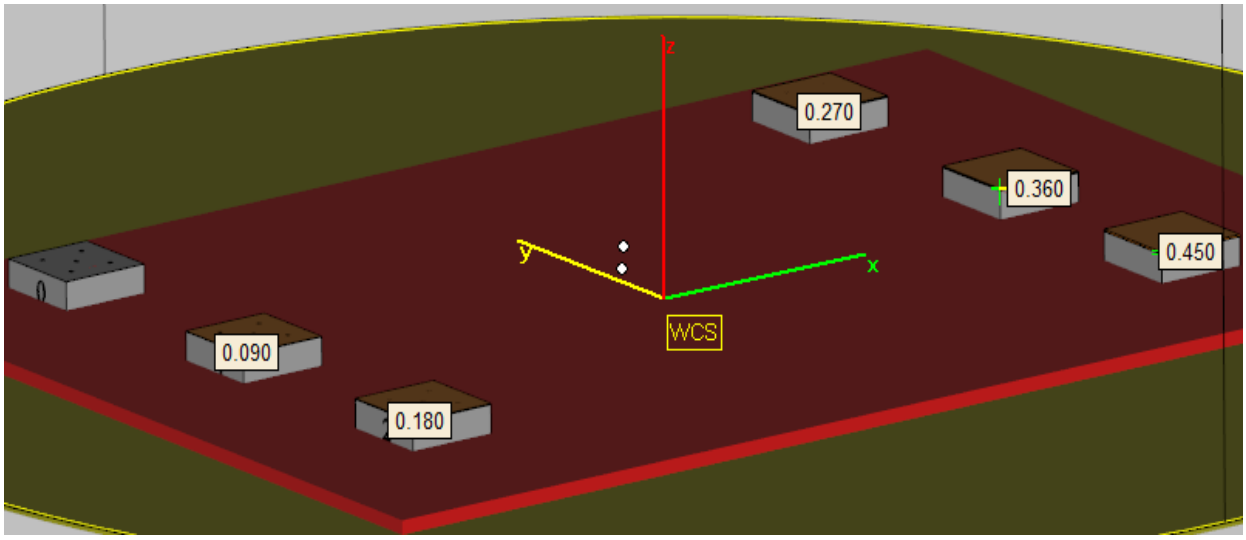

Figure 4.3 Arrangement of 6 LOF test samples in the chamber

Table 4.1 Sample IDs for the corresponding parts with different thicknesses for the top sections

Sample ID	Top section thickness [mm]	Description
0	0	Base only
1	0.09	1 layer
2	0.18	2 layer
3	0.27	3 layer
4	0.36	4 layer
5	0.45	5 layer

During the process, the camera is activated using the machine's default setting as shown in Table 4.2. The explanation given by each setting is taken from ARCAM's user manual and some communication with ARCAM engineers [96]. The gamma value (γ) is used to correct the brightness of input light using some equations similar to Equation 4.1.[97]

Equation 4.1

$$V_{out} = V_{in}{}^{\gamma}$$

Table 4.2 Camera settings for taking layer images[97]

Image Setting	Value	Explanation
Exposure time [ms]	130	how long the camera's shutter should be open
Gamma Value (γ)	0.7	Nonlinear brightness control
Filter	UV Filter	Removes light with wavelengths from 10-400nm
Auto Exposure	FALSE	automatically find best exposure

After the samples are produced, the top surface for each sample will be viewed and examined under the Alicona InfinityFocus microscope and is compared with the corresponded layer images captured during the process.

4.3. Results

The overall comparison between the parts' top surface and the corresponded layer images is shown in **Error! Reference source not found.**. In Part 0, the defect can be seen very clearly on the surface, this indicates that the defect has successfully introduced. The corresponding layer image has some brighter spot within the image, and the locations of the brighter spots are highly consistent with the location of the seeded defect. This observation indicates that a potential defect on the part's surface will be shown as a brighter spot in the layer image.

Apart from the observation that the defect appears to be brighter, a brighter line surrounding the whole part is clearly seen from every image. These brighter lines are consistent with the contour of the part or the part boundary, which indicates that the contour always appears to be brighter than the hatching and the surrounding powder cake.

Although the top sections for Part1 to Part5 are designed with fully melted cross-section, it can be clearly seen from the **Error! Reference source not found.** that, the LOFs are still clearly visible up to four layers after they were first introduced (Part 4) around the seeded LOF location but not elsewhere on the sample surface. This observation indicates that, it is highly likely that

the formation of LOF in Part1 to Part4 is influenced by the presence of previous defects at similar location.

In Table 4.3, the depth of the defects as measured with the Alicona Infinity Focus Microscope, are presented. The measurement depth is taken as the distance from the top surface to the deepest location of the defect. Some numbers are highlighted in orange with this indicating that powder particles are still visible at the bottom of defects in these cases as shown in Figure 4.4. As can be seen from the data presented in the table, the depth of defects has a tendency to become shallower after each layer. It can be seen that, on the fourth layer, no powder can be seen from the top of the part anymore, but, a depression or crater is still evident on the top surface of the sample in the location of the seeded defect. By the fifth layer, the position of defects are no longer identifiable from information gathered from the top surface.

As the comparison shows in **Error! Reference source not found.**, not all the LOFs seen under the microscope are clearly visible under the camera. Where values are highlighted in blue in Table 4.3, this indicates that the defect was not shown clearly in the layer image.

The dimension of the defect is measured in the X-Y plane and shown in Table 4.5, where only the defects with underneath powder still visible are measured. The dimension shown in the table is the diagonal length of the defect measured in the X and Y directions. As can be seen from the result, the defect is reduced in size from layer to layer.

Table 4.4 Depth of LOF measured by microscope, the fields highlighted in orange are LOF with powder still visible

Part/Hole	H1[mm]	H2[mm]	H3[mm]	H4[mm]	H5[mm]	Average [mm]
Part0	2.230	2.200	2.060	2.250	2.210	2.190
Part1	2.300	2.130	2.400	2.100	2.000	2.186
Part2	2.000	0.853	0.567	0.608	0.862	0.978
Part3	0.244	0.811	0.285	0.26	0.256	0.371
Part4	0.101	0.355	0.261	0.323	0.326	0.273
Part5	0.111	0.07	0.081	0.116	0.101	0.096

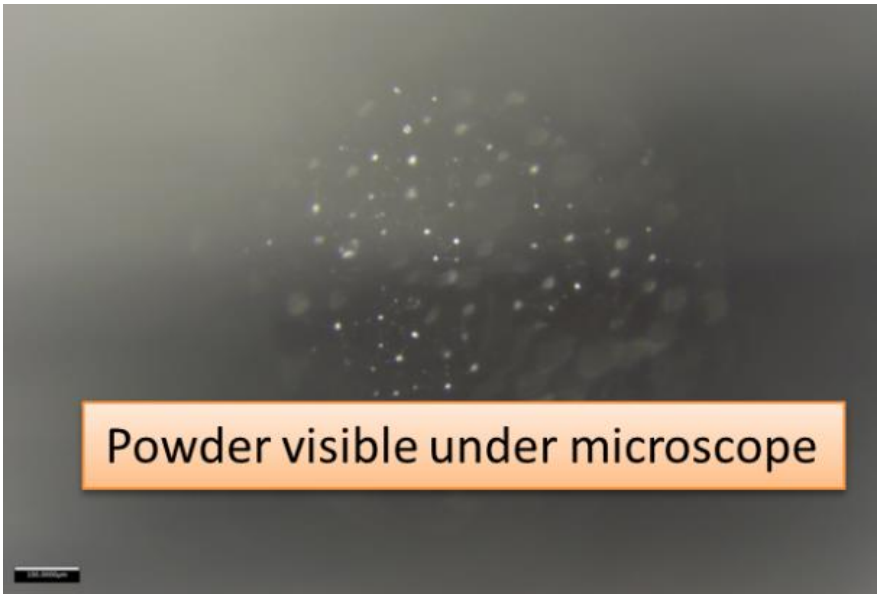

Figure 4.4 Part1_H1: the powder is still visible from the top of the layer

Table 4.5 X-Y plane dimensions of LOF measured by the microscope (only the defect with powder underneath are visible)

Part/Hole	H1[mm]	H2[mm]	H3[mm]	H4[mm]	H5[mm]	Average
Part0	1.86	1.61	2.04	2.00	1.95	1.89
Part1	1.43	1.43	1.47	1.26	1.46	1.41
Part2	1.55	1.06	1.31	1.24	1.21	1.28
Part3	-	1.19	-	-	-	1.19

The defects from the layer image are identified using the MatLab function '*graythresh*' using Otsu's threshold and the result is shown in Table 4.6. By statistically plotting the error between the actual measurement and the layer image measurement in Figure 4.5, it can be seen that the measurement error is within 50 μm and normally distributed.

The current camera system has resolution of approximately 75 μm. Since the defect dimensional error is only 50 μm in this experiment, this indicates that the dimensional error is within the systematic error.

Table 4.6 dimensions of LOF acquired from layer image using Otsu's threshold

Part/Hole	H1[mm]	H2[mm]	H3[mm]	H4[mm]	H5[mm]	Average
Part0	1.83	1.64	2.05	2.00	1.94	1.88
Part1	1.47	1.47	1.47	1.23	1.41	1.41
Part2	1.53	1.08	1.30	1.25	1.23	1.27
Part3	-	1.18	-	-	-	1.18

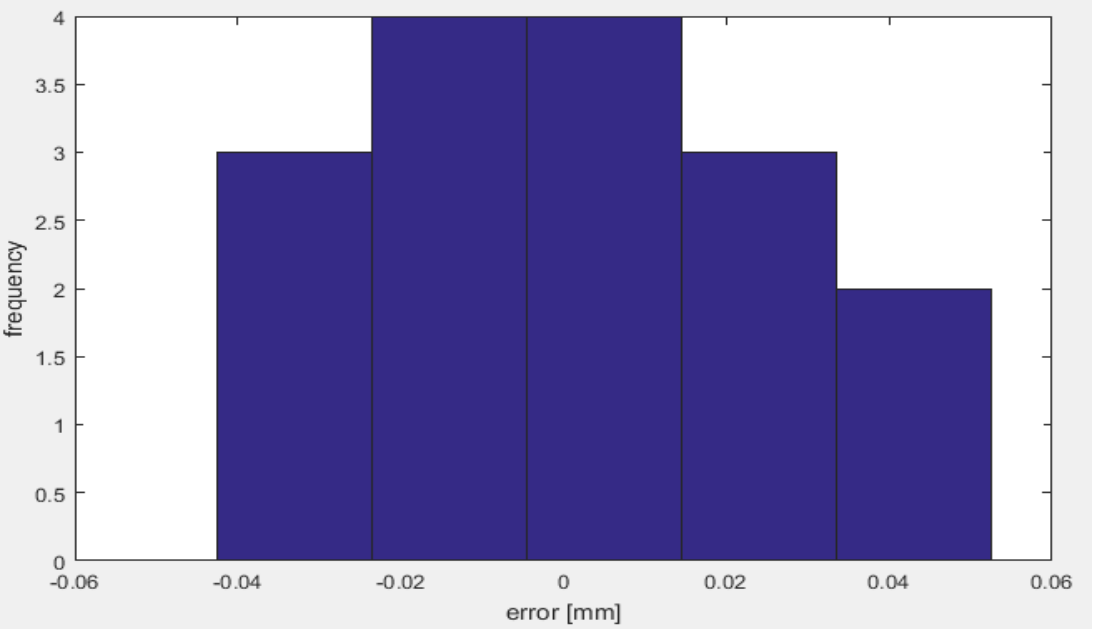

Figure 4.5 Distribution of the error between the defect size from actual part and defect size from layer image

4.4. Discussion

4.4.1. Defects on the Surface

The results section of this chapter has illustrated that the formation of defects in the current layer is greatly affected by the surface quality of previous layers. From Part1 to Part3, although the layer is designed to be fully melted, with the underneath powder is still visible, which means the molten material from the melt pool is not able to settle into the defect but only remains on the side of the defect. From the explanation made by the simulation from Bauerei[56], the propagation of defects is mainly due to the effect of surface tension on the process of material solidification.

A slight difference between this experimental result and Bauerei's simulation is that the defect reduced in size and eventually stopped rather than keeping on propagating for 10 plus layers. This could be due to the defects are seeded rather than occurring by insufficient energy density. The energy density of the process is adequate for the cubical specimens built in this experiment, so even though the defect is still propagating, the process has a tendency of ultimately rectifying the existing defect. A more detail experiment and explanation regards rectification of LOF is show in Chapter 6.

From the observations in Part0 and Part1, the powder particles are clearly visible on the bottom of the part where the defect is seeded. This observation could be due to the fact the defects are seeded rather than generated by process, thus part of the powder filled within the gap could be only loosely filled and blasted away when the part is cleaned by the PRS (powder recovery system).

The observed surfaces are dimpled at the seeded defect location, which could be mainly due to the shrinkage effect when the powder is transformed to a solid state. The powder has only 50 to 60% of the density of the solid, so when the powder material melts down and solidifies, the thickness of the solid will be less than the thickness of the powder. As the defect region has been filled with more powder than the surrounding region, the amount of shrinkage should also be larger, thus some extra shrinkage occurs and results in the dimple on the top surface as reflected in the image of Part4 shown in **Error! Reference source not found.**.

4.4.2. Brighter Defects in Layer Images

From the previous sections, it can be seen that the LOFs are appeared to be brighter than the surrounding hatching area and powder bed, which enables them to be detected. The reason the defect region being brighter could be due to the difference in emissivity.

The fundamental image capturing system of any camera is to convert light wave energy to a digital brightness value. The overall emitted wave energy can be calculated using Stefan–Boltzmann law (Equation 4.2), where P is the power of radiation per unit area, ε is the emissitivity, σ is the Stefan–Boltzmann constant, and T is the temperature of the emitting surface. From the equation, there are only two possible factors affect the image brightness value: higher emissivity or higher temperature.

Equation 4.2

$$P = \varepsilon\sigma T^4$$

The reason the LOF appears to be brighter is due to it forming a 'hole' or 'cavity' like structure on the surface. A schematic drawing is shown in Figure 4.6 to illustrate the differences in the emitting surface in different conditions.

The ideal scenario for the melted surface should be as flat as possible as shown in Figure 4.6a. When a defect has developed on the surface, the appearance of the defect is more like a 'cavity hole' as shown in Figure 4.6c. Although the material did not change itself, the shape of defect has significantly increased the surface area for energy to be emitted, therefore the relative energy emitted per unit area or the emissivity has increased. As a result, the region of the defect appears to brighter than the surrounding flat region. When the surface is a smooth crater (Figure 4.6b), there is only a slight increase in the surface area, thus the crater did not give as large contrast as a defect region, which is the reason why craters in Part4 is not obviously seen from the layer image.

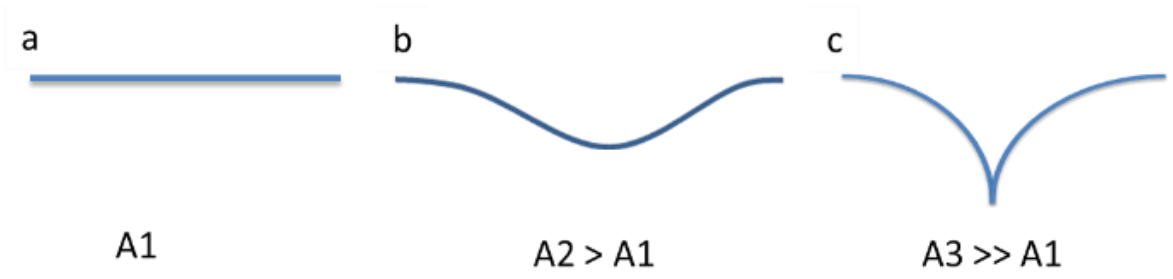

Figure 4.6 [a] normal melt surface with no defect
[b] rougher surface with a smooth crater [c] defect present on the surface

4.4.3. Brighter Boundaries in Layer Image

Apart from defects, there are three distinguishable regions in the layer images: hatching interior, the contour region powder cake and the preheated region as shown in Figure 4.7. The powder cake has no direct heat input into these regions, thus the only heat possessed is the heat conducted from the preheated region and the melted part. Due to the low thermal conductivity of Ti6Al4V powder, the heating up of the powder is not significant, thus the powder cake appear the darkest region of the image. On the other hand, the preheated region and the hatching interior is directly heated up by the input energy, thus this region is brighter than the powder cake.

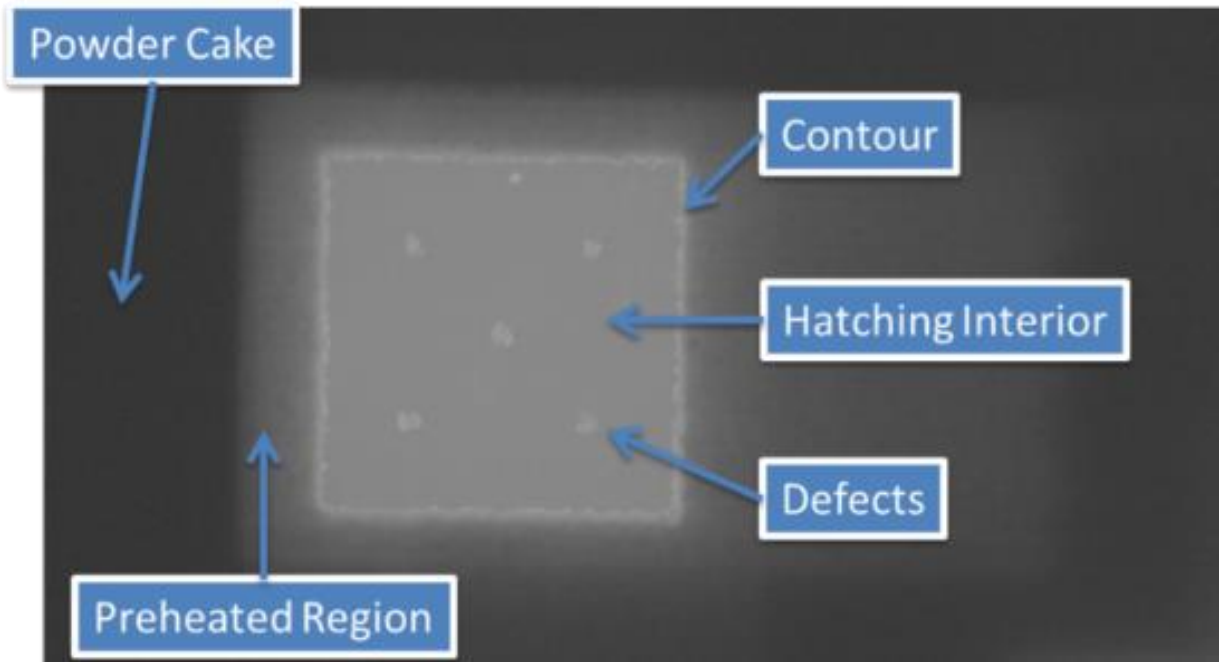

Figure 4.7 Different regions in the layer image

The contour is the brightest region of the image, which could be due to both higher emissivity and higher temperature. As the boundary of the part in each cross-section in the EBM process has great waviness, the contour region of the part is presented as a mixture of both powder and solid material. The powder has a higher emissivity due to its larger surface area, as a result, the mixture of solid and powder on the boundary region will emit more energy than the equivalent flat solid.

The second reason the contour is the brightest region could be due to the higher temperature around the boundary of the part. A simple simulation was created to understanding the cooling of the parts in the EBM process using the software mentioned in Chapter 3 Section 3.5.2.

The simulation scenario is a simple geometry of 20mm by 20mm where the part sits right on the base plate, and is surrounded by an additional 10mm powder, as shown in Figure 4.8. The part was initially set at 1800 °C and the base plate and surrounding powder is at 625 °C.

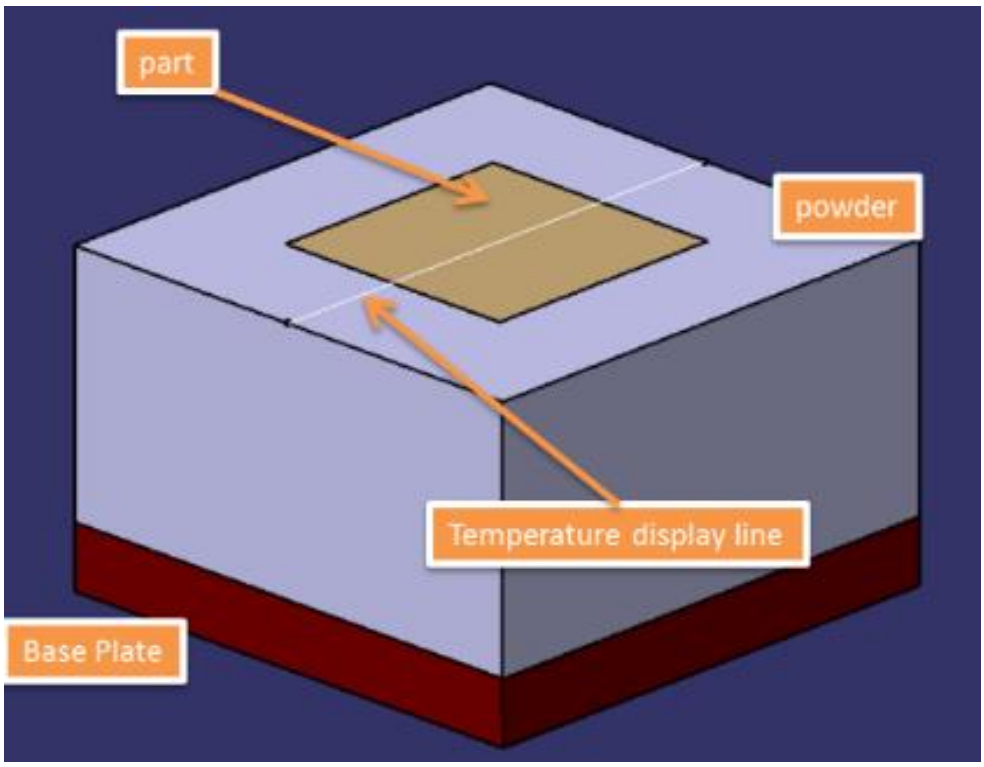

Figure 4.8 Simulation for part cooling of a sample surrounded by sintered powder

The simulation result is shown in Figure 4.9, which displays the temperature along the central line of the part as shown in Figure 4.8. From the result, it can be seen that, the boundary of the part becomes the higher temperature region from 2.7 seconds and onwards, regardless that of the initial temperature of the part is much higher. (The y-axis is ranged from 600 °C to 900 °C apart from the first section of the image, which is 600 °C to 1900 °C).

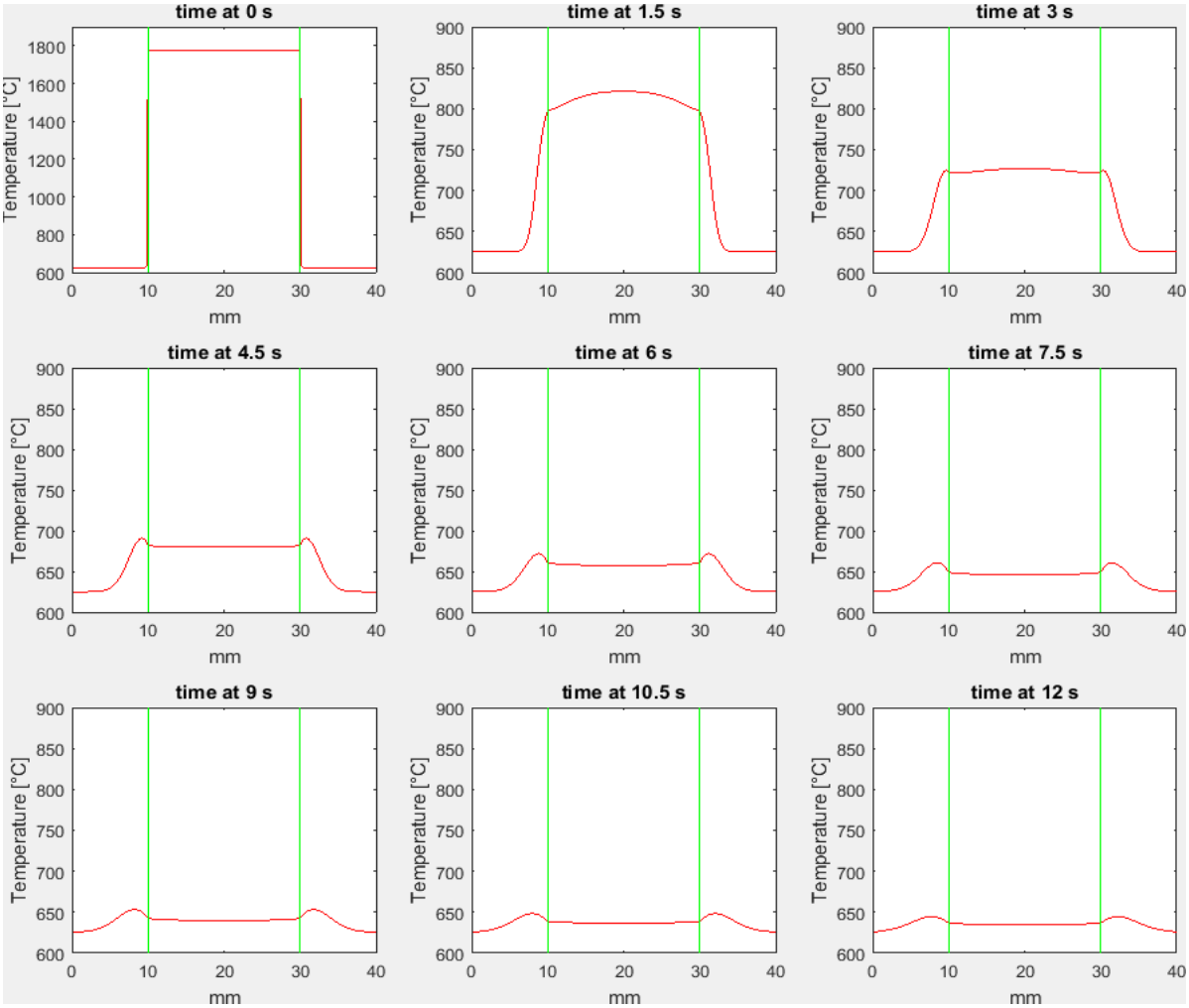

Figure 4.9 Temperature along the line indicated in Figure 4.8, the green vertical line indicates the part's border

The reason for this result can be explained as follows: although the nearby powder did not reach its melting point, when the part itself is melted, the high thermal gradient between the solid and the powder will create a rapid transfer of some thermal energy from the solid to the powder. As time moves on, the solid part exhibits much higher thermal conductivity than the powder and hence will cool down at a faster rate, but the adjacent powder which has a high

temperature cools down much more slowly. As a result, at the time when the image is taken, the contour region is hotter than the rest of the layer, as such the contour region appears brighter than the nearby solid and the surrounding powder.

As a result, at the time after the layer has completed when the image is taken, the contour region should be hotter than the rest of the layer. Due to the potential of both higher temperature and higher emissivity, the contour region appears brighter than the nearby solid and the surrounding powder.

4.4.4. Choice of the camera

It is evident from the open literature that many different types of thermal camera with near infrared (NIR) camera [98] or mid to far infrared (IR) camera [99,100] have been employed to date in both EBM and SLM process. The current installed camera has a wavelength range from the visible to the near infrared spectrum and the reason for this choice is believed to be related to the resolution.

Although an IR camera is a better choice for measuring temperature when compared to an NIR camera, the corresponding resolution is limited by the light sensor used. From commercially available IR cameras, a maximum resolution of 1024×1024 pixels can be achieved, but with NIR cameras a much higher resolution of 6576×4324 pixels can be achieved, as shown by the one installed in the current Q20 EBM machine.

The EBM process cannot monitor coaxially in contrast to the SLM process, since the energy beam is electron rather than light. The only possibility available to us is to capture the whole powder bed, where in this case this measures a maximum of a 380 mm diameter build area. With this size of build area, the NIR camera gives a resolution of 88 μm for compared with 300-400 μm for IR camera. As a result, this makes the NIR camera more favourable choice

than the IR camera (the current camera set-up has resolution of 75 to 83 µm due to the camera is not taking an image of the whole chamber).

As mentioned in the previous section, defect detection is based on the contrast in emissivity and the requirement for a temperature reading is not essential in this application. Thus, the higher resolution camera will give a better understanding on the characteristics of the part surface.

4.5. Conclusion

- The development of lack of fusion is strongly dependent on the surface quality of the previous layer. If a surface defect is present in the previous layer, the defect is likely to propagate through subsequent layers.
- The regular print parameters cannot stop such defects from propagating immediately but are able to reduce the size of the defect and eventually rectify it.
- Lack of fusion can be captured by the installed camera in the Q20 machine, on which the defect spot appears brighter than the surrounding region.
- The defects captured by the camera are within ±50 µm difference of the actual measured defect dimension, which is within the systematic error of 75 µm.
- A smooth crater on the surface does not give a significant contrast and subsequently is difficult to detect using the inbuilt the camera.
- The edges of the part appear brighter, which could be due to both the higher emissivity and the higher temperature of that region in comparison to the powder and to the rest of the component.

Chapter 5 : Identify Lack of Fusion in EBM Process with NIR Camera

5.1. Introduction

From the previous chapter, it has successfully been shown that during the EBM process, the defect on the top surface exhibited a hole like structure, which appears brighter than the surrounding region when imaging the sample in the Near Infrared (NIR) spectrum.

The experiment in the previous chapter was conducted on a simple cubic shape geometry, but an actual EBM build would generally contain parts with much more complex shape. Further investigations and developments are still required to understand whether the camera is applicable for defect detection in an industrial environment.

In the chapter, to have more knowledge of using the NIR camera for defect detection, an algorithm was designed in MatLab to analyse every image from the build and identify defects between layers. The algorithm is currently termed as LayerDD (**Layer**wise **D**efect **D**etection) in the report. The overall chapter is divided into three sections.

1) The chapter starts with an explanation of the procedures and algorithm used in LayerDD system to filter the LOF defects out from the images taken during the process.
2) The second section compares the defect prediction by the LayerDD system to the existing defect identification techniques such as CT scan, and specimen cut-ups.
3) The third section discusses the LayerDD system's advantages and technical limitations, and explores the potential of industrial or research applications.

The overall code of the LayerDD algorithm is not described in this thesis, due to the construction of the code and some core parameters are proprietary to GKN Aerospace.

5.2. LayerDD Algorithm

ARCAM Company has offered the defect analysis software of LayerQam, but it only indicates the density of the part in each layer, which is not enough detail for the aerospace industry. In addition, the algorithm used in LayerQam has not been published, which makes LayerQam result verification relatively difficult.

To have a better utilization of the raw images captured by the installed camera, an algorithm named LayerDD is developed. LayerDD system is a Lack of Fusion (LOF) detection system which consists of the installed in the ARCAM Q20+ Machine with self-developed defect detection algorithm. This section will explain in detail about how LayerDD system works.

A summary of work has been done by the supplier of the EBM machine (ARCAM AB):

- Installation of NIR Camera (Prosilica GT6600)
- Installation of the flap to protect the camera unit
- Producing Calibration Images
- Integrating the camera into the EBM system, enable image capture during process

The algorithm can be grouped into 9 steps and is summarized as follow:

Step 1. Run Calibration Images on the base plate
Step 2. Take images during the EBM process
Step 3. Correct the Image using Calibration Images
Step 4. Slice the original STL file and output the cross-sections as images
Step 5. Correlate the layer images with the STL cross-section images
Step 6. Remove contour zone and any area outside the contour zone
Step 7. Filter the potential LOF
Step 8. Stack all the LOF up to 3D model and output as STL
Step 9. Visual Inspect on the LOF through STL viewer

In the above steps, Step 1 to Step 3 are the steps to correct the distorted images due to the off-centred camera arrangement and camera-lens system. Step 4 to Step 6 the steps to remove the contour from the image by using the original layer's cross-section. Step 7 to Step 9 is the steps to identify defect and present the defect prediction in 3D visualization.

Step 1. Running Calibration Images on the Base Plate

In EBM Q series machines, images taken during the process are slightly distorted because of two reasons. The first reason is that the camera is installed off-centre of the chamber; and the second reason is that images captured pass through numerous lenses.

Undistorted images are critical for this system to correlate them with the real sample geometry. The reason for this geometry-image correlation will be explained in detail at Step5.

To correct the images from distortion, the machine manufacturer has offered a method of image calibration before each build starts. The electron beam setting when the image is calibrated is shown in Figure 5.1, and the definition for setting is explain in the following list:

- 'Time in each point' the duration of electron beam hitting the spot
- 'Beam Current' the current of electron beam'
- 'Focus offset' is represents the diameter of electron beam.

The remaining two parameters have not been explained by ARCAM. It is worth mentioning that, the metal shutter is kept open during this stage, since only low electron beam current are used. In addition, these parameters are locked down and cannot be modified without ARCAM's permission.

During the image calibration stage, the electron beam shoots at the build plate with perfect horizontal and vertical aligned equidistant dots of 3 mm apart. When the electron beam hits the base plate, the local point will gain some energy and become slightly hotter than the surrounding area. These dots are captured by the camera as shown in Figure 5.2.

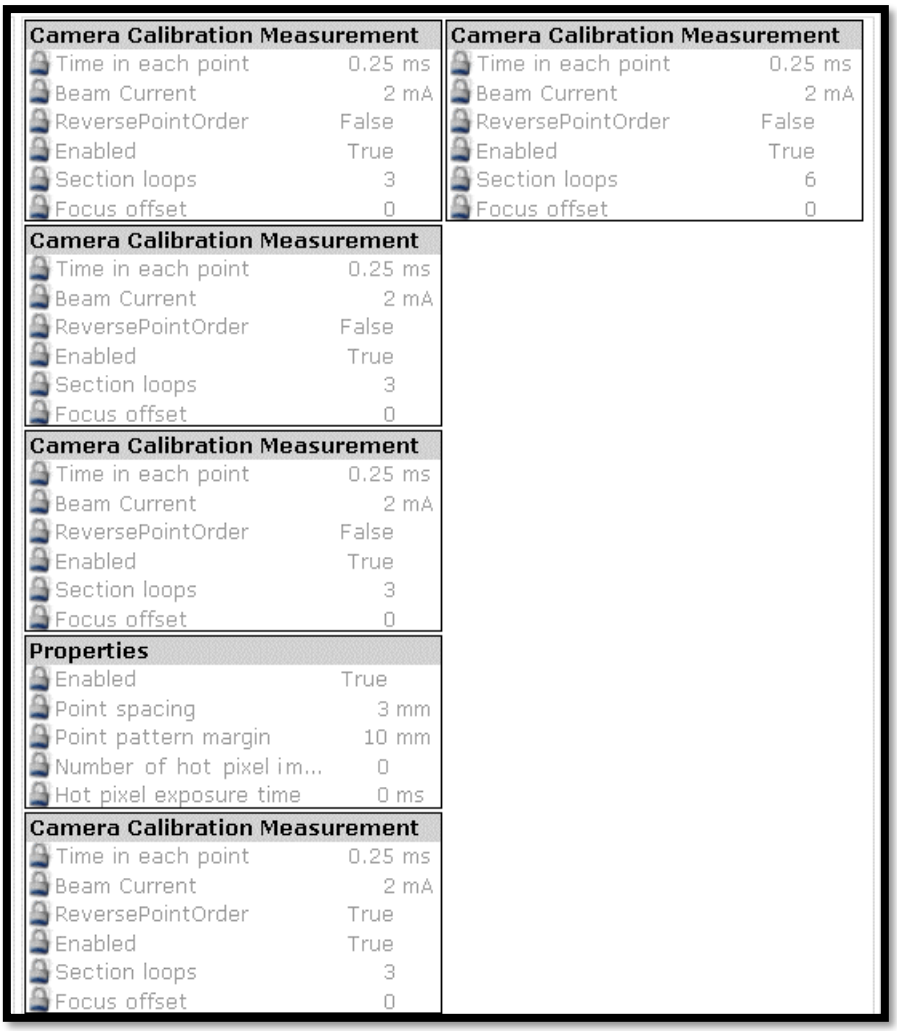

Figure 5.1 Camera and beam setting for calibration images

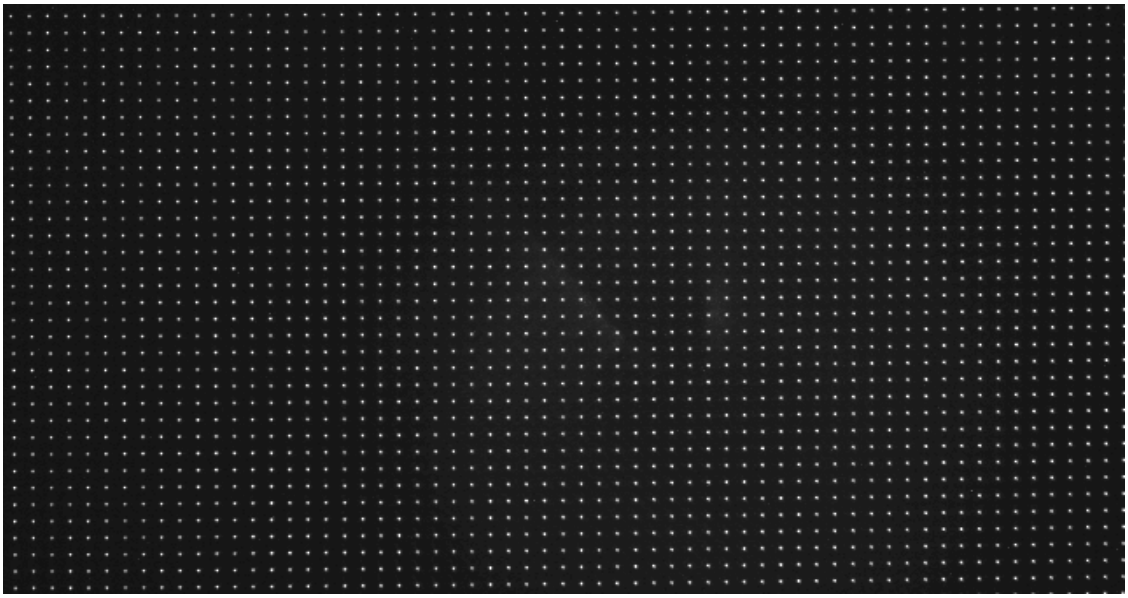

Figure 5.2 Example of calibration image captured before build has started

Step 2. Tak images during the EBM process

During the EBM process, X-ray are generated when the electron beam hits the material. The camera is designed with a protective metal shutter which is closed when the electron beam is hitting the powder bed. Thus, the image is taken right after the current layer is finished and before the table is lowered. The camera is defaulted to output grayscale images with .png extension; an example of raw image from the NIR camera is shown in Figure 5.3.

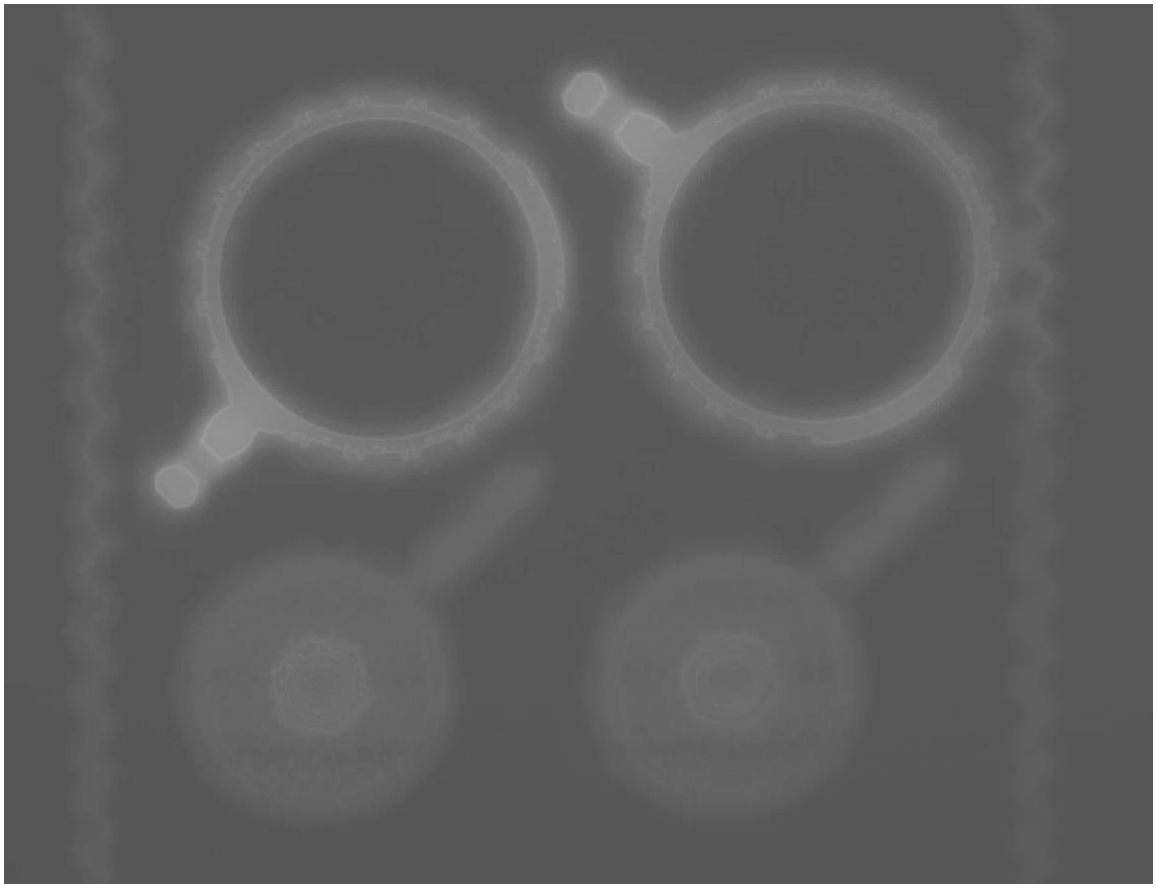

Figure 5.3 Raw image acquired from NIR camera during process

Step 3. Correct raw image using Calibration Image

After the build is completed, the images taken during the process will be corrected based on the calibration images taken in Step1. The correction step includes two stages: image rotation and image correction.

Each calibration point is made up of a cluster of brighter pixels, thus the location of each individual calibration point is assumed to be the centroid of the cluster. To find the rotated angle (θ) of the image, Equation 5.1 is used, where Y2, Y1, X2 and X1 are the locations of left-top and right-top corner points of the calibration image respectively (Figure 5.4).

Equation 5.1

$$\theta = \tan^{-1}({}^{Y2 - Y1}/_{X2 - X1})$$

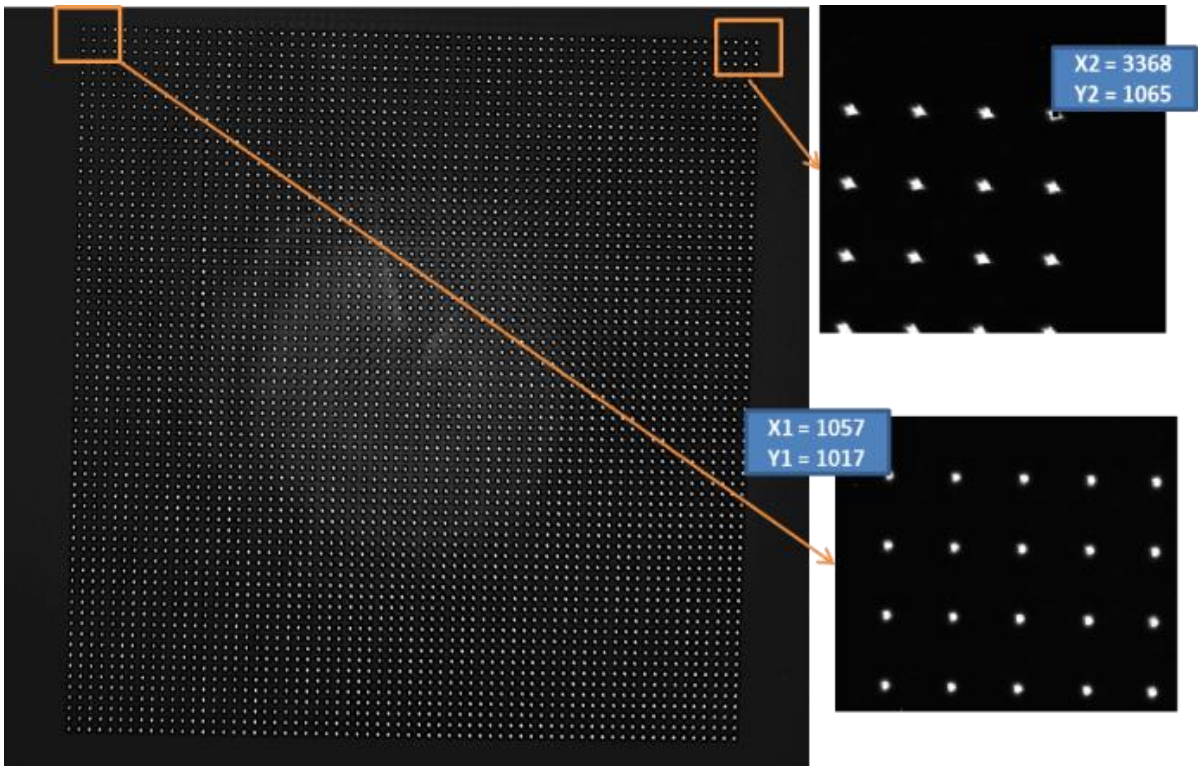

Figure 5.4 The corner the calibration image is used to calculate the angle of rotation

When the image is rotated back to normal, image correction is performed. Ideally, since dots are designed to be equidistant from each other, the number of pixels between each dot should be also a constant. But, due to the distortion of the image, the distances are varied from 34 to 39 pixels rather than a constant value.

To correct the image from distortion, the area between every four dots is defined as a sub-image, as shown in Figure 5.5 and each sub-image is corrected individually. The correction is done by using MatLab function '*imresize*', which stretches all the sub-image into equal pixel

images (e.g. 40 pixels between any 2 dots in this algorithm, 75μm/pixel). An example of a corrected image is shown in Figure 5.6.

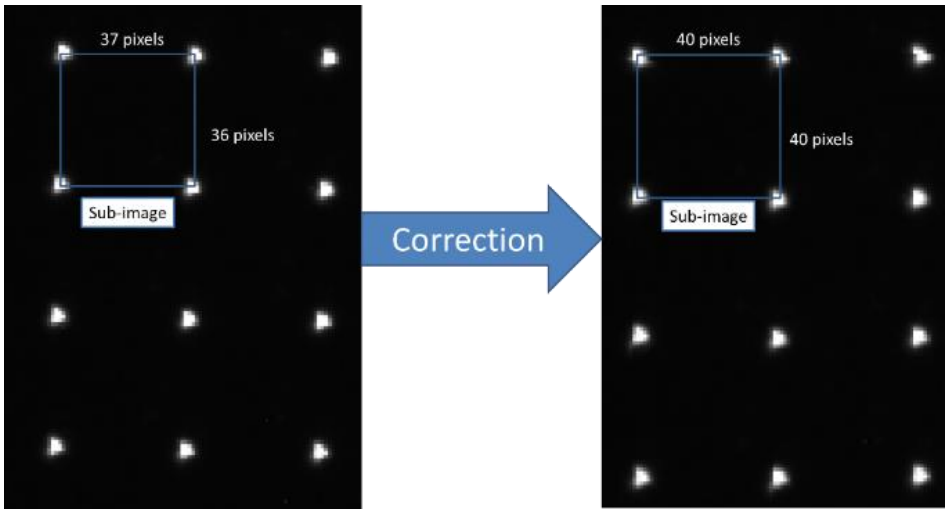

Figure 5.5 Image correction performed for each sub-image with MatLab function 'imresize'

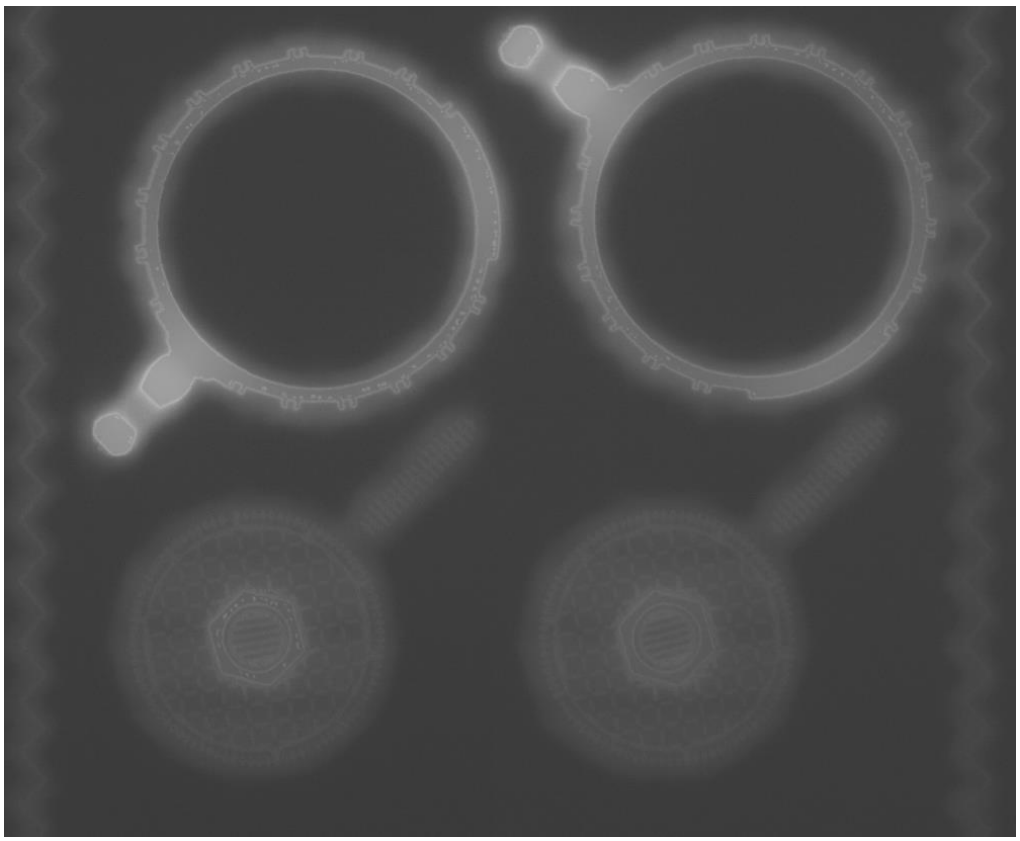

Figure 5.6 Corrected image from image in Figure 5.3

Step 4. Slice the original STL file and output each cross-section as image

In order to correlate the image with the original geometry (reasons to be explained in Step 5), the original STL file in ASCII format is imported into MatLab, and sliced into cross-sections using the method described by Eragubi Munir[101].

To have a proper overlap between cross-section and layer image, the output cross-section image must have exactly the same resolution as the layer image obtained from Step4. The drawing of the contour is done by the '*patch*' function of MatLab.

An example of a cross-section image is shown in Figure 5.7.

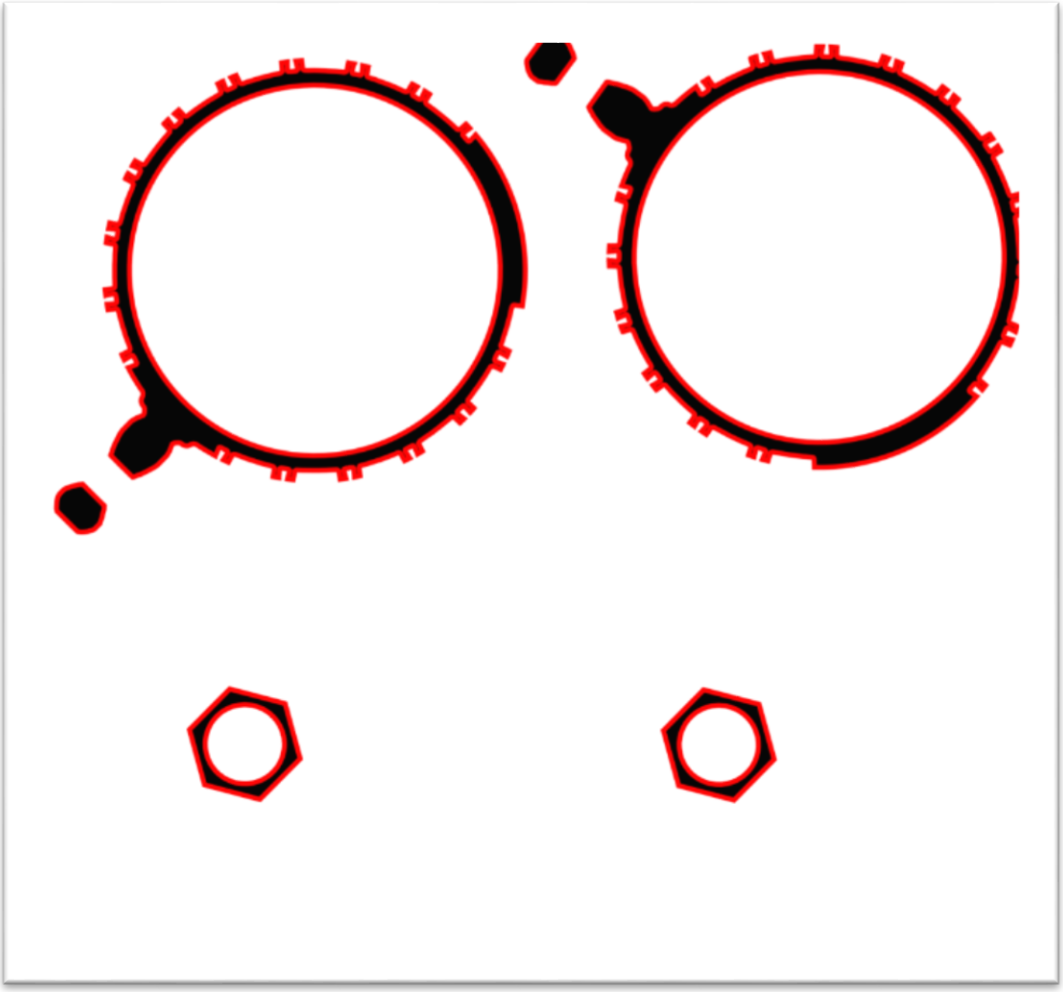

Figure 5.7 STL cross-section image corresponding to the layer image shown in Figure 5.6

Step 5. Correlate the layer image with the STL cross-section image

As explained in the previous chapter, the LOF defect is identified due to the defects appears to be brighter than the surrounding area, as the example shown in Figure 5.8. Within the LayerDD images, the value of the contours have similar brightness as any defects, thus it is impossible to distinguish contour and LOFs regions with only brightness value.

Including the contour region in the images will result in the entire contour identified as a defect and will show up in the final result. Thus in order to correctly identify the LOF within the part, the contour should be removed from the layer images. In the LayerDD algorithm, the original geometry's cross section image is used to identify the contour region from the camera images, which is why Step1 to Step4 are necessary.

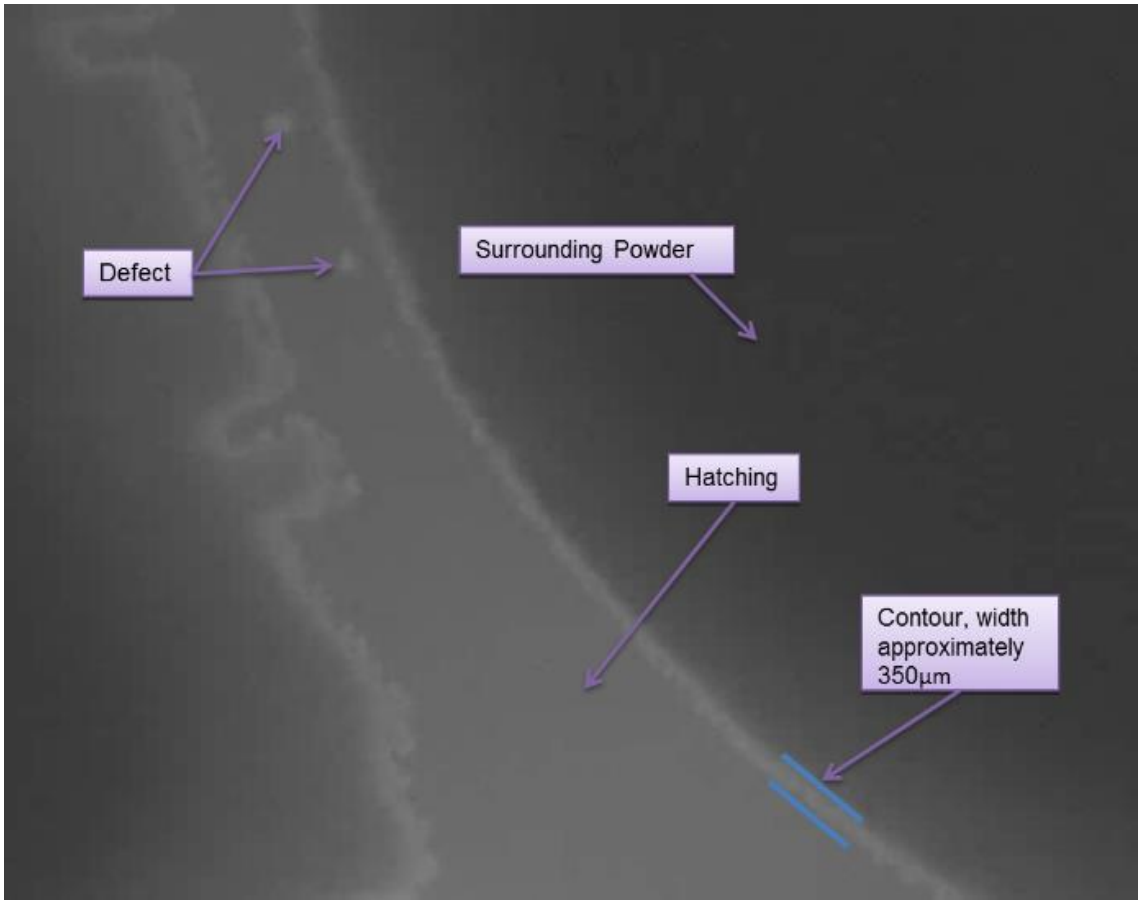

Figure 5.8 the appearance of Powder, Hatching, Contour and LOF in layer image (a sectioned image from Figure 5.6)

To correlate the images, the cross-section of the STL is overlapped to the layer image manually to an approximate location, and then followed by an auto-correlation algorithm.

Due to the contour having a higher brightness value than the surrounding area, the auto-correlation algorithm is established by maximizing the average brightness value under the cross-section. The equation to find the average brightness is shown in Equation 5.2, where $IC_i \cap IL_i$ is every overlap point between the image of contour and the layer image; n is the total number of points which overlap; and B_{avg} the average brightness of the intersection.

An example is shown in Figure 5.9 to illustrate the effect of the algorithm, and it can be seen that the higher the average brightness value under the cross-section, the better the overlapping with between the cross-section image and the layer image.

Equation 5.2

$$B_{avg} = \frac{\sum_{i=1}^{n} IC_i \cap IL_i}{n}$$

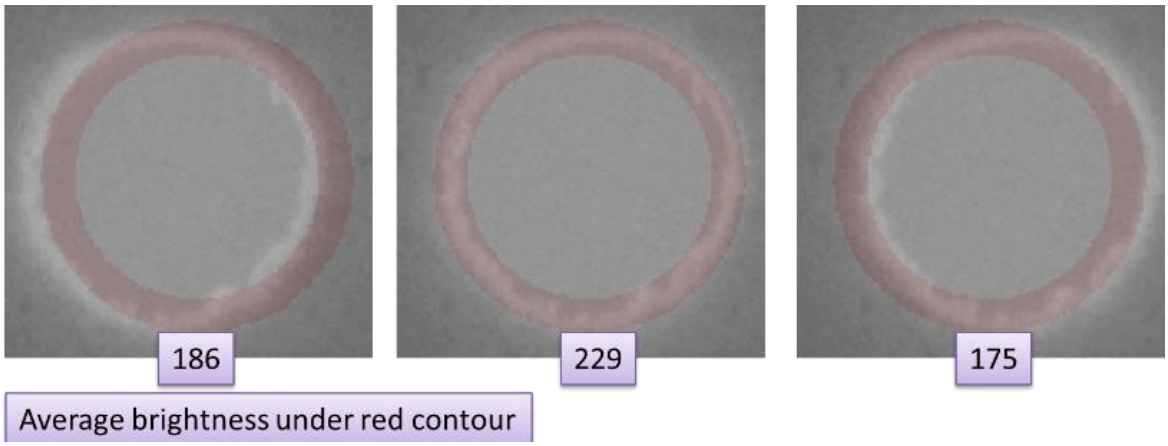

Figure 5.9 Auto Correlation: the highest the average brightness, the better the correlation of STL contour to the image's contour, where in this case the central image gives the best correlation

This correlation step (Step5) is only required to be performed once per build. As both the LayerDD image and the cross-section are consistent with their bound box coordinate, the software will record the correlation setting from this step, and the further overlapping between cross-section image and layer image is performed automatically by using the same setting.

The image shown in Figure 5.10 is an example of an overlapped image between the cross-section (shown in red) and the layer image.

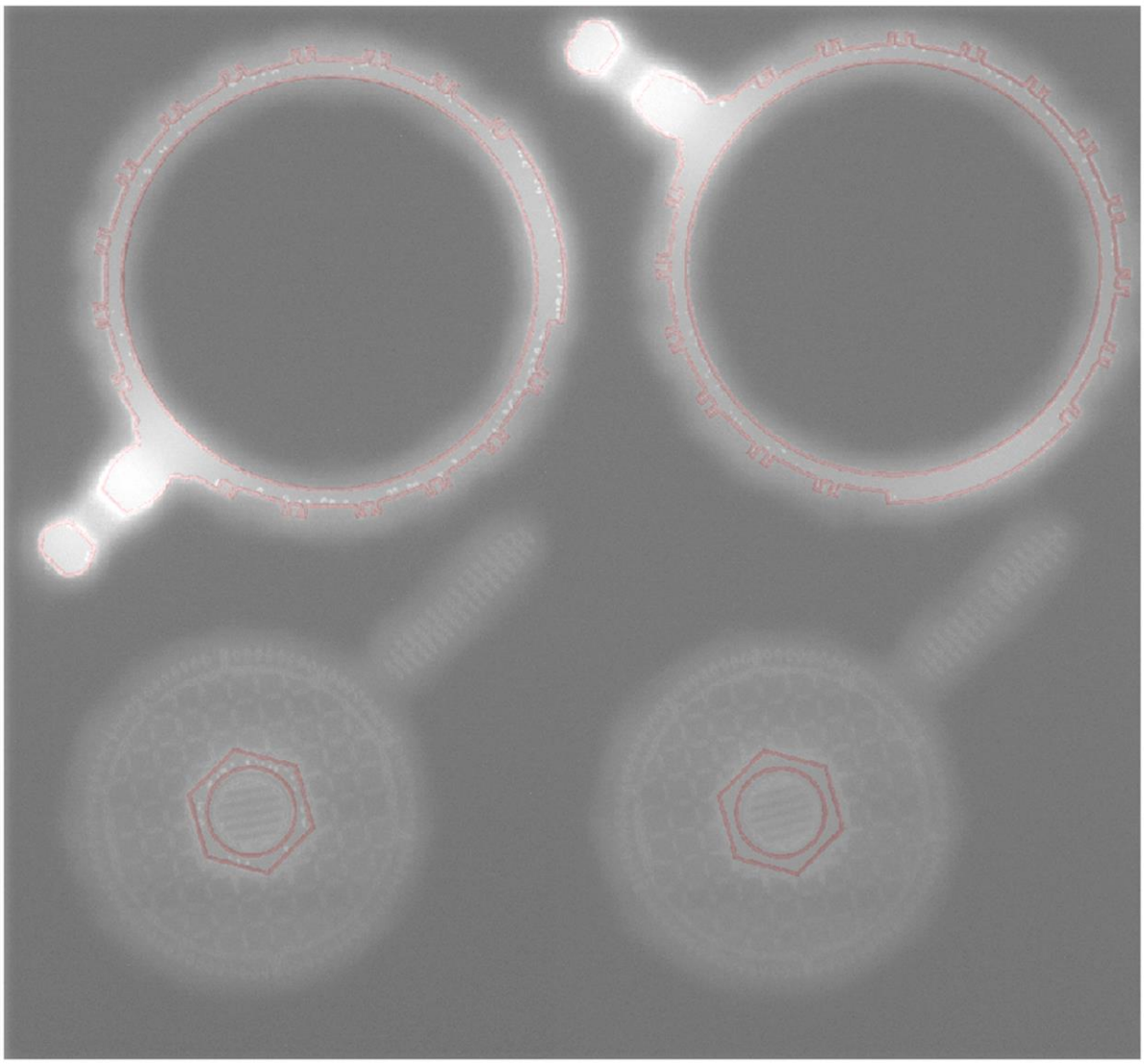

Figure 5.10 STL cross-section overlay on top of layer image, where the contour of the image is under the cross-sectioned image (image from Figure 5.7 overlapped with image from Figure 5.6)

Step 6. Remove contour region and any area outside the contour

In the LayerDD analysis, powder cake is not used for defect prediction. Thus, in this step powder cake region are excluded from the image together with the contour region. An example of cropped image is shown in Figure 5.11.

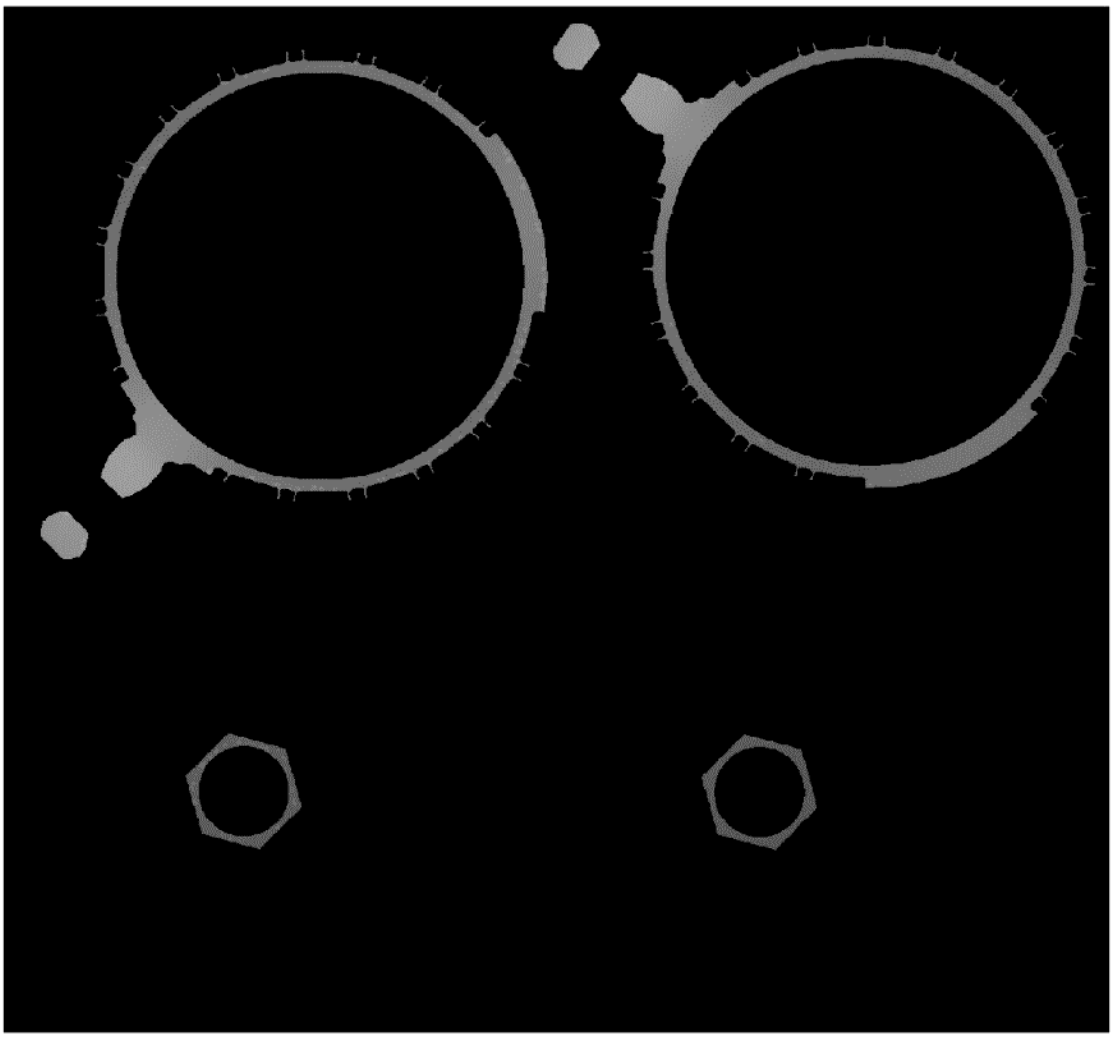

Figure 5.11 Image left with interior part only, where contour and powder cake are removed from analysis (contour and powder region removed from Figure 5.10)

Step 7. Filter the potential LOF

In the field of defect analysis technique, statistical distributions such as Otsu's method are used very popular to identify the defects. The method assumes the image have a bi-modal distribution which can be grouped into two clusters: background and foreground object. It then calculates an optimum threshold which separates the two clusters so the sum of the variances is at its minimum.[102]

As for the EBM process, the method seems to be useful when the geometry is very simple, and the background brightness is very consistent. An example is shown in Figure 5.12, which prove Otsu' threshold is capable of identifying defect from the image.

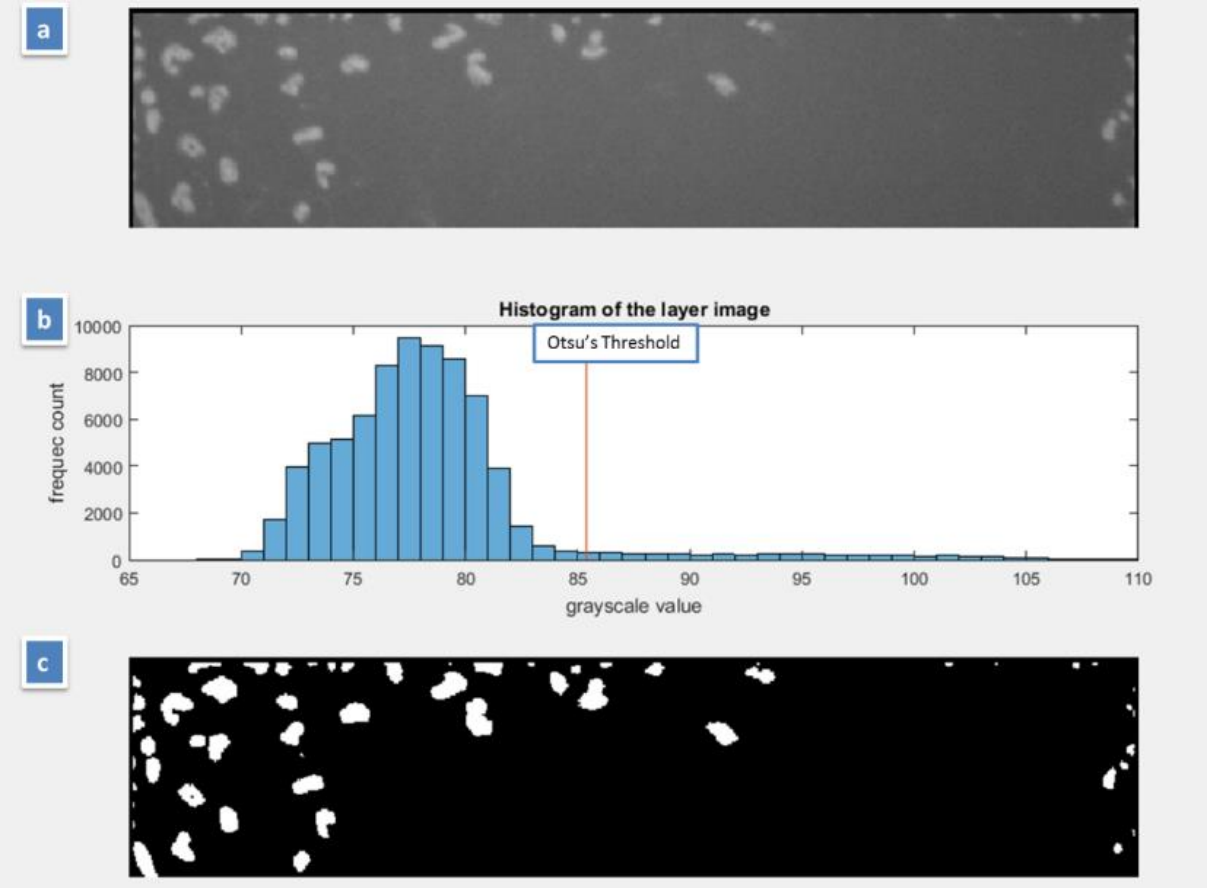

Figure 5.12 [a] Layer image of simple rectangular shape block with constant cooling rate across the part [b] Histogram of the image pixel grayscale value [c] Identified defect with Otsu's threshold

For an actual EBM component, the shapes of parts are much more complex hence the cooling rates across the part are very different, which result the temperature of the part's surface highly

inconsistent. As the brightness of pixel is directly related with the temperature of part, the background brightness is also highly inconsistent. For example, an overhang region cooled down much slower than a fully solid region, as a result, the overhang region will appear to be much brighter than the solid region.

An example of complex geometry is shown in Figure 5.13, where the part is comprised of both a thin and thick section, thus the parts layer image background value is very non-uniform. Although the histogram shows a bi-modal distribution, the Otsu's threshold has split the high cooling rate and low cooling rate region rather than identify the defects properly.

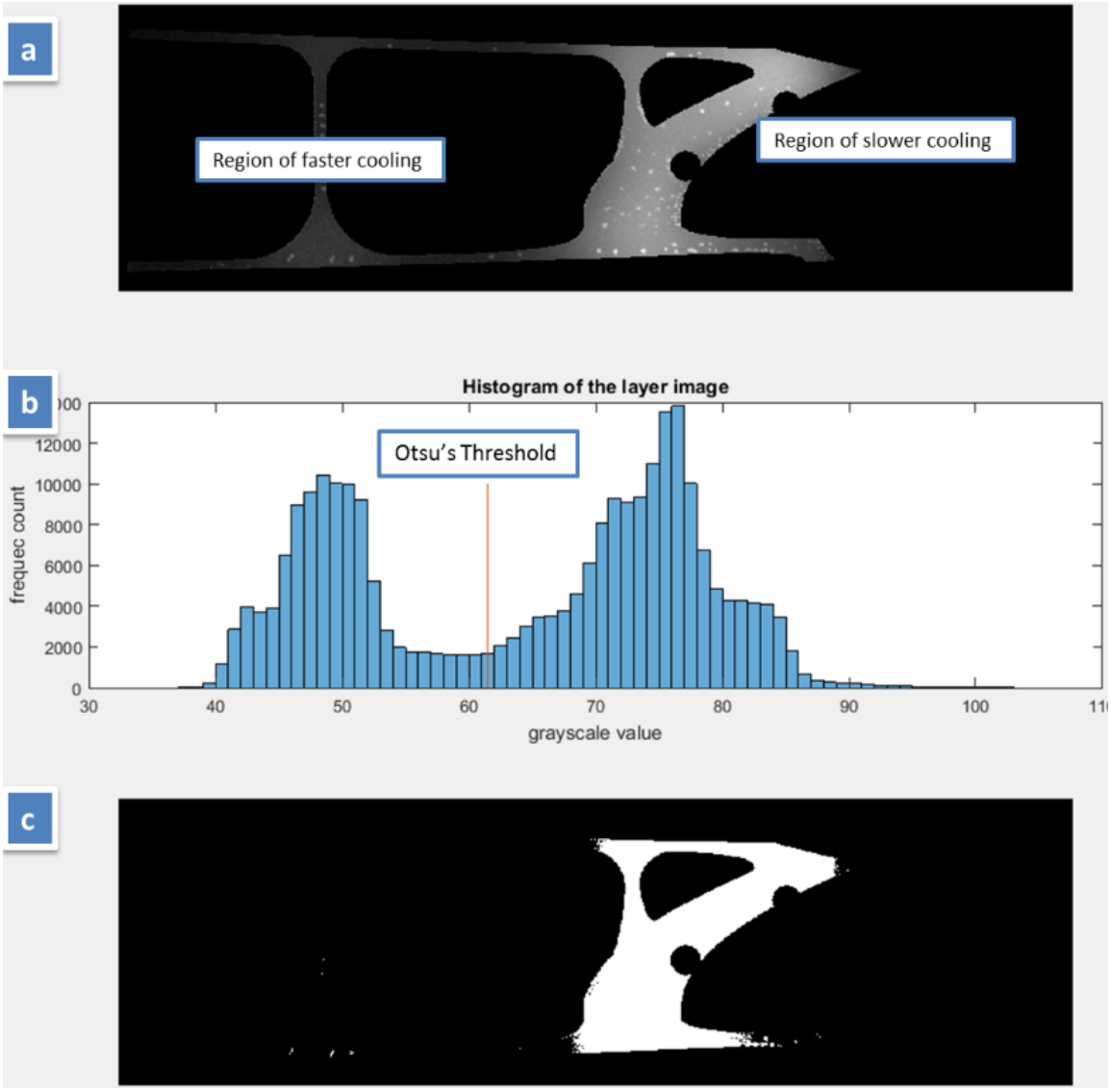

Figure 5.13 [a] Layer image complex part different cooling rate across the part [b] Histogram of the image pixel grayscale value [c] Error-identified defect with Otsu's threshold

Current Defect Detection Method

To identify the defect correctly, the current approach is selected based on the method of edge detection. From the image in Figure 5.12 and Figure 5.13 it can be seen, although the background threshold varies across the image, the LOF has the common feature of being brighter than the surrounding region. A selected spot from the Figure 5.13a is shown in Figure 5.14, where the pixel brightness is measured across the LOF, it can be seen that the grayscale value sharply rose as it approaches to the centre of LOF.

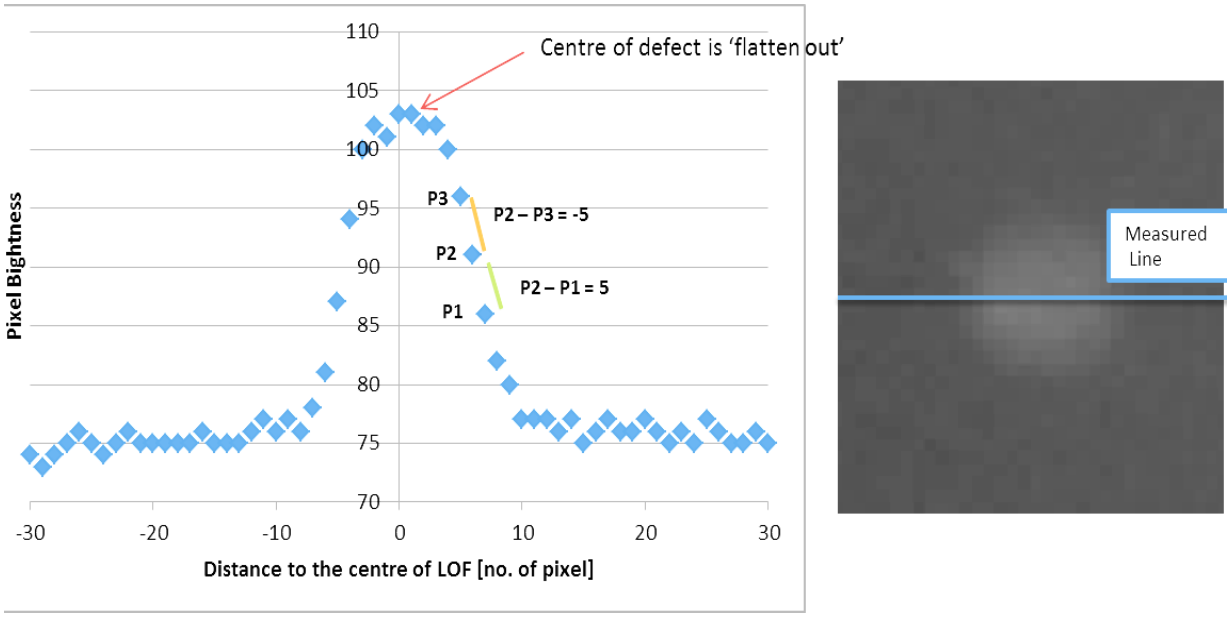

Figure 5.14 Pixels brightness measured across a selected LOF defect

Based on the above observation, each individual pixel in the image is compared with the entire adjacent region as shown in Figure 5.15. The adjacent region in this algorithm is defined as every pixel within 'x' number of pixel ranges, where 'x' is has a minimum number of 1. In general, if the 'x' value is too small, it could not give enough contrast between the current pixel and the surrounding ones, but if 'x' is too large, then amount of time required for computation is too long. As each LayerDD image is in the size of over 4000×4000 pixels, and due to the limitation of current computing power, in this experiment, it is decided to measure within 5 pixel ranges from the current pixel.

To compare the contrast of any pixel, the nearby pixel regions are divided into four different zones as indicated in Figure 5.15. The average for each zone is compared to the current pixel separately and the zone which gives highest absolute average difference is selected. If the pixel is higher than any zone over a certain threshold, it will be identified as a defect.

The reason for using divided zones rather than taking an overall average is due to the potential average out between negative contrast and positive contrast, as the example shown in Figure 5.14. From the graph, the pixel P2 the current pixel, P1 and P3 represents the surrounding pixel. Due to P2 is being on the slope of change in brightness, the difference between P1 to P2 and P2 to P3 could cancel each other out, giving a final contrast value of 0. Thus by taking a divided region, this scenario can be avoided.

The contrast value is further divided by the average brightness of the surrounding region. The reason to do this is due to the equation of Stefan–Boltzmann law (Equation 4.2), where P is the overall power of radiation, ε is the emissitivity, σ is the Stefan–Boltzmann constant, and T is the temperature of the emitting surface.

Equation 5.3

$$P = \varepsilon\sigma T^4$$

The brightness of each pixel is directly proportional to the intensity of the light which is calculated based on Equation 4.2. As explained in the section 4.4.2, the higher brightness of LOF under camera is due to relatively higher emissivity. Although temperature across the whole part can have a huge variation, if a very small region is considered, the change in temperatures can be assumed to be negligible. Thus based on Stefan–Boltzmann law, if the only difference between the LOF region and the surrounding region is emissivity, then the ratio of brightness between LOF and the surrounding region should be a constant also. Thus, the

threshold for a defect should be set by the ratio between the brightness differences to the surrounding brightness.

To express the above algorithm, the following equation is used (Equation 5.4). Where the ∂B is the maximum difference between the current pixel and surrounding pixel, B is the brightness of current pixel, and $B1_{avg}$ to $B4_{avg}$ are the average brightness from zone 1 to zone 4. The function of maximum (max) and absolute value (abs) is taken directly from MatLab built-in functions.

Equation 5.4

$$\partial B = \frac{\max(abs(B - B1_{avg}, B - B2_{avg}, B - B3_{avg}, B - B4_{avg}))}{(B1_{avg} + B2_{avg} + B3_{avg} + B4_{avg})/4}$$

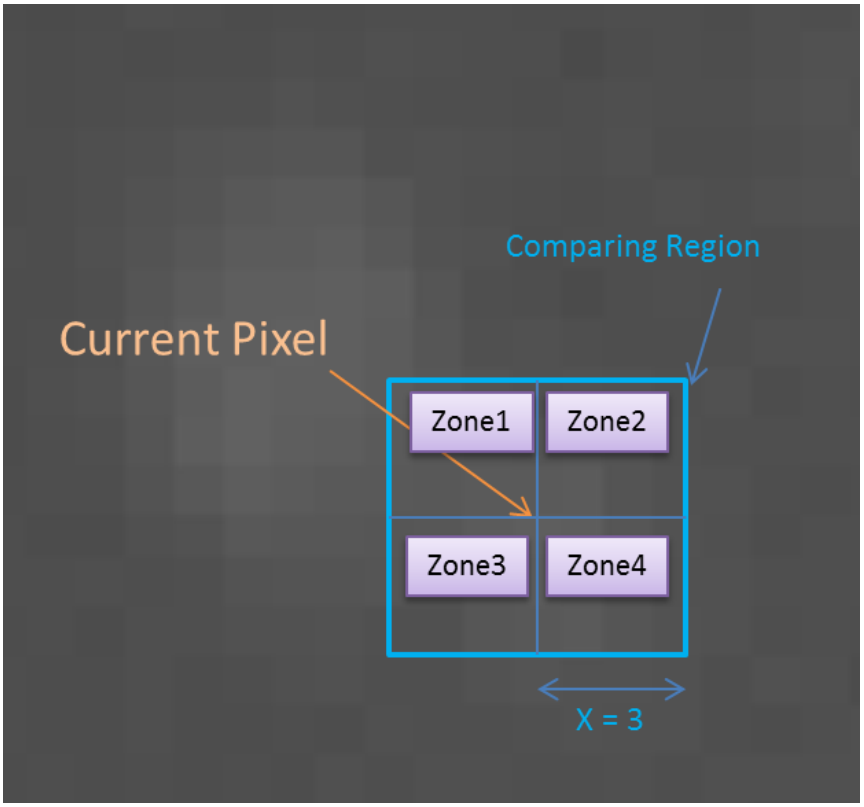

Figure 5.15 comparing current pixel with all adjacent pixels, if the pixel is brighter than the surrounding region than a certain threshold, it is identified as defect

To illustrate the effect of the current algorithm, the defect predicted for the examples from Figure 5.12 and Figure 5.13 are shown in Figure 5.16. From the result, it can be seen that the difference in background brightness has no influence on the LOF identification anymore.

Although the defect appears to be identified, but in some case the large size LOF has it centre location indicated as non-defect region. This is mainly due to the large size LOF could have the brightness flatten out at the central location of the LOF, thus giving insufficient contrast (Figure 5.14). Since it is only the central of the defect which has left out, MatLab function '*imfill*' can be used to fill up the small hole within the LOF.

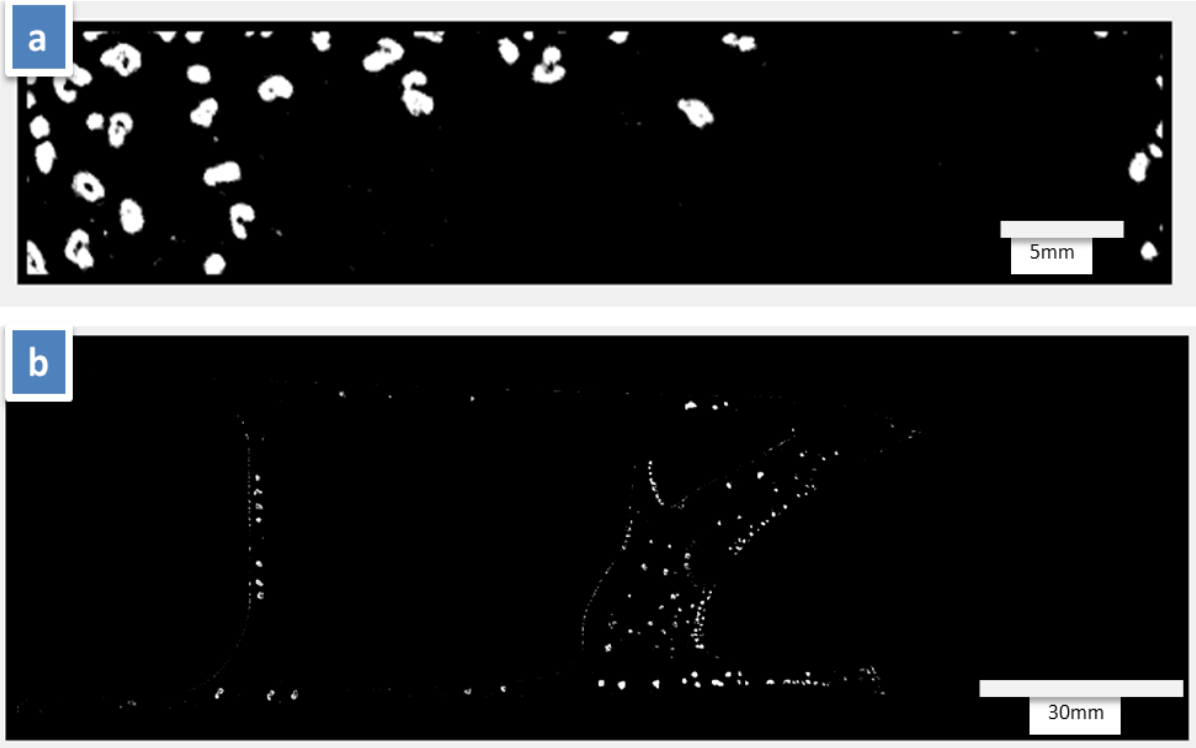

Figure 5.16 LOF identified used current developed algorithm
[a] LOF identified from Figure 5.12 [b] LOF identified from Figure 5.13

The penetration algorithm

According to the machine manufacturer, the electron beam melt pool can penetrate at least two layers. A defect existed only for one layer, could be removed by the melt pool of next layer. Thus the penetration algorithm is applied to resemble the actual EBM process to remove any singular LOF which existed in one layer only.

Step 8. Stack all the LOF up to 3D model and output as STL

As the image is able to be correlated with the cross-section of the original STL in Step5, every pixel within the image should have a unique 3D coordinate corresponded to the original build configuration. The X and Y value of LOF can be calculated from the bounding box location of the image, and the Z location will be as given from the layer number.

In this step, each LOF pixel will be assigned a unique 3D coordinate and output as a small cubic box in STL format. The reason to output as STL is for the overlay with the original build configuration.

An example of 3D LOF is shown in red in Figure 5.17.

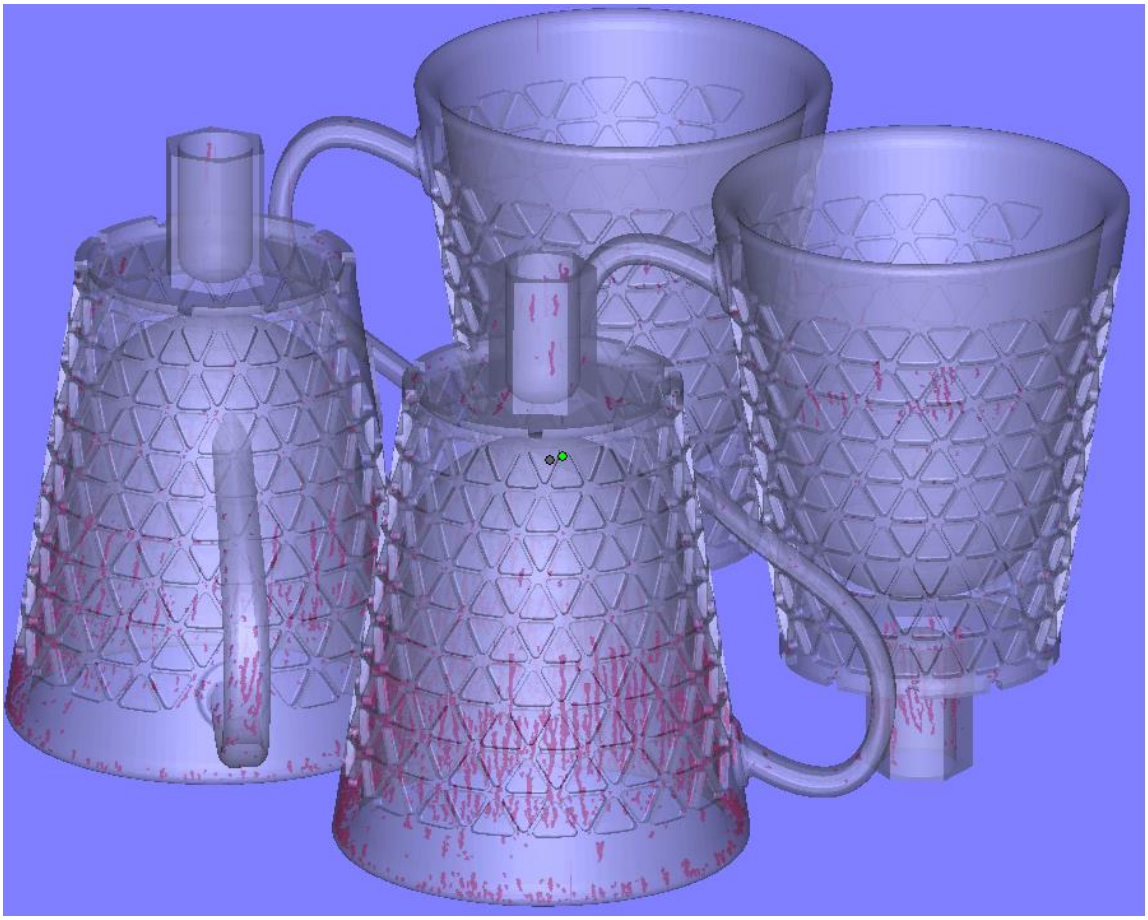

Figure 5.17 Configuration of the build with identified LOF from LayerDD, result is viewed under Magics V19

Step 9. Visual Inspect on the LOF through STL viewer

Although the current algorithm is good and stable for most of the LOF, there is still some ambiguity present. In general, the detectable defects are only the 'tunnelling' type defect, thus they will appear like a tunnel structure as shown in Figure 5.18a. Occasionally, some identified defects looks like single line, which have no characteristic of a defect, they are currently believe to be the dirt from the shielding glass, as shown from Figure 5.18b.

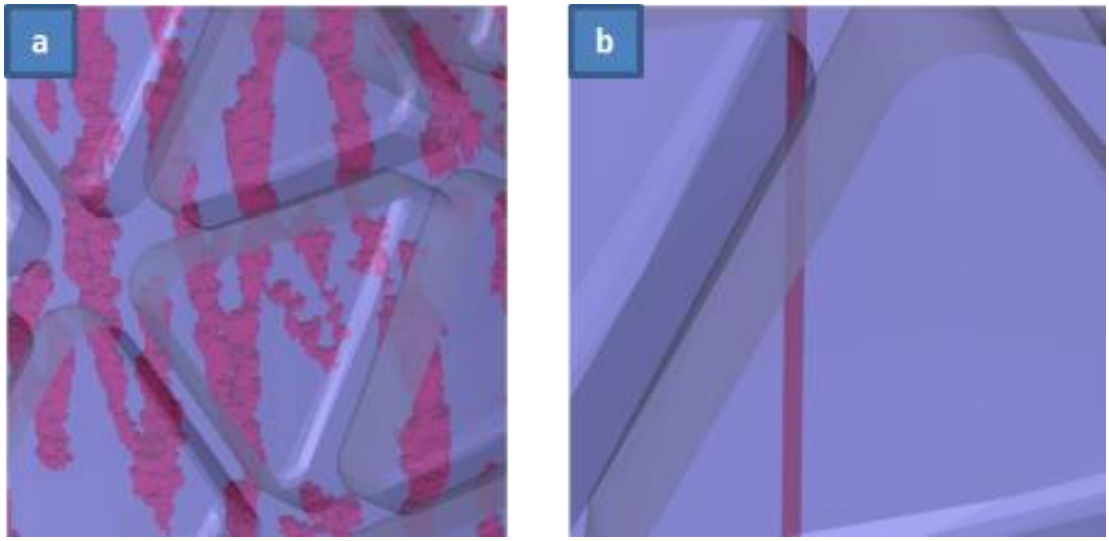

Figure 5.18 (a) Lack of fusion (tunnelling LOF) (b) dirt from the protect camera glass

'Flake' in an EBM build is the evaporated metal condensate on the heat shield which fall off during the build (Chapter 2 Section 2.3.2). Occasionally, when the 'flake' have dropped onto the part, they can be spotted by the camera. Due to the 'flake being on the heat shield, where the temperature is much lower than the powder bed, they appear much darker than the actual part. The abnormally large sizes of the defects presented in Figure 5.19 are believed to be the flakes that come from the heat shield.

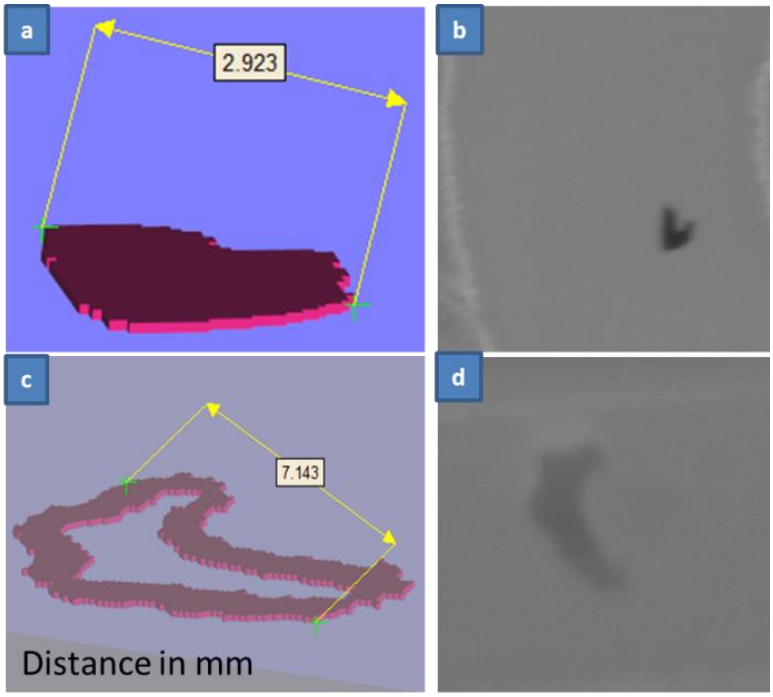

Figure 5.19[a] & [c] Identification of flakes from the LayerDD images; [b] & [d] the appearance of these defect from the image, the region of these spots appears to be extremely dark due to the cold flakes drop from the heat shield.

5.3. LayerDD Verification Experiment and Result

In this section, the defect prediction from LayerDD system is compared to other defect identification techniques, which include CT scan and cut-up specimen. Although CT scan is not an approved aerospace NDT technique, the CT scan result is assumed to be correct in this chapter due to the following reasons:

- The shape of sample used are small and simple cylindrical specimen, which are ideal for CT scan
- Only LOF type of defect is required to be verified, where the size of LOF are respectively bigger in size.
- CT is based on X-ray technique, and X-ray is a currently approved aerospace NDT technique
- CT has been used in other industries such as automotive and medical for many years

In addition to the simple specimen verification, LayerDD system has also been compared to a machined component which is more complex in shape. This comparison is illustrating how to use LayerDD result to give a better interpretation of the LOF distribution within an actual component.

5.3.1. Due to the EBM process being at an elevated temperature and any of the post NDT and inspection is being carried out at room temperature, a shrinkage factor is used on the LayerDD result. The X and Y direction's shrinkage factor are assumed to be 0.99108 and Z direction's shrinkage factor is assumed to be 0.99503. [103] LayerDD Key Variables

As mentioned in the LayerDD algorithm section, there are two key variables that directly influence the result of LOF identification. The first one is the threshold used to filter the LOF, and the other one is the assumption on the melt pool penetration depth. In this chapter, 1 layer penetration means the energy beam is only affecting on the top layer, and 2 layer penetrations beam means the energy beam is melting the top and 1 layer below.

Since the final presented result from LayerDD is a 3D model defect model, and the most popular 3D defect detection technique is Computed Tomography (CT), these two techniques will be compared with each other.

A sample has been produced in the shape of a tensile coupon using an EBM Q20 machine. The energy density of the part has been deliberately lowered to simulate the formation of LOF, and the part has printed with 0.3 mm line offset rather than the default of 0.22mm.

The CT scan is performed by NorthStar Imaging, and the defects are told to be filtered by the Otsu Method. As there are different datum system used in LayerDD and CT scan, the overlay between the results is performed manually to an approximated location and then automatically correlated to best fit using Polyworks 'Best Fit' function.

LOF has been introduced successfully as shown in Figure 5.20. In the figure, the result of LayerDD is displayed as red and the CT scan result is displayed green. The LayerDD result is produced with LOF threshold set to 0.037 and with penetration algorithm of 2 layers. The result appears to be very convincing, but with a more detailed inspection on the comparison, there is some miss-correlation between the two LOF predictions, as shown in Figure 5.20.

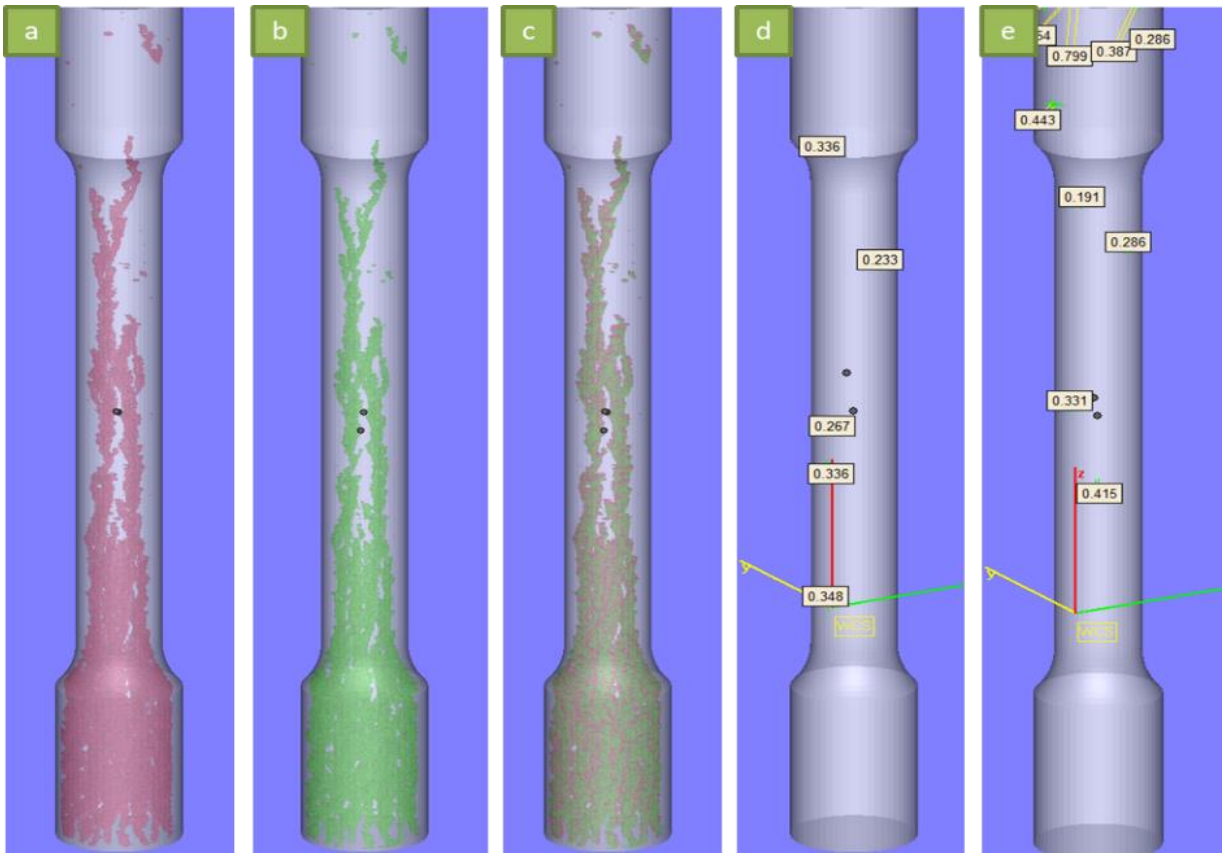

Figure 5.20 [a] LayerDD with Layer Penetration = 2, LOF Threshold = 0.037; [b] CT; [c] Overlap between LayerDD and CT; [d] LOF in CT but not LayerDD; [e] LOFs in LayerDD but not CT

Similar to any defect filter technique, the number of defect detected is directly relative the defined threshold. From Table 5.1, by lowering the threshold more noise will be detected, but the number of missed LOF will reduce also. The effect of the penetration algorithm is very obvious also, by changing the layer of penetration to a single layer, the number of missed LOF decrease, but it more noise detected.

It is worth mentioning, some of the LOFs are not appearing in the LayerDD result regardless of the parameters setting. By reviewing the raw images data, the region of interest has no

indication of LOF, this suggest the camera used in the process is not capable of capture certain types of LOF.

Table 5.1 LayerDD parameters affect the LOF identification result

Layer Penetration	LOF Threshold	No. of LOFs in CT but not LayerDD	No. of LOFs in LayerDD but not CT
1	0.03	2	220
1	0.033	3	128
1	0.037	3	69
1	0.041	3	46
2	0.03	5	21
2	0.033	5	15
2	0.037	5	12
2	0.041	10	8

5.3.2. LOF Size Investigation

In this test, samples with size 25mm×25mm×15mm are induced with top-to-bottom LOF as shown in Figure 5.21. In all the samples, the cross sections of the LOF are design to be square with variable size from 0.05 mm to 0.8 mm. Since the geometries are designed with seeded holes, by default print theme, the contour will be scanned along the boundary of the hole during the melt stage. But in a real EBM process, the LOF region will have no contour around the defect. Thus, in order to better resemble the actual LOF formation, the contour setting in the melt step is turned off for all the samples.

In this experiment, there are 4 samples produced in total, each individual part is cut with electric discharge machining (EDM), then polished to be viewed under the light microscope. The EDM location should be half way between the top and bottom of the sample and perpendicular to the build direction. The location of the cutting plane is measured from the bottom of the sample after the specimen has been polished.

The setting used in LayerDD analysis is with LOF Threshold of 0.037 and Layer penetration assumed to be 1 layer. Due to uncertainty associated with measured distance and the angle of the cutting plane, the defects identified in LayerDD result are taken at a range of +/- 0.1 mm from the measured locations.

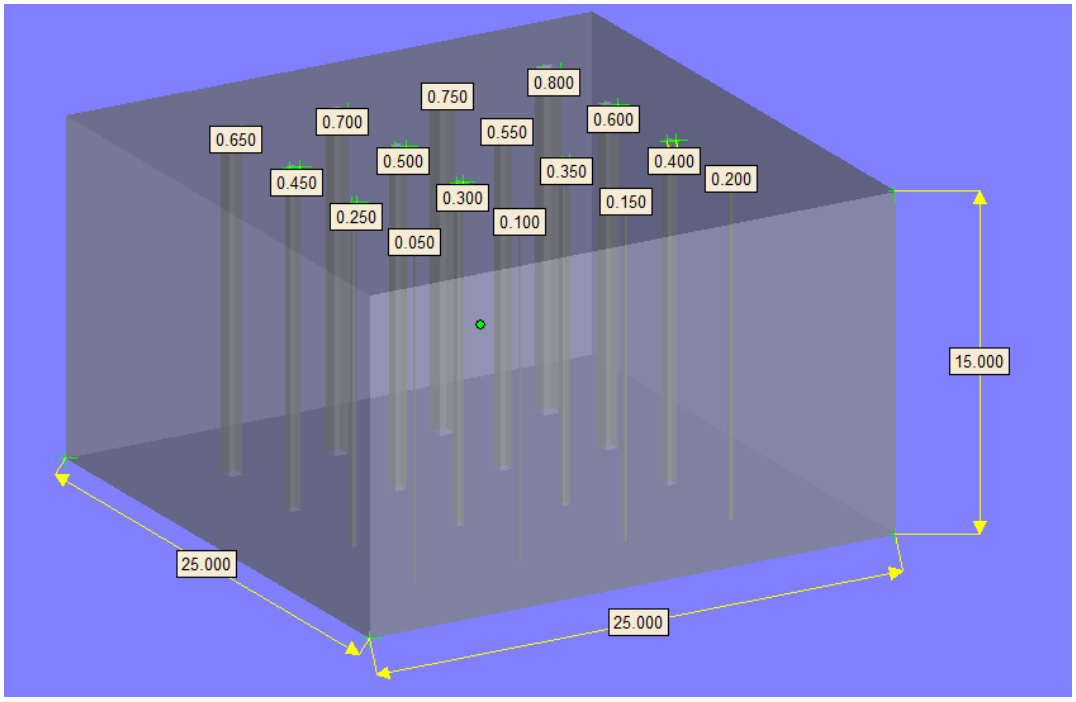

Figure 5.21 Sample induced with LOF from top to bottom, the defects are seeded with size varied from 50µm to 800µm

All four samples have successfully produced with defects, but those with dimensions less than 450µm are not seen under the sectioned sample or in LayerDD result. By overlapping the LayerDD predicted result onto the cut-up observation, the result is shown in Figure 5.22.

From the overall view, it can be see that the defect identified by the LayerDD system is generally larger than the size identified from the sectioned sample. In addition, the appearance of the defect in LayerDD is more circular than the defect that appeared in the cut-up cross-section.

Table 5.2 and Table 5.3 show the dimension of the defect, where the dimension of LayerDD result is acquired by measuring the STL output from the LayerDD result, and the cut-up dimension is measured with software ImageJ.

Table 5.2 LOF size measure under microscope after the specimen is cut open and polished

Design Size [µm]	Sample 1		Sample 2		Sample 3		*Sample 4*	
	X [µm]	Y [µm]	X [µm]	Y [µm]	X [µm]	Y [µm]	*X [µm]*	*Y [µm]*
450	28	14	30	38	73	56	170	129
500	300	288	287	211	0	0	113	154
550	408	404	425	411	377	317	347	263
600	637	418	449	443	353	367	452	421
650	641	470	372	463	473	549	623	511
700	651	708	463	589	700	520	662	452
750	641	812	551	539	737	725	669	626
800	799	789	635	652	787	620	580	587

Table 5.3 LOF size measured from STL produced by using LayerDD

Design Size [µm]	Sample 1		Sample 2		Sample 3		Sample 4	
	X [µm]	Y [µm]	X [µm]	Y [µm]	X [µm]	Y [µm]	X [µm]	Y [µm]
450	0	0	149	149	0	0	297	223
500	372	297	446	372	372	372	149	223
550	595	520	446	520	446	520	372	297
600	669	595	446	520	520	520	520	520
650	743	743	446	520	595	669	669	595
700	743	743	520	595	743	595	669	595
750	818	892	595	669	743	743	743	669
800	892	892	669	818	892	743	743	743

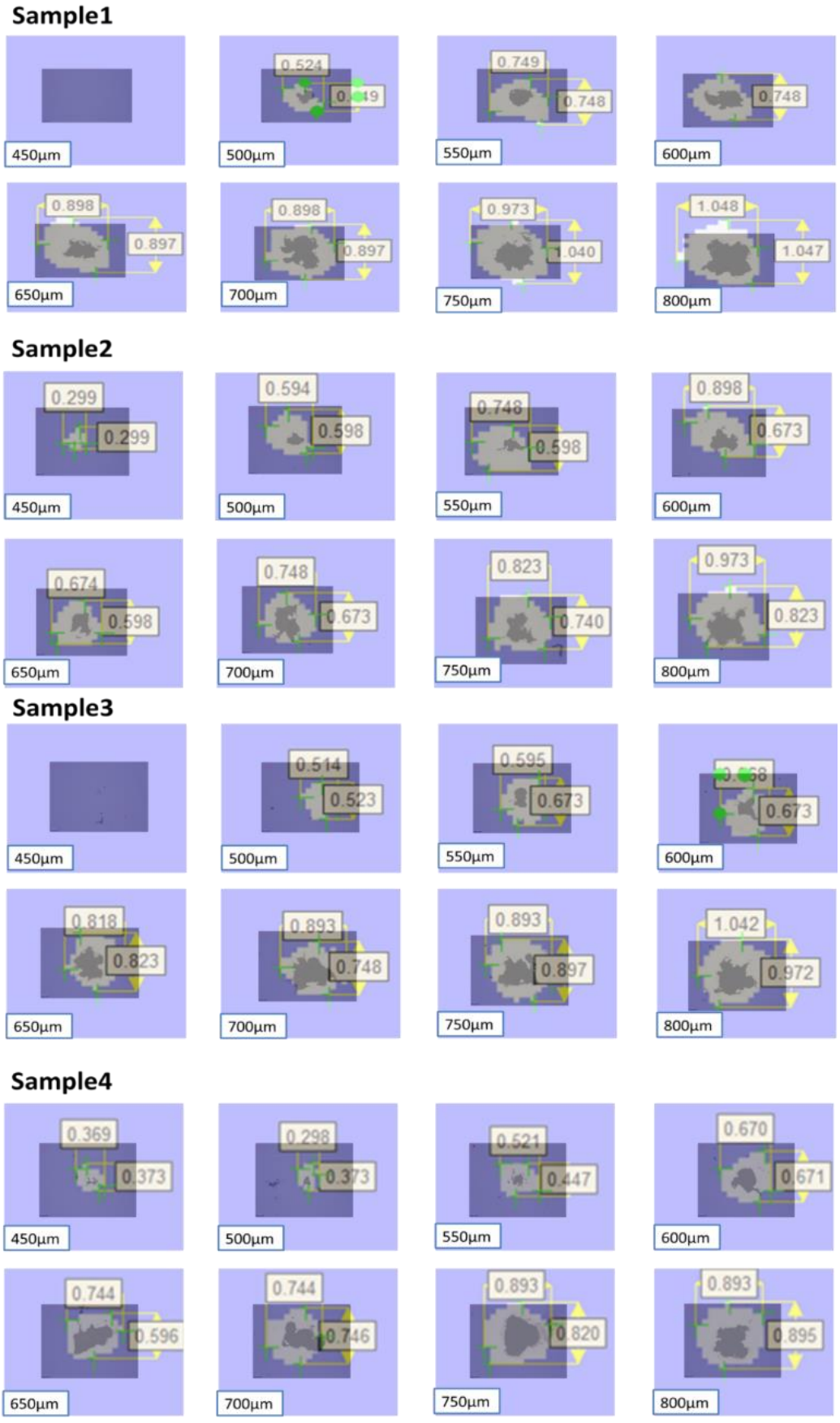

Figure 5.22 Comparison between LayerDD identified defect and defect under cut-up sample with defect seeding dimension larger than 400µm

In Table 5.2 and Table 5.3, apart from the differences in defect size between the two techniques, there are some defects found from cut-up specimen but did not show-up in the LayerDD result. These defects have maximum size less than 73 μm, which is small than the minimum resolution of the camera.

One of the defects that appears in Sample 3 under LayerDD, has not been found from the cut-up specimen, this could be due to two reasons: The defect could be healed due to the next few layers' melt pool penetration or the cut-up plane has missed the location of defects, since this defect (Sample3, 500 μm) has only existed for a single layer.

The results shown in Figure 5.23 are the differences between the sizes measured under the microscopic and the size predicted by the LayerDD system. It can be seen from the graph, the LOF predicted by LayerDD is always larger than the actual measured LOF size (0 to 350μm); and there is no clear relationship between the error in size and dimension of induced defect.

By plotting the distribution of the defect size error, the result is shown in Figure 5.24. With the exception of the defect not being captured by LayerDD, all of the defect's dimensions are larger than the actual measured defect dimension which have values up to 300 μm. This result conflicts with the defect dimension comparison result from the Chapter 4.

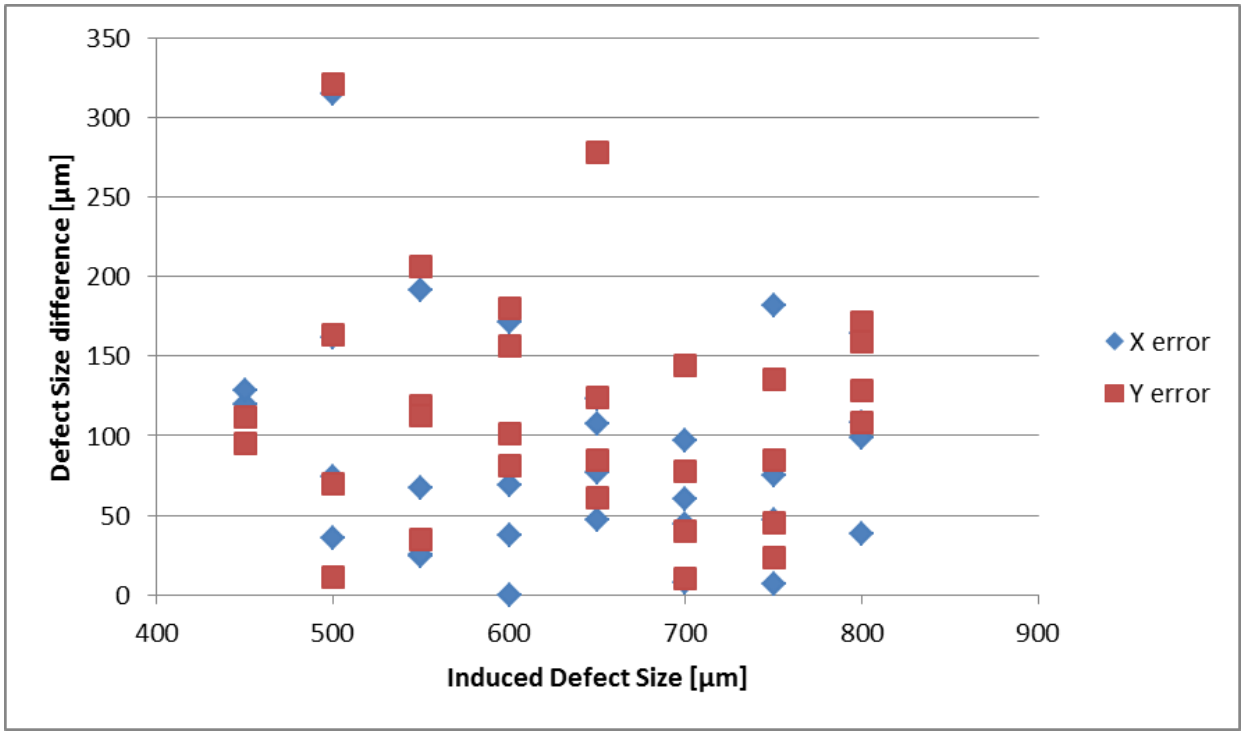

Figure 5.23 LOF size difference between measurement taken by LayerDD and cut-up specimen by microscope. Y-axis indicated the difference between two measurement, and X-axis is the induced defect designed size

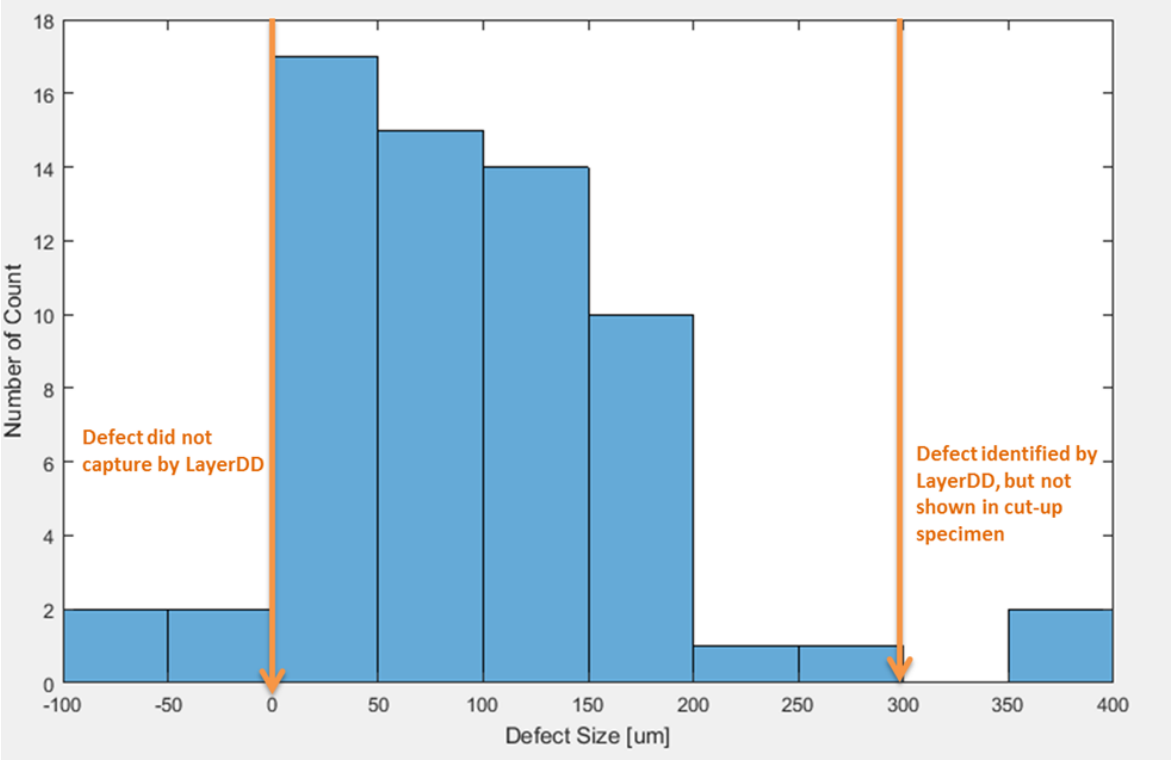

Figure 5.24 Statistical distribution of defect size error between LayerDD and cut-up measurement

5.4. Discussion

From the previous verifications section, the LayerDD has proven to be the very effective for detecting LOF defects. The comparison between LayerDD and CT scan has correlated very well for both LOF's location and shape. Generally speaking, LayerDD is an in-process LOF detection technique, thus the LOF predicted by the system could be different to any post process LOF identification technique, such as size or location.

The detection of smaller size defects in LayerDD is not as effective as the large size LOF. The LOF with dimension less than 75 µm does not seem to be detectable using LayerDD. In addition, there are some LOFs presented in CT scan, which cannot be detected by the LayerDD system.

The core of the LayerDD algorithm is still based on an image analysis technique, thus the system is expected to be greatly influenced by the user defined threshold. Based on the application of the LayerDD system and level of criticality of the component, different threshold setting can be used. The following paragraphs will discuss some key limitations of LayerDD system which are related to powder bed AM or EBM process.

5.4.1. Penetration Algorithm

The machine manufacturer stated that, during the EBM process, the typical melt pool depth should be at least 200µm. With considering this characteristic of the melt pool, the penetration algorithms of two layers (2×90 µm = 180 µm) should be applied to LayerDD system. Unfortunately, from the result in Table 5.1, it can be seen that with 2 layer penetration, some small LOF have been missed out. The reason for this observation could be explained as shown in Figure 5.26.

In an ideal melt condition, as no defect is present in the layer, the surface should be perfectly flat and no LOF should ever form (Figure 5.25). From previous chapter, it was mentioned that

the formation of LOF defect is a problem in material solidification and a LOF formed on the top surface is a 'hole' like structure with few layers depth. Under the camera, this LOF will appear as a brighter spot due to the higher emissivity.

In Figure 5.26, although the existing LOF defect is very likely to propagate upward, it is still possible the defect could stop in one single layer. If the layer on top of current defect has melted properly, then no LOF indication will be found on the second layer. Due to the 'hole' like structure it could potentially be deeper than the depth of melt pool, thus a small region of un-melted powder could still remain. As the LOF has existed for one layer only, it is removed by the LayerDD penetration algorithm.

On the other hand, if the depth of LOF was not very deep, then the next layer's melt profile could give enough penetration to rectify the defects. In this scenario, without the penetration algorithm, extra defects could be identified from the LayerDD system but not show in the final part.

To resolve this problem, the depth of the melt pool and depth of the defects must be known. Unfortunately, in the current LayerDD system, both of the above information are not available, which raises a potential error for the current LayerDD system.

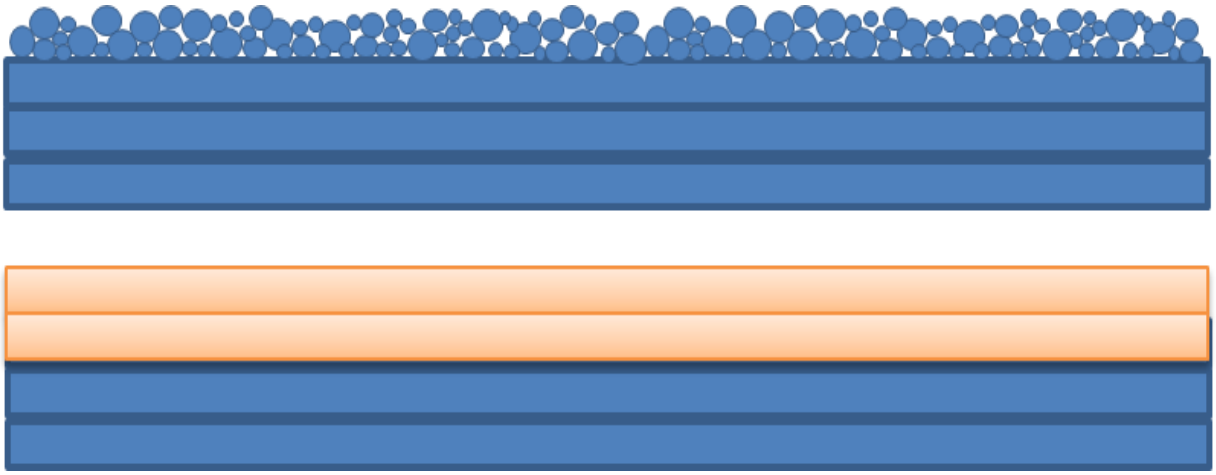

Figure 5.25 Schematic drawing for ideal EBM process with melt pool penetrated at least two layers of powder (180 μm)

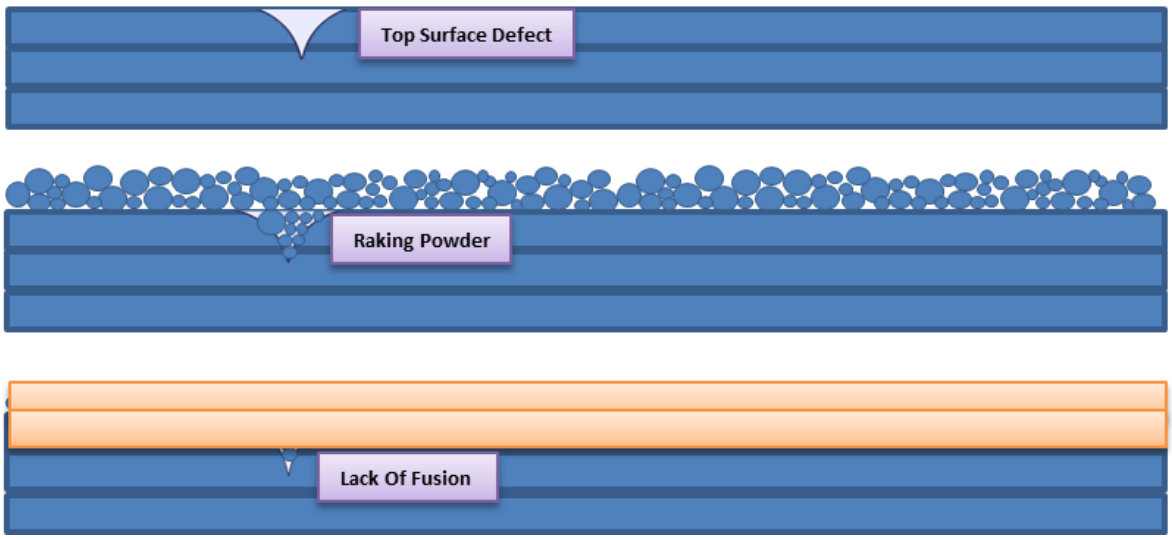

Figure 5.26 single layer LOF where melt pool could not penetrate deep enough, thus a defect is remain underneath the surface (schematic drawings)

5.4.2. Uneven Layer Thickness

One of the features with the camera installed in the ARCAM Q20 machine that is able to take rake images with the flash on, which is the moment after the powder has swiped and before the layer pre-heat started.

Figure 5.27 shows the rake image of a layer from a commercial build. From the image, two regions can be easily distinguished from each other: a bright region and a dark region. The very bright region was observed to be the area with no powder deposited thus the melted part appears to be shiny; the dark region is the area where powder has been deposited properly thus no light is reflected. There could be two reasons hypothesised for this observation:

1. Due to the difference in cooling across the part, the top layer is distorted by the thermal stresses, which results in some area being raised higher than the layer thickness. With the elevated height, the powder is not able to be deposited on top of the part when the powder bed is lower by one layer.
2. Insufficient powder deposition due to lack of powder

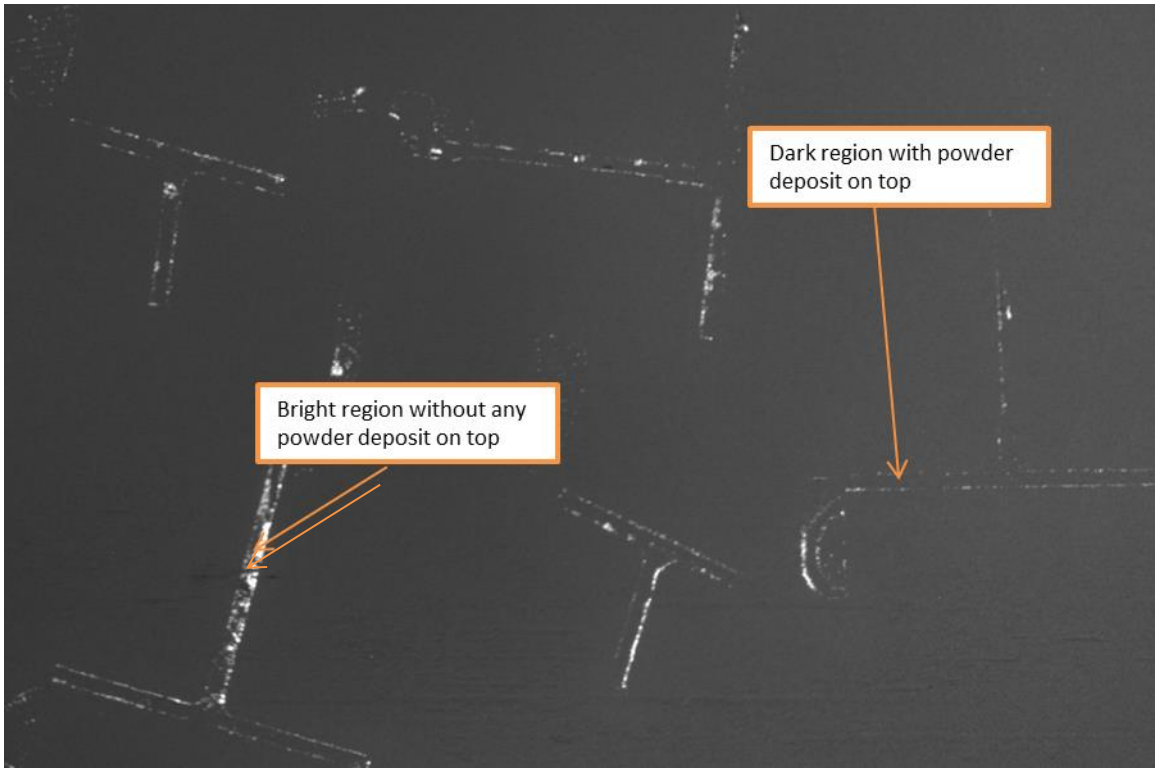

Figure 5.27 Example of a rake where the shining spot are the location without any powder on top of it

In general, a sufficient amount of powder is always checked prior to the build starting and the powder-rake system is design to guarantee each layer has sufficient powder to cover the layer, thus lack of powder should not be the reason for this observation. In addition, the finished part is dense enough to indicate there is sufficient material supply to each part.

By using MatLab to analyse all the images and separate the brighter and dark region, the result is graphed and shown in Figure 5.28. Missing powder on the y-axis of the graph represents the brighter region where no powder has deposited.

By analysing every layer across the build, the average amount of powder missing is around 27.9%. Since the produced parts are 99.98% dense, this means the amount of powder put into the part must equal to the overall mass of the part. Additionally, since the density of powder is less than the solid, the shrinkage from powder to solid states also needs to be considered.

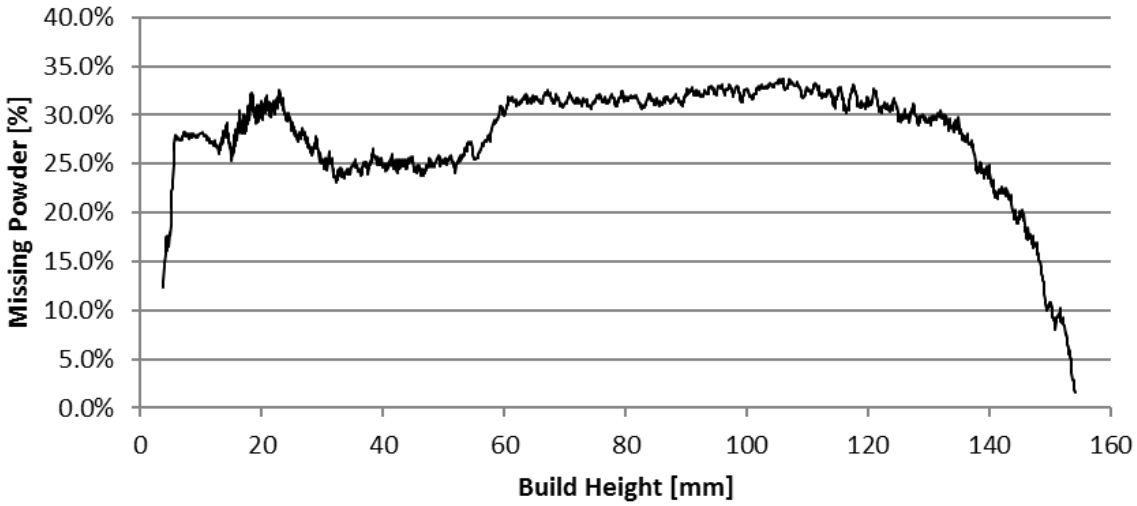

Figure 5.28 Percentage of area uncovered with powder thought the build for the configuration shown in Figure 5.27

From the above information, the equation to calculate average actual layer thickness will show in Equation 5.5 to Equation 5.7, Where is the M overall mass of the part; L_a and L_i is the actual layer thickness and assumed layer thickness; N is total number of layer of any built part; ρ_p * and ρ_B is the powder density and bulk density, η is the percentage of powder on the layer measured from the image.

Equation 5.5

$$M = L_a \times N \times \rho_p \times \eta$$

Equation 5.6

$$M = L_i \times N \times \rho_B$$

With Equation 5.5 and Equation 5.6, the equation is derived into:

Equation 5.7

$$L_a = L_i \times \rho_B / (\rho_p \times \eta)$$

For ARCAM Q20 Plus system, the layer thickness default is 0.09 mm; TiA6Al4V has a bulk density of 4.4 g/cm^3 and powder estimated tap density is about 2.9 g/cm^3; the percentage area covered with powder through the example shown in Figure 5.28 has an average of 72.1% (η = 1-27.9%).

By using Equation 5.7, the average layer thickness depositing onto the powder bed is about 0.189mm. Unfortunately, only the average layer thickness can be calculated from the image, the actual fluctuation of powder thickness cannot be calculated without knowing the waviness of the surface. But the result already indicates that, the thickness of each layer is much higher than the expected layer thickness of 90μm.

This scenario happens regularly for the EBM process, especially when the parts are complex and cooling rates across the parts are highly un-even. This highlights another limitation of the LayerDD system. As demonstrated by the previous chapter, the LayerDD image is not able to give enough contrast to identify a smooth crater formed in a layer, which is due to neither higher temperature nor very high emissivity.

By the time powder is raked onto the next layer, extra thickness of powder will be deposited on top of the crater, and if the melt pool is not able to penetrate all the powder, a 'gap' between these two layers could be left with un-melted powder, thus a defect is formed. With both layers appear to be normal, the LayerDD system is not capable of detecting such defects.

A schematic drawing is shown in Figure 5.29 to illustrate the above hypothesis, where the defect is nearly perpendicular to the vertical direction and the size of these defects are relatively large. Figure 5.30 shows some actual built part examples with internal defect just as describe above, and the length of defect is more than 300 μm.

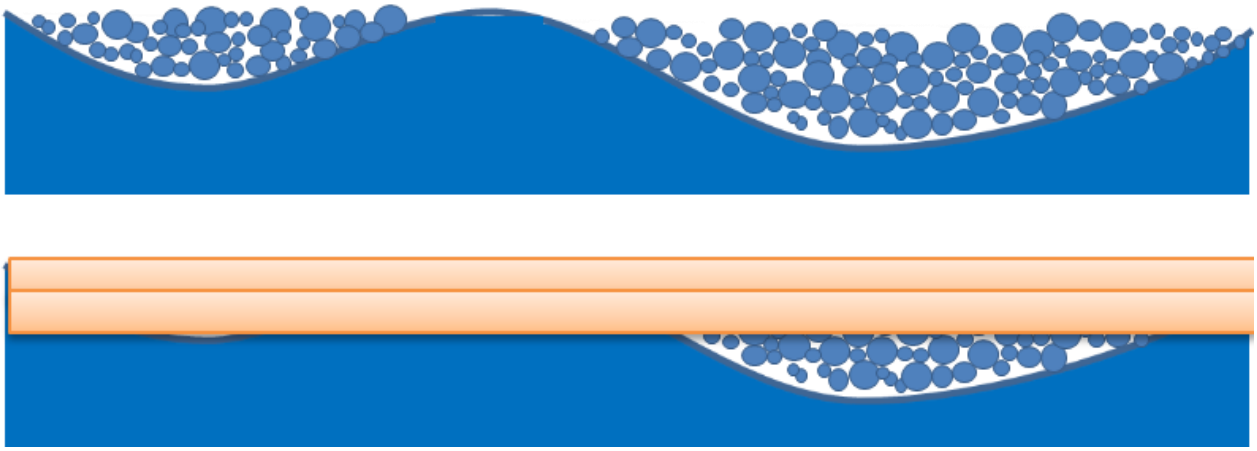

Figure 5.29 Uneven distribute powder where if the powder depth if too high, the electron beam is not sufficient enough to penetrate whole depth, a section of defect will be remain

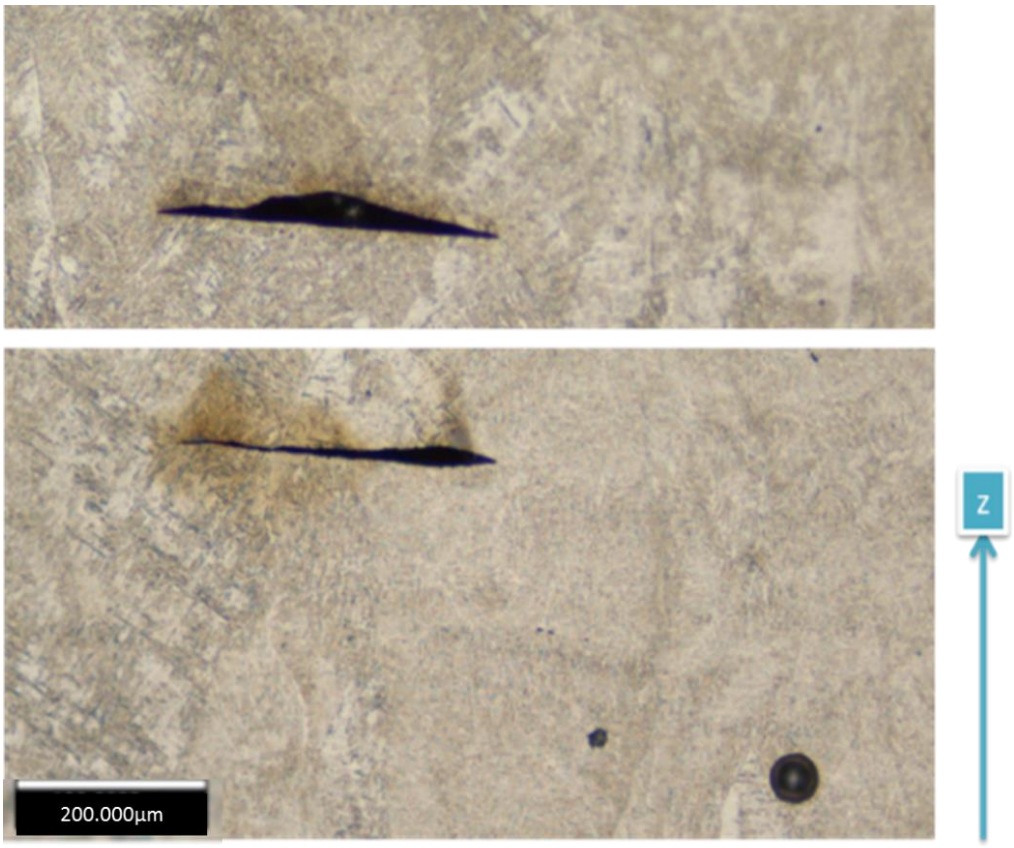

Figure 5.30 LOF causing by incomplete penetration due to potential un-even layer thickness

5.4.3. Inaccuracy of LayerDD result

As seen from the previous chapter 4 (Section 4.3) the defect error between the image and the actual defect size within ±50 µm, but in this section the error has increased up to 300 µm. In addition, the location of defect for complex geometry is not as good as for a simple cubic geometry. There could be three potential factors affecting the accuracy of LayerDD result.

The first factor is the datum system. For a common EBM part, some dimensional inaccuracy is associated with the high surface roughness. In general, the datum system used in CT scan is based on the sample scanned orientation; and for the cut-up sample, the datum used generally refer to a certain surface or cylindrical centre. As for LayerDD system, the datum is the actual build orientation, which is a datum almost impossible to be achieved by any post inspection technique. Thus, the uncertainties of the defect in 3D space are greatly influenced by the different datum system between LayerDD and any post NDT technique.

The second error is the estimation on the shrinkage factor. The shrinkage factor used in the EBM process is developed from a simple EBM shape and not for a highly complex shape. Although the residual stress within the heated EBM build is not as high as for a cold bed SLM process, it can still development some residual stress within the part. When the part is complex, the distortion from thermal stress and the in-accuracy of shrinkage factor could cause significant difference between in-process and post-process measurements.

The last potential error is the LayerDD system in-capable of capture what happens beneath the layer. Since the melt pool depth is often more than a layer, thus it could have a great influence on the detected defect size.

A schematic diagram is shown in Figure 5.31, to illustrate the possible reason of changing in defect dimension. Figure 5.31a shows the layer where the defect has formed and LayerDD has detected and measured the size on the surface. The melt pool on the next layer have depth more than a layer, thus reduces the size of the defect on the previous layer as shown in Figure 5.31c. As for a powder bed process, the shape of melt pool is very hard to predict, as it is influenced by many process variables such as: beam speed, local temperature, powder distribution and local surface condition etc. Similar observation and simulation of defect propagation has given by A.Bauerei et al. [104]

Since the defect has change shape due to the melt pool on the next layer, and the camera is not able to detect it, as a consequence, the actual defect size is generally smaller than the result from LayerDD system. In Figure 5.32, the diagram schematically shows the difference between actual defect size and LayerDD identified defect size.

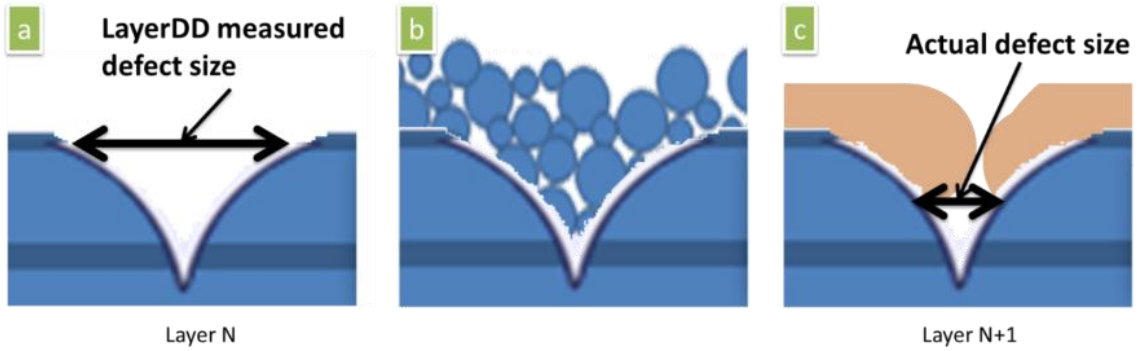

Figure 5.31 [a] developed defect measure by LayerDD [b] deposition of powder onto the layer [c] the melt pool solidified, reduces the size of defects.

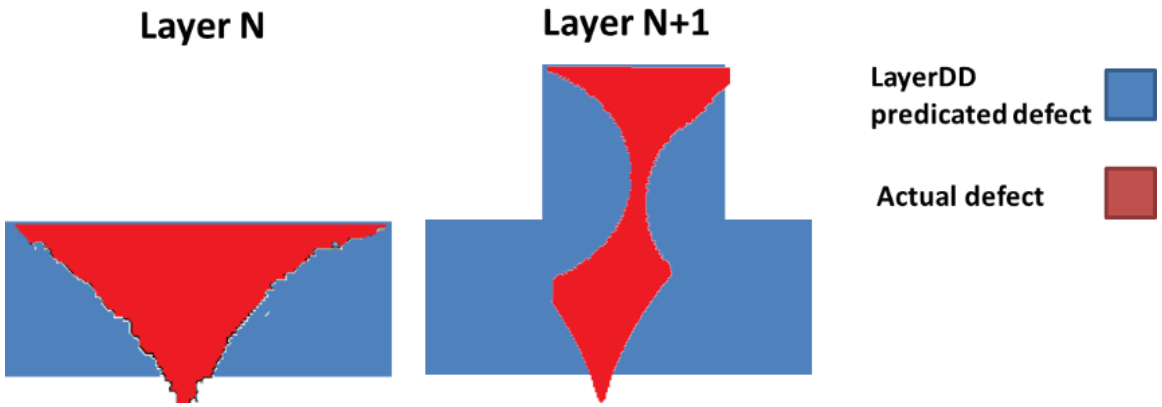

Figure 5.32 Difference between LayerDD (shown in blue) identified defect vs potential actual defect (shown in red)

5.4.4. Contour or Part Boundary

This is one of the current limitations with the current defect identification technique. As explained in the LayerDD Algorithm section, the contours have similar brightness level as the LOF region, and therefore have to be removed prior to defect filtering. Thus, at current stage of development, any LOF near the contour region will be un-detectable by the LayerDD system.

5.4.5. Summary of Advantages and Disadvantages of LayerDD system

As the most popular NDT technique used in aerospace, Computed tomography and X–ray are commonly used. The result or accuracy of the above techniques is greatly influenced by the size or complexity of the component.

The biggest advantage of the LayerDD system is that the defect identification is performed on the whole build rather than each individual part. Although the resolution of the LayerDD system is not as high as CT or X-ray, its predicted result does not restricted by the shape or size of the components.

Another advantage of LayerDD system is the in-process capability, where the result can be attained more quickly than a post process inspection, which is essential for process development. As for the current the stage of development, the time for analysing an image takes approximately 20 seconds, for a maximum build of around 4000 layers, it could take up to maximum of 24 hours. In addition, the time to analyse the build is not delayed by cooling and removal of the build or PRS of the part. For any other testing technique, the part is required to be taken out, and sent to another department for analysis. If the NDT required cannot be perform in-house, it will take even longer, sometimes up to a few weeks to get a result.

One of the unavoidable drawback is the additional time in the EBM system of 3 seconds per layer due to the opening/closing protective shutter and imaging time, the cost of the additional time will be explained in more detail in the later section.

5.4.6. Current Defect Standard

Although both in-process monitoring and post-process monitoring test have a common aim to find defects within the part, the methodologies are fundamentally different. The current aerospace NDT standard is generally based on geometry or size of defect. For example: X-ray or CT-scan identify defect size based on the density contrast of material; Fluorescent Penetrant

Inspection (FPI) is based on crack size and depth. All these techniques commonly asked the same question: ‘what is the minimum defect size that can be detected’ and the answer to the question is fairly straight forward.

On the other hand, LayerDD takes the image and reconstructs them similar to a CT scan, but the system finds defects is based on the thermal contrast and emissivity difference, which is more likely to be due to a ‘process error’ rather than geometry error. Thus, the in-process prediction of defect is based on the theory of the defect formation and detection, not on the size of defect formation. This indicates that, regardless of the defect size, if the defect is does not happen on top of the layer, then the defect detection is impossible.

As mentioned earlier, defects such as gas pore or in-between layer defect are not able to be detected with such a technique. On the contrary, apart from identification of ‘tunnel’ defect, LayerDD has shown the ability to clearly indicate ‘flakes’ that have fallen into the part, since the ‘flakes’ give a very clear contrast in the images. In this case, to detect a flake formation within the part, CT scan or X-ray will have difficulties, as there is not enough density contrast.

5.4.7. LayerDD Industrial and Further Applications

In this section, the cost for LayerDD is calculated and compared with other inspection or testing technique. In addition, the potential industrial application of the system is discussed with respect to the cost model. The process cost and time used in this section is not from any actual quote, but a rough estimation from many engineers’ personal experience.

In this study, only the cost of running LayerDD is calculated, and the development cost of the software will not be considered. The detail of calculation is illustrated in Appendix: Cost of LayerDD System.

The relationship between the total costs of LayerDD and height for a build is shown in Figure 5.33. The plot is produced by assuming the build layer is 0.09mm with average layer time of 60 seconds.

Table 5.4 presents the cost break down for a typical 300mm height build, and it can be seen that the main impact on the cost is the storage of the raw images data. If the LayerDD system has proven to be very accurate and all the raw images can be replaced, then only the final result needs to be stored. By cutting down the raw data storage cost, the next highest cost contribution is the time to capture images during the process as shown in Table 5.5

Thus the two main focuses of technology development for LayerDD is to 1) improve the accuracy and robustness of LayerDD system; 2) reduce the time of taking image (opening and close the camera protecting shield).

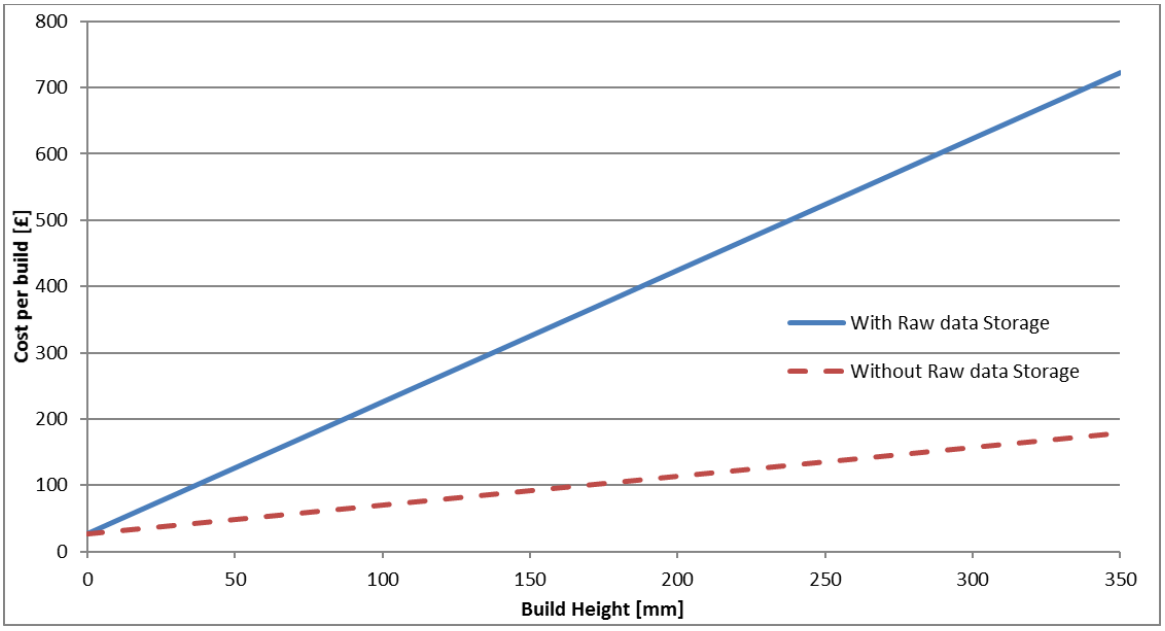

Figure 5.33 LayerDD cost with and without the need of raw images storage

Table 5.4 Cost break down for LayerDD system of a typical 300 mm height build, red highlighted the main cost of the system

Subject	cost (£)	per unit	Total Cost (£)	Percentage
LayerDD Hardware	0.475	hour	26.39	4.23%
Additional EBM time	0.031	layer	103.33	16.56%
Camera Calibration	1.84	build	1.84	0.29%

Analysis Process Cost	20	build	20.00	3.21%
Analysis Result Storage	5.6	build	5.60	0.90%
		Over All Cost	**623.83**	**100.00%**

Table 5.5 Cost break down without raw data storage, red highlighted the main cost of the system

Subject	cost (£)	per unit	Total Cost (£)	Percentage
LayerDD Hardware	0.475	hour	26.39	16.79%
Camera Calibration	1.84	build	1.84	1.17%
Analysis Process Cost	20	build	20.00	12.73%
Analysis Result Storage	5.6	build	5.60	3.56%
		Over All Cost	**157.16**	**100.00%**

5.4.8. Business Case of LayerDD

As a characteristic of the EBM process, the parts are usually printed with contour and hatching. Thus, in many situations, the EBM parts can look perfectly good from outside but could be very porous from inside. Although HIP treatment is often used to close-up the internal defect, it cannot fix defects with openings. Since the EBM process always produces part with high surface roughness, this makes finding defect on the surface very challenging. As a consequence, many post processes will need to be done before the defects can be revealed.

The examples shown in Figure 5.34a-c indicate a surface of an EBM product where LOF has developed within the part due to un-suitable machine parameters. Figure 5.34a is the LOF prediction from LayerDD; Figure 5.34b is the as printed surfaces which did not show any indication of defects; Figure 5.34c is the surface after HIP treatment and chemical milling.

In this component, the LOF has developed and travelled to near the surface of the part and created openings, which the HIP process failed to close up. Due to the nature of chemical milling, liquid has passed through the small openings and attacked the nearby material, which leaves the defect on the surface as shown in the figure.

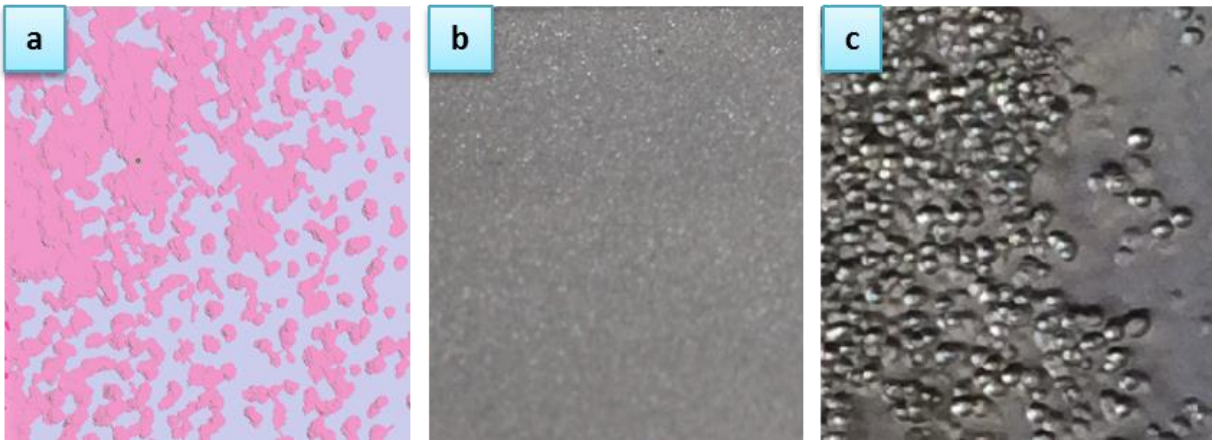

Figure 5.34 [a] Internal LOF identified by LayerDD [b] part surface right after EBM process which show no indication of defect [c] defect reveal after the part gone through HIP treatment and then chemical milled

In the current Aerospace Additive Manufacturing environment, various types of post process are required to assess the quality of parts, such as CT scan, X-ray, and FPI etc. Any of these tests will cost extra time and money. If the post process is in-house it could take at least a few days to a week and if the post process need sub-contract, the time could be even longer. A rough cost estimation of the above post-processes is shown in Table 5.6.[105]

To compare the situation with and without the LayerDD system, the process flows is simplified and described as shown in Figure 5.35. The original overall process can be summarized as printing plus post process, where the print stage includes all the build preparations, melting and powder removal stages etc. and post process will include any testing or inspection method required on the product. Cost of scrap part is exactly the same as like the cost of the good part, as it is assumed that it is not possible to identify scraps before the whole process ends.

By adopting LayerDD system, the overall process will slightly be modified. The print process will be assessed in between each individual layer, and decide whether to stop the process if a major defect has been found. The new procedure is capable of eliminating potential scrap parts at much earlier stage than the original process flow.

Table 5.6 General Post-process cost for EBM[105]

	unit cost	Average Time [in house]	Average Time [sub-contract]	Total Cost for 10 Samples [£]

Hot Isotropic Pressing [HIP]	£500/Batch	2 days	3 weeks	500
X-ray traveller specimen	£40/sample	2 days	3 weeks	400
Tensile Testing Traveller Specimen	£100/sample	2days	3 weeks	1000
Fatigue Test Traveller Specimen	£440/sample	3 days	4 weeks	4400
Tensile Testing Exacting Specimen	£160/sample	3 days	4 weeks	1600
Fatigue Test Exacting Specimen	£500/sample	3 days	4 weeks	5000
Computed Tomography [CT]	£2000-£4000/part	2 days	3 weeks	20000-40000

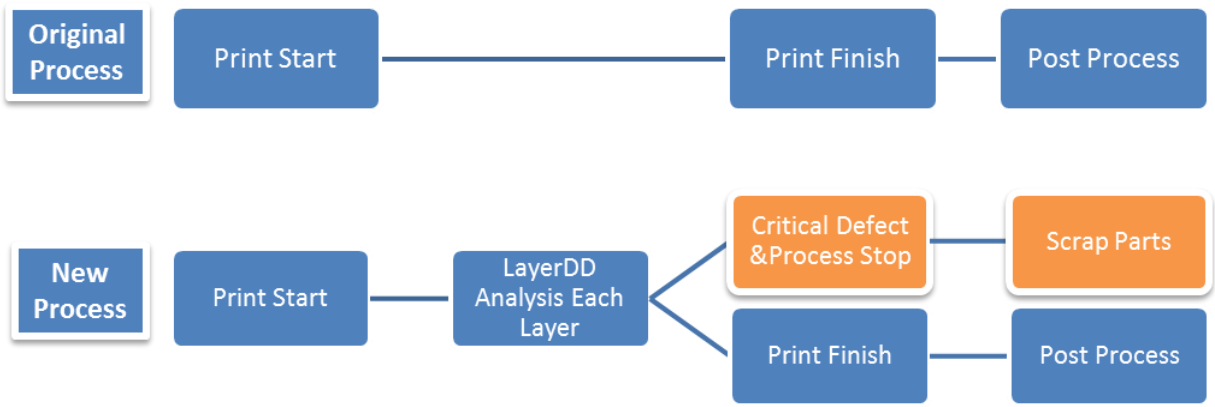

Figure 5.35 the new process with adapting of LayerDD system compared to the original process

To assess the overall cost of the process, the original process will be part cost plus post process cost with the overall scrap rate, as shown in Equation 5.8, where B is the build cost, PP is the overall cost for the post process and SR is the estimated scrap rate of the build. The new process cost calculated by Equation 5.9 will include the saving on the scrap part, where LDD is the additional cost for LayerDD system, $F\%$ is the percentage of build finished if it is aborted before the end.

Equation 5.8

$$Origianl\ Cost = (B + PP) \times (1 + SR)$$

Equation 5.9

$$New\ Cost = (B + LDD) \times F\% \times SR + (B + LDD + PP)$$

Equation 5.10

$$Cost\ Saving\ per\ build = \text{Original Cost} - \text{New Cost}$$

From both of the equations there are five variables in total. In order for a better comparison between the two different costs, B, F% and LDD are assumed to be constant in this scenario. Build Cost (B) are assumed to be £3000 to represent a typical EBM full height build; the LayerDD cost (LDD) is assumed to be £157, which is the value calculated in the previous section; the percentage of a build finished (F%) is assumed to be 50%, since a failed build can be stopped at any point of the process.

The two remaining parameters kept as variable are the post process cost and the overall scrap rate. The post processing required on the product can be greatly varied from build to build, since different parts could have a very different qualification standard, for example an engine blade could require a full detail CT scan but a demonstrator part could have no post process at all. Scrap rate can be also very different base on the stability of the process, during the product research stage, if the theme is not suitable for the geometry, more build failure could be seen; on the other hand, a robust theme in a production scenario should have relatively low scrap rate.

The plot shown in Figure 5.36 is the predicted cost saving per build as calculated by Equation 5.10. From the graph, it shows there are more savings when the scarp rate and post process cost are high. During the research stage of the product, the process is imperfect and it is more likely to produce parts with a higher volume of defects, thus the LayerDD system is very effective in preventing the critical builds from going forward. As the process moves toward into production environment, the amount of LOF within the part becomes less and less and eventually the

LayerDD system will become redundant as it is currently not able to substitute any post process. In addition, the LayerDD system analyses the build rather than each individual part, so if the post process for the build is very expensive, then the relative cost of LayerDD system will become cheaper.

Occasionally, the time for product development is more critical than its cost. A similar prediction is made and the result of time save per build is shown in Figure 5.37. Due to the characteristic of the in-situ monitoring, the analysis result can be obtain even before the part come out from the chamber, thus a huge time saving can be achieved when the scrap rate is high and in-house post process ability is limited.

For both of the results of cost and time saving, the red highlighted region is indicating the breakeven point of adapting LayerDD system, and as the result indicates, when the process is very stable, the requirement for the LayerDD system could become unnecessary.

Furthermore, all the above calculations are assumed LayerDD system does not replace any type of post inspection technique. But, in some case the result of LayerDD system could be used to help to reduce the cost of NDT, such as to perform the X-ray only on the highly defective region rather than taking a full CT scan. As the relative cost of LayerDD system is very low compared to any other technique, by further developing the system into more a robust algorithm, the LayerDD system could be capable of substituting some of the post-processes, hence the potential saving on both time and cost could be more significant.

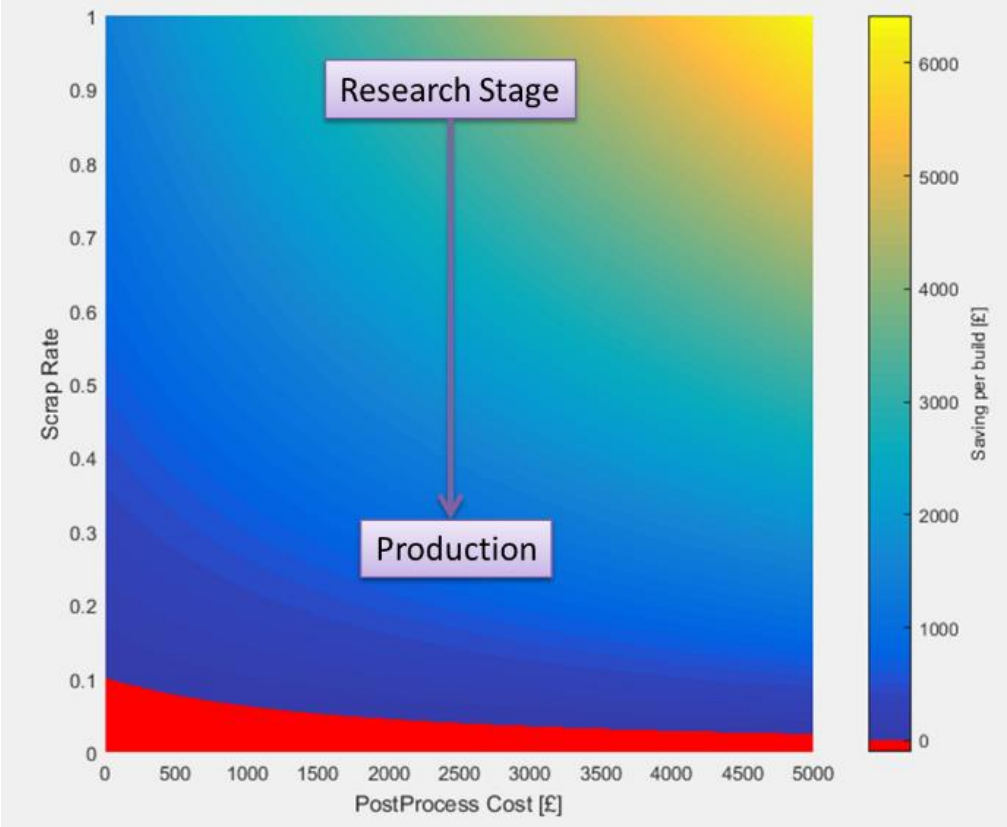

Figure 5.36 Potential cost saving by using LayerDD system

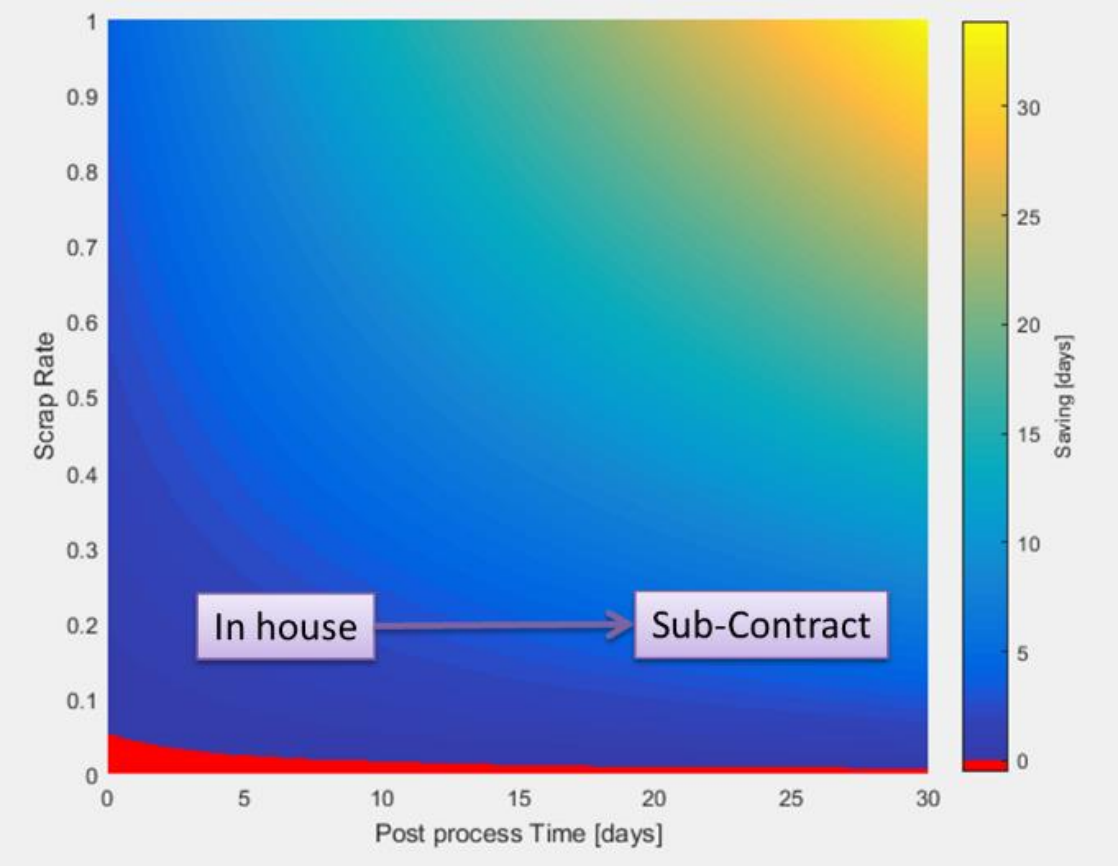

Figure 5.37 Potential time saving by using LayerDD system

5.5. Conclusion

- LayerDD has proved successful in identifying LOF during the EBM process, but at this stage, it is not able to identify LOF in the contour regions, due to the similar brightness between contour and LOF regions appears under a thermal camera.
- The LOF identified from LayerDD are generally larger in size and slightly different in shape to those in cut-up and CT scanned specimens. This is mainly due to a different datum system and the defect shape change after each layer.
- Any LOF less than 75 µm cannot be detected using LayerDD because of resolution limitations.
- LayerDD can also be used to detect 'flake' formation during the EBM process.
- LayerDD is an in-situ monitoring technique, which monitors the process itself thus the method of defect identification is also process related. Some defect formation scenarios are not able to be identified such as:
    - Uneven powder layer distribution might cause some LOF beneath a layer that can't be detected by LayerDD.
    - Penetration Algorithms can be used to significantly reduce the error of non-LOF measurements, but it could be omitted from the LOF that only last for a layer.
- In the aerospace industry, the estimated cost of LayerDD for a standard full height build is £157, but if storage of all the raw images is required, then the cost is £623.
- A LayerDD system could be especially useful during the product research stage, it not only saves time during prototyping but also reduces overall cost.
- The further development of LayerDD should be focused on the robustness and accuracy of the system, in order to remove the necessity to store raw image data.
- Additional development should improve the shielding mechanism on the camera to reduce the time spent to take images.

Chapter 6 : Closed Loop LOF Rectification

In general, parts with internal defects are fixed with a post process HIP treatment, but a key limitation of the HIP process is that it is unable to close up defects open to the surface. The gas and keyhole porosities present are usually small and contained within the part, thus the HIP treatment is suitable to close up or minimizing this type of porosity. However, LOF defects are generally much bigger and very irregular in size. If the LOF defects have 'tunnelled' to the surface, then the HIP process is not capable of removing this type of defect.

In an ideal EBM process, the best scenario is to produce a part without any LOF present. In order to achieve a LOF free part, two different approaches can be considered: The first one is to ensure the entire volume of the part is printed with ideal parameter settings; the second one is to rectify the LOF during the process with a closed loop control algorithm.

Current EBM system made by ARCAM has used a 1D thermal model and many pre-defined functions to predict the heat input in each location of the build. Since the prediction is never been perfect, the energy input can be flawed in some regions, which eventually results in LOF formation. Thus, a closed loop system is the current preferred method as this method can be used to fix the defect during the process.

As the LayerDD algorithm can be used to help identify lack of fusion (LOF) type defects during the process, a possible development for Layer DD is to employ it for defect rectification. This application would help fix LOF defects or stop them from propagating upward. As explained in the theory of LOF, the formation of LOF is when the energy density is too low, and the previous surface is defective or very rough. Based on the observations of many EBM builds and the result in Chapter 4, LOF rectification cannot be achieved immediately with the default parameter supplied from ARCAM.

In order to fix the defect, a hypothesis of Close Loop LOF Fixing Algorithm (CLF) has been suggested in this chapter. There are two difficulties regarding in-process defect rectification:

1) As explained by Bauereiß's simulation [Chapter2 2.3.1], due to rapid cooling and high surface tension of molten material, the defect underneath the current layer has a great influence on the material solidification.
2) As indicated in the previous two chapters, when the defects have formed on the top surface, it often appears as a cavity with at least few layers depth (Chapter 4 Table 4.4).

Thus, in order to prevent the LOF from propagating and remove the LOF from the previous layer, an excess amount of energy is required to create a large melt pool which is sufficient to melt both the existing defect and several layers below it. In this way, the melt pool solidification will be least affected by the existing LOF.

Modifying the process parameters to fix the defects will generally result in additional energy being applied to the melt pool, this will be referred to as the "fixing parameters". This change in the parameters can cause the resulting surface of the layer to deteriorate. The deteriorated surface could also be the initialization site for new LOF formation, thus the fixing parameter not only needs to rectify the underlying defect, but also needs to create a smooth top surface which prevents new LOF from regenerating.

When a LOF has been identified, the fixing parameters should be activated on the subsequent layer from where LOF has been detected, thus the computation of the defect location and the fixing parameters melting strategy could be done during the raking and preheating of the next layer. The advantage of this is no additional process time apart of the thermal imaging itself. As shown in processing cost calculated in the previous chapter, additional process time is very costly.

A diagram is shown in Figure 6.1 to illustrate the strategy to fix the existing LOF. The expectation of the algorithm is to be able to detect the LOF and then fix the detected LOF in the next layer. Following this, the printing should revert back to the default machine parameter after the defect has been fixed.

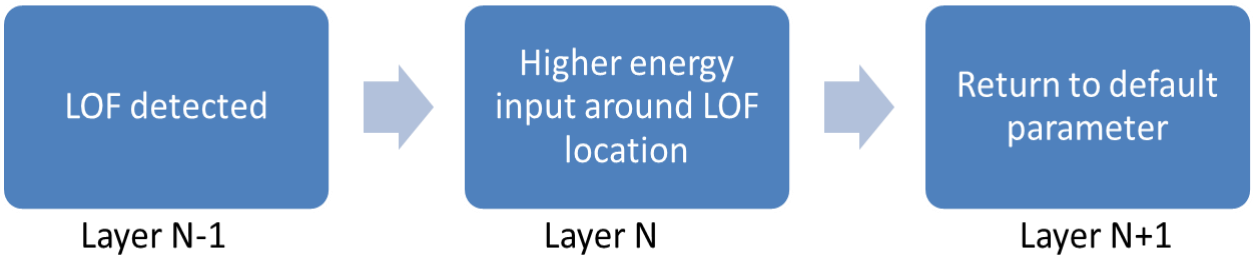

Figure 6.1 Closed Loop LOF rectification in EBM process

In order to prove the above idea, the following experiment has been conducted. The aim of this experiment is to prove the potential of stopping LOF propagation during the EBM process and rectify the existing LOF underneath. As it is not possible to access the core system of Q20 plus EBM control, the experiment is conducted with some adjustments from the above algorithm.

During the EBM process, the build observation and the parameter modification will be carried out manually instead of being automatically controlled using software. In addition, the modified parameter will be applied to the whole layer rather than only around the LOF location.

6.1. Experiment Procedure

6.1.1. Build Configuration

The test specimens are designed to be simple rectangular blocks with cross-section dimension of 35mm by 15mm as shown in Figure 6.2. In total, there are three melt groups, with two separate specimens in each group. The specimens in Group 1 are the control specimens are that printed with the Q20 Plus default parameters through the build and without any parameter modifications. The specimens in Group 2 and Group 3 are the experimental specimens that undergo a process where defects are introduced and then fixed with different parameters settings, this process is repeated throughout the build

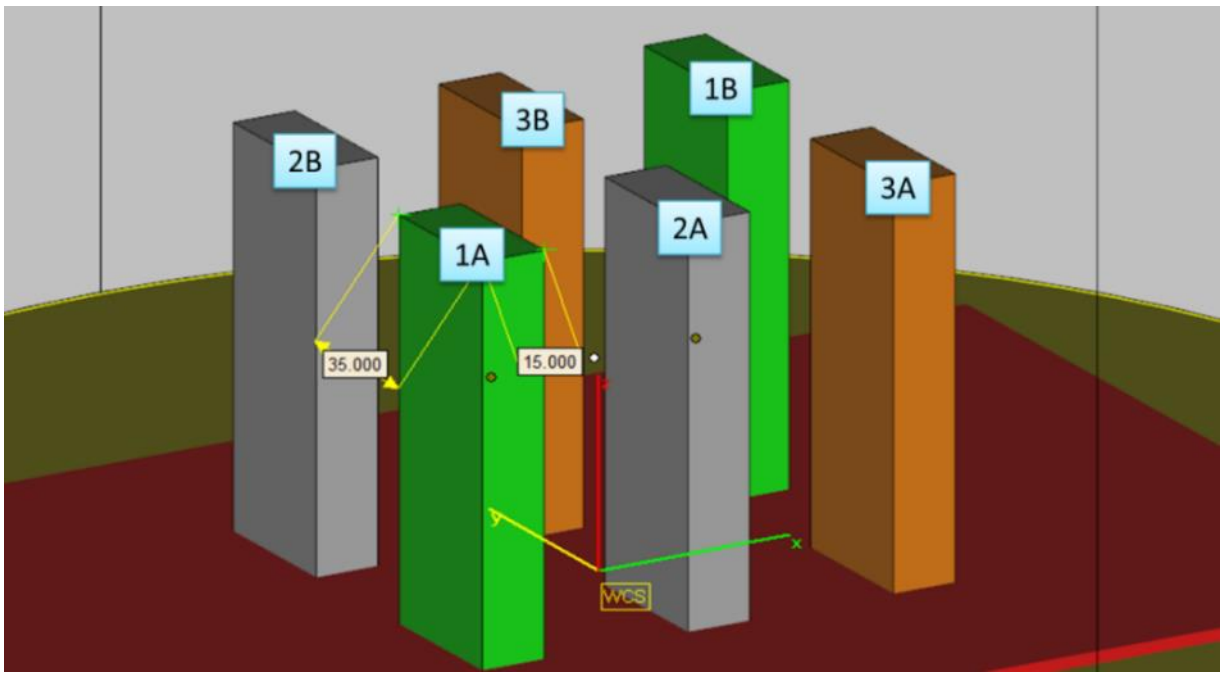

Figure 6.2 DOE: Control Group 1 (green); Experiment Group 2 (grey); Experiment Group 3 (orange)

6.1.2. Machine Parameters

Three parameters were selected to be modified in this experiment, these are: hatch line offset (LO), beam diameter (D) and beam speed (S). The hatch line offset is defined as the distance between adjacent hatching lines; beam diameter is the measure of the distribution of the electron beam at full width at half maximum intensity (FWHM); and beam speed is the nominal

traverse speed of the moving beam. In the Q20 plus EBM system, apart from the defined input value, these parameters are influenced by other built-in functions.

Line offset is influenced by a function named ‘Line Offset Compensation’ [Chapter3 3.2.7], which has been informed is an equation modifying line offset value base on Scanlength value. The detailed equation has not been given by the machine manufacturer.

Beam diameter is defined by the variable of ‘Focus Offset’ with units in milli-ampere, which is the electrical current passing through the magnetic coil that controls the electron beam diameter. The relationship between ‘Focus Offset’ and beam diameter is shown in Chapter3 section 3.2.1. The ‘Focus Offset’ value could further be affected by Thickness Focus function. The machine manufacturer states that the function is only activated when overhanging structure is detected. With this experiment’s configuration, there are no overhanging surfaces included, thus this function should never be activated.

The nominal beam speed in the EBM system is defined by the variable ‘Speed Function’. The ‘Speed Function’ is a table that extracts the beam speed based on the ‘Speed Function’ number and the beam current. As for the Q20 Plus system, the beam current is designed to be kept constant at 28mA, thus the relationship between the ‘Speed Function’ and the nominal speed is almost linear as shown in Figure 6.3.

After the beam speed has been determined by the ‘Speed Function’, the beam speed is further affected by the turning function [Chapter3 3.2.5] which is defined by Equation 6.1, where PF, $EF1$, and $EF2$ are ARCAM defined variables, d is the distance from the turning point, si is the proportion of speed increased, S_1 is the speed before the turning function and S_2 is the speed after the turning function is used.

The equations shown below are given for the older version of the ARCAM machine, although there is no confirmation from ARCAM that it is the still applicable for the most recent version of machine, it is assumed that the equation is still applicable. Another function named the Thickness Function [Chapter3 3.2.6], which works in a similar way to the Thickness Focus function, but instead of adjusting the beam diameter, it modifies the beam speed. The Thickness Function should also be in-activate during this experiment as there is no overhanging structures in this build.

Equation 6.1

$$si = PF \times e^{(-S_1 \times (EF1 \times d - EF2 \times S_1))^2)}$$

Equation 6.2

$$S_2 = S_1 \times (1 + si)$$

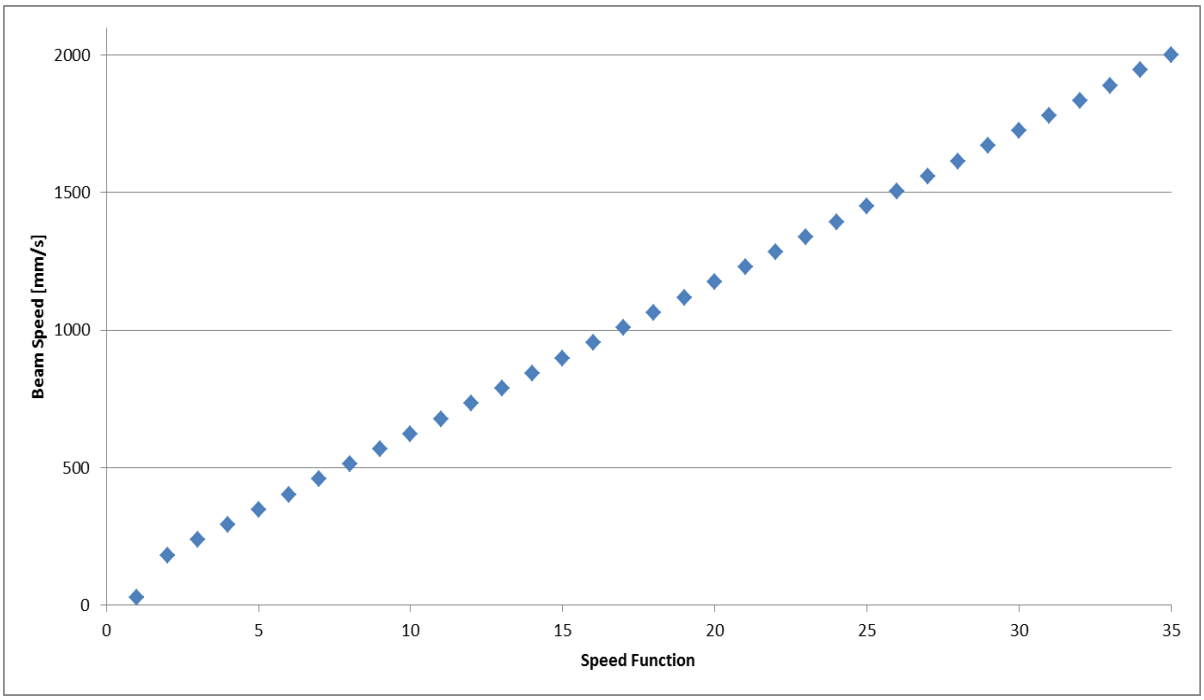

Figure 6.3 Beam speed vs Speed function with a beam current of 28mA

Table 6.1 shows the summarized parameter settings used for this experiment. There are three categories used in this experiment. Category 1 contains only Setting 0, which is the default parameter setting supplied with the Q20 Plus system by ARCAM. Category 2 is used to mimic

LOF formation, which includes only one Parameter Setting D with Line Offset value of 0.33mm. Category 3 is the fixing parameter sets used to rectify the induced defect by Parameter Setting D. This category contains 13 different parameter settings with one default parameter and 12 modified parameters with each parameter set having only one variable changed from the default setting.

Table 6.1 Parameter settings for closed loop control (blue text high-lights the modified variable).

Category	Parameter Settings ID	Line Offset (LO)/[mm]	Beam Diameter (D)/[mm]	Beam Speed (S)/[mm/s]
1	0	0.22	0.6	1945
2	D	**0.33**	0.6	1945
3	0	0.22	0.6	1945
	L1	**0.16**	0.6	1945
	L2	**0.11**	0.6	1945
	L3	**0.07**	0.6	1945
	L4	**0.03**	0.6	1945
	S1	0.22	0.6	**1449.3**
	S2	0.22	0.6	**1063.8**
	S3	0.22	0.6	**843.5**
	S4	0.22	0.6	**623.2**
	F1	0.22	**0.4**	1945
	F2	0.22	**0.23**	1945
	F3	0.22	**0.20**	1945
	F4	0.22	**0.18**	1945

6.1.3. Parameter Modification during the Process

The parameter modification is performed according to the diagram shown in Figure 6.4. To introduce the LOF formation like a real process, the parameter setting D is selected to print the test specimen for 16 to 17 layers. After the LOF has been introduced, the fixing parameters will be applied on the subsequent layer to rectify the introduced LOF. The test specimens in Group 2 will use one fixing parameter setting and test specimens in Group 3 will use a different one. This process will repeat itself until all the Parameter Settings in Category 3 have been carried out.

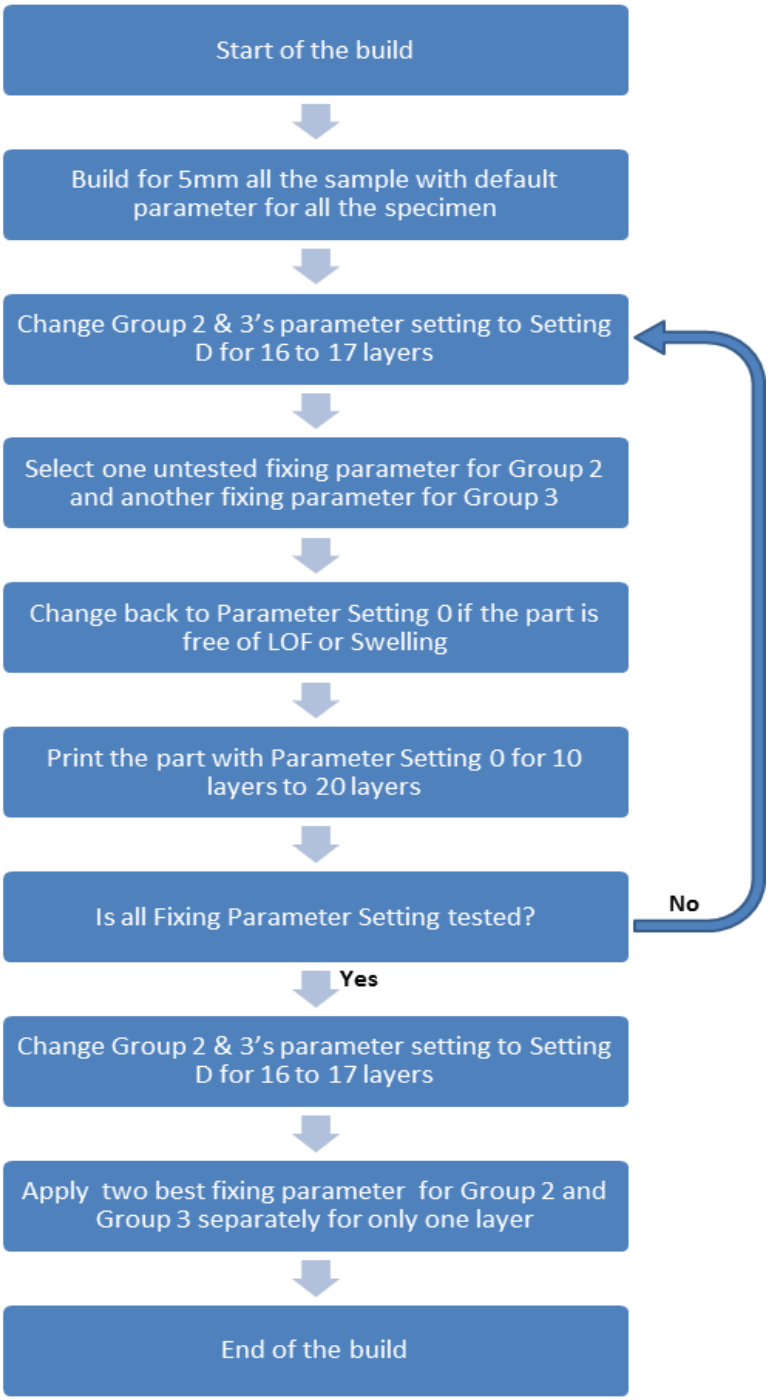

Figure 6.4 Process flow diagram for testing each Fixing parameter settings on the induced LOF

During the build, there are two scenarios that need to be looked at. The first one is whether all the LOF has been fixed, the second one is whether the part is swelling due to excessive energy. Although the LOF analysis will be performed at the end of the build, the software is not yet available to analyse the image when the build is running. Thus, all the LOF will be determined by inspecting the layer images manually and looking through the build chamber window.

Swelling in this study is defined as the edge of part elevated upwards due to a higher energy density beam being used. The consequence of swelling could very likely stop the build, thus parameters must return to the Parameter Setting 0 when swelling has been seen on the part. In this experiment, the number of layers where the fixing parameter has been applied is referred as the 'Fixing Layer Number'.

The current EBM system does not consist of any closed loop systems, thus all the parameter changes have to be performed manually during the process. As for the EBM control software version 5, there are few challenges that need to be noted when manually interrupting the process:

1. EBM control system always pre-calculates the melt information in advance (1 to 3 layers in general), thus a parameter modification during the process could not activated immediately but after one to four layers. However, if the process has been paused and restarted, the modified parameters will start on the current layer.

2. Any layer of an EBM build can be summarized into four stages: powder raking, preheat, melt and post heat. After the EBM print has paused, once the build has restarted, the process will be back to the first stage of the current layer regardless what stage is on. As in this case it is the powder raking stage.

In order to overcome the above challenges, the following method is adopted which is described in Figure 6.5. From Figure 6.5, Layer N represents the current layer, and Layer N-1 indicates one layer before Layer N. The parameter modification for the current layer (Layer N) is carried out at previous layer (Layer N-1), as EBM control has already planned the Layer N-1's melting strategy, the actual parameters should be un-affected before Layer N-1 has ended. As Layer N starts, the process is paused and restarted when the rake has just started to move. By doing this, the machine restarts the raking procedure, and the modified parameter should be activated for

Layer N. The drawback of doing this is losing approximately one second of the process time, which is considered to be negligible in this study.

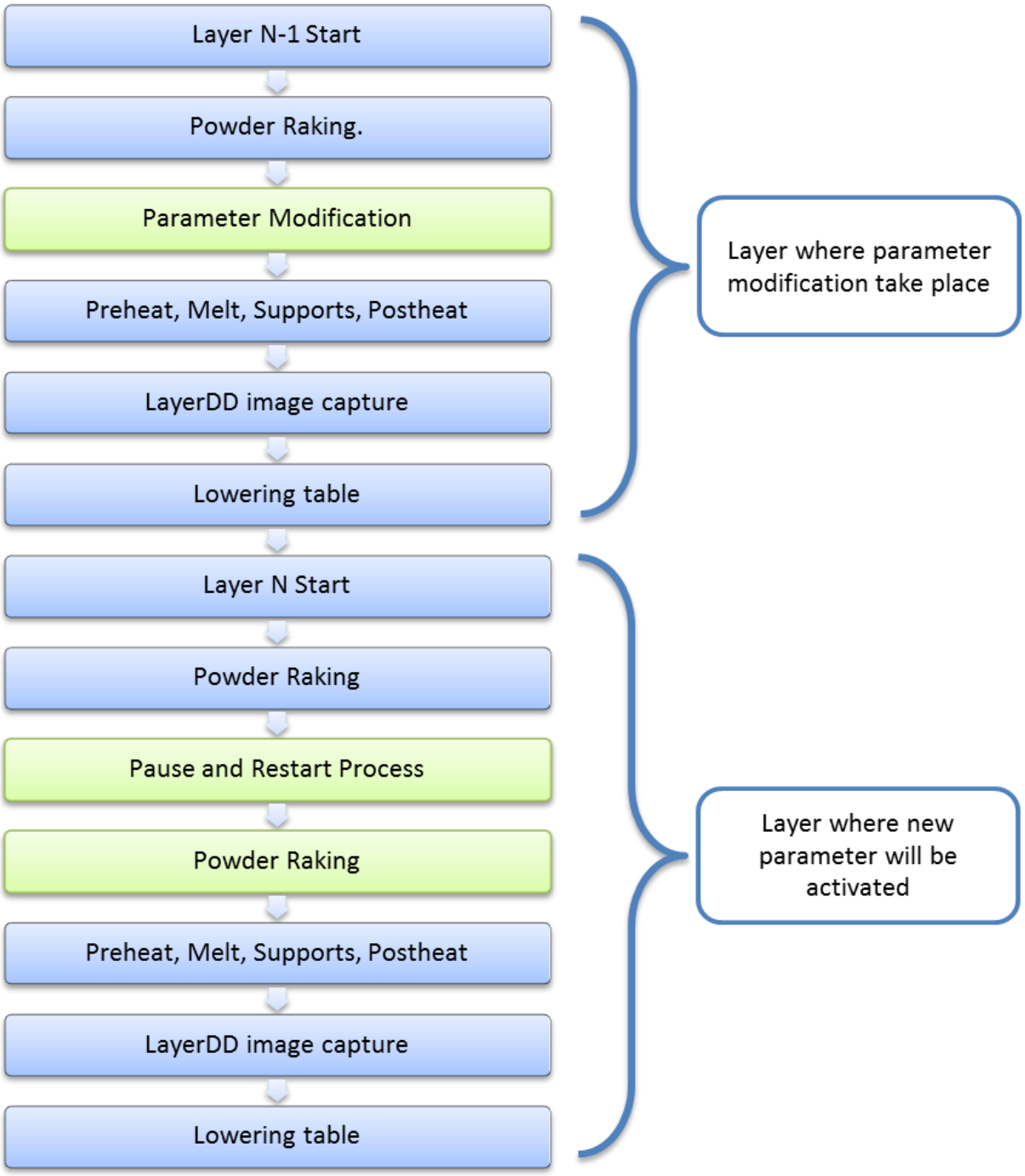

Figure 6.5 Flow diagram of how to modify machine parameters during the process with least amount of influence.

6.1.4. Energy Density Ratio

The expression of Energy Density (ED) for the EBM process is shown in Equation 6.3, where V is the accelerating voltage, LO is the line offset, LT is layer thickness, and S is beam speed.

Equation 6.3

$$ED = {}^{V \times I}/_{LO \times LT \times S}$$

The ARCAM Q20 Plus system have so many built-in function which are not open in the public domain. As a result, for this experiment the Logfile Reader is used to analyse the energy density through the build, the detail description of Logfile Reader is states in Chapter3 3.5.1.

Figure 6.6 shows the energy density for Control Group 1 produced by the Logfile Reader. From the graph it shows that, the energy density between each layer has large fluctuations from 60 J/mm^3 to 100 J/mm^3, it is believed this is mainly due to the hatching orientation being different for each layer. The Q series EBM machine's default setting is to rotate the hatching 67 degrees per layer, thus the distribution of Scanlength for each layer is very different. Although beam speed is not affected by the Scanlength anymore, functions such as Turning Function and Line Offset Compensation can still influence the overall energy input.

In order to easily understand the effect of changing each parameter, the expression of the Energy Density Ratio (EDR) is used. The EDR is defined as a percentage energy density of the experimental group to the control Group 1. As the specimens in each group have an identical cross section, the hatching strategy should also be the same. Although each layer is rotated by a different angle, within the layer, all specimens are printed with exactly the same angle. Thus, the energy density in Group 1 (the control group with default theme) should also be the energy density value for any other group if the parameters are un-modified. By taking the ratio between any groups to Group 1, the value should be least affected by the hatching angle. An example

of EDR graph for Group 2 is shown in Figure 6.7. As what can be seen from the graph, the normal print has EDR of 100% and the EDR for creating LOF is between 60 to 70%.

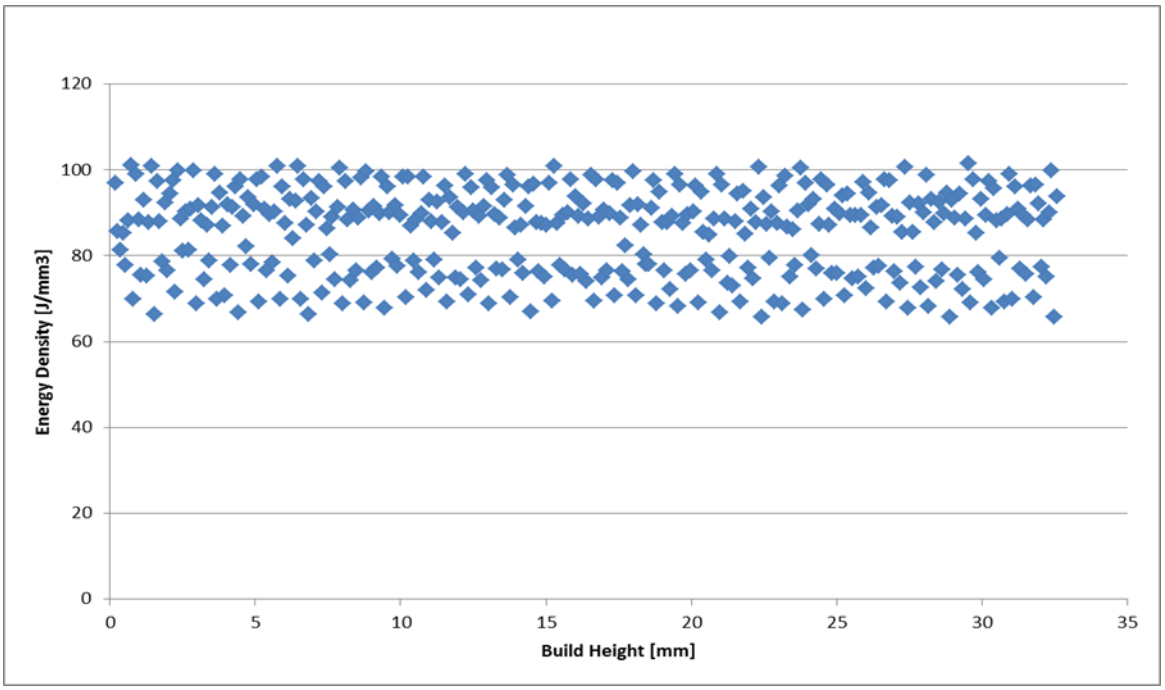

Figure 6.6 Energy Density of Group 1 through the build

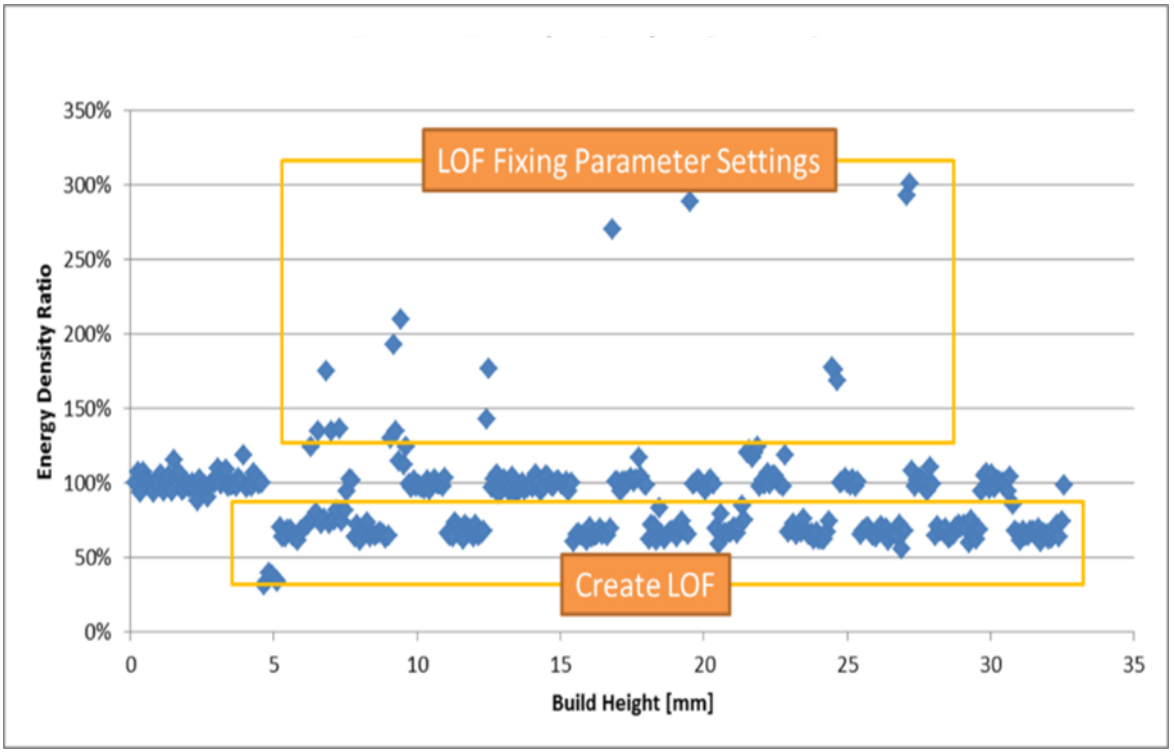

Figure 6.7 Example of Energy Density Ratio for Group 2.

6.1.5. Defect Analysis

In this experiment, LayerDD is used to analyse the amount of LOF for each layer after the build has completed. The LayerDD is used with a 0.037 threshold setting and with one layer penetration only. In addition, LOFs are divided into two categories: new LOF and tunnelled LOF from the previous layer.

New LOF is any newly formed LOF where no LOF is present in the similar location from the previous layer. Tunnelled LOF is the LOF in this layer which is the consequence of the last layer's LOF in the similar location. A schematic diagram of tunnelled LOF and New LOF is shown in Figure 6.8.

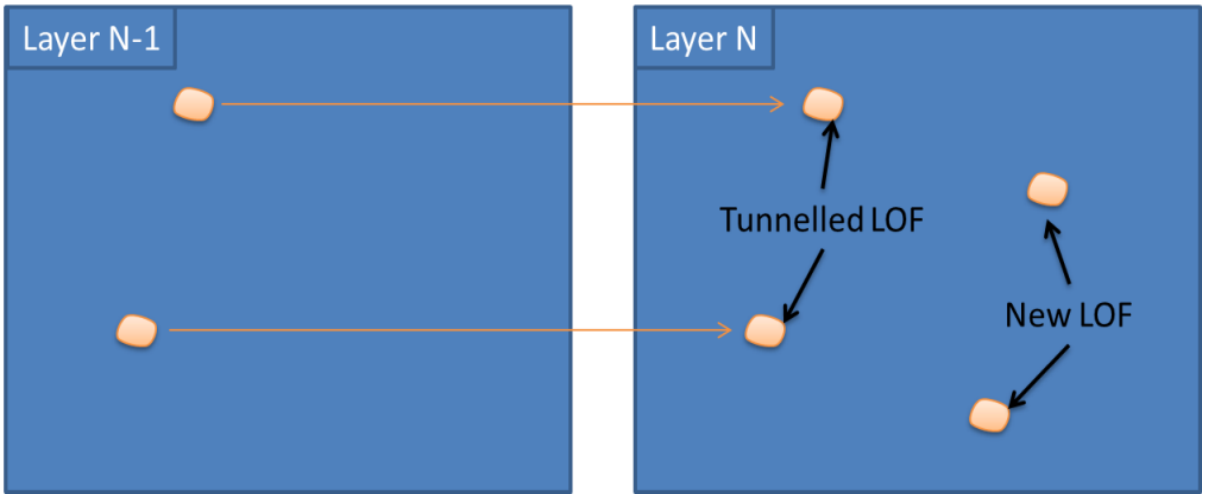

Figure 6.8 Diagram of New LOF and Tunnelled LOF

6.1.6. Top Surface Analysis

The top surface quality is one of the most important factors causing LOF initiation, so it is necessary to analyse the top surface quality created by the fixing parameter. In an EBM build, any single layer in a melt group can be applied with one parameter only. As there are three melt groups in this experiment, and one of them is used as control, which left with two melt groups can be can be used for testing top surface quality.

the end of the build, the defect are induced in a similar way as before, and two most effective fixing parameter settings are selected to rectified the defect for one layer only and then the whole build will be stopped. In this way, the fixing parameter is performed on the last layer of the build, and the effect of fixing parameter on top surface quality can be studied. The surface roughness of the top surface is studied using an Alicona Infinity Focus machine, according to ISO4288 standard. The direction of roughness measurement is parallel and perpendicular to the hatching direction.

Furthermore, the samples will be section cut along the vertical direction using an EDM machine at the location where most LOF has occurred. The section will be viewed under a microscope to investigate whether the fixing parameters have rectified the underneath layer's LOF. To assess the effectiveness of the fixing parameters, Defect Fixing Depth (DFD) is used. DFD is defined as the distance between the tips of LOF boundaries to the top of the surface as the example shown in Figure 6.9.

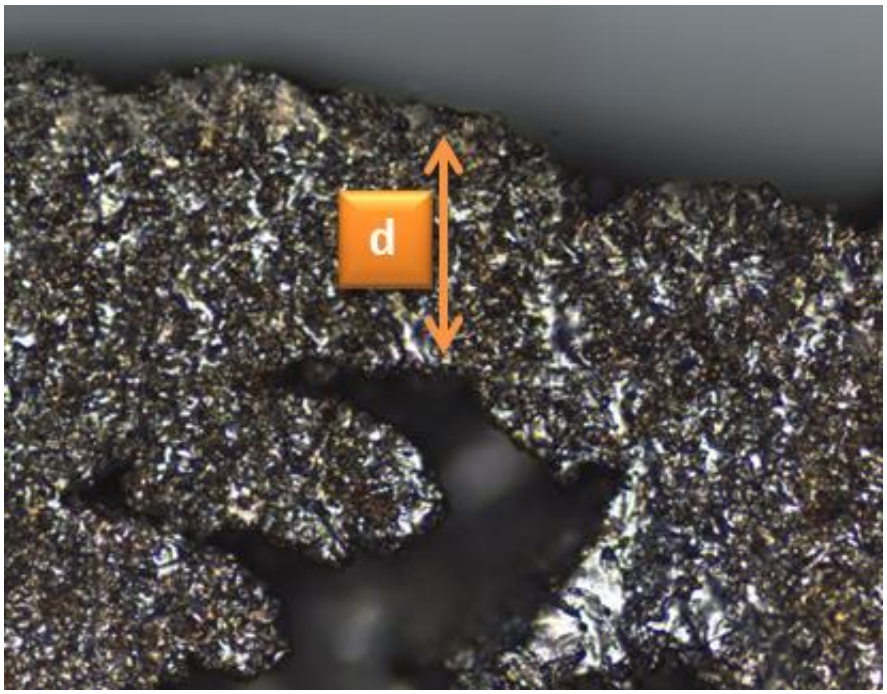

Figure 6.9 DFD: distance between the tips of LOF to the top surface.

6.2. Results

6.2.1. Introducing LOF

Figure 6.10 shows an example of 3D defect model given by LayerDD system. The locations of defects are more likely to be clustered around the edge rather than at the centre of the part. Figure 6.11 shows the number of LOFs developed from the start of parameter setting D until the fixing parameters are applied. From the graph, it can be seen that the introduced LOF number increases as the number of layer increase. However, it is also noticed there is the occasional decrease (dip in the line) in LOF numbers along the upward trend. The decrease in the number of defects could be due to two scenarios, the first scenario is that two nearby LOFs merge into one bigger one, and the second scenario is some of the small LOFs could randomly stop from propagation. As for the control specimen 1A and 1B, there is no LOF detected by LayerDD system.

As the defect seeding is through parameter modification, the number of LOFs introduced is not consistent with each other, and this can be also seen from Figure 6.11. Thus in order to have a standard comparison between the different fixing parameters, the amount of defects in each layer when the fixing parameter applied is expressed as a percentage of Defect Remaining (DR) shown in the following equation, where D_c is the number of LOF in the current layer and D_i is total number of defects introduced to the layer part before the fixing parameter is used.

Equation 6.4

$$DR = {}^{D_c}/_{D_i} \times 100\%$$

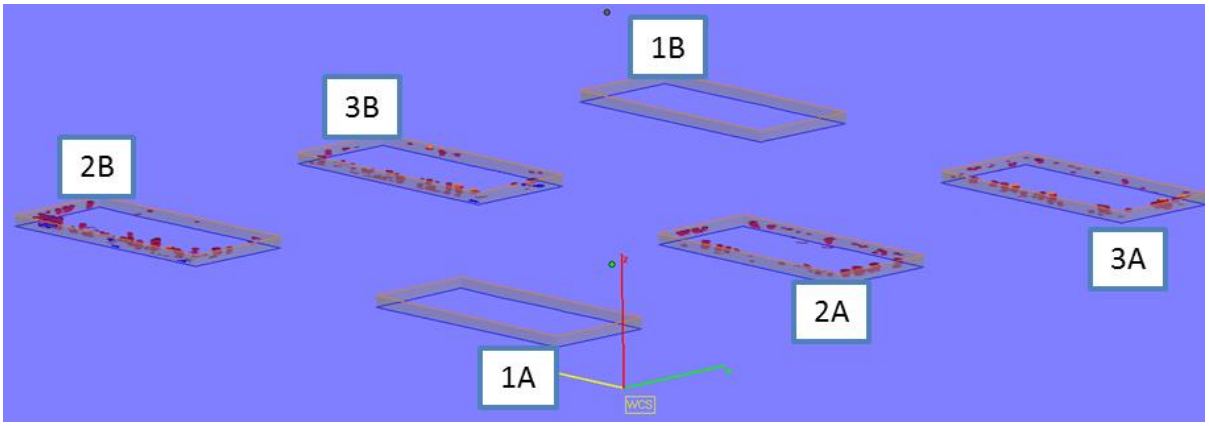

Figure 6.10 predicted LOF from LayerDD

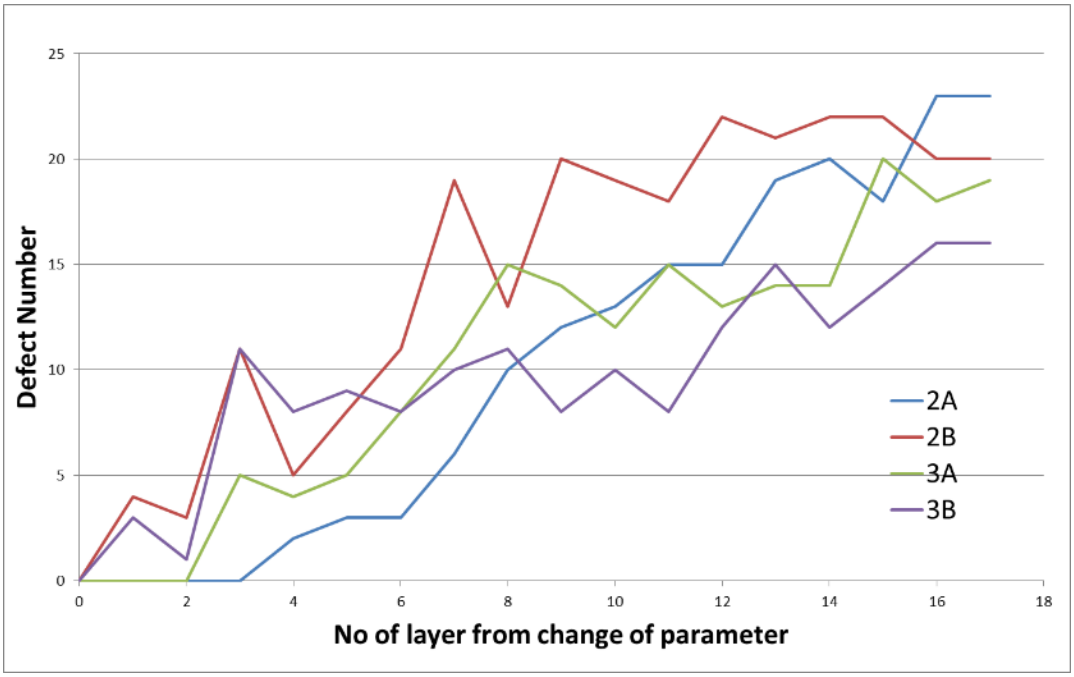

Figure 6.11 Number of LOF developed for the result shown in Figure 6.10

6.2.2. Effect of Reducing Line Offset

From Figure 6.12, it can be seen that all LO fixing settings reduce the number of LOF when the parameter has changed, however none of the parameter settings are capable of fixing the defect within a layer. In addition, when the Line offset is changed to less than 0.11mm, part swelling is observed before all the LOF has been rectified.

In addition, from Table 6.2, It is worth mentioning that, the EDR acquired by the equation and Logfile reader value is highly inconsistent especially when the LO value is very low.

Table 6.2 Results for the fixing parameters setting with modified Line Offset

Setting	LO [mm]	EDR from equation	EDR from LogFile reader	Fixing Layer Number	LOF disappear at layer:	Swelling
0	0.22	1	1	18	18	No
L1	0.16	1.38	1.24	15	15	No
L2	0.11	2	1.45	5	5	Yes
L3	0.07	3.14	2.47	2	7	Yes
L4	0.03	7.33	2.89	1	4	Yes

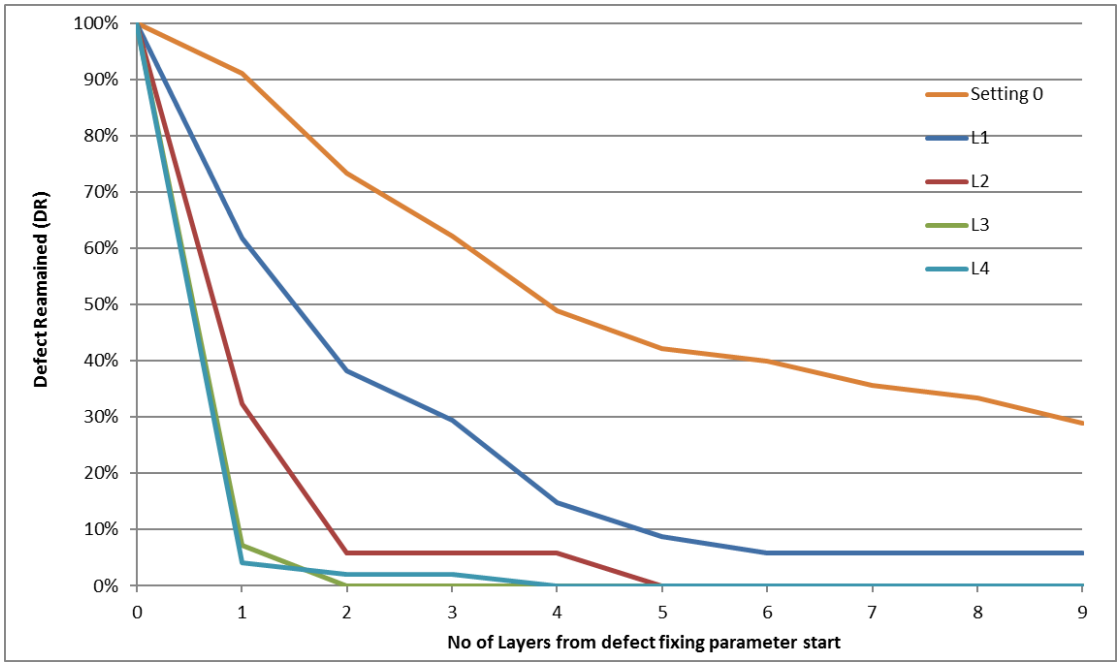

Figure 6.12 Effect of changing Line Offset value on LOF fixing

6.2.3. Effect of Reducing Beam Speed

Table 6.3 shows the summary of the fixing parameters by reducing the beam speed. In the new Q series machine, the beam current is kept constant at 28mA through the entire hatching process. Thus, the beam speed can be easily found from a supplied look up table of Beam Speed vs. Current. With beam current and beam speed known, the Energy Density ratio (EDR) can be calculated using the equation of energy density. From Table 6.3, the value of EDR shows good consistency between theory value and Logfile Reader value.

From the results shown in Figure 6.13, both parameter settings of S3 and S4 has successfully removed all the LOF. Parameter setting S4 has caused some minor swelling to the part which

can be seen from the chamber window. In addition, from the LOF analysis, it shows fixing parameter S4 has regenerated significant amount of LOF after the LOF has been rectified.

Table 6.3 Results for the fixing parameter settings with reduced beam speed (green highlights the parameters that have removed all LOF within one layer)

Setting	Beam Speed [mm/s]	EDR from equation	EDR from Log file reader	Fixing Layer Number	LOF disappear at layer:	Swelling
0	1945	1	1	18	18	No
S1	1449.3	1.35	1.33	4	4	No
S2	1063.8	1.71	1.74	2	2	no
S3	843.5	2.33	2.28	1	1	no
S4	623.2	3.12	2.97	2	1	Yes

By reviewing the raw LayerDD images, the images for fixing parameter settings S3 and S4 are shown in Figure 6.14 and Figure 6.15. It can be seen from the images, both fixing parameters have stopped the LOF from propagating, but defects have regenerated in S4 which is shown as the high peak indicated in the graph of Figure 6.13.

By inspecting the Log file after the build, it seems that parameter setting S4 had been mistakenly activated for two layers, which could be the key reason for the LOF regeneration.

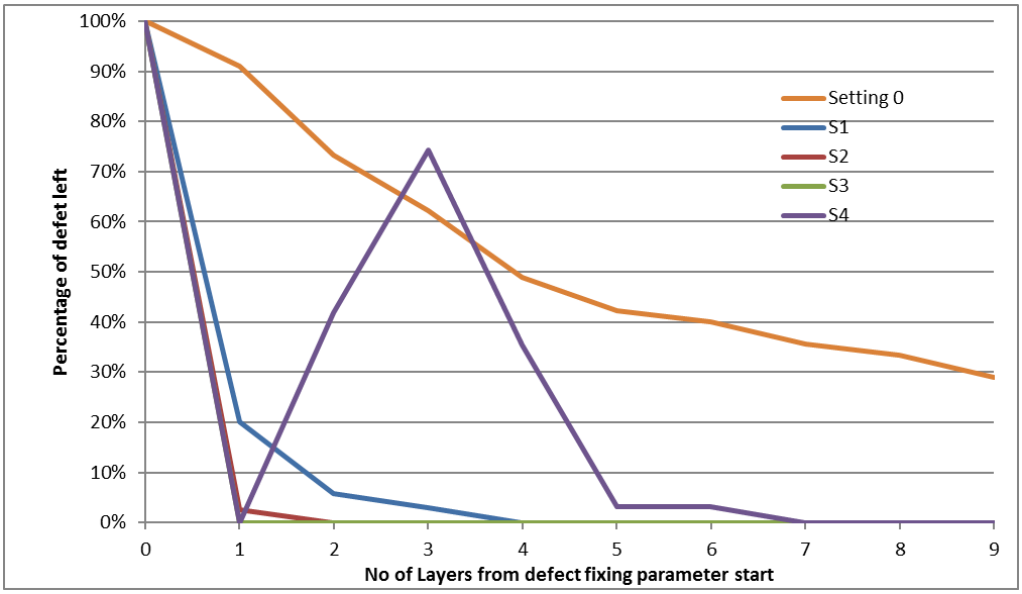

Figure 6.13 Effect of reducing beam speed on LOF fixing

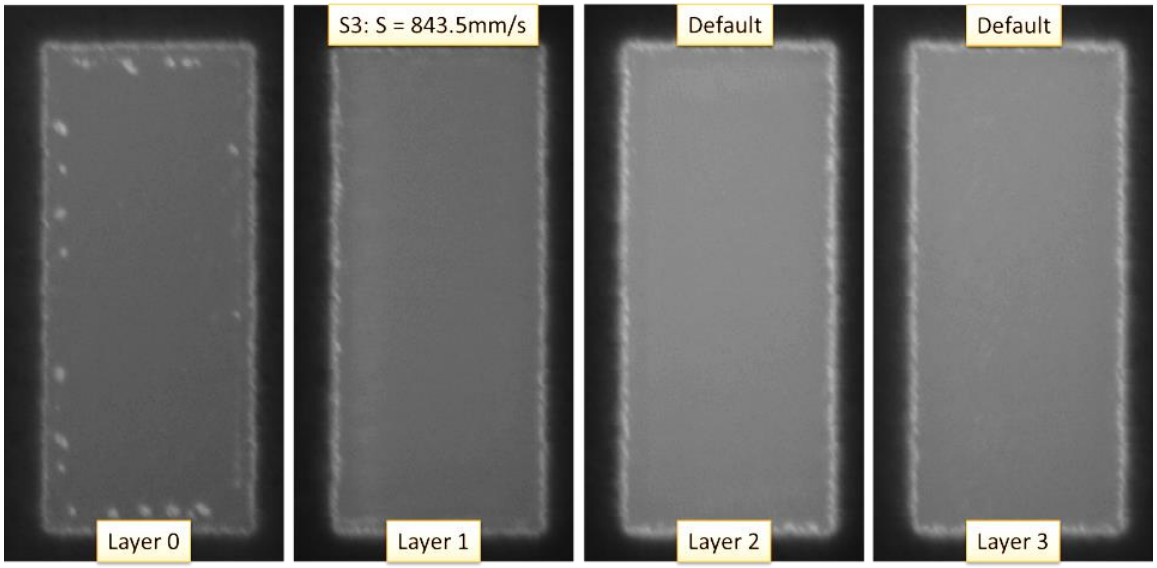

Figure 6.14 Smooth top surface under LayerDD after the LOF is fixed with S3 (In order to see a better image quality, the contrast has increased in these images)

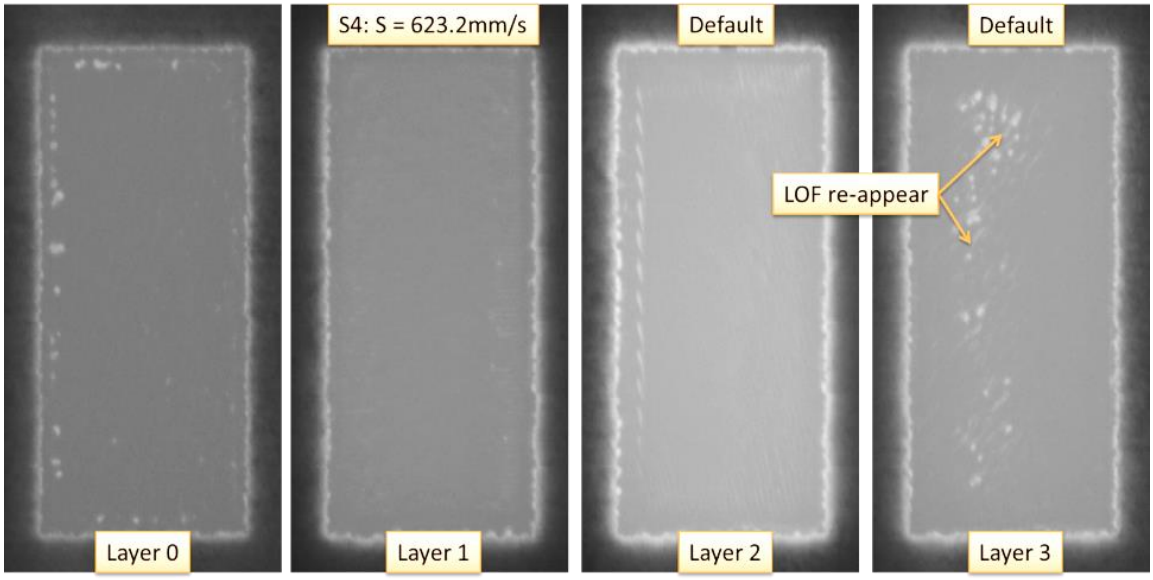

Figure 6.15 LOF re-appear after the original LOF has been fixed S4 (In order to see a better image quality, the contrast has increased in these images)

6.2.4. Effect of Using Highly Focused Beam

As described by the Energy Density equation in Equation 6.3, change beam diameter does not actually have any influence on the overall energy density, but it changes the energy distribution of the beam.

As indicated in Table 6.4, none of the parameter sets caused the part to swell, and the fixing parameter set with beam diameter 0.18 mm (F4) has fixed the LOF within one layer. In

addition, during the process, it is noted that there is extra spatter formation associated with fixing parameter F4.

Similar to fixing parameter S4, regeneration of LOF is also been found with fixing parameter F4. Figure 6.17 shows the LayerDD image for fixing parameter F4, it can be seen the image brightness is not very consistent through the part's surface, which is potentially indicating some high surface roughness. The result of the high surface roughness can eventually develop into some minor LOF on the following layers.

Table 6.4 Results for fixing parameters settings with modified beam diameter (green highlights the parameters that have removed all LOF within one layer)

Setting	D [mm]	EDR from equation	EDR from Log file reader	Fixing Layer Number	LOF disappear at layer:	Swelling
0	0.6	1	1	18	No	No
F1	0.4	1	1.01	7	6	No
F2	0.23	1	1.04	3	2	no
F3	0.20	1	0.99	3	2	no
F4	0.18	1	1	1	1	no

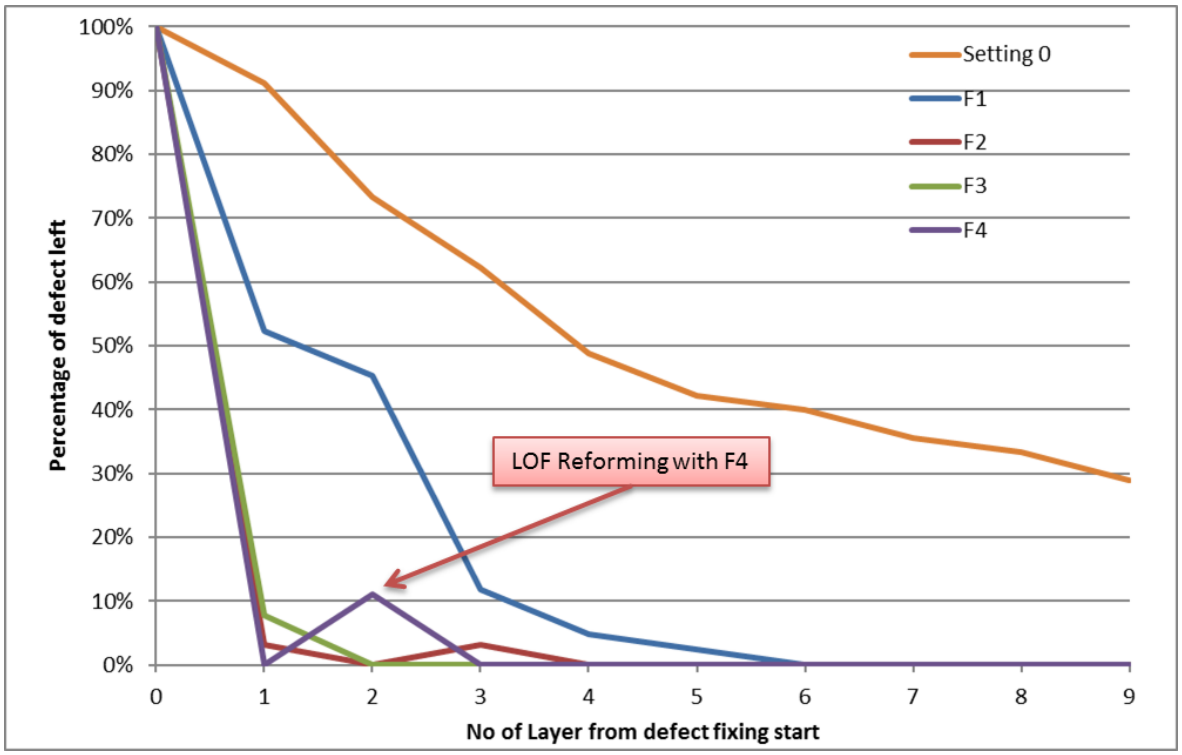

Figure 6.16 Effect of reducing beam diameter on LOF fixing

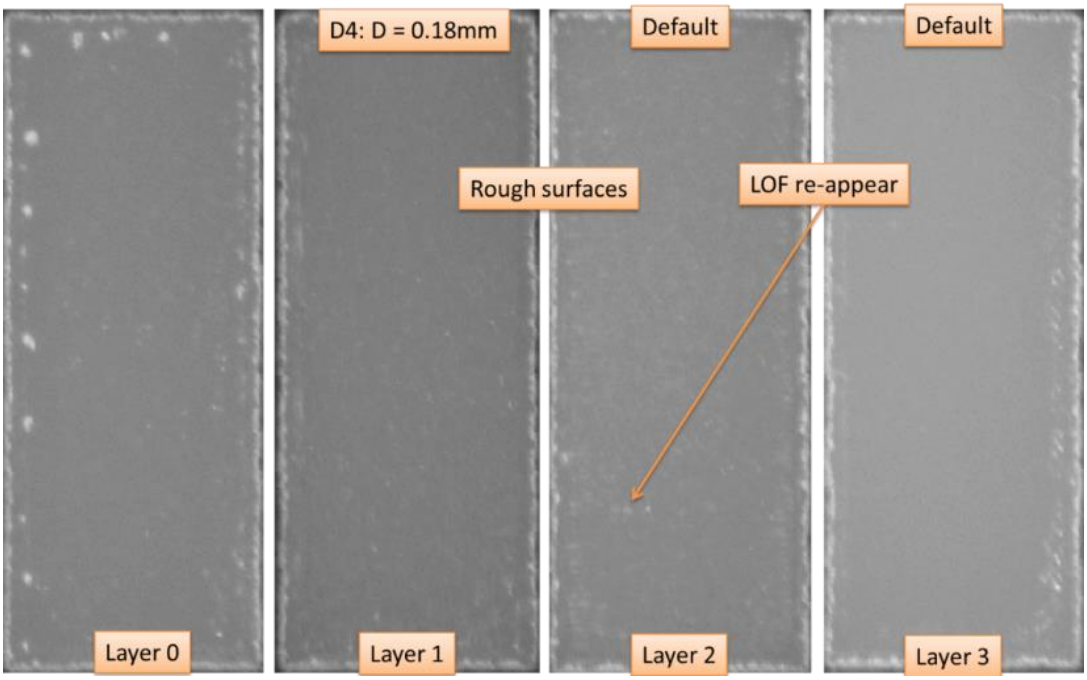

Figure 6.17 Un-even surface after fixing parameter with beam diameter 0.18 (In order to see a better image quality, contrast have increased in these images)

6.2.5. Results of Fixing Parameters S3 & F4 on Top Surface

Two fixing parameters are required to be selected to print the last layer of two experimental melt groups. By analys the effectiveness for each parameter settings, the best fixing parameter seems to be S3.

The other two fixing parameters which also gives one layer defect rectification are S4 and F4, but both fixing parameters have a negative impact on the top surface quality. Since S3 is already selected for one melt group, then investigation on the effect of reducing beam diameter (F4) could be more beneficial.

The last layer for each group is shown in Figure 6.18. From the overall view on the three samples, the surface finish of fixing parameter S3 is very similar to the control sample, which are smooth with the melt tracks slightly visible. In contrast, the surface of fixing parameter F4 appears much worse with many dimples all over the layer. By comparing the roughness value in Figure 6.18b, the results indicate the roughness value of the fixing parameter F4 is much

worse than the control sample. On the other hand, fixing parameter S3 has slightly better surface roughness than the control sample.

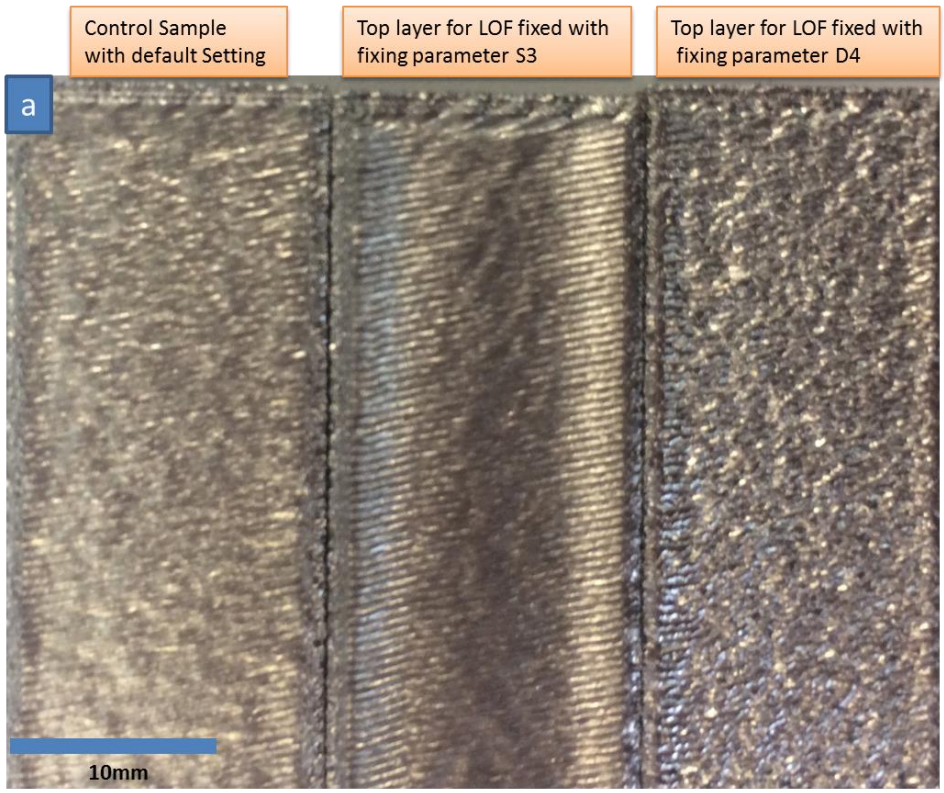

	Ra [µm]	Rz [µm]
L1	4.47	35.45
L2	2.56	25.29

	Ra [µm]	Rz [µm]
L3	3.21	25.93
L4	3.04	22.61

	Ra [µm]	Rz [µm]
L5	14.83	68.57
L6	5.26	35.17

Figure 6.18 [a] Image of top surface taken by a normal camera [b] surface roughness measurement taken at parallel and perpendicular to the hatching direction

After cutting the sample along the vertical cross-section which shown in Figure 6.19, the LOF can be seen very clearly under the microscope. As expected, none of the LOF has tunnelled upwards to the surface for both of the fixing parameter settings. By using the results from LayerDD, it can be found where defect is presented at the previous layer.

From the image shown in Figure 6.19, all the tunnelled LOF is identified and the value of Defect Fixing Depth (DFD) measured. Among each of fixing parameters, the distribution of DFD seems to have great variation, this is mainly a result of not being able to guarantee the cutting plane is at the tip location for all the LOF or the melt pool has inconsistent melt depth. It can be seen from the measured result, the smallest DFD in S3 is 483µm and the smallest DFD in F4 is 249 µm. This further indicates that the fixing parameter setting S3 is more likely to fix underneath LOF than fixing parameter setting F4.

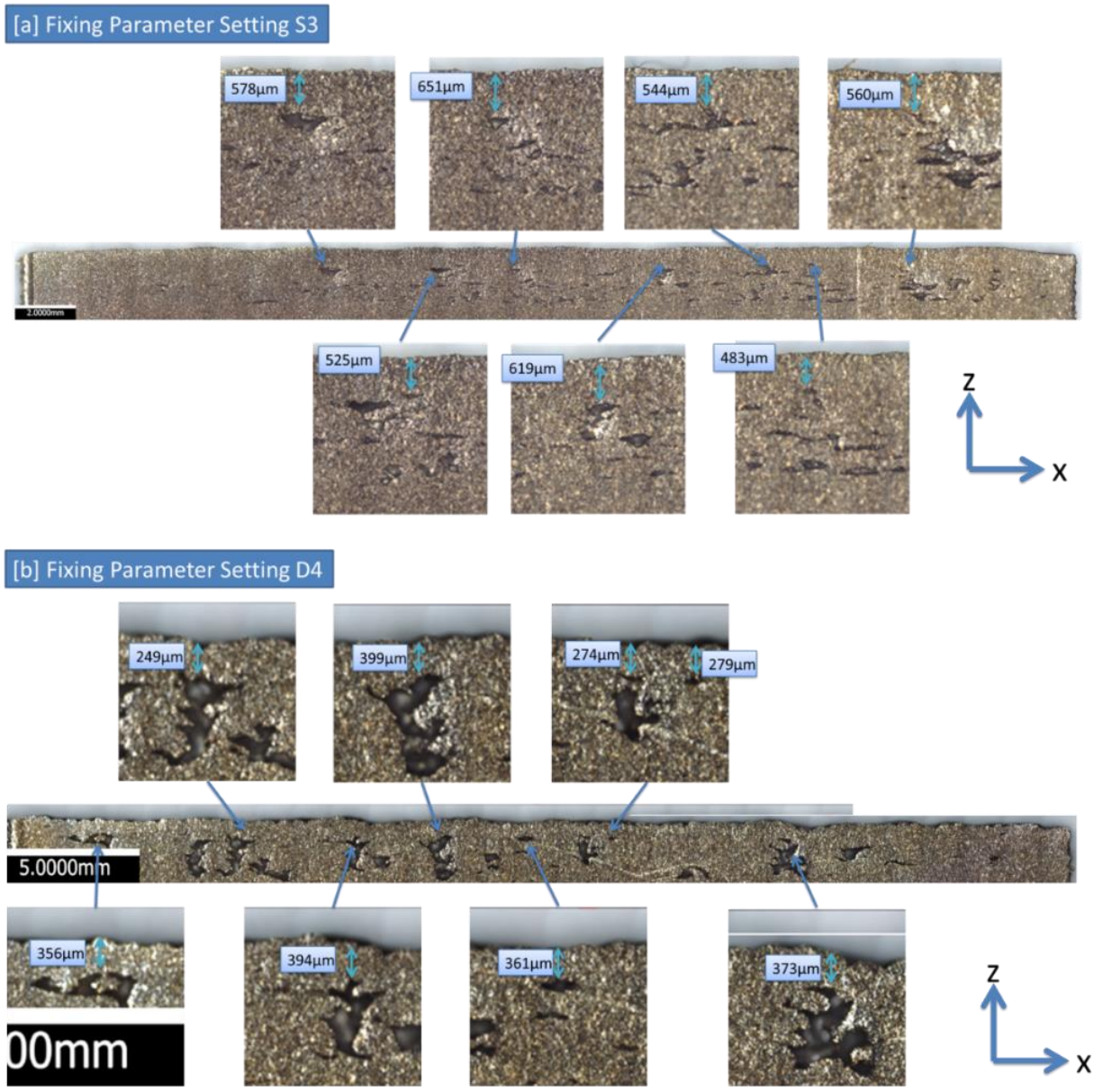

Figure 6.19 vertical cross-section viewed at the top of specimen, where the depth of melt pool penetration of each parameter can be measured.

6.2.6. Results Summary

Equation 6.5Equation 6.5

$$DRP = {\sum_{i=2}^{i=n+1} \frac{D_i}{D_{i-1}} \times 100\%}\Big/{n}$$

Table 6.5 Summary of defect fixing parameters (green highlights the successful removal LOF parameters, red indicates the fixing parameter which are regenerating LOF)

Parameter Settings ID	Line Offset (LO)/[mm]	Beam Diameter (D)/[mm]	Beam Speed (S)/[mm/s]	EDR	Defect Removal Probability per layer
0	0.22	0.6	1945	1.00	10±5%
L1	**0.16**	0.6	1945	1.24	33±9%
L2	**0.11**	0.6	1945	1.45	65±7%
L3	**0.07**	0.6	1945	2.47	93±3%
L4	**0.03**	0.6	1945	2.89	96±3%
S1	0.22	0.6	**1449.3**	1.33	80±2%
S2	0.22	0.6	**1063.8**	1.74	97±3%
S3	0.22	0.6	**843.5**	2.28	100%
F1	0.22	**0.4**	1945	1.01	50±8%
F2	0.22	**0.23**	1945	1.04	96±3%
F3	0.22	**0.20**	1945	0.99	95±4%

Equation 6.5From the table, it can be seen that, LOF produced during the process can be better fixed by modifying the parameters to increase the energy density (in this case reducing the beam speed) or reducing the beam diameter to increase the focus. In order to stop LOF from propagating when using the Q20 system, fixing parameter settings S3, S4 and F4 can be used. Unfortunately, fixing parameter settings S4 and F4 seems to have re-created LOF due to the increase in roughness of the top surfaces.

By comparing the top surface and DFD values between fixing parameter settings S3 and F4, the surface of fixing parameter S3 is significantly smoother and the melt pool penetration seems much deeper, as a result fixing parameter S3 is the favoured parameter setting for defect rectification.

To illustrate the key effect of a good fixing parameter setting, Figure 6.20 shows an example of the difference between the effect of the default parameters setting and the newly developed parameter setting S3 on the existing LOF.

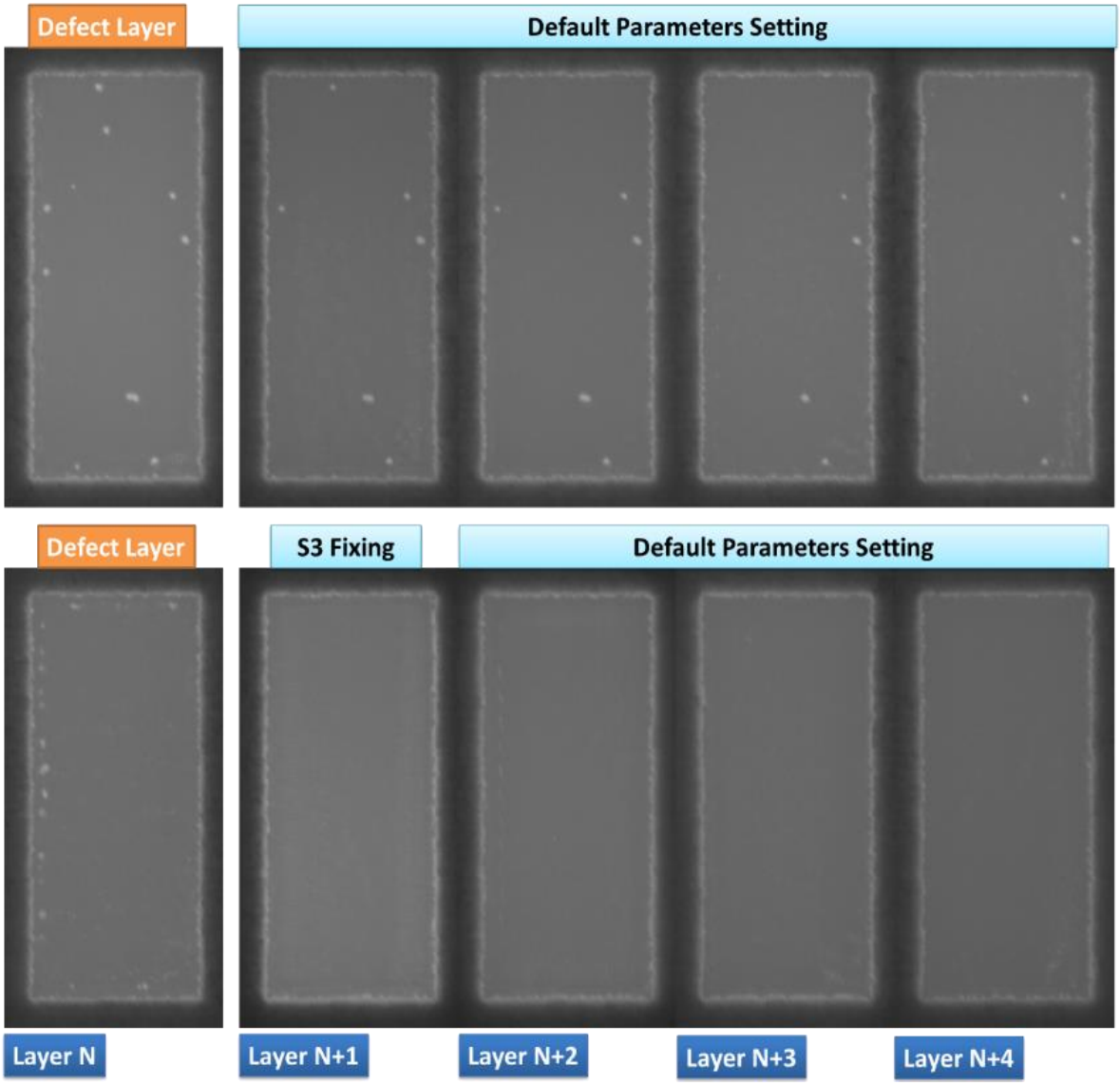

Figure 6.20 LayerDD images illustrating the advantage of the newly developed fixing parameter compared to default parameter settings, where the newly fixing parameter is capable of removing defects within a layer and create high quality top surfaces.

6.3. Discussion

6.3.1 Actual Line Offset

As you can see from the results section, there is disagreement between the predicted energy density and the energy density value from the Log File Reader, and this could be the result of Line Offset compensation. By investigating further into the Logfile, there is another section recording the number of scan lines in each layer and each melt group, as shown in Figure 6.21.

As mentioned in the Methodology Section [Chapter3 3.5.1], the Scanlength Histogram is recording the distribution of Scanlength in each layer, thus the total number of scan melt tracks is the sum of number in Scanlength distribution.

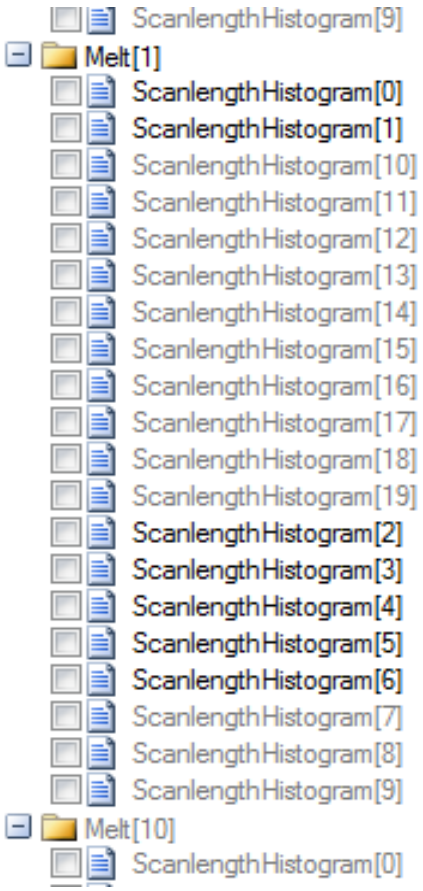

Figure 6.21 Scanlength Histogram in ARCAM EBM's log file

When the Line Offset value is changed, the corresponding number of hatching lines should change also, this gives an estimation of the energy density ratio (EDR). For example, if the number of hatching line is doubled, the indicated overall energy density should be also double.

In Table 6.6, three EDR values are predicted by the different methods are presented: EDR from energy density equation, EDR from the LogFile Reader and EDR predicted from the number of hatching lines. The result indicates that the EDR are consistent with each other when the line offset value is high. However, as the Line Offset value is reduced, the EDR from the equation appears to be different from the other two values.Due to existence of many unknown functions within the EBM system, the probability of the line offset being automatically modified is very high. Thus, in this experiment, it is assumed that, the input value for line offset does not represent the actual line offset value, the actual line offset will be calculated from the EDR acquired from LogFile Reader and the reference Line Offset value of 0.22mm by using the following Equation 6.6.

Equation 6.6

$$Actual\ LO = \frac{0.22}{ED\ Ratio\ from\ LogFile\ Reader}$$

Table 6.6 EDR acquired by different method, 0.22mm is the default Line Offset

LO [mm]	EDR from equation	EDR from LogFile Reader	EDR from Scanlength Distribution	Actual LO [mm]
0.33	0.66	0.68	0.68	0.32
0.22	1	1	1	0.22
0.16	1.375	1.24	1.28	0.18
0.11	2	1.45	1.42	0.15
0.07	3.14	2.47	1.53	0.09
0.03	7.333333333	3	2.9	0.07

LRP normalize

When beam speed and beam diameter parameter are changed, the total number of hatching lines should remain constant, but when the line offset values is modified, the total number of hatching lines will be changed also. As a consequence, the frequency of the beam striking the LOF is changed. For example, when the line offset is half that of the default value, the number of hatching lines is doubled, which is similar to the frequency of melting the layer twice. In order to better understand the effect of the melt pool on the LOF removal probability (LRP), the LRP should be free from the influence of hatching frequency. Thus, to normalize the LRP, following equation is used.

Equation 6.7

$$LRP = 1 - (1 - LRP)^{1/FR}$$

Where the *LRP* is the LOF removal Probability in Equation 6.5Equation 6.5

$$DRP = {\sum_{i=2}^{i=n+1} \frac{D_i}{D_{i-1}} \times 100\%} \Big/ {n}$$

Table 6.5, FR is the ratio of number of hatching lines of the fix parameter to the default parameter, which is represented by the energy density ratio calculated from log file.

6.3.2 Thermal Model of Melt Tracks

As a general overview on the graph in Figure 6.22, increasing in the energy density will improve the chance of fixing the LOF, but the plotted lines in the graph for line offset and speed are very different. By comparing the defect removal probability in Figure 6.22, the result strongly favours the parameter settings with lower beam speed. In addition, the variation in focus offset has no influence on the value of energy density, but also removes LOF better than using narrower line offset. All the above observations obviously indicate that energy density by itself is not an ideal indicator to estimates the probability of LOF removal.

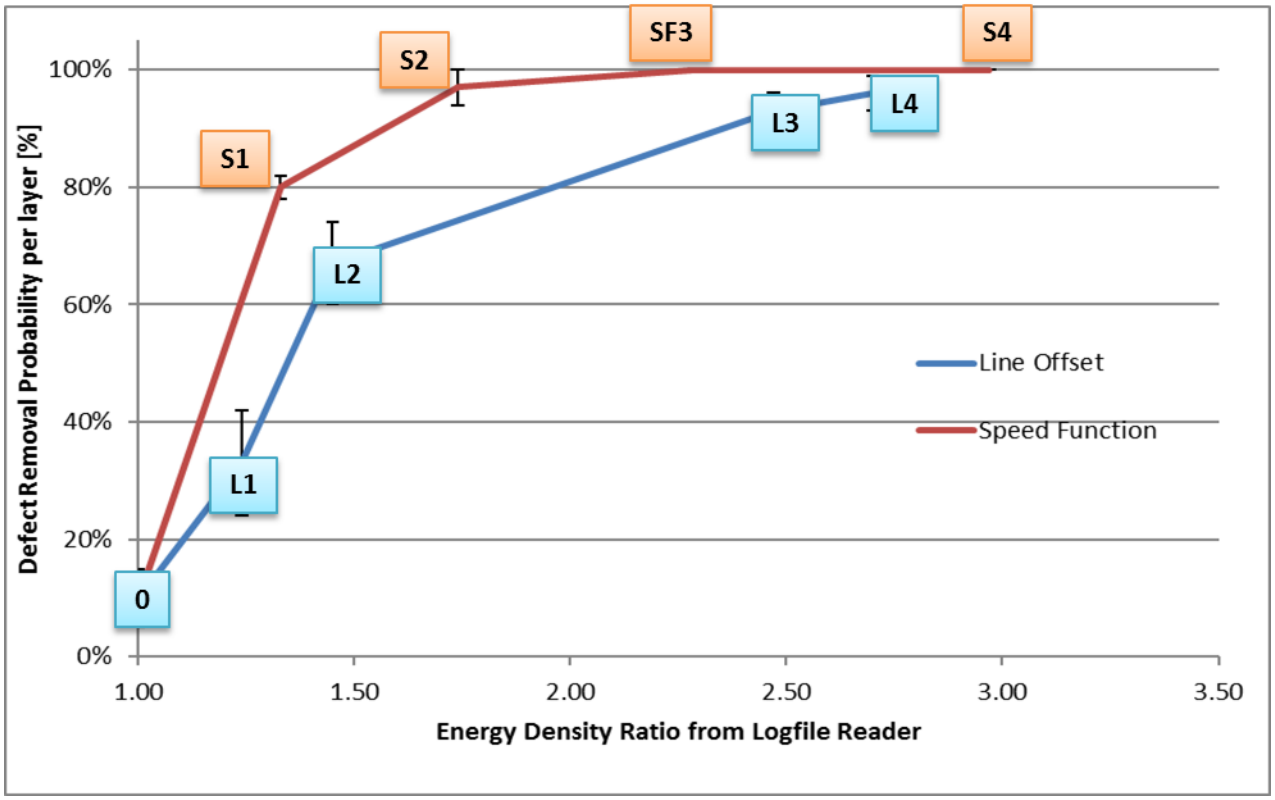

Figure 6.22 defect removal probability vs energy density ratio for different fixing parameter with different Line Offset (LO) and beam speed

To further understand the effect of changing parameters on the ability of LOF fixing, a thermal model was performed on all the parameters settings used in this experiment. The detail of the thermal calculation of the model is explained in Methodology Chapter [Chapter3 3.5.2].

The simulation conditions are as shown in Figure 6.23 and Figure 6.24. A solid rectangle 3mm wide by 60mm length by 2mm depth is pre-set in the model. The solid is surrounded by 1.5mm width of powder. A single layer of powder with a thickness of 90µm is applied on top. The hatching strategy will be a 'zigzag' pattern with the Turning Function activated. The simulation takes account of all the melt tracks until the melt profile is finished.

The turning function is described in the literature review section, which is an ARCAM design function to increase the beam speed at the turning point to compensate for the heat from adjacent beam. The Equation 6.8 and Equation 6.9 are given by ARCAM and shown as follow.

The predefined variable in the equation are set with $PF = 0.9$, $EF1 = 0.00025$ and $EF2 = 0$ (ARCAM Q20 Plus default setting).

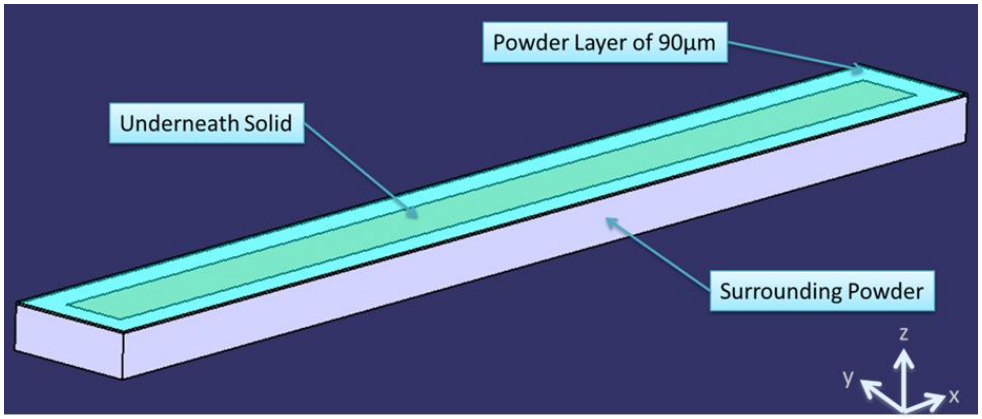

Figure 6.23 Simulation of melt profile with 90µm of powder on top of the solid

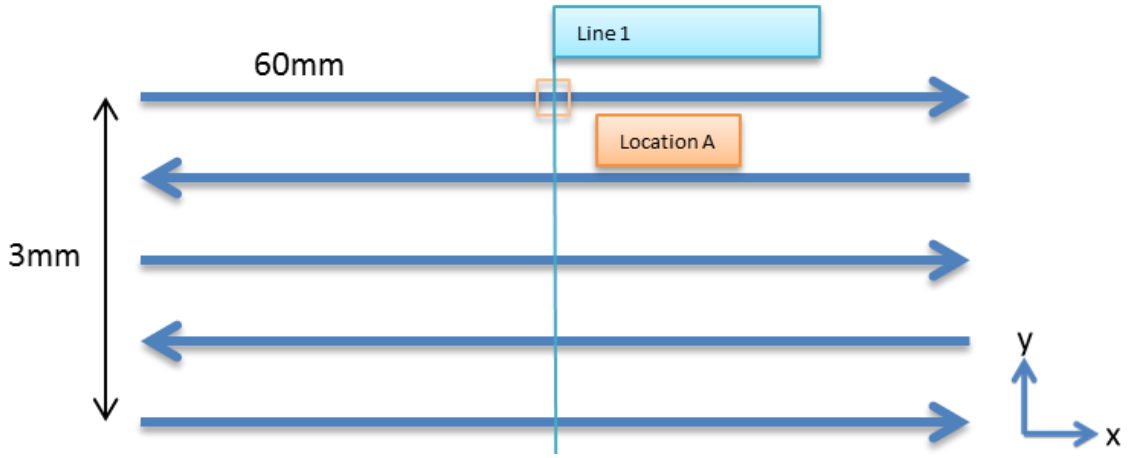

Figure 6.24 Schematic showing the simulation of Figure 6.23. The melt profile is 3mm×60mm and the hatching strategy is in zig-zag mode.

Equation 6.8

$$si = PF \times e^{(-S_1 \times (EF1 \times d - EF2 \times S_2))^2)}$$

Equation 6.9

$$S_2 = S_1 \times (1 + si)$$

During the simulation, multiple melt tracks are simulated rather than single track simulation described in many literature reviews. The reason to consider a multi melt track is to account

for the effect of previous heated melt tracks as they can possess residual heat energy which can raise the surrounding temperature and increase the size of melt pool.

The input value for line offset is not used in this simulation as the equation of Line Offset Compensation is unknown. The line offset values used for the simulation is assumed to be the actual line offset value derived from Log File Reader shown in Table 6.6.

Table 6.7 Simulation Parameters

Parameter Settings ID	Actual Line Offset (LO)/[mm]	Beam Diameter (D)/[mm]	Beam Speed (S)/[mm/s]
0	0.22	0.6	1945
L1	0.18	0.6	1945
L2	0.15	0.6	1945
L3	0.09	0.6	1945
L4	0.07	0.6	1945
S1	0.22	0.6	1449.3
S2	0.22	0.6	1063.8
S3	0.22	0.6	843.5
S4	0.22	0.6	623.2
F1	0.22	0.4	1945
F2	0.22	0.23	1945
F3	0.22	0.20	1945
F4	0.22	0.18	1945

Simulation Results

The simulated melt profile for all the parameter setting is shown in from Figure 6.25 to Figure 6.28, the location of the melt profile is taken at Line 1, indicated in Figure 6.24. As expected, due to the heat from previous melt track, the depth of melt profile is increasing as the melt pool moves on. Due to the high curvature shape of the melt pool and insufficient overlap between each melt track, the majority of the melt profiles have a waviness shape.

The best fixing parameter not only needs to stop the defect from propagation, but also need to fix the LOF layer in the underneath layer.

The fixing parameters with a narrowed Line Offset value does not seem to have a great impact on the depth of the melt pool but only makes the bottom melt profile smoother. The overall energy density for parameter setting L4 is almost three times that of the default setting, but the depth of melt profile has only increased from 0.17mm to 0.2mm, this indicates that most of the energy is spent re-melting the same spot rather than going deeper into the profile.

On the other hand, the graphs in Figure 6.27and Figure 6.28 indicate that reducing beam speed and beam diameter is very helpful in increasing the melt pool depth, which means it is more likely to eliminate the underneath LOF.

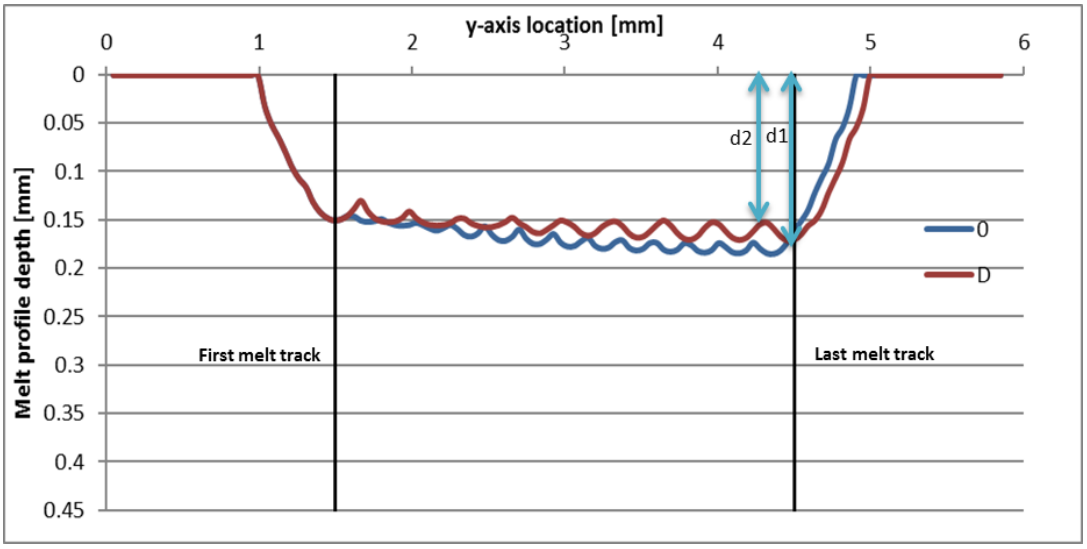

Figure 6.25 Melt profile for Parameter settings 0 and D across Line 1 indicated in Figure 6.24

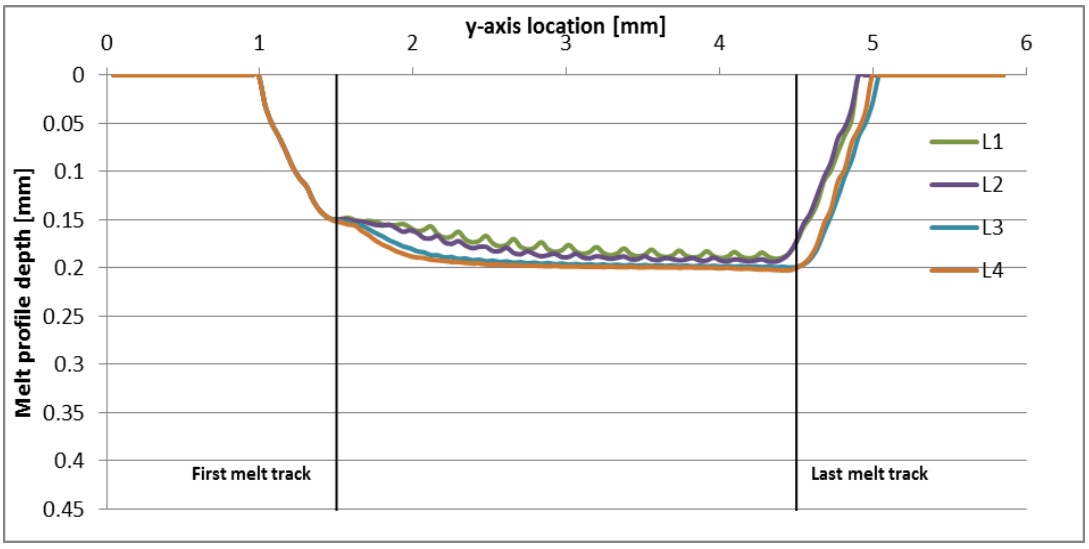

Figure 6.26 Melt profile for fixing parameter settings L1 to L4 across Line 1 indicated in Figure 6.24

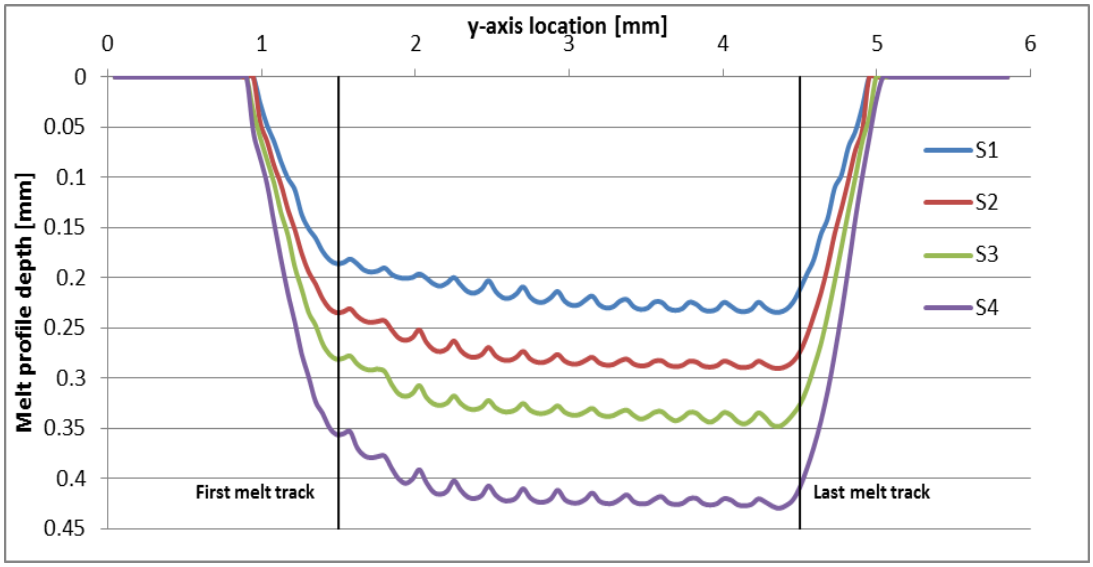

Figure 6.27 Melt profile for fixing parameter settings S1 to S4 across Line 1 indicated in Figure 6.24

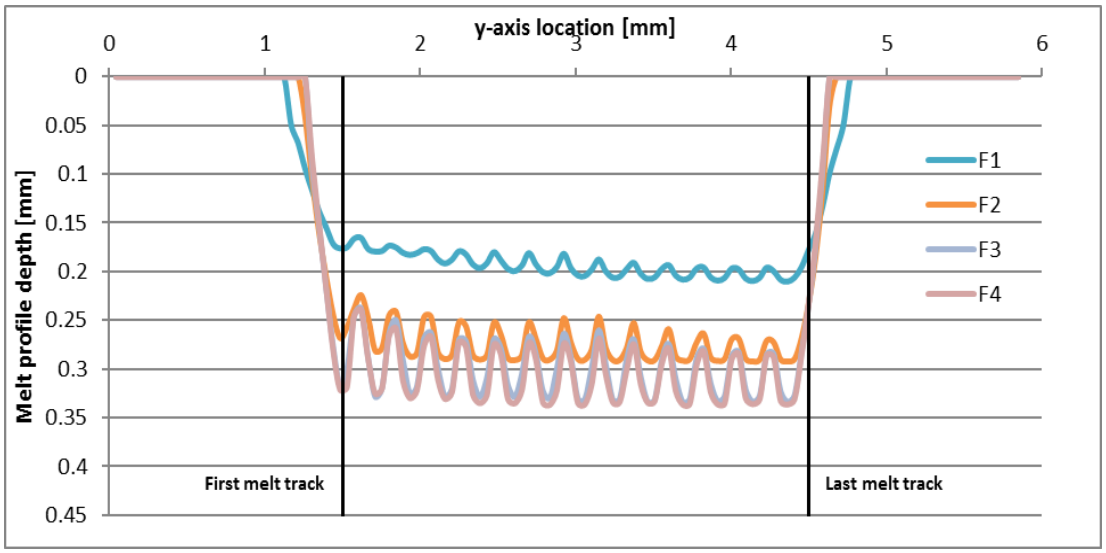

Figure 6.28 Melt profile for fixing parameter settings F1 to F4 across Line 1 indicated in Figure 6.24

By investigating each individual melt pool dimension at Location A (Figure 6.24), the result are shown in Table 6.8, where ‘d1’, ‘d2’ corresponding melt pool peak, trough depth as indicated in Figure 6.25; ‘d’ is the average depth between ‘d1’ and ‘d2’; ‘W’, ‘L’, ‘A’ and ‘V’ are the corresponding width, length, cross-sectional area and volume of the melt pool as described in Figure 6.29; ‘Number of Re-melt’ is the number of times a spot has been re-melted by the electron beam; The ‘LOF Remove Probability‘(LRP) presented in the table is the calculated LRP without the influence from the hatching frequency by using Equation 6.7.

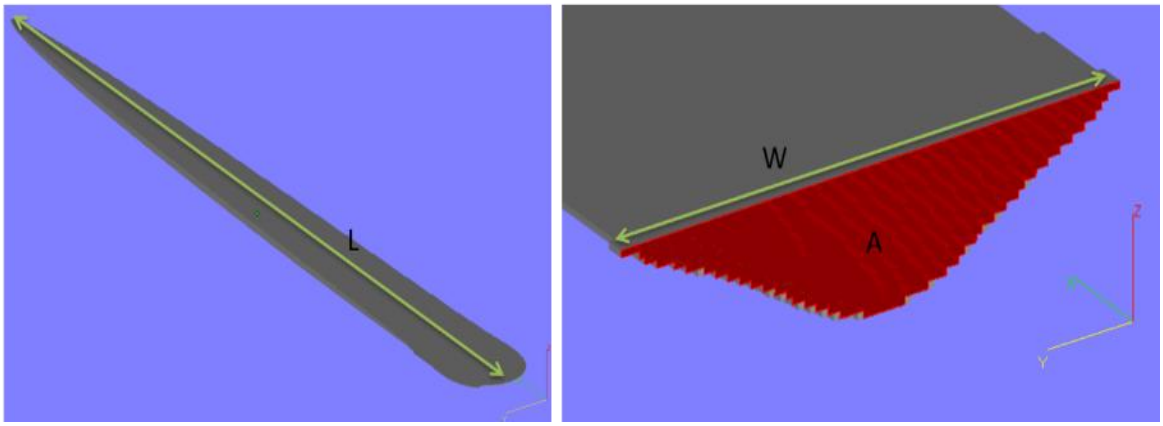

Figure 6.29 Melt Pool Length (L), Width (W) and cross-sectional area (A)

Table 6.8 Simulation result for the melt pool at Location A (Figure 6.24)

Parameter ID	EDR	d [mm]	A [mm^2]	W [mm]	L [mm]	V [mm^3]	Number of Re-melt	LRP
D		0.166	0.111	1.025	9.630	0.632	3	
0	1	0.178	0.122	1.062	11.115	0.807	4	10%
L1	1.24	0.185	0.128	1.071	12.105	0.900	5	28%
L2	1.45	0.191	0.130	1.069	13.005	0.998	7	52%
L3	2.47	0.198	0.142	1.099	15.300	1.263	12	66%
L4	3	0.201	0.146	1.099	16.290	1.369	15	66%
S1	1.35	0.232	0.166	1.135	12.690	1.252	5	80%
S2	1.71	0.288	0.223	1.171	13.680	1.858	5	97%
S3	2.33	0.344	0.277	1.237	14.085	2.418	5	100%
S4	3.12	0.427	0.356	1.265	13.950	3.173	5	100%
F1	1	0.208	0.124	0.858	14.175	1.070	3	50%
F2	1	0.269	0.113	0.592	14.805	1.117	2	96%
F3	1	0.316	0.111	0.560	14.175	1.049	2	95%
F4	1	0.326	0.113	0.546	13.995	1.022	2	100%

Based on the result shown in Table 6.8, by using a regression and factor of importance analysis (MatLab built-in function: `fitensemble` and `predictorImportance`), the factors of importance for each variable in Table 6.8 is presented in Table 6.9. By the definition of the `predictorImportance function`, a higher number indicates a highly important factor.

From Table 6.9, the analysis indicates that the most important factor affecting LOF rectification is the depth of the melt pool, and least important factor is the number of re-melt. This result

also confirms the assumption made in the previous section, where the Energy Density is not a good indicator for LOF rectification.

Table 6.9 Factor Importance predicted by using MatLab regression analysis

Factor	Factor of Importance
Energy Density Ratio	0.24
Cross-sectional Area[mm^2]	0.84
Melt Pool Width [mm]	0.0618
Melt Pool Length [mm]	1.7378
Melt Pool Volume [mm^3]	0.0421
Number of Re-melt	0.0470

6.3.3 Melt Pool Depth

By plotting the LRP vs depth of melt pool (d), the graph shown in Figure 6.30. The general appearance of the graph is an asymptotic smooth curve with LRP increasing as the melt pool depth increases. By finding the best fitted curve, the equation of the curve is shown in Equation 6.10.

By using the equation and the graph, a critical melt pool depth of 0.174mm can be derived. The critical melt pool depth indicates that if the melt pool depth is less than 0.174mm, the parameter setting is more likely to create LOF rather than remove them.

In addition, by solving the equation, it indicates that if the fixing parameter setting have mean melt pool depth of 0.33 mm, the parameter setting has a 99.9% chance of rectifying the LOF.

Equation 6.10

$$LRP = 1 - e^{-33.5\times(d-0.174)}$$

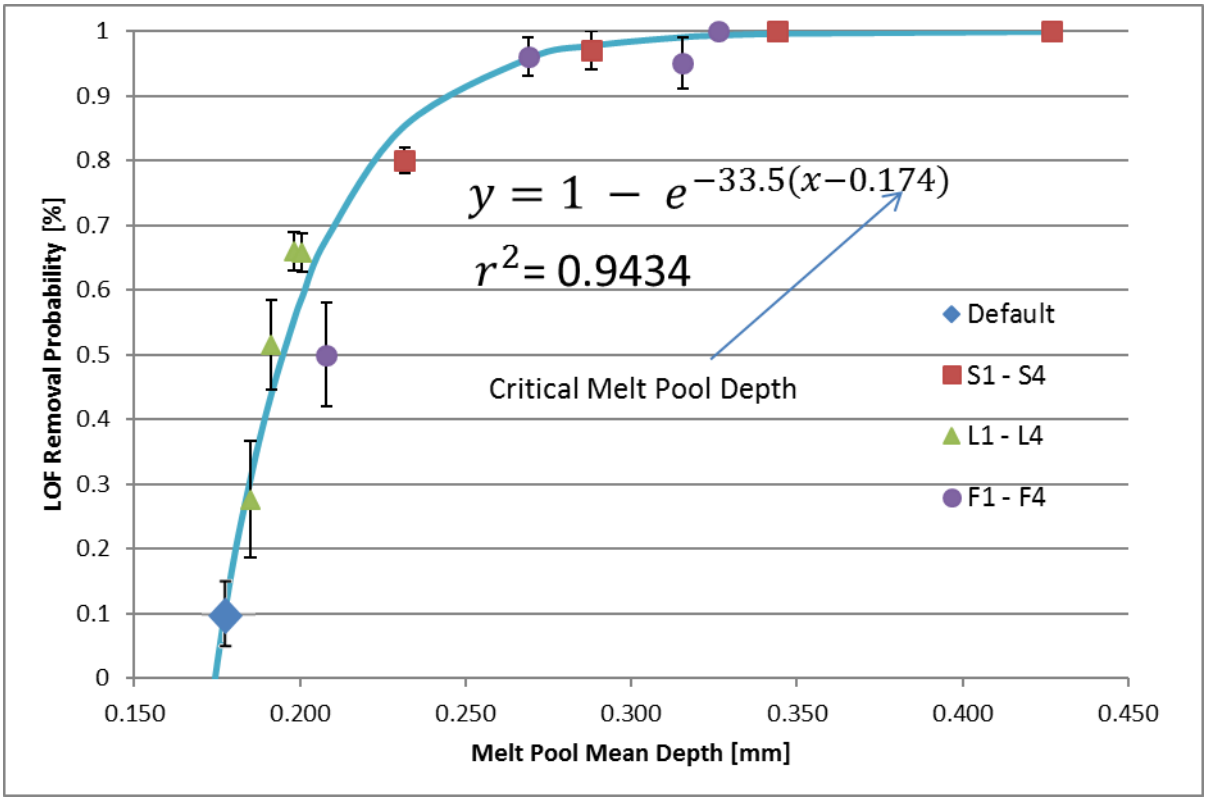

Figure 6.30 LOF fixing percentage vs Melt pool depth

The reason behind why a shallow melt pool is not sufficient to fix LOF is mainly due to the effect of surface tension. The Bond number is a measure for the ratio of the gravity force over surface tension. The equation for Bond number is shown in Equation 6.11, where ρ, g, L and σ denote the density, gravity, characteristic length scale and surface tension, respectively.

Equation 6.11

$$Bo = \frac{\rho \times g \times L^2}{\sigma}$$

As for Ti6Al4V liquid, the density is ~3750 kg/m^3, gravity is 9.81 m/s^2, and surface tension is ~1588m N/m^2. [106] The characteristic length of a melt pool is generally the smallest dimension of width, length and depth, and in this experiment, the depth of melt pool is always the smallest dimension. By evaluating the Bond number, the value is between 2.5×10^{-3} to 6×10^{-4}, which indicates the most dominant force over the melt pool is the surface tension rather than gravity.

The thermal properties for surface tension of Ti6Al4V decreases as the temperature increases, this creates a Marangoni flow with the central of melt pool flowing upward.[107] A schematic diagram is drawn in Figure 6.31 showing the difference in melt pool behaviour with and without LOF present. As shown in Figure 6.31a, if the top surface is perfectly flat, the direction of cooling should evenly spread across the bottom of the melt pool and the melt pool will solidify as a normal melt track.

A LOF type defect generally exists as a gap without any material. If the melt pool is small and shallow, the surface tension will prevent the melt pool from flowing into the crack and the bottom of the melt pool will be just suspend above the gap, as shown in Figure 6.31b. Due to the bottom of melt track not being in contact with any solid, the cooling of the melt pool at the bottom will be negligible compared to the rest of the region. This results in multiple Marangoni flows within the melt pool. Since the melt pool is very shallow, when the material solidifies, surface tension will more likely pull apart the melt pool into two individual melt regions which eventually form the new LOF.

Thus, regardless of how narrow the line offset is, as long as the depth of the melt pool is not sufficient to overcome the LOF, LOF is more likely to keep on propagating. On the other hand, with a larger and deeper melt pool, the relative influence of LOF on the melt pool will become smaller, which gives more chance to eliminate underneath defects.

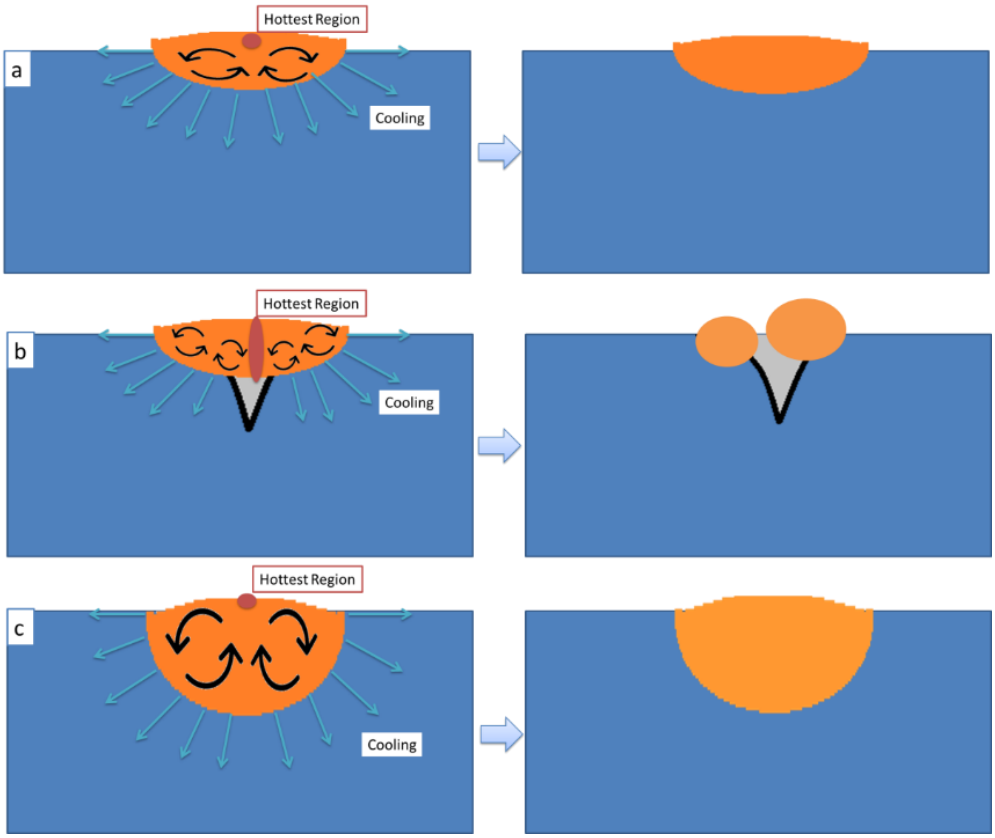

Figure 6.31 Solidification of melt pool [a]ideal melt pool without any LOF present [b] melt pool with a LOF under the layer [c] very deep melt pool is less likely to be affected by the existing LOF

6.3.4 LOF Re-creating

As shown in the result section, although both parameter settings S3 and F4 have stopped the LOF from propagation, fixing parameter F4 has recreate some new LOF afterward. During the process, it is observed that extra amount of spattering associated with fixing parameter F4 and a bad top surface quality has been also found after the build. It is believed that the surface degraded by fixing parameter F4 is mainly due to the shape of melt pool being too narrow and the overlap between melt tracks are insufficient.

Melt Pool Shape

By taking a more detailed observation of the final top surface of F4 and S3 in Figure 6.32, the surface of S3 appears to be very flat, but the surface of F4 exhibits the sinusoidal shape of peaks to troughs with a distance of approximately 120 µm. The reason for this appearance is

believed to be mainly caused by the surface tension and insufficient overlap between the melt tracks.

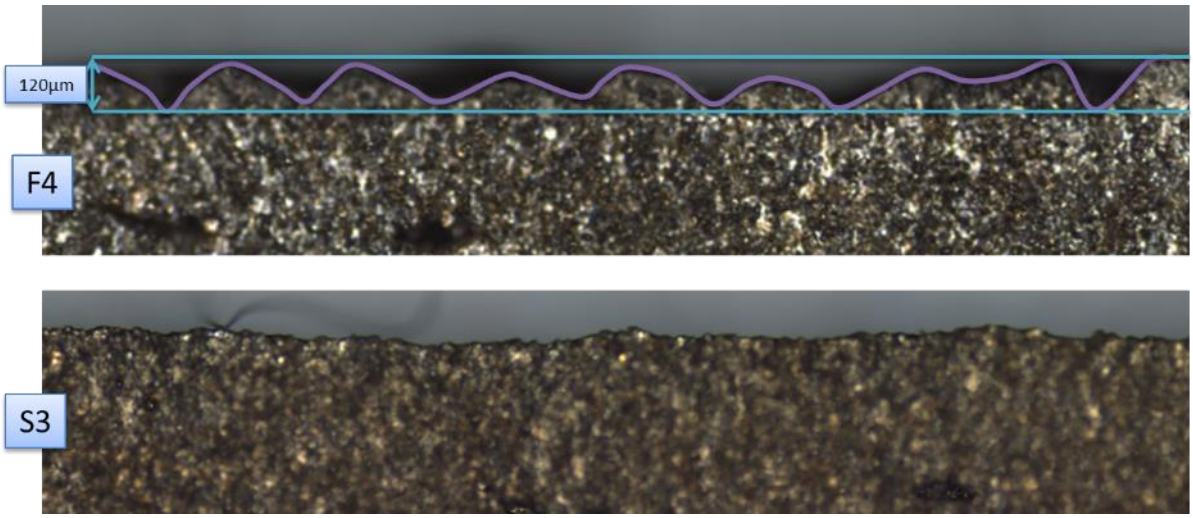

Figure 6.32 top surface for F4 and S3

As mentioned in previous section, the shape of melt pool is dominated by surface tension. The effect of surface tension will create a Marangoni effect with a central flow of the melt pool vertically upward. From the melt pool simulation, the shape of melt pools for fixing parameter S3 and F4 are predicted and shown in Figure 6.33.

When the beam is focused to a smaller diameter, the shape of the melt pool will become narrower and deeper. As a consequence, vertical Marangoni flow within the melt pool will become more dominant than the horizontal flow. The upward flow is very likely to push to the top of melt pool which makes the melt pool more convex. Although the melt pools produced by S3 are similar depth to F4, due to S3's much wider melt pool, the lateral force will more likely smooth the melt pool and create less convex surfaces.

Apart from the Marangoni flow effect, due to the overall shape of F4's melt pool being much narrower and longer, the melt pools are more likely to 'ball-up' in order to minimize the surface energy. Similar observations have been given by Myriam et al[108], who suggest the meniscus height of the melt pool decrease linearly with the melt pool's width.

Since the melt pool becomes much narrower, the overlap between the melt tracks will become very large compared to the size of meniscus as shown in Figure 6.34a, which eventually result in the waviness appearance indicated in Figure 6.32. However, if the melt pool is much wider, there will be more overlap between each melt track, thus the surface will become much flatter (Figure 6.34b).

As a consequence, the high waviness on the top surface influences the melt pool's solidification due to the reasons stated in section 6.3.3, thus the LOF is generated from the un-even surfaces.

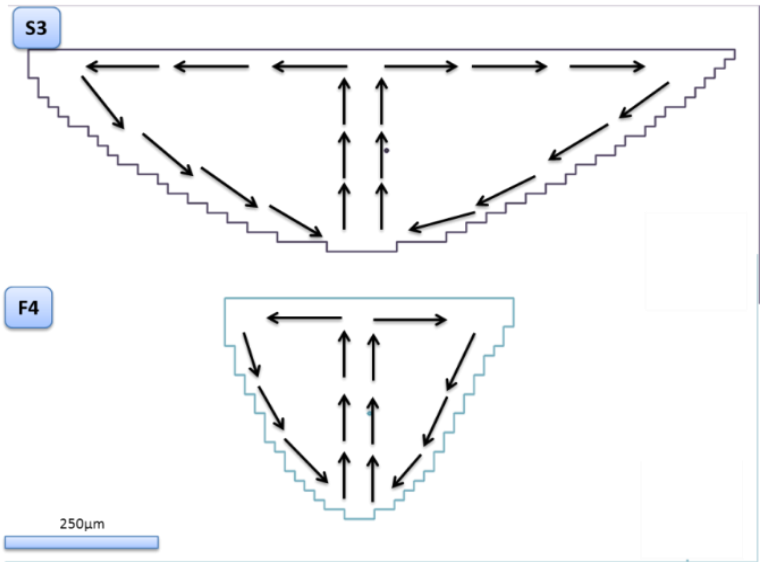

Figure 6.33 Marangoni effect within the melt pool for F4 and S3

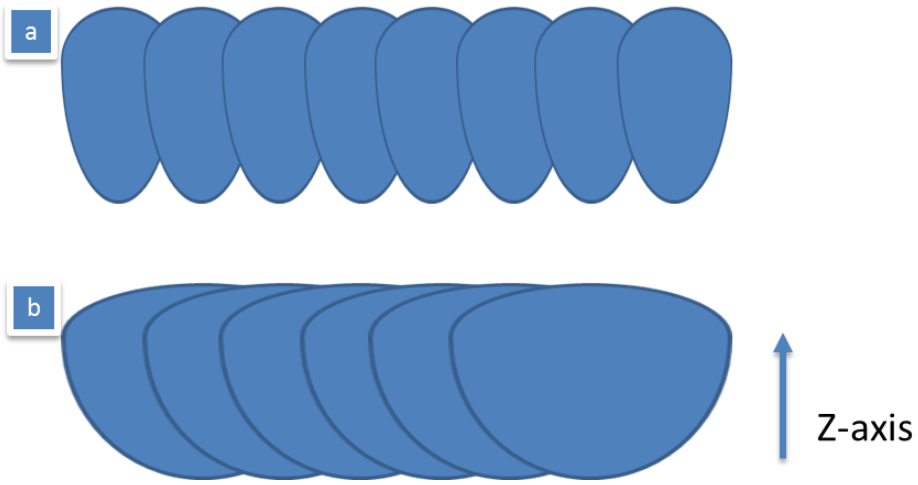

Figure 6.34 [a] narrow melt pool with large meniscus result in waviness surface
[b] wider melt pool create a much flatter surface

Apart from the waviness of the cross-section, the top surface also appears to be bumpy and dimpled as shown in Figure 6.35, this is the other consequences of surface tension along the melt track direction. A similar observation has been recorded by many researchers,[109,110,111] and is describe as the balling effect due to a large melt pool's length to width ratio.

Due to the effect of surface tension, molten material will likely become more spherical in shape to minimize the surface energy. As the melt pool becomes much narrower, the more likely it is for molten material to colligate along the melt track to reduce the total surface energy. Figure 6.36 shows the melt track shape at location A (Figure 6.24), where the length to width ratio of F4 is significantly larger than S3 and default paramter setting. Thus, during the melting process, the melt tracks of F4 are more likely to lose its original shape and break apart into small individual melt pools as shown in Figure 6.35.

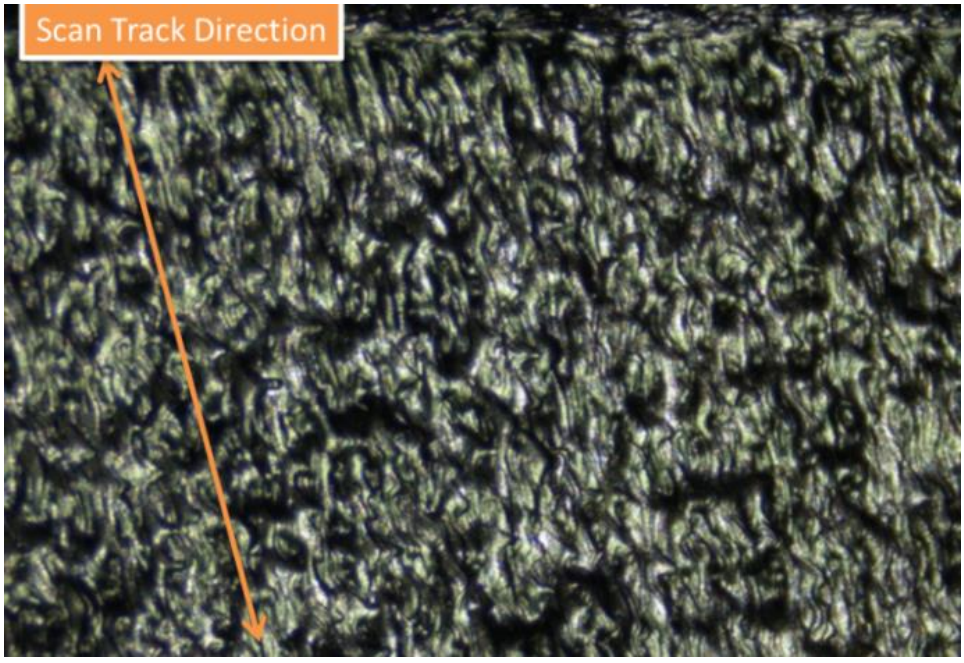

Figure 6.35 Bumpy top surface of F4 parameter setting

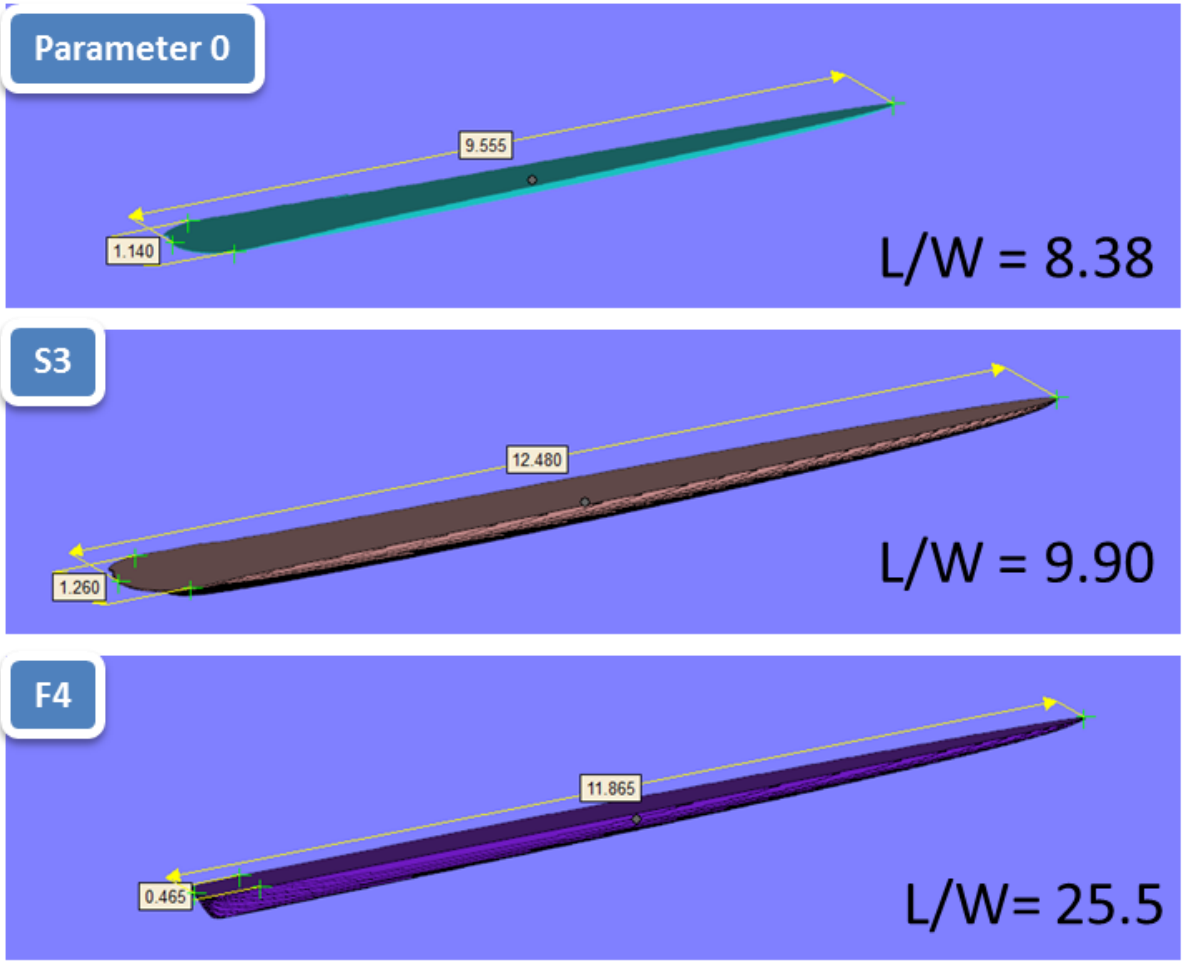

Figure 6.36 Melt track shape for S3, F4 and default parameter setting with Length/Width ratio

Spattering

During the experiment, more spatter formation was observed when the beam diameter is narrowed. In general, spatter is the ejection of molten liquid. With the EBM process, powder is surrounding the melt pool, and the ejection of material will sometimes include the cold or heated powder particles.[112] Since the material has been ejected away, the local melt zone could be left with insufficient material which could cause some extra degradation in surface quality.

The spattering formations are generally related with the gas flow from the melt pool due to the vaporization of material, and the momentum of the gas flow is generally related with the recoil pressure formed within the melt pool.

In Figure 6.37, the shape of the keyhole is predicted by assuming the mesh in the simulation has a temperature higher than the boiling temperature of the material. In order to maintain the keyhole from collapsing, the internal pressure must be higher or equal to the force required to close the keyhole. As the EBM process is under high vacuum, the main force available to close keyhole is the surface tension. The pressure generated by the surface tension is generally expressed as the ratio of surface tension and the radius of curvature, which in this case is assumed to be the diameter of the keyhole opening. Due to the high focus of the electron beam in F4, the keyhole shape is deep and narrow. The radius of the keyhole for F4 is only about one third of S3, thus the recoil pressure of F4 should be approximately triple the pressure within S3. The high internal pressure of F4 leads to a high velocity of gas flow from the melt pool, causing more material to be 'blown' away by the metal vaporization.

In addition, the speed the melt pool travels is directly related with the speed of the beam, due to fixing parameter F4 having faster beam speed than S3, the liquid flow within the melt pool also has higher momentum. It is hypothesis that the high momentum of the melt pool is also a contributing factor to the formation of extra spattering.

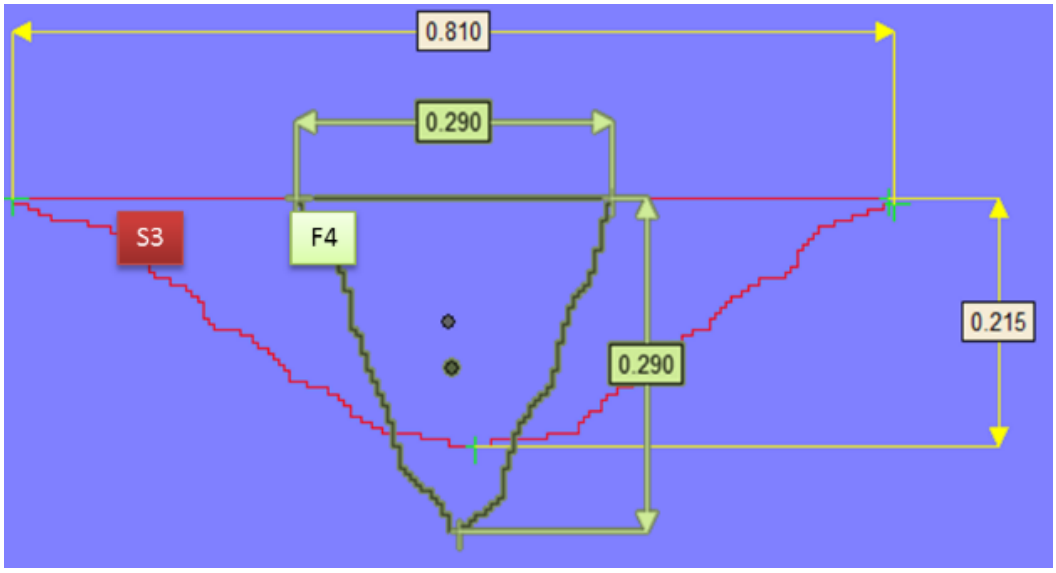

Figure 6.37 potential melt pool keyhole in F4 & S3

6.4. Benefit of using Closed Loop Fixing (CLF) system

To CLF system is built based on the LayerDD system. Thus, apart from the cost of LayerDD itself, the design of the CLF system should fix all the identified LOF during the process and not incur additional hardware cost or process time to the current Q20 plus system. The development cost should only be related with software development of the closed loop system which needs to be integrated within the existing EBM control.

Although the CLF system can fix LOF during the process, but the fixing parameter should not be activated consecutively, due to the defect fixing technique input extra energy into the substrate which could incur potential part swelling. Thus, the baseline algorithm should be decent enough to produce parts with adequate/minimum amount of LOF.

As the CLF system is a potential upgrade to the current control system, thus the main benefits of using CLF are:

- Faster Research and Product Development cycles
- More capable of producing LOF free parts
- Reduces the scrap rate during production.
- Improved capability to manufacture defect free parts at a minimal cost

6.5. Conclusion:

The above experiments have proved that it is possible to rectifiy identified LOF during the EBM process, and the closed loop LOF rectification system can potentially save both time and cost on EBM process development.

In this experimental study, three different parameter settings were investigated with the aim of fixing the artificially introduced lack of fusion: Line Offset, Speed Function, and Focus Offset. The result indicates that the key factor influencing the LOF removal probability was the depth of the melt pool.

- Reducing the Line Offset increases the depth of melt pool only slightly, this is a result of the high residual heat from the previous melt tracks and their influence on the current melt track. Unfortunately, as the depth of the melt pool increased very little, it didn't significantly help with LOF removal, but increases the chance of part swelling.
- Reducing the Focus Offset reduces the overlap between melt tracks, this is very helpful in increasing the depth of melt pool and stopping LOF propagation. Since changing the Focus Offset does not actually increase the energy density of the layer, it has the least chance of part swelling. The key disadvantages of using a highly focused beam are that it could increase risk of spattering, balling, reduce top surface quality and increase the risk of LOF regeneration.
- Reducing the speed of the beam by lowering the Speed Function gives a bigger and deeper melt pool. This gave the best result for successfully removing LOF in the current Q20 Plus system. The result shows a significant melt pool penetration to remove exisitng LOF and gives a very smooth top surface finish to prevent LOF from regenerating.

Chapter 7 : Influence of HIP on EBM TI6Al4V Part with Induced Defect

7.1. Introduction

Hot-Isostatic–Pressing (HIP) is an aerospace approved technique to close residual internal and to achieve the desired metallurgical characteristics for the casted or additive manufactured parts. The effect of HIP treatment improves the part's dynamic materials properties such as fatigue or fracture toughness.

HIP treatment generally coarsens the EBM microstructure (both β grains and α/β plate thickness) but maintains the same Widmanstädten sub-structure. It has been reported[113,114] that during HIP treatment, Ti6Al4V powder particles are directly transformed from powder to a solid form via solid-state transformation, with the resulting microstructure showing more of spherical- or equaxed- prior β-grains along with plates like α/β substructure.

During the EBM process, lack of fusion (LOF) defects will contain numerous of un-melted powder, which will later transform directly into a solid form upon HIP treatment. Therefore it is expected that there should be an in-homogeneity in local microstructure near to LOF region i.e., a boundary with a distinguishable microstructure features obtained from core of (AM melt, solidified and HIP'ed) and at the vicinity of LOF after HIP. Although the Ti6Al4V material properties for EBM or HIP has been reported in the literature, but it is expected that a slight change in local microstructure close to LOF region after HIP could potentially become a weak point to the whole geometry especially during dynamic loading conditions.

This chapter manly investigates the difference in material properties due to the presence of un-melted powder of EBM process after HIP treatment. The study is demonstrated by both microstructure cut-ups and mechanical (static and dynamic) property testing.

In this experiment, the EBM default Q20 parameter settings were used as shown in Table 7.1. The powder used was plasma atomized, and the condition of HIP was performed at 925±10 °C and 100 MPa for two hours. For the fatigue test, after HIP process, the samples were annealed at condition in line with AMS 4928 (704 ºC, 2hours, argon cooled to 420 ºC and then cooled either in argon or in air to room temperature). Every sample from the test were printed with unique ID on the sample to retain configuration control.

Table 7.1 Setting used for the produce EBM samples

Preheat	Ti6Al4V_Q20-Preheat-4.2.57.2
Melt	Ti6Al4V_Q20-Melt-4.2.57.2
Support	Ti6Al4V_Q20-wafer-4.2.57.2

7.2. Design of Experiment

7.2.1. Test 1: Study of Microstructure In-homogeneity

To study the microstructure in-homogeneity due to induced defects after HIP process, samples with dimension of 10×10×10 mm^3 were produced with an induced defect size of 4.0×4.0×4.5 mm^3 (Figure 7.1). The centre of the induced defect is located 3 mm above the bottom of the cubic specimen.

Four samples were printed in total, two samples were HIP'ed, and the remaining two were not HIP'ed. Specimens from each condition (HIP'ed and Un-HIP'ed) were metallographically prepared in both vertical and horizontal direction as shown in Figure 2, and investigated using light optical microscopy. The summary of tests is listed in Table 7.2.

Table 7.2 Test 1 samples summary

Specimen ID	***Condition***	***Direction of cutting plane***
T1_1	Un-HIP	Horizontal
T1_2	Un-HIP	Vertical
T1_3	HIP'ed	Horizontal
T1_4	HIP'ed	Vertical

The overall summary of experimentation for sample 3 and 4 are listed below:

1) HIP at standard HIP cycle conditions for the selected parts
2) Cutting
3) Polishing
4) Etching
5) Microscopic observation

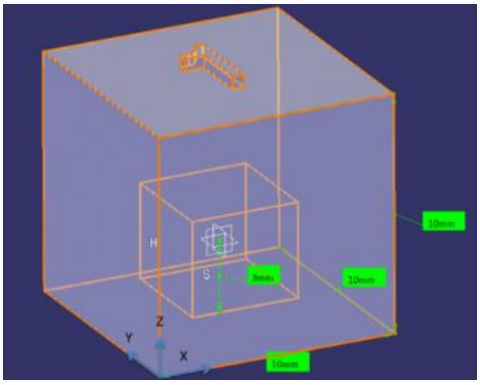

Figure 7.1 Induced defect size of 4×4×4.5mm^3 into a cube with size 10×10×10mm^3

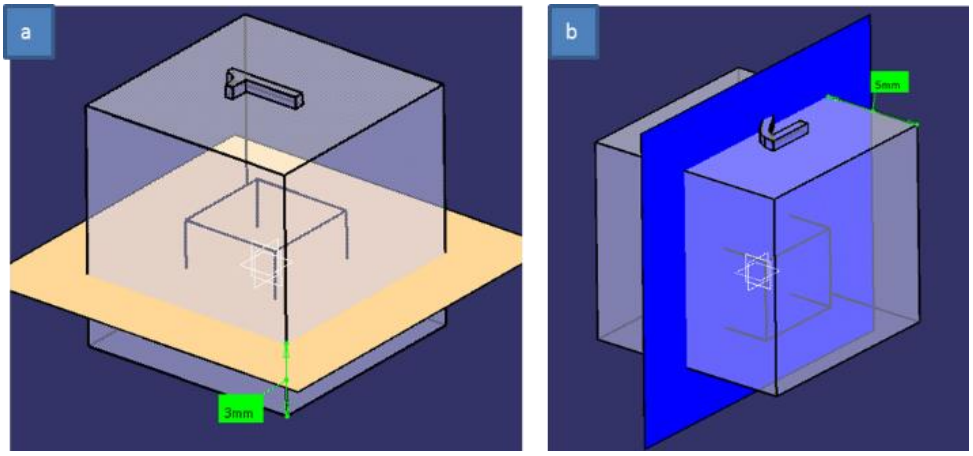

Figure 7.2 a) Horizontal microscopic observation with cutting plane 3mm above the bottom of cube
b) Vertical microscopic observation with cutting plane 5mm from the edge

7.2.2. Test 2: Static Properties (tensile test)

The test blanks were produced with square cross-section with seeded defect in between the gauge section as shown in Figure 7.3. All the samples were 2D X-ray'ed to verify the presence of predetermined induced defects. Upon completing X-ray inspection, a round tensile bar was extracted. The reason for having an initial square cross-section is to have a high X-ray imaging sensitivity, which requires a smooth specimen surface and consistent thickness. The smooth

surfaces on the squared samples were obtained using of wire EDM finishing (see the flow chart of the task mentioned above in Figure 7.4).

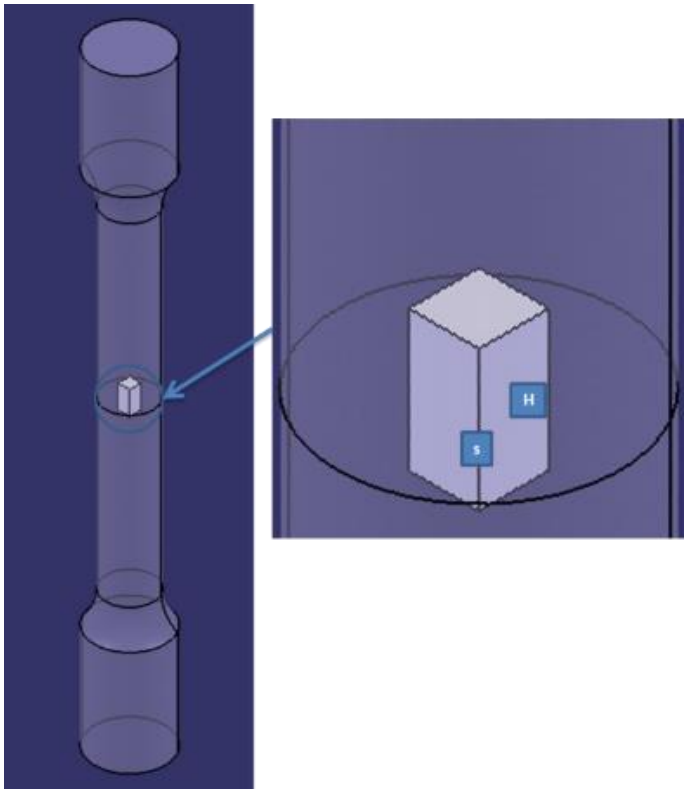

Figure 7.3 Tensile specimen with induced defect at the central location of the gauge section

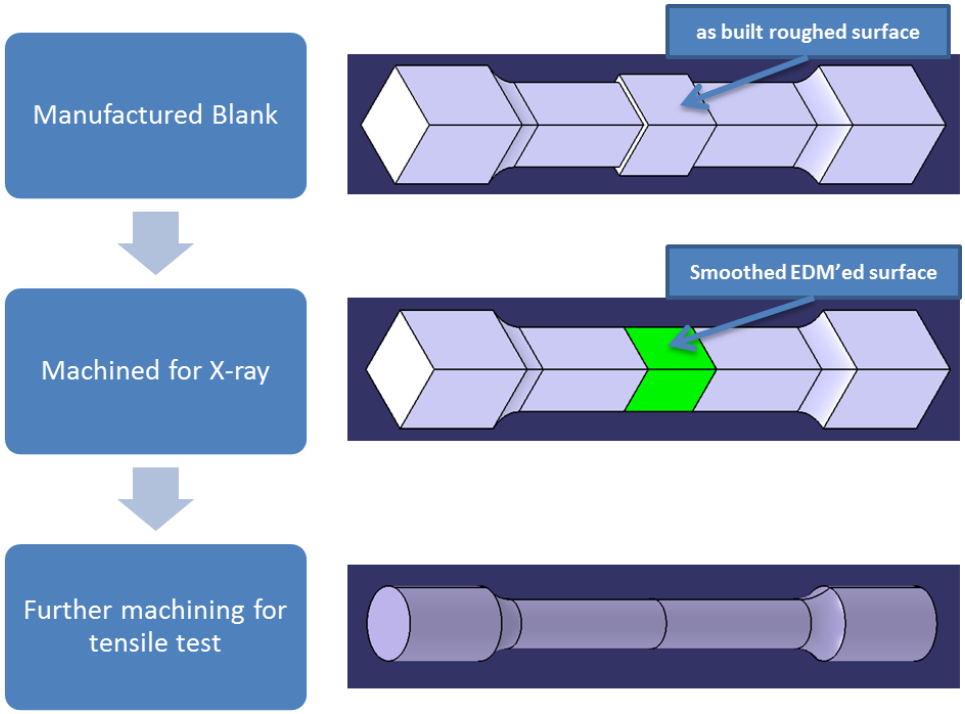

Figure 7.4 Flow Chart: (a) as-fabricated EBM squared test blank, (b) Machined external surface region highlighted in Green for X-ray inspection (where the induced defects are present), (c) X-ray inspection of the coupons, and (d) cylindrical tensile specimen extracted after X-ray.

The cylindrical tensile pieces were produced as per ASTM E8 as shown in Figure 7.5. Table 7.3 summarises the total number of the specimens used to assess the tensile and fatigue performances. The tensile test matrix consists of 6 control specimens (T2_0) and 3 set of specimen for each variable defect size as shown in Table 7.3**.** The induced defect sizes were varied from 1 mm to 4.5 mm (S-width) by 4 mm (H-height) at the central location of the gauge section as indicated in Figure 7.3. The variable P indicated in Table 7.3 is the ratio between cross-section area of defect over the cross-section area of gauge section.

Figure 7.6 shows a nesting configuration of the test samples within a build, where all the samples were placed with a minimum spacing of 5 mm from each other. All the samples were produced using Arcam's standard Q20 theme.

Table 7.3 Tensile test matrix, T2_1 to 6 are the control samples without any induced defects. T2_7-27 are seeded with variable size defect from 1mm to 4.5mm with defect height 4mm

Specimen ID		***Width - S (mm)***	***Height - H (mm)***	***Area Ratio of Defect to the gauge's cross sectional area – P (%)***	***No. of Samples***
T2_1 to 6	Controlled Samples	0	0	0	6
T2_7 to 9	Induced Defect Samples	1	4	2	3
T2_10 to 12		1.7	4	5.74	3
T2_13 to 15		2.5	4	12.4	3
T2_16 to 18		3	4	17.9	3
T2_19 to 21		3.5	4	24.37	3
T2_22 to 24		4	4	31.83	3
T2_15 to 27		4.5	4	40.28	3

Figure 7.5 ASTM E8/E8M standard test specimen of diameter 8mm

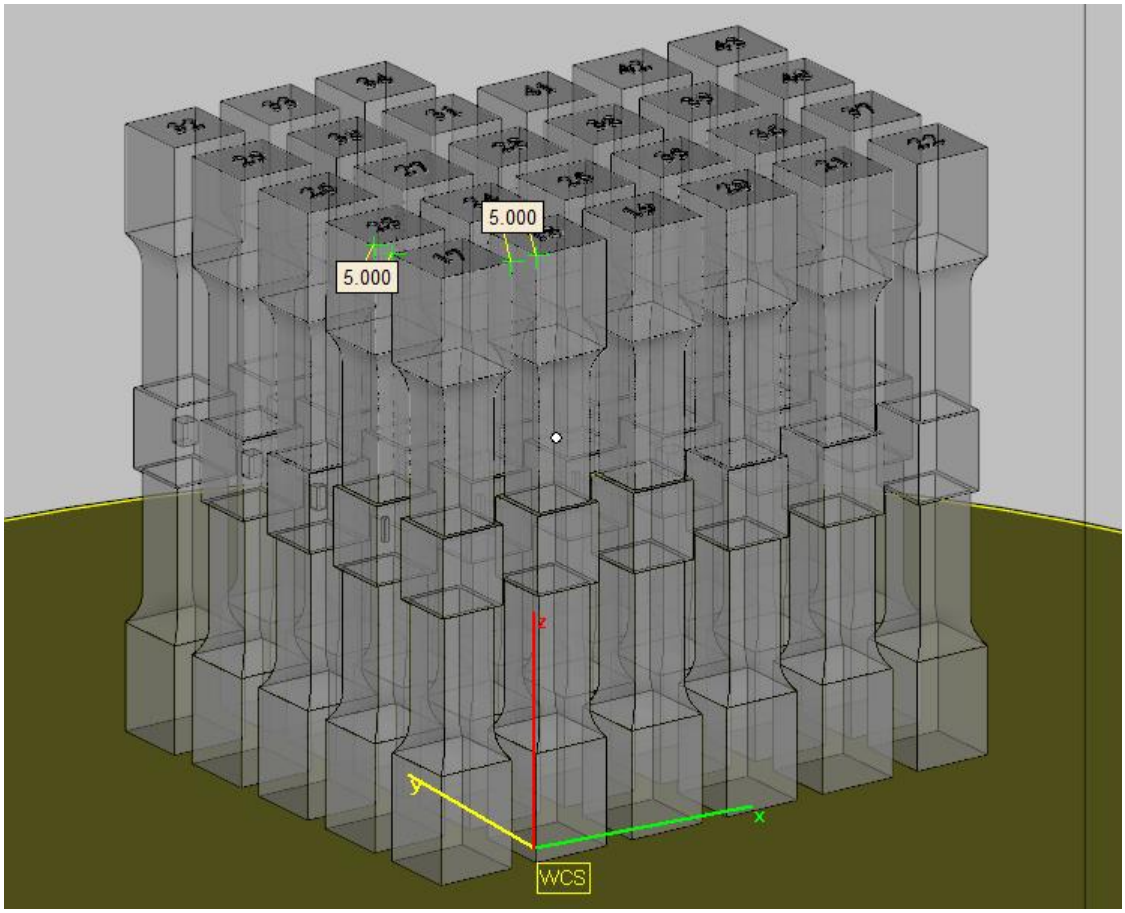

Figure 7.6 Build configuration for tensile test specimens; samples are placed with 5mm gap between each other

7.2.3. Test 3: Fatigue Test

The fatigue samples are designed with 4 seeded defects as shown in Figure 7.8. The overall sample dimensions are 18×18×130 mm^3 and each defect has a dimension of 1mm×1mm×4mm. The build is done on a rectangular plate and the parts are directly built from base plate without any support structures. There are twenty samples in total, 5 of the control samples should be free of any seeded defects, and 15 samples are seeded with defects.

The samples have gone through a standard HIP cycle to close-up the seeded defects followed by annealing. The samples are then machined as shown in Figure 7.7. The machining is performed slightly off centre to have a better chance of exposing the region of seeded defect on the surface of fatigue sample.

In total only 14 samples were tested, 5 control samples free of defects and 9 samples with seeded defect. As the fatigue test is funded through an industrial related project with a very specific purpose, a fatigue load of 800 MPa was used. The fatigue tests were performed according to test standard EN6072 with R-Ratio of 0.1 at frequency of 50 Hz.

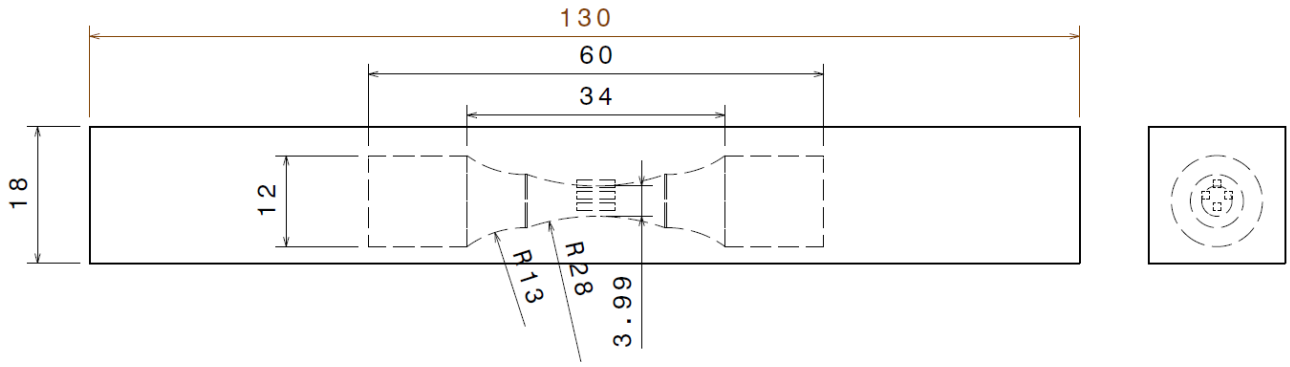

Figure 7.7 Extraction of fatigue coupon from the EBM blank

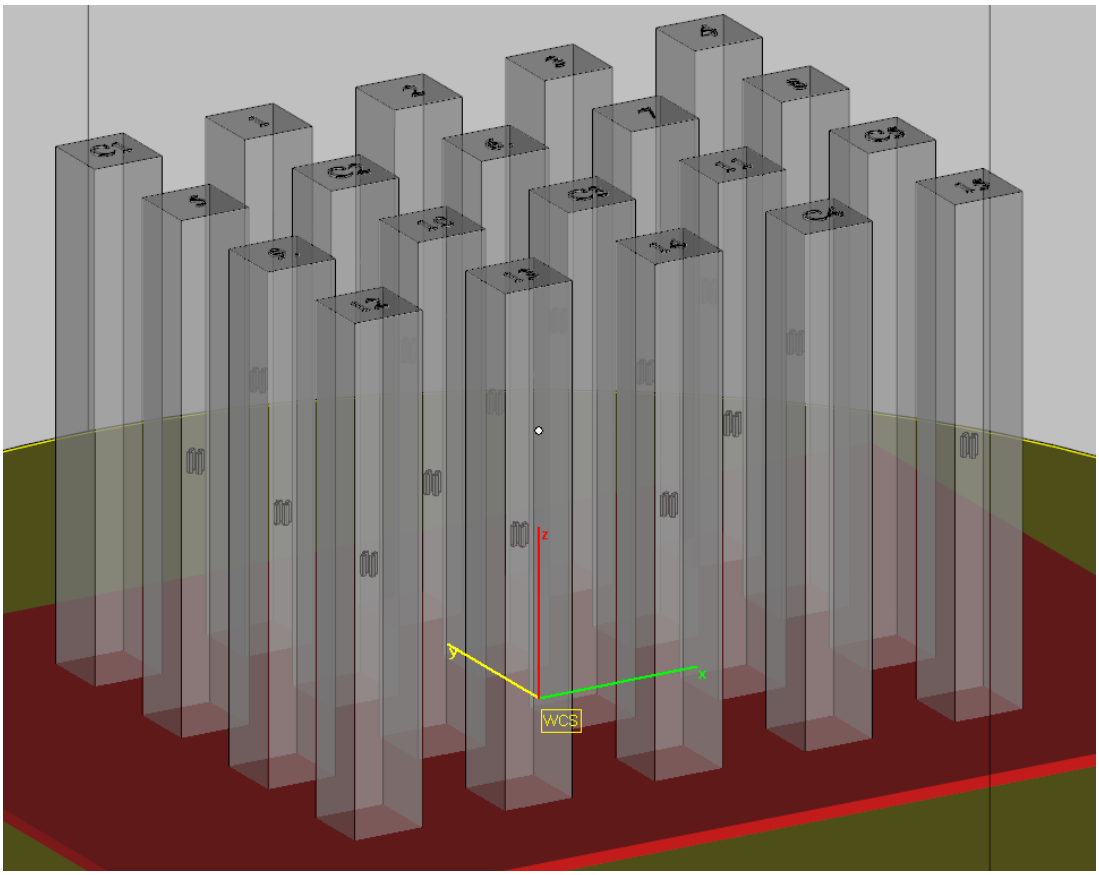

Figure 7.8 Fatigue sample configuration

7.3. Results and Discussion

7.3.1. Test 1 Microstructure

The un-HIP'ed T1_1 and T1_2 have been cut to verify the presence of the induced defect. Metallography sample preparation of the both specimen was not successful due to the presence of loose semi-sintered powder. In Figure 7.9, the size of defect was measured by Vernier calliper and the defect sizes and the location were within 0.2 mm tolerances of the designed geometry.

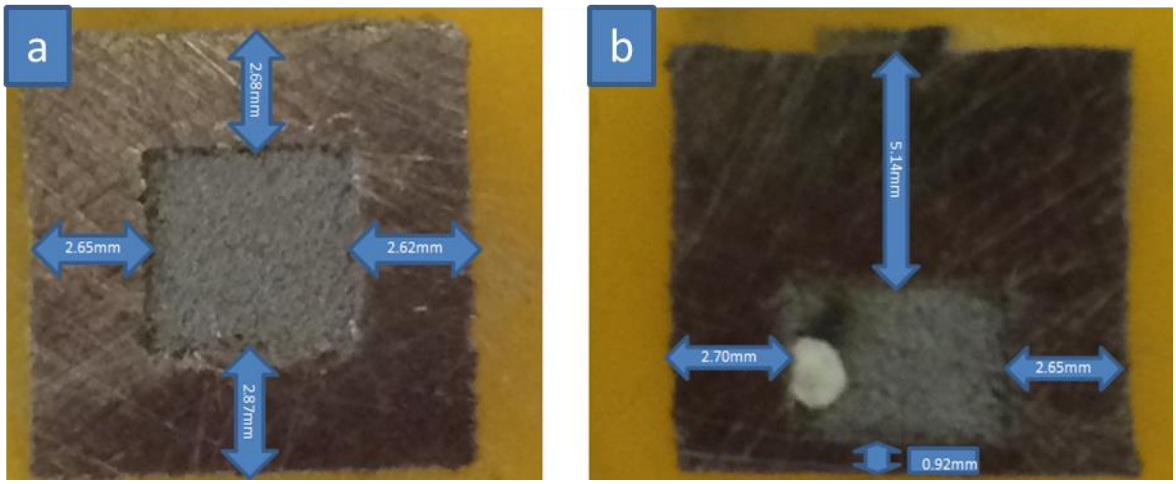

Figure 7.9 Un-HIP samples of (a) T1_1 specimen, which sectioned horizontally; (b) T1_2 specimen, which sectioned vertically

Figure 7.10 shows a clear evidence of shrinkage in samples T1_3 and T1_4 after HIP treatment. The density of the semi-sintered powder is approximately 60% of the solid material and hence shrinkage has been observed upon hot-isostatic pressing as shown in Figure 7.10. Also, the shrinkage was observed towards one side of the specimen (bottom) and this type of unbalanced shrinkage was expected due to the fact that the induced defect was off centre as shown in Figure 7.1.

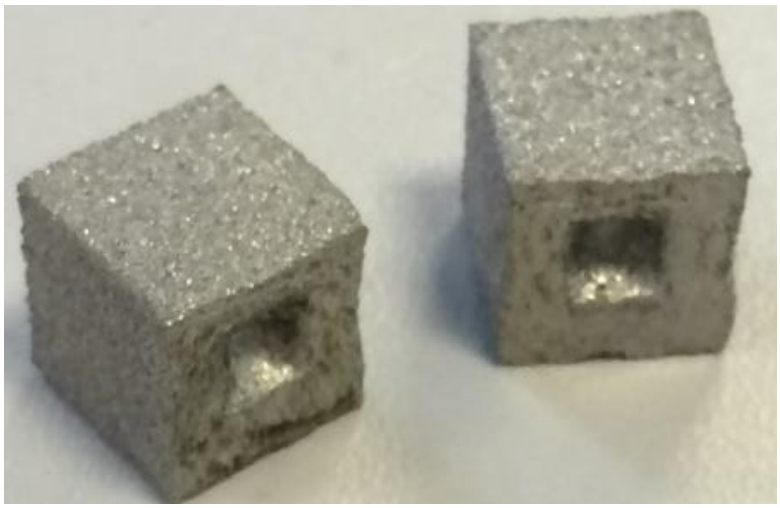

Figure 7.10 HIP'ed samples of T1_3 and T1_4 with shrinkage on the bottom face due to induced defect is off-centre located

Figure 7.11 and Figure 7.14 show an overview of the cut-up of T1_3 and T1_4, respectively. The micrograph shown in the figures indicate a very distinguishable microstructure, and clear boundaries between the microstructure can be observed. By measuring the distance between boundary line and the edge of the specimen, the results are consistent with the designed dimension of the induced defects (see Figure 7.11 and Figure 7.14).

Figure 7.12 and Figure 7.13 shows the microstructure of the horizontal cross section of sample (T1_3) in X-Y plane (see Figure 1 for co-ordinate of sample) at higher magnification (X500); whereas, Figure 7.15 show a microstructure in vertical cross-section of the sample (T1_4) in Y-Z plane. From the overall appearance of the α-plates morphology, it can be classified into two different features, i.e., (i) basket weave Widmanstätten lamellae-like microstructure in beta matrix and, (ii) annealed plate-like or more of equiaxed/spherical-like structure in the beta matrix mixed with lath-like basket weave structure.

Figure 7.11 Specimen T1_3 at X50 magnification (X-Y plane view)

By measuring the image shown in Figure 7.12 and Figure 7.15, the lamellae-like microstructure from EBM-HIP region has alpha laths with a width value between 1.5 to 4.5 µm, and the length is measured to be 2 to 10 time of the width. As for the equaxed-like structure from defect closed-HIP in Figure 7.13 and Figure 7.15 the width is between 5 to 10 µm.

The first basket weave Widmanstädten lamellar microstructure is formed as a result of high cooling rate noticed in EBM process, although HIP treatment has coarsened the plate thickness without altering the morphology of the α plates. Similar findings have been reported by Al-Bermani et al. [115]

Whereas, the second annealed or spherical-like or more of equaxed α-plate was due to the diffusion bonding occurs along the boundaries of powder particles. Under temperature and the pressure, the deformation produces recrystallized α and β equaxed grains at the former powder particle boundaries. As for the lath-like structure spotted within the particle could be due to the diffusion is slower in the centre than the boundaries. [113,114]

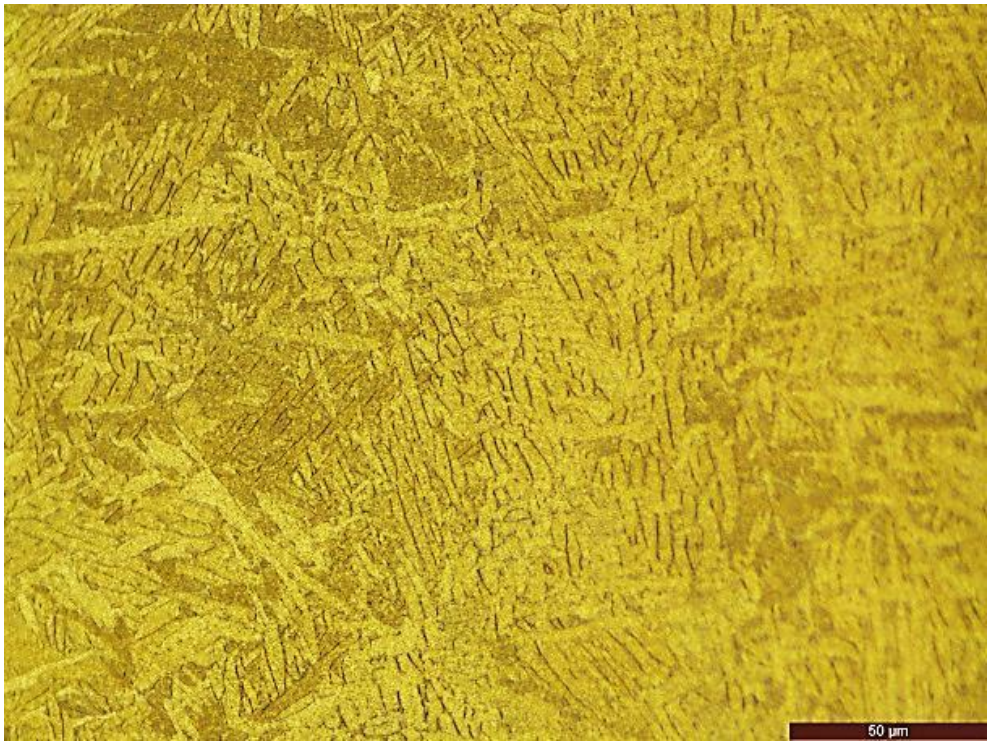

Figure 7.12 Specimen T1_3 at EBM–HIP Region X500 magnification, lamella Widmanstädten microstructure is observed (X-Y plane View)

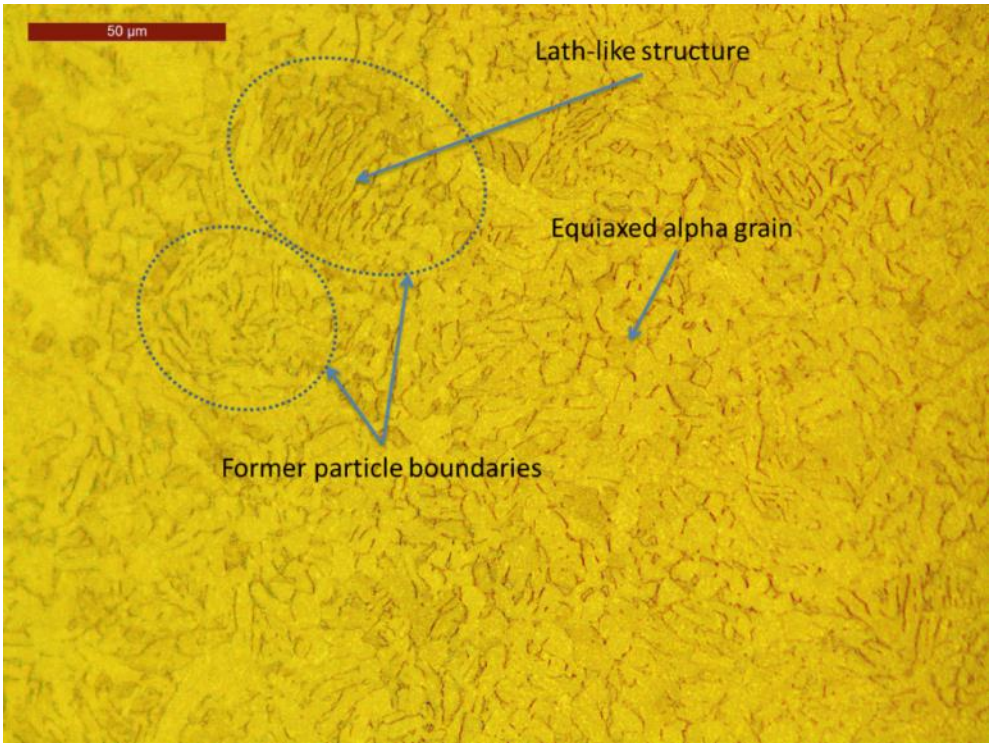

Figure 7.13 Specimen T1_3 at Defect Close-HIP Region X500 magnification, spherical- or equaxed- prior β-grains along with plates like α/β substructure has been observed (X-Y plane view). From the image, it can be see some former particle boundaries is still visible

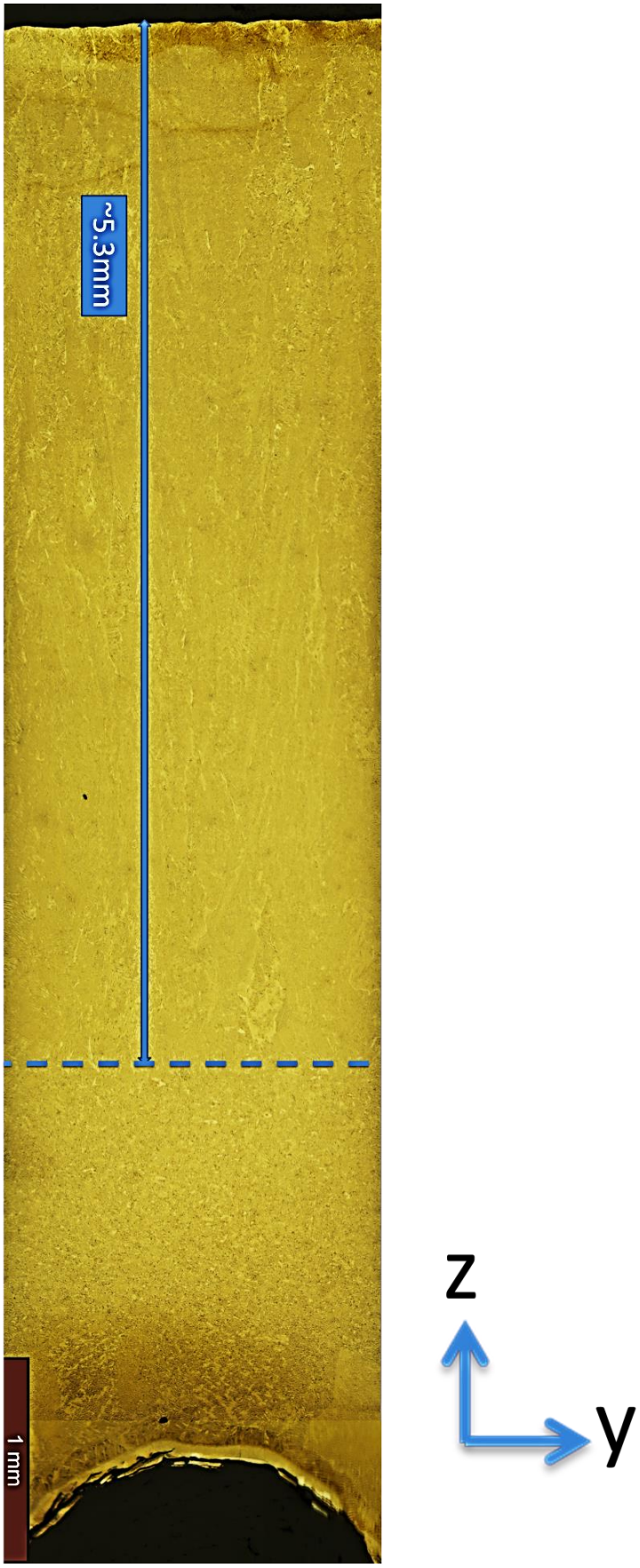

Figure 7.14 Specimen T1_4 at X50 magnification (Y-Z plane view)

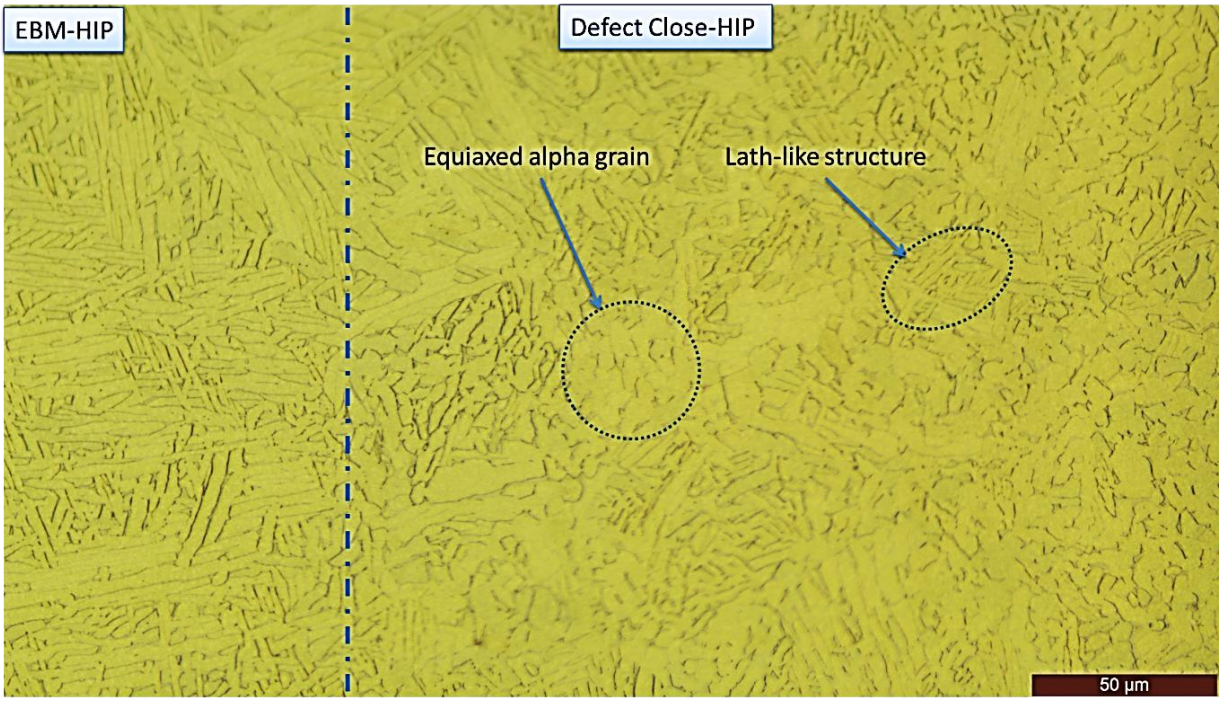

Figure 7.15 Specimen T1_4 at X500 magnification with Defect Close–HIP and EBM–HIP Region next to each other (Y-Z plane view)

7.3.2. Test 2 Tensile Test

After the samples have been successfully made by EBM process, they are cut with wire EDM and viewed under X-ray to prove the defects have successfully induced. The induced defect viewed under X-ray were found to be slightly different than the designed size. As shown in Table 7.4, the defect is about 0.3 mm larger in X and Y direction, and 0.3 mm shorter in Z – Direction.

The undersize of induced defect in Z-direction is mainly due to the melt pool over penetration on the overhang surfaces. The oversize of defect in X-Y plane also indicates the under size of the bulk material, which is mainly due to the melting strategy of EBM control.

In general, the surface roughness of EBM parts is very high and part dimension are normally measured by callipers. When measurement is taken by callipers, the measurement location is the most external surface of the part as shown in Figure 7.16. But, when the sample is

photographed under X-ray, the high surface roughness appears less dense than solid material; therefore the dimension taken by X-ray is always smaller than the dimension of the callipers. Figure 7.16 indicates the difference between two different methods of measurement. Similar finding were presented by Hernández-Nava et al[116], who manufactured lattice structure using EBM process, indicating that the dimension of lattice strut measured by computed tomography differed from the design dimension.

Table 7.4 T2 defect size viewed under X-ray compare to the intended defect size

ID	Designed			X-Ray			Difference		
	X	*Y*	*Z*	*X*	*Y*	*Z*	*X*	*Y*	*Z*
T2_7	1	1	4	1.3	1.35	3.75	0.3	0.35	-0.25
T2_8	1	1	4	1.3	1.3	3.75	0.3	0.3	-0.25
T2_9	1	1	4	1.3	1.3	3.8	0.3	0.3	-0.2
T2_10	1.7	1.7	4	2	2	3.7	0.3	0.3	-0.3
T2_11	1.7	1.7	4	2	2	3.8	0.3	0.3	-0.2
T2_12	1.7	1.7	4	2	2	3.75	0.3	0.3	-0.25
T2_13	2.5	2.5	4	2.8	2.8	3.75	0.3	0.3	-0.25
T2_14	2.5	2.5	4	2.9	2.85	3.75	0.4	0.35	-0.25
T2_15	2.5	2.5	4	2.8	2.8	3.7	0.3	0.3	-0.3
T2_16	3	3	4	3.3	3.4	3.75	0.3	0.4	-0.25
T2_17	3	3	4	3.3	3.4	3.75	0.3	0.4	-0.25
T2_18	3	3	4	3.35	3.3	3.7	0.35	0.3	-0.3
T2_19	3.5	3.5	4	3.8	3.9	3.7	0.3	0.4	-0.3
T2_20	3.5	3.5	4	3.9	3.9	3.7	0.4	0.4	-0.3
T2_21	3.5	3.5	4	3.9	3.9	3.7	0.4	0.4	-0.3
T2_22	4	4	4	4.3	4.4	3.7	0.3	0.4	-0.3
T2_23	4	4	4	4.35	4.35	3.7	0.35	0.35	-0.3
T2_24	4	4	4	4.35	4.4	3.75	0.35	0.4	-0.25
T2_25	4.5	4.5	4	4.7	4.8	3.7	0.2	0.3	-0.3
T2_26	4.5	4.5	4	4.8	4.85	3.75	0.3	0.35	-0.25
T2_27	4.5	4.5	4	4.85	4.9	3.7	0.35	0.4	-0.3
				Average			0.31905	0.34762	-0.269

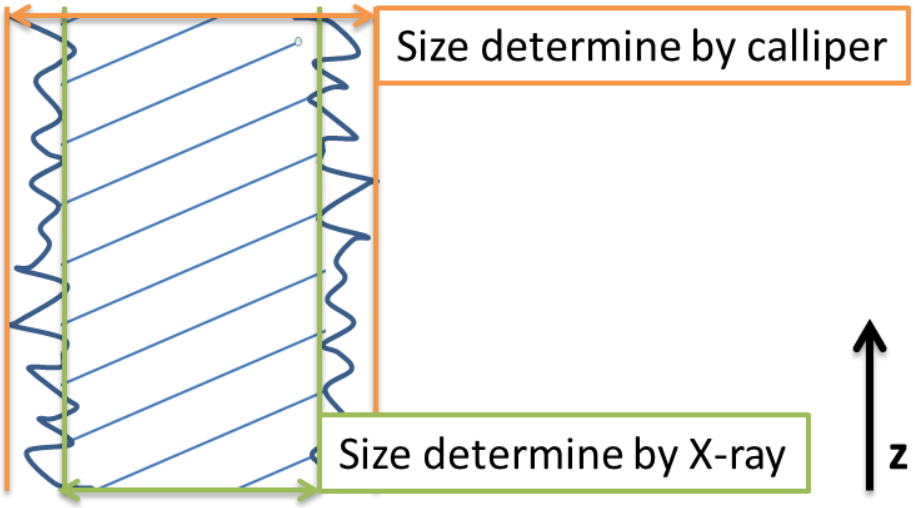

Figure 7.16 The size difference from manufacturing by EBM process measured by different method

The machining and tensile test was carried out by EXOVA; test results are shown in Figure 7.17, Figure 7.18 and Figure 7.19. From the graphs, it can be seen that there is a big scattering of the data, however there is still a trend (p value = 3.68×10^{-6}) showing a decrease in strength, associated with increase in the size of induced defect. The amount of strength decreased is approximately 2.7 MPa per 10% of induced defect.

From the literature review section, Al-Bermani[115], indicates the tensile properties of HIP EBM parts having a yield strength range from 840 MPa to 880 MPa, while the Near Net Shape HIP tensile properties found by Kim et al[117] are at approximately 826 Mpa. By looking at the yield strength graph, the result indicates the yield strength of EBM-HIP sample is 846 MPa; in addition, by extrapolating the graph, the yield strength will be 816 MPa if the sample is fully powder-HIP. Both values of the yield strengths are very similar to what found from literature review.

Thus, the slight decrease in material properties could mainly be due to the difference in the strength of microstructure. Regarding the elongation result shown in Figure 7.19, there is no clear correlation (p value = 0.068) between amounts of defect induced and the tensile elongation.

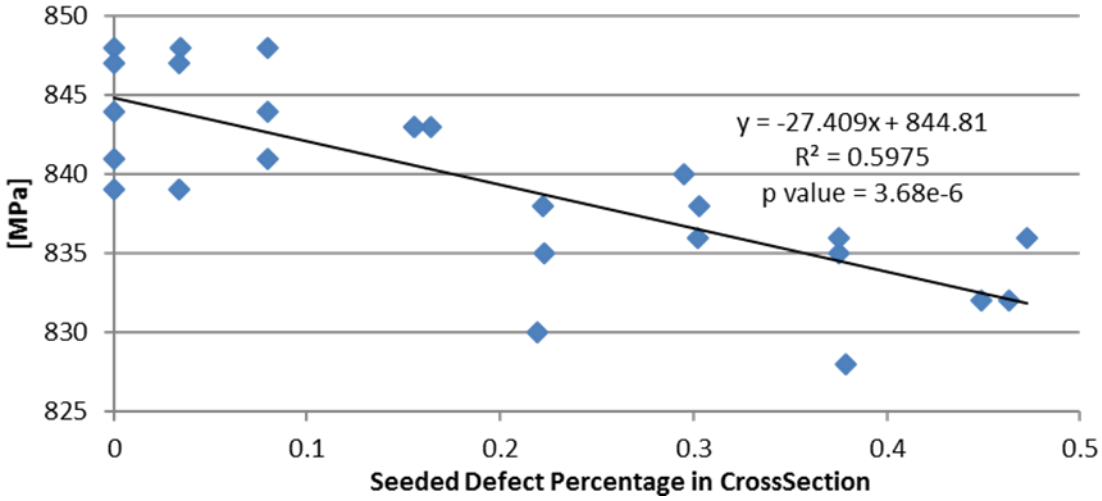

Figure 7.17 Yield Strength vs. Defect Percentage

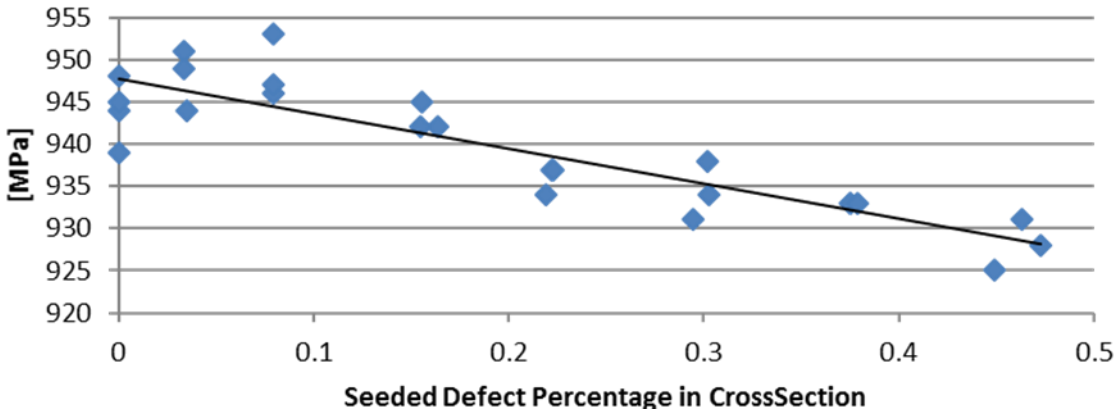

Figure 7.18 UTS Vs. Defect Percentage

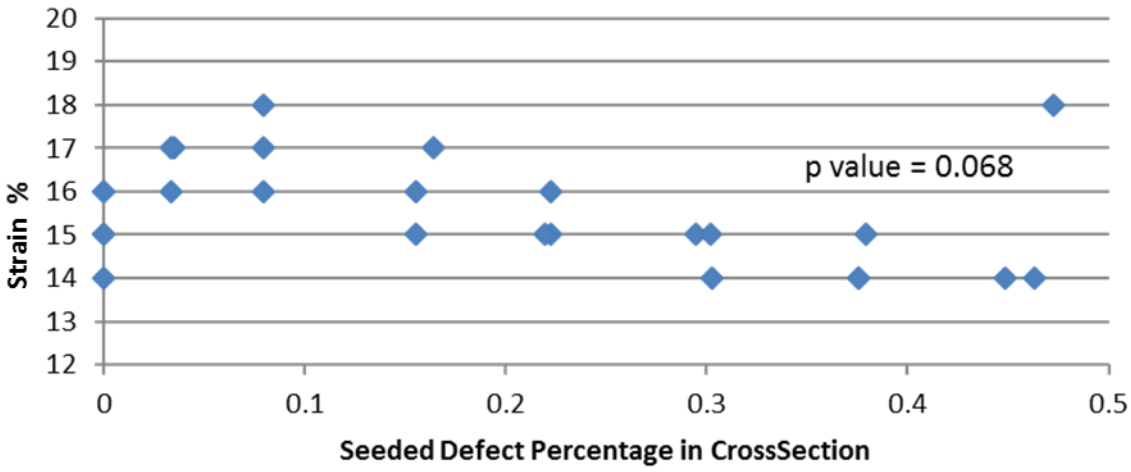

Figure 7.19 Elongation vs. Defect Percentage

7.3.3. Test 3: Fatigue Test

Fatigue test results are shown in Table 7.5. The life cycles achieved are sorted in order in Figure 7.20. From the graph, the control samples can be clustered into two different groups. For sample C3 and C5 the lifetime is extremely lower than any other result.

When observing the samples under microscope, the images indicate there some un-expected deep grooves on the surface which is suggested to be related with bad turning/machine process (Figure 7.21). By excluding these two samples, the remaining three control samples have lifetimes which are consistent with the specification privately supplied from ARCAM to GKN AMC and the literature review data with EBM-HIPped samples.[118,119,120]

Table 7.5 Fatigue sample test result

Sample ID	Load [MPa]	Cycles	Initiation Site	SEM observation
C1	800	1,049,576	centre	possibly at α grain boundaries
C2	800	1,224,285	1/3 D below surface	possibly at α grain boundaries
C3	800	85,681	surface	Turning initiated crack
C4	800	883,429	surface	-
C5	800	30,600	surface	Turning initiated crack
7	800	108,168	Primary: 1/6D below surface; Secondary: 1/6D below surface	Consolidated powder particles
8	800	124,007	1/6D below surface	Consolidated powder particles
9	800	819,209	1/4D below surface	α plate colony
10	800	454,155	1/4D below surface	-
11	800	588,733	Primary: 1/6D below surface; Secondary: 1/8D below surface	-
12	800	99,585	surface	-
13	800	212,744	1/4D below surface	Consolidated powder particles
14	800	629,837	1/4D below surface	α plate colony
15	800	737,363	Primary: 1/5D below surface; Secondary: in centre	α plate colony

By investigating the fractured surface under the microscope, three different types of fracture surface can be observed. In Figure 7.22, the image comes from the samples with fatigue life between 100k to 200k cycles with the observed microstructure being similar to powder particles consolidate by the HIP process; Figure 7.23 shows the samples with fatigue life from

400k to 800k cycles, the observed fracture surface shows microstructure similar to α plate colony; Figure 7.24 shows the control sample with high fatigue life of 800k to 1200k cycles, where the fracture appears to come from grain boundaries.

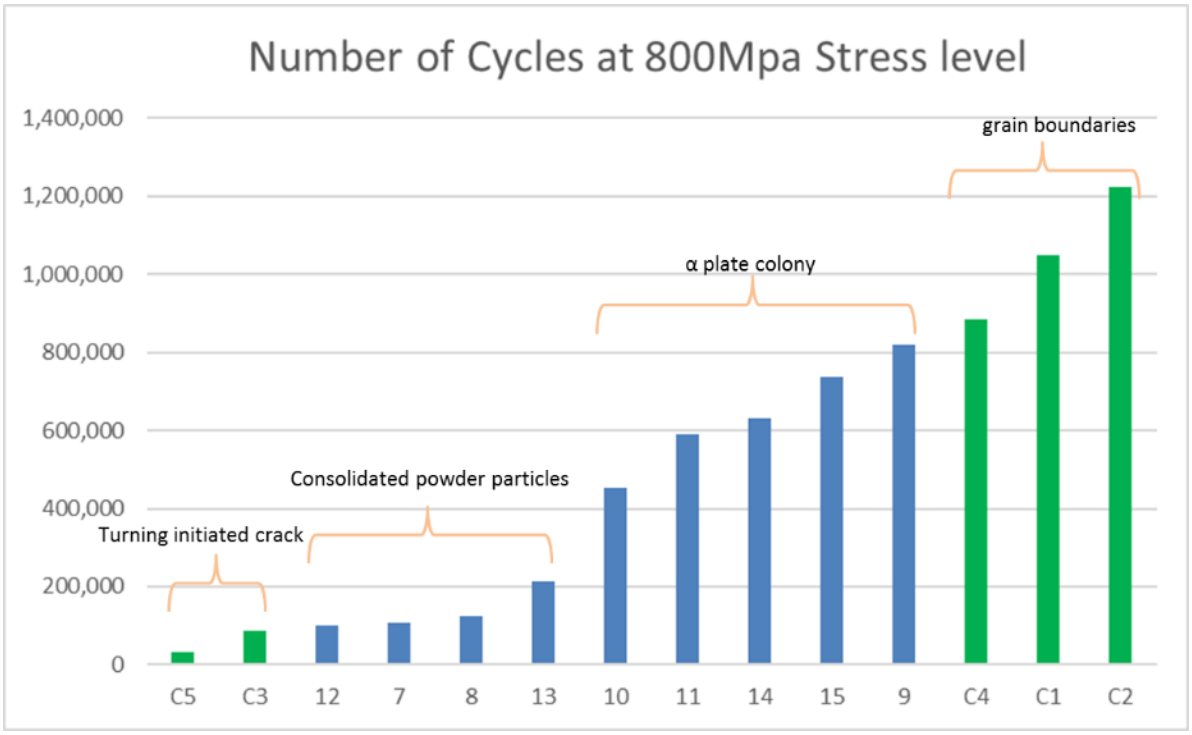

Figure 7.20 Fatigue cycles sort from least to most; green colour indicates the control samples

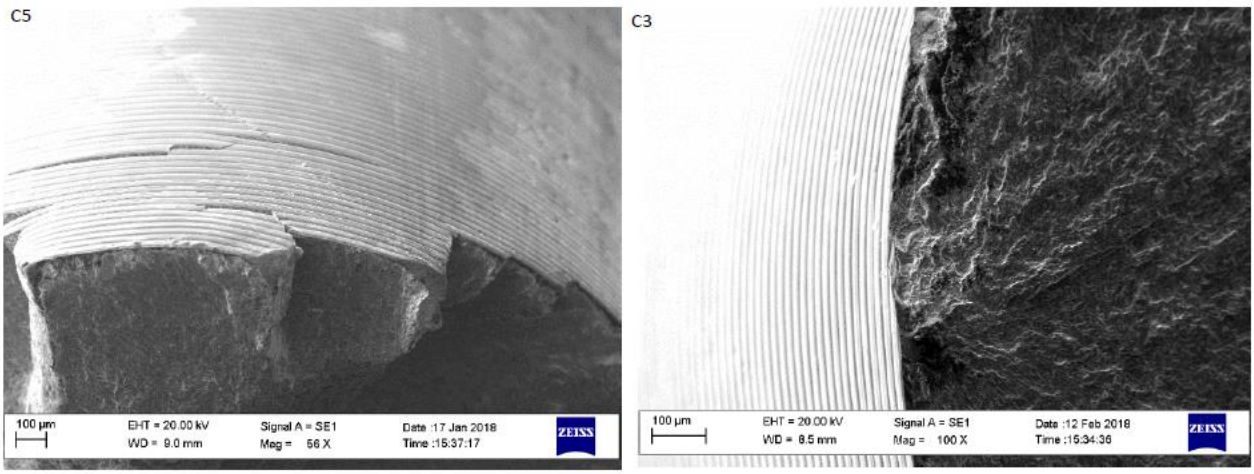

Figure 7.21 Sample having very low fatigue life due to cracks initiated at improper machined surface

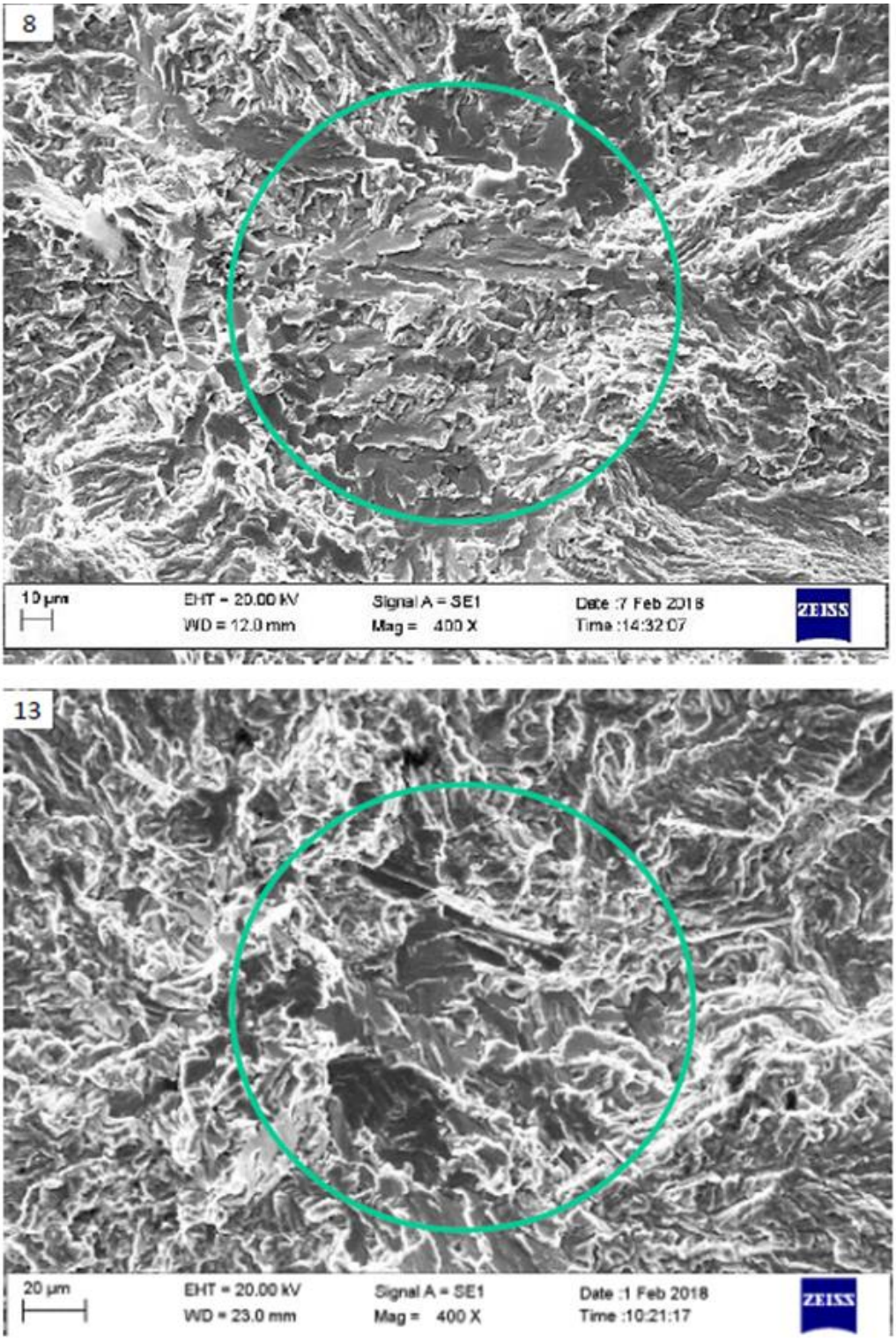

Figure 7.22 consolidated powder particle upon HIP (Sample 8&13)

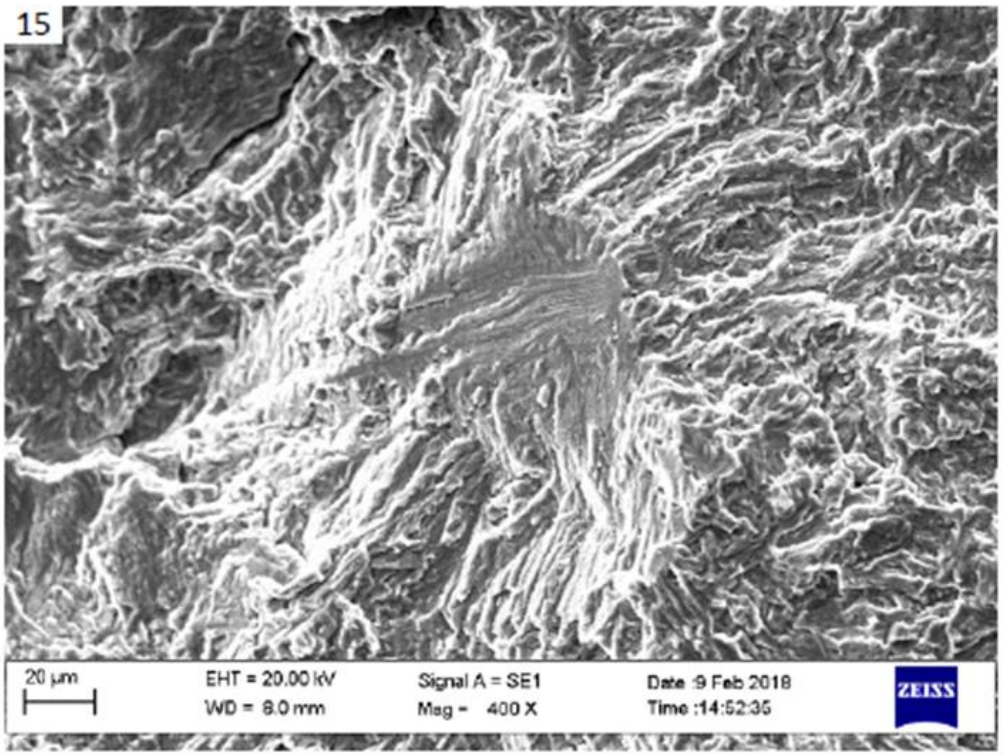

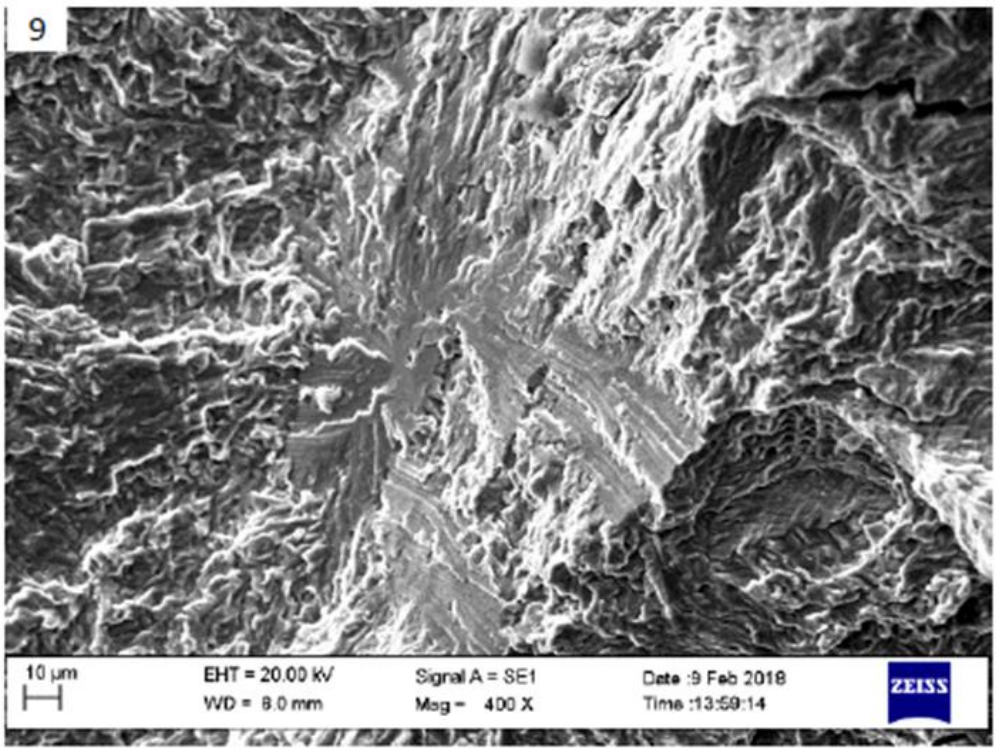

Figure 7.23 α plate colony (Sample 9 &15)

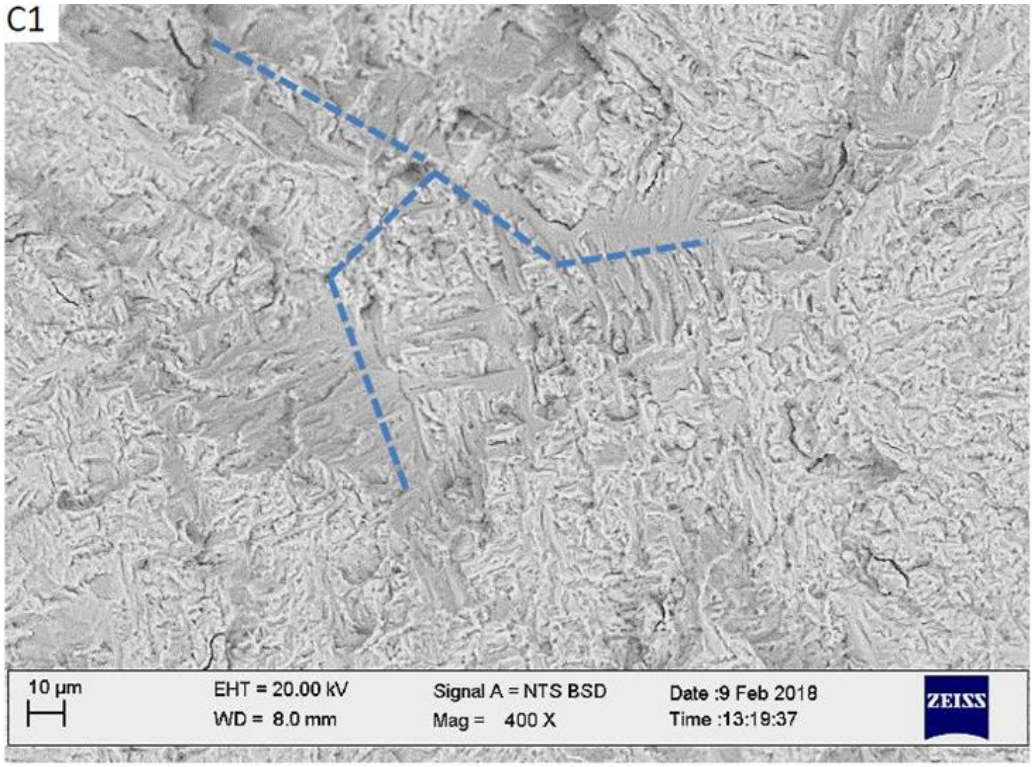

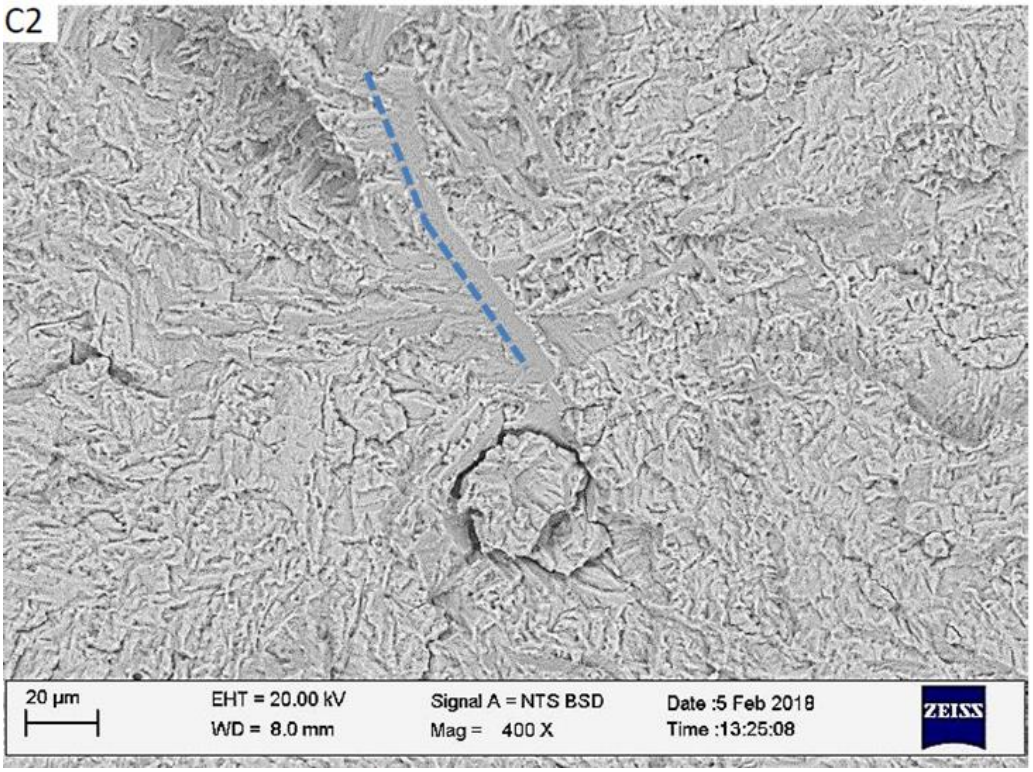

Figure 7.24 Back Scatter images showing initiation for very high HCF life samples at grain boundaries

From the results, excluding the turning issue samples, all the experiment samples have lower fatigue life than the control samples. From the current literature review result on near net shape (NNS) HIP Ti6Al4V components, the fatigue life at 800 MPa ranges from 10k to 30k cycles.[121,122] Zhang et al. have suggested due to the transfer from powder to solid material, imperfect bonding between particles can occur, thus reducing the fatigue life. In addition, clusters of alpha laths, which have similar crystallographic orientation, can be also result in crack initiation and rapid crack propagation. Furthermore, based on the observation from Zuo et al, the crack initiation in Ti6Al4V sample could be also caused by microstructural inhomogeneity.[123] All the above reasons could cause the seed defects sample have a lower fatigue life than fully EBM-HIPped samples.

By comparing the results from this chapter to the MMPDS data, (Figure 7.25), it can be seen that the fatigue properties for the controlled sample are better than cast, sheet and plate Ti6Al4V data. Due to the wide spread of the fatigue life, the samples with seeded defects have properties better than casting only.

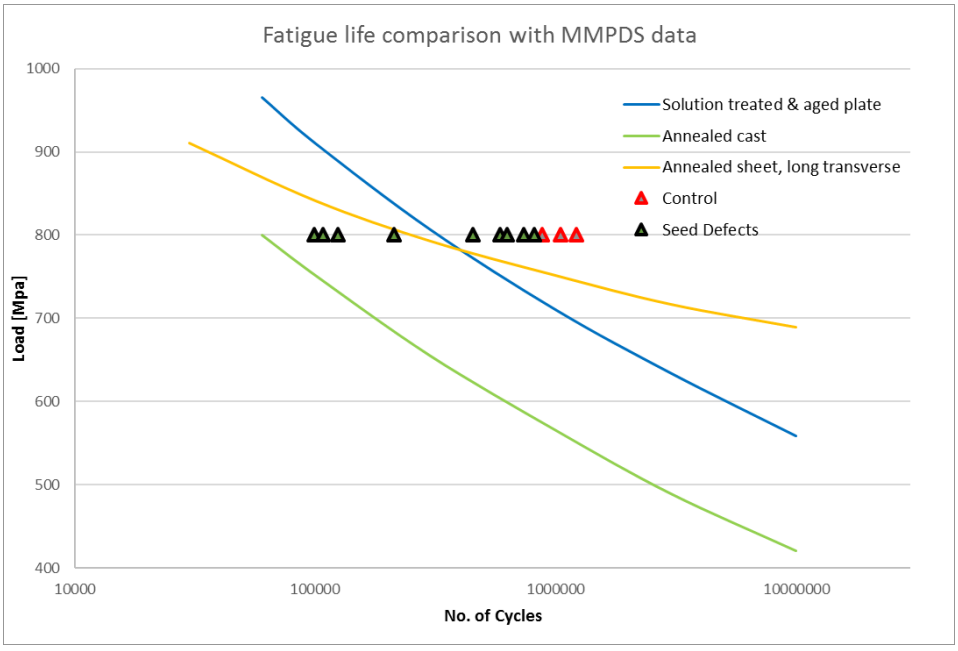

Figure 7.25 Comparison between MMPDS data sets and current test result

7.4. Conclusion

- There is a clear difference between the microstructure of the EBM-HIP region and the Powder-HIP region, which appears to have a different morphology. The EBM-HIP region maintains a lamellar morphology, but the Powder-HIP region has short and spherical morphology.

- Yield Stress and UTS decreases with increase in the seeded defect size

- The tensile elongation has no clear indication of being affected by the size of the induced defect.

- Through introducing seeded defects into an EBM component, fatigue life could be lowered by the possible improper bonding of HIP or inhomogeneous microstructures.

- The fatigue life of EBM-HIP samples is better than MMPDS annealed cast, sheet and plate data but the seeded defect with HIP samples only behaved better than cast data.

Chapter 8 : Conclusion

In an Electron Beam Melting (EBM) process, a Lack of Fusion (LOF) type defect is detrimental to the final part's mechanical properties. This type of defect is generally large in size and often filled with un-melted powder. Due to the nature of the process, this type of defect can travel from layer to layer until the build stops.

Tests have been performed to study this type of defects and the results show that the formation of LOF depends heavily on the previous layer's surface condition. The research indicates that if a cavity is presented in the previous layer, the solidification of the material on the next layer is affected and a similar cavity is more likely to form again.

A Near Infra-Red (NIR) camera has been installed by the machine manufacturers (ARCAM) into an EBM machine, which is able to capture an image after each layer is completed. Because the appearance of LOF on the top surface is a cavity like structure which exhibits higher emissivity, the appearance of LOF is much brighter than the surrounding regions in these images.

Although ARCAM has integrated the camera into the machine, they didn't provide any successful defect predication models from these images. In this research, an algorithm is developed which referred as LayerDD. The algorithm analyses all the images and capable of identifying the LOF from layer to layer. The output of LayerDD can be in STL format, which is designed to be overlapped with the original build configuration. When comparing the defect prediction from LayerDD to CT scan data and cut-up sample images, results show a good consistency in both size and shape but some minor miss-correlations are still seen to occur.

The camera is designed to take the image of the top surface only, thus any changes under the layer are left un-detected. This raises the first limitation of the system. The second limitation is the inability to identify defects near the layer edges. This is because the LayerDD system

excludes contour regions from the analysis to avoid the aforementioned brightness discrepancies around the layer boundaries, which are similar to the brightness of a defect region.

The cost of the LayerDD system is evaluated in this research. The value shows that the cost and time for the LayerDD system is beneficial for products undergoing research and development, but is relative costly if the machine is in a stable state during the production process. The above cost analysis is based on the LayerDD system not replacing any other NDT technique, however if LayerDD is proven to be trustworthy then there is potential to use the LayerDD system to greatly improve defect detection and classification.

Since LayerDD systems can be used to identify top surface defect during the process, it should be possible to carry out methods to rectify these defect during the printing process. Tests have been performed with parameters modified from the default EBM Q20 parameters. The modified parameters include changes in Line Offset (distance between adjacent scan lines), Speed Function (beam speed) and Focus Offset (beam diameter).

Each parameter setting has been evaluated and its corresponding ability of defect rectification assessed. The results indicate that defect rectification is best linked to the depth of the melt pool regardless what parameter set has been used. In addition, the experiments also show that if the parameter has produced a very narrow melt pool (e.g. reduced focus offset) it carries a higher risk of spattering during the process leading to a dimpled top surface, which could reproduce the defects after they have been rectified on the previous layer.

A material testing plan has been presented in the last chapter of this research. The test aimed to study the effect of LOF on the final material properties after the HIP treatment. The result indicates there are different microstructures between EBM-HIP regions and Powder-HIP regions. Tensile tests have been performed and showed that Yield Stress and UTS decrease

slightly with an increase in seeded defect size (a 40% of induced defects with HIP process for instance will reduce UTS process by an average of 11MPa). The tensile elongation showed no indication of being linked to the induced defect. Fatigue tests were also performed, and indicated that the fatigue life could be lowered due to possible improper bonding upon HIP and/or inhomogeneous microstructures.

Chapter 9 : Further Work

The LayerDD System

The current LayerDD system is capable of identifying Lack of Fusion (LOF) within the part by excluding the layer edge regions. But, the contour of the part is as important as the interior and is more important if the part is undergoing HIP. Thus, a separate algorithm should be developed enable LayerDD to identify open surface defects.

In addition, as mentioned in the LayerDD chapter, raw image file storage is very costly for the aerospace industry, so it is good practice on pretence of cost reduction to delete the raw images once analysis is complete. This requires the software to be more reliable and robust. As such, more tests and more cross-validations should be made on the LayerDD system.

Close Loop Control

The close loop control (CLC) algorithm has been tested exclusively on simple geometries at this time. One of the possible limitations of CLC is adapting the fixing parameter for overhanging surfaces. Due to the presence of support structures, LOF defects are very likely to originate from support surfaces, but the cooling rate at the overhang is very low and much thus much more likely to cause swelling. By applying a powerful melt track on the overhang surfaces, it is possible to fully penetrate the material to the detriment of geometry accuracy. Subsequently overhanging surfaces should be tested with specialised parameter combinations.

In the current stage, because the core of ARCAM EBM control is not in the public domain, the fixing is performed manually on each layer on which it is needed. A real close loop control system should allow a fully automated process, and the fixing parameter should apply automatically to any region where LOF has been identified. For example, when LOF has been identified, the modified parameter should activate on the next layer with the modified melt path

including a circular track encompassing the defect at a radius of 5mm diameter around the identified LOF centre. This calls for both additional algorithm development and system control modification on existing EBM machines.

Reference

[1] Hopkinson, N., Hague, R. and Dickens, P. eds., 2006. Rapid manufacturing: an industrial revolution for the digital age. John Wiley & Sons.

[2] Berman, B., 2012. 3-D printing: The new industrial revolution. Business horizons, 55(2), pp.155-162.

[3] Atzeni, E. and Salmi, A., 2012. Economics of additive manufacturing for end-usable metal parts. The International Journal of Advanced Manufacturing Technology, 62(9-12), pp.1147-1155.

[4] Lipton, J.I., Cutler, M., Nigl, F., Cohen, D. and Lipson, H., 2015. Additive manufacturing for the food industry. Trends in food science & technology, 43(1), pp.114-123.

[5] Mueller, B., 2012. Additive manufacturing technologies–Rapid prototyping to direct digital manufacturing. Assembly Automation, 32(2).

[6] Schiller, G.J., 2015, March. Additive manufacturing for aerospace. In Aerospace Conference, 2015 IEEE (pp. 1-8). IEEE.

[7] Lim, S., Buswell, R.A., Le, T.T., Austin, S.A., Gibb, A.G. and Thorpe, T., 2012. Developments in construction-scale additive manufacturing processes. Automation in construction, 21, pp.262-268.

[8] Russell, A., 1955. The Rev. William Gregor (1761-1817), Discoverer of Titanium. Mineralogical Magazine, 30, pp.617-624.

[9] Al-Bermani, S.S., 2011. An investigation into microstructure and microstructural control of additive layer manufactured Ti-6Al-4V by electron beam melting (Doctoral dissertation, University of Sheffield).

[10] Chen, G.Z., Fray, D.J. and Farthing, T.W., 2000. Direct electrochemical reduction of titanium dioxide to titanium in molten calcium chloride. nature, 407(6802), p.361.

[11] Zhang, W., Zhu, Z. and Cheng, C.Y., 2011. A literature review of titanium metallurgical processes. *Hydrometallurgy*, *108*(3), pp.177-188

[12] Leyens, C. and Peters, M. eds., 2003. Titanium and titanium alloys: fundamentals and applications. John Wiley & Sons.

[13] ASTM International standard for Titanium

[14] Ivasishin, O.M., Markovsky, P.E., Matviychuk, Y.V., Semiatin, S.L., Ward, C.H. and Fox, S., 2008. A comparative study of the mechanical properties of high-strength β-titanium alloys. Journal of alloys and compounds, 457(1), pp.296-309.

[15] Kosaka, Y., Fox, S.P., Faller, K. and Reichman, S.H., 2005. Properties and processing of TIMETAL LCB. Journal of materials engineering and performance, 14(6), pp.792-798.

[16] Antonysamy, A.A., 2012. Microstructure, texture and mechanical property evolution during additive manufacturing of Ti6Al4V alloy for aerospace applications.

[17] Inagaki, I., Takechi, T., Shirai, Y. and Ariyasu, N., 2014. Application and features of titanium for the aerospace industry. Nippon steel & sumitomo metal technical report, 106, pp.22-27.

[18] Donachie, M.J., 2000. Titanium: a technical guide. ASM international.

[19] Boyer, R.R., 1996. An overview on the use of titanium in the aerospace industry. Materials Science and Engineering: A, 213(1-2), pp.103-114.

[20] Peters, M., Kumpfert, J., Ward, C.H. and Leyens, C., 2003. Titanium alloys for aerospace applications. Advanced Engineering Materials, 5(6), pp.419-427.

[21] Boyer, R.R., 2010. Attributes, characteristics, and applications of titanium and its alloys. JOM Journal of the Minerals, Metals and Materials Society, 62(5), pp.21-24.

[22] Inagaki, I., Takechi, T., Shirai, Y. and Ariyasu, N., 2014. Application and features of titanium for the aerospace industry. Nippon steel & sumitomo metal technical report, 106, pp.22-27.

[23] Froes, F.H. and Imam, A.M., 2010. Cost affordable developments in titanium technology and applications. In Key Engineering Materials (Vol. 436, pp. 1-11). Trans Tech Publications.

[24] Nabhani, F., 2001. Machining of aerospace titanium alloys. Robotics and Computer-Integrated Manufacturing, 17(1), pp.99-106.

[25] Ezugwu, E.O. and Wang, Z.M., 1997. Titanium alloys and their machinability—a review. Journal of materials processing technology, 68(3), pp.262-274.

[26] https://goo.gl/images/Ae52M6 (Access on 25/5/2018)

[27] Gibson, I., Rosen, D.W. and Stucker, B., 2010. Additive manufacturing technologies (Vol. 238). New York: Springer.

[28] Bikas, H., Stavropoulos, P. and Chryssolouris, G., 2016. Additive manufacturing methods and modelling approaches: a critical review. The International Journal of Advanced Manufacturing Technology, 83(1-4), pp.389-405.

[29] Frazier, W.E., 2014. Metal additive manufacturing: a review. Journal of Materials Engineering and Performance, 23(6), pp.1917-1928.

[30] ARCAM Training Document- Introduction - 2013

[31] Gunenthiram, V., Peyre, P., Schneider, M., Dal, M., Coste, F., Koutiri, I. and Fabbro, R., 2018. Experimental analysis of spatter generation and melt-pool behavior during the powder bed laser beam melting process. Journal of Materials Processing Technology, 251, pp.376-386.

[32] C. Qiu, C. Panwisawas,M.Ward, et al., On the role ofmelt flowinto the surface structure and porosity development during selective laser melting[J], Acta Mater. 96 (2015) 72–79.

[33 Yadroitsev, I., Gusarov, A., Yadroitsava, I. and Smurov, I., 2010. Single track formation in selective laser melting of metal powders. Journal of Materials Processing Technology, 210(12), pp.1624-1631.

[34] Ly, S., Matthews, M., Guss, G., Rubenchik, S. and Khairallah, S., 2017. Dynamics of Droplet Ejection from Metal Powder Bed Layer in Laser Additive Manufacturing as Probed by

High Speed Imaging (No. LLNL-CONF-739438). Lawrence Livermore National Lab.(LLNL), Livermore, CA (United States).

[35] Ladewig, A., Schlick, G., Fisser, M., Schulze, V. and Glatzel, U., 2016. Influence of the shielding gas flow on the removal of process by-products in the selective laser melting process. Additive Manufacturing, 10, pp.1-9.

[36] Wakabayashi, M., Jatco Corp, 1991. Spatter-free electron beam welding apparatus with spatter catching device associated therewith. U.S. Patent 5,075,532.

[37] Guo, C., Ge, W. and Lin, F., 2015. Effects of scanning parameters on material deposition during Electron Beam Selective Melting of Ti-6Al-4V powder. Journal of Materials Processing Technology, 217, pp.148-157.

[38] Rai, R., Burgardt, P., Milewski, J.O., Lienert, T.J. and DebRoy, T., 2008. Heat transfer and fluid flow during electron beam welding of 21Cr–6Ni–9Mn steel and Ti–6Al–4V alloy. Journal of Physics D: Applied Physics, 42(2).

[39] Fabbro, R., Hirano, K. and Pang, S., 2016. Analysis of the physical processes occurring during deep penetration laser welding under reduced pressure. Journal of Laser Applications, 28(2).

[40] Chhabra, R.P., 1993. Bubbles, drops, and particles in non-Newtonian fluids. CRC PressI Llc.

[41] Gharbi, M., Peyre, P., Gorny, C., Carin, M., Morville, S., Le Masson, P., Carron, D. and Fabbro, R., 2013. Influence of various process conditions on surface finishes induced by the direct metal deposition laser technique on a Ti–6Al–4V alloy. Journal of materials processing technology, 213(5), pp.791-800.

[42] Egry, I., Holland-Moritz, D., Novakovic, R., Ricci, E., Wunderlich, R. and Sobczak, N., 2010. Thermophysical properties of liquid AlTi-based alloys. International Journal of Thermophysics, 31(4-5), pp.949-965.

[43] Lu, Z. and Huang, P., 2011. The Mechanism of Undercut Formation and High Speed Welding Technology. In Arc Welding. InTech.

[44] Kruth, J.P., Froyen, L., Van Vaerenbergh, J., Mercelis, P., Rombouts, M. and Lauwers, B., 2004. Selective laser melting of iron-based powder. Journal of Materials Processing Technology, 149(1), pp.616-622.

[45] Gunenthiram, V., Peyre, P., Schneider, M., Dal, M., Coste, F. and Fabbro, R., 2017. Analysis of laser–melt pool–powder bed interaction during the selective laser melting of a stainless steel. Journal of Laser Applications, 29(2).

[46] Yadroitsev, I. and Smurov, I., 2011. Surface morphology in selective laser melting of metal powders. Physics Procedia, 12, pp.264-270.

[47] Gong, H., Rafi, K., Gu, H., Ram, G.J., Starr, T. and Stucker, B., 2015. Influence of defects on mechanical properties of Ti–6Al–4V components produced by selective laser melting and electron beam melting. Materials & Design, 86, pp.545-554.

[48] Duley W W 1999 Laser Welding (New York: Wiley Interscience)

[49] Dinwiddie, R.B., Dehoff, R.R., Lloyd, P.D., Lowe, L.E. and Ulrich, J.B., 2013, May. Thermographic in-situ process monitoring of the electron-beam melting technology used in additive manufacturing. In Thermosense: Thermal Infrared Applications XXXV (Vol. 8705, p. 87050K). International Society for Optics and Photonics.

[50] Ammer, R., Rüde, U., Markl, M., Jüchter, V. and Körner, C., 2014. Validation experiments for LBM simulations of electron beam melting. International Journal of Modern Physics C, 25(12).

[51] Karlsson, J., Norell, M., Ackelid, U., Engqvist, H. and Lausmaa, J., 2015. Surface oxidation behavior of Ti–6Al–4V manufactured by Electron Beam Melting (EBM®). Journal of Manufacturing Processes, 17, pp.120-126.

[52] Algardh, J.K., Horn, T., West, H., Aman, R., Snis, A., Engqvist, H., Lausmaa, J. and Harrysson, O., 2016. Thickness dependency of mechanical properties for thin-walled titanium parts manufactured by Electron Beam Melting (EBM)®. *Additive Manufacturing*, *12*, pp.45-50.

[53] Sames, W.J., Medina, F., Peter, W.H., Babu, S.S. and Dehoff, R.R., 2014, December. Effect of process control and powder quality on Inconel 718 produced using electron beam melting. In 8th International Symposium on Superalloy 718 and Derivatives (pp. 409-423). John Wiley & Sons, Inc..

[54] Gratzke, U., Kapadia, P.D., Dowden, J., Kroos, J. and Simon, G., 1992. Theoretical approach to the humping phenomenon in welding processes. Journal of Physics D: Applied Physics, 25(11), p.1640.

[55] Achebo, J.I., 2012. Complex behavior of forces influencing molten weld metal flow based on static force balance theory. Physics Procedia, 25, pp.317-324.

[56] Bauereiß, A., T. Scharowsky, and C. Körner. "Defect generation and propagation mechanism during additive manufacturing by selective beam melting." Journal of Materials Processing Technology 214.11 (2014): 2522-2528.

[57] S. M. Gaytan, L. E. Murr, F. Medina, E. Martinez, M. I. Lopez, and R. B. Wicker, “Advanced metal powder based manufacturing of complex components by electron beam melting,” Materials Technology: Advanced Performance Materials, vol. 24, no. 3, pp. 180–190, 2009.

[58] Puebla, Karina, et al. "Effect of melt scan rate on microstructure and macrostructure for electron beam melting of Ti-6Al-4V." (2012).

[59] Aboulkhair, Nesma T., et al. "Reducing porosity in AlSi10Mg parts processed by selective laser melting." Additive Manufacturing 1 (2014): 77-86.

[60] Gong, Haijun, et al. "Analysis of defect generation in Ti–6Al–4V parts made using powder bed fusion additive manufacturing processes." Additive Manufacturing 1 (2014): 87-98.

[61] Tammas-Williams, S., Zhao, H., Léonard, F., Derguti, F., Todd, I. and Prangnell, P.B., 2015. XCT analysis of the influence of melt strategies on defect population in Ti–6Al–4V components manufactured by Selective Electron Beam Melting. Materials Characterization, 102, pp.47-61.

[62] Photo supplied from GKN AMC

[63] AP&C: 'Designed for additive manufacturing', 2014. Available at http://advancedpowders.com/our-plasma-atomized-powders/designed-for-additive-manufacturing/

[64] Sames, W.J., List, F.A., Pannala, S., Dehoff, R.R. and Babu, S.S., 2016. The metallurgy and processing science of metal additive manufacturing. International Materials Reviews, 61(5), pp.315-360.

[65] Loeber, L., Biamino, S., Ackelid, U., Sabbadini, S., Epicoco, P., Fino, P. and Eckert, J., 2011, August. Comparison of selective laser and electron beam melted titanium aluminides. In Proceedings of the Solid Freeform Fabrication Symposium, Austin, TX, USA (pp. 8-10).

[66] Ali, H., Ma, L., Ghadbeigi, H. and Mumtaz, K., 2017. In-situ residual stress reduction, martensitic decomposition and mechanical properties enhancement through high temperature powder bed pre-heating of Selective Laser Melted Ti6Al4V. Materials Science and Engineering: A, 695, pp.211-220.

[67] H. Atkinson and S. Davies, "Fundamental aspects of hot isostatic pressing: an overview," Metallurgical and Materials Transactions A, vol. 31A, no. 12, pp. 2981–3000, 2000.

[68] ASTM F2924-12 Standard specification for additive manufacturing Ti6Al4V with powder bed fusion

[69] Mankins, J.C., 1995. Technology readiness levels. White Paper, April, 6.

[70] Tapia, G. and Elwany, A., 2014. A review on process monitoring and control in metal-based additive manufacturing. Journal of Manufacturing Science and Engineering, 136(6), p.060801.

[71] Price, S., Lydon, J., Cooper, K., & Chou, K. (2013, August). Experimental temperature analysis of powder-based electron beam additive manufacturing. In Proceedings of the Solid Freeform Fabrication Symposium (pp. 162-173).

[72] Rodriguez E, Mireles J, Terrazas CA, Espalin D, Perez MA, Wicker RB, Approximation of absolute surface temperature measurements of powder bed fusion additive manufacturing technology using in situ infrared thermography, AdditManuf (2015), http://dx.doi.org/10.1016/j.addma.2014.12.001

[73] Mireles, J., Terrazas, C., Medina, F., & Wicker, R. (2013). Automatic feedback control in electron beam melting using infrared thermography. In Proceedings of the Solid Freeform Fabrication Symposium.

[74] Mireles, J., Terrazas, C., Gaytan, S. M., Roberson, D. A., & Wicker, R. B. (2015). Closed-loop automatic feedback control in electron beam melting. The International Journal of Advanced Manufacturing Technology, 78(5-8), 1193-1199.

[75] Zenzinger, G., Bamberg, J., Ladewig, A., Hess, T., Henkel, B., & Satzger, W. (2015, March). Process monitoring of additive manufacturing by using optical tomography. In *41ST ANNUAL REVIEW OF PROGRESS IN QUANTITATIVE NONDESTRUCTIVE EVALUATION: Volume 34* (Vol. 1650, pp. 164-170). AIP Publishing.

[76] Berumen, S., Bechmann, F., Lindner, S., Kruth, J. P., & Craeghs, T. (2010). Quality control of laser-and powder bed-based Additive Manufacturing (AM) technologies. Physics procedia, 5, 617-622.

[77] Craeghs, T., Bechmann, F., Berumen, S., & Kruth, J. P. (2010). Feedback control of Layerwise Laser Melting using optical sensors. Physics Procedia, 5, 505-514.

[78] Jean-Pierre Kruth, Peter Mecelis. (2009). U.S. 'PROCEDURE AND APPARATURS FOR IN-SITU MONITORING AND FEEDBACK CONTROL OF SELECTIVE LASER POWDER PROCESSING', Patent No. 2009/0206065 A1

[79] Craeghs, T., Bechmann, F., Berumen, S., & Kruth, J. P. (2010). Feedback control of Layerwise Laser Melting using optical sensors. Physics Procedia, 5, 505-514.

[80] Clijsters, S., Craeghs, T., Buls, S., Kempen, K., & Kruth, J. P. (2014). In situ quality control of the selective laser melting process using a high-speed, real-time melt pool monitoring system. The International Journal of Advanced Manufacturing Technology, 75(5-8), 1089-1101.

[81] Lott, P., Schleifenbaum, H., Meiners, W., Wissenbach, K., Hinke, C., & Bültmann, J. (2011). Design of an optical system for the in situ process monitoring of selective laser melting (SLM). Physics Procedia, 12, 683-690.

[82] Scharowsky, T., Osmanlic, F., Singer, R. F., & Körner, C. (2014). Melt pool dynamics during selective electron beam melting. Applied Physics A, 114(4), 1303-1307.

[83] Neef, A., Seyda, V., Herzog, D., Emmelmann, C., Schönleber, M., & Kogel-Hollacher, M. (2014). Low Coherence Interferometry in Selective Laser Melting. Physics Procedia, 56, 82-89.

[84] Kleszczynski, S., zur Jacobsmühlen, J., Reinarz, B., Sehrt, J. T., Witt, G., & Merhof, D. (2014). Improving process stability of laser beam melting systems. In Proceedings of the Frauenhofer Direct Digital Manufacturing Conference.

[85] Bernd Reinarz. (2015). U.S. 'Method and Divice for Producing Components in a Beam Melting Installation' Patent No.US 20150115490 A1

[86] ARCAM Training Document- Process Setting - 2017

[87] ARCAM communication – Chrisoffer Sjogren

[88] SODICK machine training documents

[89] Sih, S.S. and Barlow, J.W., 2004. The prediction of the emissivity and thermal conductivity of powder beds. Particulate Science and Technology, 22(4), pp.427-440.

[90] Mills, K.C., 2002. Recommended values of thermophysical properties for selected commercial alloys. Woodhead Publishing.

[91] Rodriguez, E., Mireles, J., Terrazas, C.A., Espalin, D., Perez, M.A. and Wicker, R.B., 2015. Approximation of absolute surface temperature measurements of powder bed fusion additive manufacturing technology using in situ infrared thermography. Additive Manufacturing, 5, pp.31-39.

[92] Klassen, A., Bauereiß, A. and Körner, C., 2014. Modelling of electron beam absorption in complex geometries. Journal of Physics D: Applied Physics, 47(6).

[93] Tabata, T., Andreo, P. and Shinoda, K., 1999. Fractional energies of backscattered electrons and photon yields by electrons. Radiation Physics and Chemistry, 54(1), pp.11-18.

[94] Al-Bermani, S.S., 2011. An investigation into microstructure and microstructural control of additive layer manufactured Ti-6Al-4V by electron beam melting (PhD Thesis, University of Sheffield,2011).

[95] Price, S., Lydon, J., Cooper, K. and Chou, K., 2013, August. Experimental temperature analysis of powder-based electron beam additive manufacturing. In Proceedings of the Solid Freeform Fabrication Symposium (pp. 162-173).

[96] ARCAM user manual 2017

[97] ARCAM engineer communication: Marcus Renås

[98] Zenzinger, G., Bamberg, J., Ladewig, A., Hess, T., Henkel, B., & Satzger, W. (2015, March). Process monitoring of additive manufacturing by using optical tomography. In *41ST ANNUAL REVIEW OF PROGRESS IN QUANTITATIVE NONDESTRUCTIVE EVALUATION: Volume 34* (Vol. 1650, pp. 164-170). AIP Publishing.

[99] Mireles, J., Terrazas, C., Medina, F., & Wicker, R. (2013). Automatic feedback control in electron beam melting using infrared thermography. In Proceedings of the Solid Freeform Fabrication Symposium.

[100] Jean-Pierre Kruth, Peter Mecelis. (2009). U.S. 'PROCEDURE AND APPARATURS FOR IN-SITU MONITORING AND FEEDBACK CONTROL OF SELECTIVE LASER POWDER PROCESSING', Patent No. 2009/0206065 A1

[101] Eragubi, Munir. "Slicing 3D CAD Model in STL Format and Laser Path." (2013).

[102] Otsu, N., 1979. A threshold selection method from gray-level histograms. *IEEE transactions on systems, man, and cybernetics*, *9*(1), pp.62-66.

[103] Communicate with Simon Mckown (GKN process specialist) and ARCAM service engineering.

[104] Bauereiß, A., T. Scharowsky, and C. Körner. "Defect generation and propagation mechanism during additive manufacturing by selective beam melting." Journal of Materials Processing Technology 214.11 (2014): 2522-2528.

[105] GKN Internal Communication.

[106] Tille, J. and Kelly, J.C., 1963. The surface tension of liquid titanium. British Journal of Applied Physics, 14(10), p.717.

[107] Semak, V.V., Knorovsky, G.A., MacCallum, D.O. and Roach, R.A., 2006. Effect of surface tension on melt pool dynamics during laser pulse interaction. Journal of Physics D: Applied Physics, 39(3), p.590.

[108] Gharbi, M., Peyre, P., Gorny, C., Carin, M., Morville, S., Le Masson, P., Carron, D. and Fabbro, R., 2013. Influence of various process conditions on surface finishes induced by the direct metal deposition laser technique on a Ti–6Al–4V alloy. Journal of materials processing technology, 213(5), pp.791-800.

[109] Kruth, J.P., Froyen, L., Van Vaerenbergh, J., Mercelis, P., Rombouts, M. and Lauwers, B., 2004. Selective laser melting of iron-based powder. Journal of Materials Processing Technology, 149(1), pp.616-622.

[110] Lu, Z. and Huang, P., 2011. The Mechanism of Undercut Formation and High Speed Welding Technology. In Arc Welding. InTech.

[111] Yadroitsev, I. and Smurov, I., 2011. Surface morphology in selective laser melting of metal powders. Physics Procedia, 12, pp.264-270.

[112] Ly, S., Rubenchik, A.M., Khairallah, S.A., Guss, G. and Matthews, M.J., 2017. Metal vapor micro-jet controls material redistribution in laser powder bed fusion additive manufacturing. Scientific reports, 7(1), p.4085.

[113] Xu, L., Guo, R., Bai, C., Lei, J. and Yang, R., 2014. Effect of hot isostatic pressing conditions and cooling rate on microstructure and properties of Ti–6Al–4V alloy from atomized powder. *Journal of Materials Science & Technology*, *30*(12), pp.1289-1295.

[114] Murr, L.E., Quinones, S.A., Gaytan, S.M., Lopez, M.I., Rodela, A., Martinez, E.Y., Hernandez, D.H., Martinez, E., Medina, F. and Wicker, R.B., 2009. Microstructure and mechanical behavior of Ti–6Al–4V produced by rapid-layer manufacturing, for biomedical applications. *Journal of the mechanical behavior of biomedical materials*, *2*(1), pp.20-32.

[115] Al-Bermani, S.S., Blackmore, M.L., Zhang, W. and Todd, I., 2010. The origin of microstructural diversity, texture, and mechanical properties in electron beam melted Ti-6Al-4V. Metallurgical and materials transactions a, 41(13), pp.3422-3434.

[116] Hernández-Nava, E., Smith, C.J., Derguti, F., Tammas-Williams, S., Léonard, F., Withers, P.J., Todd, I. and Goodall, R., 2016. The effect of defects on the mechanical response of Ti-6Al-4V cubic lattice structures fabricated by electron beam melting. Acta Materialia, 108, pp.279-292.

[117] Kim, Y., Kim, E.P., Song, Y.B., Lee, S.H. and Kwon, Y.S., 2014. Microstructure and mechanical properties of hot isostatically pressed Ti–6Al–4V alloy. Journal of Alloys and Compounds, 603, pp.207-212.

[118] Zhao, X., Li, S., Zhang, M., Liu, Y., Sercombe, T.B., Wang, S., Hao, Y., Yang, R. and Murr, L.E., 2016. Comparison of the microstructures and mechanical properties of Ti–6Al–4V fabricated by selective laser melting and electron beam melting. *Materials & Design*, *95*, pp.21-31.

[119] Hrabe, N., Gnäupel-Herold, T. and Quinn, T., 2017. Fatigue properties of a titanium alloy (Ti–6Al–4V) fabricated via electron beam melting (EBM): Effects of internal defects and residual stress. *International Journal of Fatigue*, *94*, pp.202-210.

[120] Edwards, P. and Ramulu, M., 2014. Fatigue performance evaluation of selective laser melted Ti–6Al–4V. *Materials Science and Engineering: A*, *598*, pp.327-337.

[121] Voice, W., 2006. Net-shape processing applied to aero-engine components. ROLLS-ROYCE PLC DERBY (UNITED KINGDOM).

[122] Zhang, K., Mei, J., Wain, N. and Wu, X., 2010. Effect of hot-isostatic-pressing parameters on the microstructure and properties of powder Ti-6Al-4V hot-isostatically-pressed samples. Metallurgical and Materials Transactions A, 41(4), pp.1033-1045.

[123] Zuo, J.H., Wang, Z.G. and Han, E.H., 2008. Effect of microstructure on ultra-high cycle fatigue behavior of Ti–6Al–4V. *Materials Science and Engineering: A*, *473*(1-2), pp.147-152.

Appendix

Appendix A – EBMQ20 Specification

GT6600/6600C

GiGE VISION

Description

NEW: High sensitivity 29 Megapixel KAI camera for outdoor imaging

The Prosilica GT6600 is a 29 Megapixel camera with a Gigabit Ethernet interface (GigE Vision®). The GT6600 is a rugged camera designed to operate in extreme environments.

- Truesense KAI-29050 sensor
- Power over Ethernet (PoE)
- Ethernet surge suppression
- Gamma, multiple LUT, color correction
- Metadata (Chunk data)
- Clock synchronization (IEEE1588)
- Wide operating temperature range
- Global shutter (digital shutter)

- **Models:**
  - GT6600, 6576 x 4384, 4 fps, CCD mono
  - GT6600C, 6576 x 4384, 4 fps, CCD color

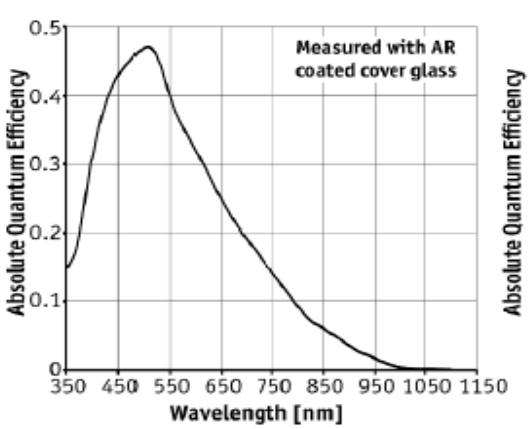
Measured with AR coated cover glass
Absolute Quantum Efficiency
0.5
0.4
0.3
0.2
0.1
0
350 450 550 650 750 850 950 1050 1150
Wavelength [nm]

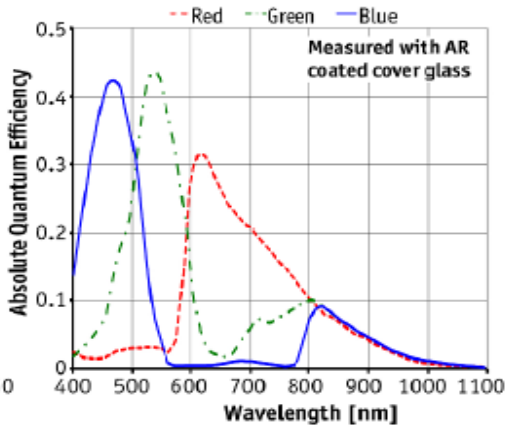
Red
Green
Blue
Measured with AR coated cover glass
Absolute Quantum Efficiency
0.5
0.4
0.3
0.2
0.1
0
400 500 600 700 800 900 1000 1100
Wavelength [nm]

Specifications

Prosilica GT	6600
Interface	IEEE 802.3 1000baseT
Resolution	6576 x 4384
Sensor	Truesense KAI-29050
Sensor type	CCD Progressive
Sensor size	Type 35 mm
Cell size	5.5 µm
Lens mount	F-Mount (M58 optional)
Max frame rate at full resolution	4 fps
A/D	14 bit
On-board FIFO	128 MB
	Output
Bit depth	14 (mono) - 12 (color) bit
Mono modes	Mono8, Mono12, Mono12Packed, Mono14
Color modes YUV	YUV411Packed, YUV422Packed
Color modes RGB	RGB8Packed, BGR8Packed, RGBA8Packed, BGRA8Packed
Raw modes	BayerGR8, BayerGR12, BayerGR12Packed
	General purpose inputs/outputs (GPIOs)
TTL I/Os	1 input, 2 outputs
Opto-coupled I/Os	1 input, 2 outputs
RS-232	1
	Operating conditions/Dimensions
Operating temperature	-20°C ... +50°C
Power requirements (DC)	PoE, or 7-25 VDC
Power consumption (12 V)	6.6 W @12 VDC
Mass	372 g
Body Dimensions (L x W x H in mm)	96 x 66 x 53.3 (including connectors, w/o tripod and lens)
Regulations	CE, FCC Class A, RoHS (2011/65/EU)

Appendix B: Cost of LayerDD system

Cost of LayerDD

The cost of LayerDD can be dividing into four prospective:

- Hardware
- The additional process time
- Analyse cost
- Analyse data storage

Hardware

Although the NIR camera is built with the exiting machine, unfortunately the additional cost of the camera was not given by ARCAM, thus the following cost will be based on the current camera set up. The cost of the camera will be about £15000, and the set-up of the NIR camera system will be estimated to be £2000:

In a common industrial environment, the hardware will be depreciate in 5 years, thus the hourly rate of camera system will be:

Equation 1

$$\frac{17000}{5years * 8760hour/year} = £0.38/hour$$

Additionally, the EBM machine's utility rate will not be 100%, an optimistic scenario should have machine usage rate of 80%, which will gives an hourly rate of £0.475/hour (0.38/0.8 = 0.475).

Additional EBM Process Time

Since the camera is designed to be open when the electron beam is not active, thus it taken additional time to the process. By using a stop watch, the average time for the camera system

is approximately 3s per layer. Additional, in order for LayerDD to work, the camera calibration will take maximum 3min per build.

By assuming there should be one operator per machine, the hourly cost for an operator is approximately £20/hour in a research scenario. As during the production situation, one single operator should be able to maintain 2 to 3 EBM machines.

As for one EBM machine, the price for one machine is about £1,000,000, with the maintenance cost of £35,000 per year per machine. Similar to camera, the depreciation cost for the EBM machine.

Thus the hourly rate for the EBM process is:

Equation 2

$$\frac{£1000000}{5years * \frac{8760hour}{year}} + \frac{35000}{8760} + \frac{20}{2} = £36.8/hour$$

If each layer taken additional 3 second of process time, this will add a cost of £0.031 per layer together with 3 minute of calibration cost at £1.84/build.

Analysis Cost

Although majority of the work will be done by the computer automatically, but there is still need some extra time to set up a LayerDD analysis task. An experienced operator should able to set up the job with an hour. Thus the additional labour cost should be £20/build.

The software requires MatLab to analysis but the cost will be not included in the running cost, which only be the initial development will cost.

Analysis Data Storage

The LayerDD system generate raw data about 10MB/image, as a mandatory storage plan in Aerospace, all the log file data should be store as long as the product life last. An average cost of storage is approximately £14,000 per TB of storage. This will come to a cost of £0.14/image.

The analysis result is currently stored as Magics file, where the size is very dependent on the quantity of LOF within the build. Base on hundred plus EBM build and LayerDD result, the Magics file size have never exceed 400MB. Thus, the maximum cost to store one LayerDD result is £5.6/build.